

Universitat de València  
Departament de Física Teòrica



**Performance Enhancement of a Small Animal  
Positron Emission Tomograph based on  
Continuous Crystals and Silicon  
Photomultipliers**

Tesis Doctoral en Física

Programa de Doctorado en Física: RD. 1393/2007

Ane Miren Etxebeste Barrena

Abril de 2017

Directores:

Gabriela Llosá Llácer  
Josep F. Oliver Guillén  
José Bernabéu Alberola



Dra. Gabriela Llosá Llácer, Investigadora Ramón y Cajal del Consejo Superior de Investigaciones Científicas (C.S.I.C.),

Dr. Josep F. Oliver Guillén, Técnico Superior de Investigación de la Universitat de València,

Dr. José Bernabéu Alberola, Profesor de la Universitat de València.

CERTIFICAN:

Que la presente memoria *Performance Enhancement of a Small Animal Positron Emission Tomograph based on Continuous Crystals and Silicon Photomultipliers* se ha realizado bajo su supervisión en el Departament de Física Teòrica de la Universitat de València por Dña. Ane Miren Etxebeste Barrena y constituye su tesis para optar al grado de doctora en Física.

Y para que así conste, firman el presente certificado en Burjassot a 25 de abril de 2017.

Fdo.: Gabriela Llosá Llácer Fdo.: Josep F. Oliver Guillén Fdo.: José Bernabéu Alberola





*A mis queridos padres,*

*Miguel Ángel y Maite,*

*por su apoyo incondicional.*



# Table of contents

<b>List of figures</b>	<b>vii</b>
<b>List of tables</b>	<b>xv</b>
<b>List of Abbreviations</b>	<b>xix</b>
<b>Introduction</b>	<b>1</b>
<b>1 Positron Emission Tomography</b>	<b>5</b>
1.1 PET Basics . . . . .	5
1.2 PET Physics . . . . .	6
1.2.1 Positron emission . . . . .	6
1.2.2 Annihilation . . . . .	6
1.2.3 Coincidence detection . . . . .	7
1.3 Image Effects . . . . .	7
1.3.1 Degradation caused by Physical Effects . . . . .	8
1.3.1.1 Positron Range . . . . .	8
1.3.1.2 Acollinearity . . . . .	8
1.3.1.3 Depth of interaction . . . . .	9
1.3.1.4 Detector size . . . . .	11
1.3.2 Degradation caused by Coincidence Detection Method . . . . .	12
1.4 PET Detectors . . . . .	15
1.4.1 Scintillator crystal . . . . .	16
1.4.1.1 Scintillator process in inorganic scintillators . . . . .	16
1.4.1.2 Properties of the ideal Scintillator for PET . . . . .	17
1.4.1.3 Scintillator crystal surface: roughness and coating . . . . .	19
1.4.2 Photodetector . . . . .	20
1.4.2.1 Photomultiplier Tubes (PMTs) . . . . .	21
1.4.2.2 Silicon Detectors . . . . .	21

1.4.3	Detector parameters . . . . .	25
1.4.3.1	Energy resolution . . . . .	25
1.4.3.2	Timing resolution . . . . .	26
1.4.3.3	Spatial Resolution: pixelated and continuous crystals . . . . .	26
1.5	Overview of position estimation methods in monolithic crystals . . . . .	27
1.5.1	Anger Logic or Centre of Gravity . . . . .	28
1.5.2	Statistical Methods based on precalibration process . . . . .	28
1.5.2.1	Least Squares (LS) Criterion . . . . .	28
1.5.2.2	Chi Square ( $\chi^2$ ) . . . . .	28
1.5.2.3	Nearest Neighbours . . . . .	29
1.5.2.4	Maximum Likelihood (ML) . . . . .	29
1.5.3	Neural networks (NN) based positining algorithms . . . . .	29
1.5.4	Analytical and theoretical models of the light distribution . . . . .	30
1.6	Data Acquisition in PET . . . . .	32
1.6.1	Data acquisition mode: 2D and 3D PET . . . . .	32
1.6.2	Data formats . . . . .	33
1.6.2.1	Line Integral Approximation and Sinograms . . . . .	34
1.6.3	Data sampling and reduction . . . . .	35
1.6.3.1	Angular Sampling . . . . .	36
1.6.3.2	Axial Sampling . . . . .	36
1.6.3.3	Maximum ring difference (RD) . . . . .	37
1.7	Image Reconstruction . . . . .	37
1.7.1	2D Analytical Reconstruction Methods . . . . .	39
1.7.2	3D Analytical Reconstruction Methods . . . . .	44
1.7.2.1	3D reprojection algorithm (3DRP) 3D reconstruction method . . . . .	44
1.7.2.2	Rebinning methods . . . . .	44
1.7.3	Iterative Reconstruction Methods . . . . .	46
1.7.3.1	Maximum Likelihood Expectation Maximization (ML-EM) . . . . .	48
1.7.3.2	Ordered Subsets Expectation Maximization (OSEM) . . . . .	49
1.8	Monte Carlo Simulations . . . . .	50
1.9	NEMA NU-4 2008 Standard . . . . .	50
<b>2</b>	<b>Detector Head Characterization</b>	<b>53</b>
2.1	Detector description . . . . .	53
2.1.1	Scintillator crystals . . . . .	53
2.1.2	SiPM array . . . . .	54

2.1.3	Electronics . . . . .	54
2.1.4	Position determination set-up . . . . .	55
2.2	Detector characterization . . . . .	57
2.2.1	Pedestal measurement of the MAROC2 . . . . .	58
2.2.2	Discriminator threshold of the MAROC2 . . . . .	59
2.2.3	Energy Resolution . . . . .	62
2.2.4	Time Resolution . . . . .	63
2.3	Monte Carlo Simulations . . . . .	64
2.3.1	Properties of materials and surfaces included in the simulations . . . . .	65
2.3.2	Properties of the SiPM array performance . . . . .	66
2.3.3	Simulation validation . . . . .	66
2.4	Position Determination . . . . .	68
2.4.1	Previous studies . . . . .	70
2.4.1.1	Optimization of the distance from the source to the crystal surface . . . . .	70
2.4.1.2	Effect of the VS0 and VS1 models on simulated diffuse and specular reflectors . . . . .	71
2.4.1.3	Comparison of the model performance with experimental data using diffuse and specular reflectors . . . . .	72
2.4.1.4	Parameter selection for Position Reconstruction algorithm in experimental data with white painted crystals . . . . .	72
2.4.2	Determination of X-Y resolution . . . . .	78
2.4.3	X-Y bias determination with simulated data . . . . .	80
2.4.4	DoI resolution and Bias for experimental data . . . . .	80
2.4.5	DoI resolution and bias for validated simulations. . . . .	82
2.4.6	DoI resolution and bias for simulated optimized geometries . . . . .	82
2.4.6.1	Aspect Ratio of the Scintillator . . . . .	83
2.4.6.2	Effect of reflector type on DoI . . . . .	85
2.5	Two head PET prototype . . . . .	88
2.6	Conclusions . . . . .	90
<b>3</b>	<b>Simulation Study of a Full Ring Prototype</b>	<b>93</b>
3.1	Simulated Full Ring scanners . . . . .	94
3.1.1	Geometry of the simulated scanners . . . . .	94
3.1.2	Monte Carlo simulation . . . . .	96
3.1.2.1	Material and Surfaces properties . . . . .	96
3.1.2.2	Scanner Geometry implementation . . . . .	99

3.1.2.3	Sources and phantoms . . . . .	102
3.1.3	Digitizer and Coincidence sorter . . . . .	103
3.2	Performance study of the Position Estimation method when applied to a Full ring . . . . .	103
3.3	Image Reconstruction . . . . .	108
3.3.1	Image Reconstruction methods . . . . .	109
3.3.2	Impact of the Position Estimation artefacts in the image reconstruction	109
3.4	Comparison of the performance of the scanners . . . . .	113
3.4.1	Spatial Resolution . . . . .	114
3.4.2	Scatter Fraction, Count Losses, and Random Coincidence Measurements . . . . .	121
3.4.3	Sensitivity . . . . .	128
3.4.3.1	NEMA sensitivity . . . . .	128
3.4.3.2	Sensitivity Map . . . . .	129
3.4.3.3	Image Reconstruction of Homogeneous regions . . . . .	133
3.5	Discussion . . . . .	136
3.6	Conclusions . . . . .	138
<b>Conclusions</b>		<b>139</b>
<b>Resumen</b>		<b>141</b>
Introducción . . . . .		142
Caracterización de la cabeza detectora . . . . .		142
Caracterización de un escáner de anillo completo basado en simulaciones . . . . .		149
Conclusiones . . . . .		156
<b>References</b>		<b>159</b>
<b>Appendix A GATE Generic Repeater to build a scanner based on tapered crystals</b>		<b>167</b>
<b>Appendix B Contributions related to the thesis</b>		<b>169</b>

# List of figures

1.1	Illustration of an ideal LoR. . . . .	6
1.2	Relationship between the acollinearity and the angular deviation from collinearity and the radius of the scanner when the annihilation occurs at the centre of the scanner. . . . .	9
1.3	Parallax error caused by DoI uncertainty . . . . .	10
1.4	Scintillator crystals. In (a) a block of 64 pixelated crystals and in (b) monolithic white painted crystal. . . . .	11
1.5	Intrinsic spatial resolution of a pair of face-to-face detectors. The figure is taken from [15] . . . . .	12
1.6	Types of coincidence events. From left to right: True, Scatter, Random, Multiple coincidences. The figure is based on [6]. . . . .	13
1.7	Illustration of the different types of multiple coincidences. . . . .	15
1.8	Energy band structures of an inorganic activated scintillator. The figure is from Knoll [19]. . . . .	17
1.9	An example of Stokes effect for LSO scintillator with a $Ce^{3+}$ luminescence centre taken from [20]. Left, the energy levels of the activator depending on the configuration of the lattice. Right, the emission and absorption spectra for the electron transitions shown in the left. . . . .	18
1.10	A PN junction in equilibrium where the Fermi level is constant along the system. The built-in potential along the depletion zone is depicted. . . . .	22
1.11	A PN junction with an external voltage ( $V_a$ ) applied. . . . .	23
1.12	The analytical model for the light distribution and the representation of the three considered contributions to the detected light. . . . .	31
1.13	Comparison of 2D PET measurements and fully 3D. In 2D mode direct and cross planes (organized into direct planes) are collected, but in 3D mode all oblique planes are collected [41]. . . . .	33

1.14	The projection $p(x_r, \phi)$ obtained by the integration along parallel LoRs at an angle $\phi$ [43]. . . . .	34
1.15	Left, a 2D object consisting of several circular regions of different activities. Right, the sinogram of that object. . . . .	35
1.16	Axial Sampling: span of 7 . . . . .	37
1.17	Michelograms for 16 ring scanner: (a) 2D PET with a span of 7 and (b) 3D PET with a span of 7 and a RD of 15. . . . .	38
1.18	2D central section theorem, showing the equivalence between the 1D Fourier transform of the projection and the central section at the same angle through the 2D Fourier transform of the object [43]. . . . .	40
1.19	Left, an efficient manner of back-projecting in which for a given angle the value of the projection is back-propagated for each $x_r$ . Right, the back-projection at a given angle is equivalent to placing the 1D transform of the projection into a line (array) representing $F(v_x, v_y)$ at the same angle. The oversampling can be clearly seen in the right [47]. . . . .	40
1.20	In the left, in (a) ideal synthetically generated sinogram for a hot and cold rod phantom and in (c) the corresponding filtered sinogram are shown. In the right, in (b) the back-projection of the sinogram and in (d) the back-projection of the filtered sinogram are presented. . . . .	43
1.21	Flow diagram to represent iterative process of optimizations. Figure from [48]	48
2.1	The detectors employed in the measurements: (a) several scintillator crystals with 5 and 10 mm thicknesses painted white and covered with a specular film, (b) the SiPM array from AdvanSiD and (c) 5 mm thick crystal coupled to the SiPM which is connected to the PCB. . . . .	55
2.2	Experimental set-up for the position estimation. . . . .	56
2.3	Geometry (not to scale) of the experimental set-up for interaction position determination. On the left the set-up for the transversal resolution and on the right DoI resolution set-up. . . . .	57
2.4	Measured pedestals (a) of the electronic board and ASIC, (b) with the SiPM connected to it without applying bias, (c) applying 3 V overvoltage bias and (d) obtained with the whole detector and 3 V overvoltage bias for one channel. . . . .	58
2.5	Distribution of the pedestals of the 64 channels of the detector. . . . .	59
2.6	The distribution of the maximum intensity channel is shown in (a) and (b) for different DAC1 threshold values using 5 and 10 mm thick crystal respectively. . . . .	60
2.7	The measured spectra is shown in (a) and (b) and for different DAC1 threshold values using 5 and 10 mm thick crystal respectively. . . . .	60



2.8	The effect of the DAC1 threshold in measurements. (a) and (b) show the percentage of the total charge distribution in each pixel, (c) and (d) show the estimated DoI distribution and (e) and (f) show the normalized energy spectrum applying a threshold value of 800 and 1150 (a.u.) respectively for 15000 events using an electronically collimated $^{22}\text{Na}$ source. . . . .	61
2.9	$^{22}\text{Na}$ spectra using 10 mm thick crystal measured with MAROC2 readout board. Energy spectrum in ADC units without pedestal subtraction is shown in (a) and the calibrated energy spectrum in keV units is shown in (b). . . .	63
2.10	Schematic of the set-up for time resolution measurement. . . . .	64
2.11	Coincidence resolution time measurement with a $^{22}\text{Na}$ point-like source. . .	64
2.12	Agreement between the percentage of the total detected mean charge distribution for experimental and simulated data for different values of the probability of having specular reflections using 5 mm thick crystal and the beam located in the central position . . . . .	66
2.13	Comparison of the simulated (black) and experimental (green) normalized charge accumulation for two positions, central position and the one close to the edge, for 5 and 10 mm thick crystals. . . . .	67
2.14	Resolution (FWHM) for a central point at different distances. . . . .	70
2.15	X-Y contours of the DRIPs at HM and at TM for simulations with ideal specular reflector and diffuse reflector. On the left modelling specular reflections with the same weight as the direct light (VS1) and on the right without modelling reflections (VS0). . . . .	71
2.16	X-Y contours at HM and at TM for experimental data for specular reflector and white painted (diffuse reflector) 10 mm thick crystals. . . . .	72
2.17	Fit of a profile through the maximum of the reconstructed interaction position distribution for a 10 mm thick crystal with a Gaussian function (solid line) and with a Lorentzian function (dashed line). . . . .	73
2.18	X-Y contours at HM and at TM of the DRIP for experimental data (beam located at the corner position) and different values of AL. . . . .	75
2.19	X-Y contours of the DRIP at HM and at TM for different models. . . . .	76
2.20	X-Y and Y-Z projection of the interaction position distribution for the position located at the edge of 10 mm thick crystal are shown in (a) and (b) respectively applying VS0 model and in (c) and (d) applying VS1 model. The Z-coordinate increases towards the SiPM. . . . .	78

2.21	Contours at HM and at TM of the X-Y projections of the distributions of the reconstructed position interactions for a point-like source in four different positions for the 5 mm thick crystal ((a),(b)) and for the 10 mm thick crystal ((c),(d)) and VS0 model. . . . .	79
2.22	Y-Z projection of the reconstructed position distribution (a,c) and DoI error distribution (b,d) for 5 and 10 mm thick crystals respectively. Data were acquired with a collimated point source incident on the detector surface at a 45° angle. . . . .	81
2.23	Y-Z projection of the reconstructed position distribution (a,c) and DoI error distribution (b,d) for 10 mm thick crystal with specular reflector using VS0 and VS1 respectively. Data were acquired with a collimated point source incident on the detector surface at a 45° angle. . . . .	81
2.24	Y-Z projection of the reconstructed position distribution (a,c) and DoI error distribution (b,d) for 5 and 10 mm thick crystals respectively. . . . .	82
2.25	The charge distribution of different events that have interacted at different depths along the crystal: (a) 5 mm and (b) 1 mm from the photodetector using validated simulations of the 10 mm thick crystal. . . . .	83
2.26	Y-Z projection of the reconstructed position distribution for the validated simulation with 10 mm thick crystal and different value of the AR, (a) AR=1.2, (b) AR=1.78 and (c) AR=2.4. . . . .	84
2.27	DoI distribution errors by sections (a) for AR=1.2 and (b) for AR=2.4. . . . .	85
2.28	(a) DoI bias and resolution (error bar) by sections and (b) DoI resolution by DoI sections. . . . .	85
2.29	DoI distribution errors by sections for ideal specular reflector (a) using VS0 model and (b) VS1 model. . . . .	87
2.30	(a) DoI bias and FWHM (error bar) and (b) DoI resolution by DoI sections for 100% specular reflector using VS1 model and VS0 model. . . . .	87
2.31	Y-Z (DoI) projection of the reconstructed position distribution (a) for the 100% diffuse reflector using VS0 model, (b) for mixed reflector using VS0 model and (c) for 100% specular reflector using VS1 model. . . . .	88
2.32	(a) DoI bias and FWHM (error bar) and (b) DoI resolution by DoI sections for different reflectors. The shape of the DoI error distribution of last three sections for diffuse reflector and for validated simulation is not Gaussian, the distributions have large tails. . . . .	88
2.33	The PET prototype developed at IFIC. . . . .	89

2.34	(a) Transverse, (b) coronal and (c) sagittal plane of the reconstructed image of two $^{22}\text{Na}$ point sources of 1 mm nominal diameter with the prototype. . . . .	89
3.1	Scanner geometries. Left: scanner based on 16 tapered crystals. Right: equivalent scanner based on 12 cuboid crystals. . . . .	95
3.2	Inner ring of the scanner as a function of the $l_{gap}$ for cuboid system and for tapered system for different thickness of the crystal. . . . .	96
3.3	$^{176}\text{Lu}$ decay scheme to $^{176}\text{Hf}$ source:larawebfree. . . . .	97
3.4	Volumes of the sources of the Monte Carlo simulations to simulate the natural radioactivity of LYSO crystals. Left, simulated volumes for cuboid configuration. Right, simulated volumes for tapered configuration. . . . .	98
3.5	Spectrum of the Lutetium natural radioactivity in singles mode in the full ring geometry: (a) for ideal energy resolution and (b) for an energy resolution of 12% at 511 keV. . . . .	99
3.6	Ring Repeater. Images from GATE user's guide. . . . .	100
3.7	Illustration of the default orientation of the creation of a tapered volume in GATE with respect to the global reference system. Figure (a) shows the view of a tapered crystal from X-axis and figure (b) from Z-axis. . . . .	101
3.8	Illustration of the use of the ring-repeater with autorotation option enabled applied to tapered crystals in different configurations and illustration of the use of generic repeater. In (a) the ring-repeater is applied to re-orientated tapered crystals in a cylindrical scanner orientated along Z-axis (default orientation), in (b) is applied to tapered crystals re-orientated as in figure (a) in a scanner with box shape, in (c) it is applied to tapered crystals (default orientation) in a scanner with box shape and in (d) the generic repeater has been used to position each of the crystal in a cylindrical scanner along Z-axis. . . . .	102
3.9	Schematics of the positioning of the sources for spatial resolution measurements in transaxial plane. The dashed line represent the inner radius of the scanner and the points the positions of the sources at 5 mm, 10 mm, 15 mm and 25 mm from the center of the scanner. The size of the sources is not to scale. . . . .	114
3.10	Transversal and coronal central slices of the superposition of the reconstructed images of the 4 positions of the point-like sources using FBP algorithm applied to a FoV of 60.2 mm×60.2 mm×18 mm with a voxel size of 0.2 mm×0.2 mm×0.4 mm for tapered (a,c) and cuboid (b,d) geometry. . . . .	119

3.11	Operations applied to sinograms according to NEMA to obtain total counts, true counts and scatter plus random counts for each acquisition and each slice. The collected sinogram (a), the sinogram with the mask applied (b), the aligned sinogram (c) and the sum projection (d) for cuboid configuration and mouse-like phantom are shown. . . . .	122
3.12	Count rate capability for the full ring based on cuboid crystals with a coincidence dead-time of 10 $\mu$ s. (a) shows the count rates estimated following NEMA standard and (b) represents ground-truth count rates obtained from Monte Carlo information. . . . .	124
3.13	Count rate capability using: (a,b) the mouse-like phantom and (c,d) the rat-like phantom for the system based on cuboid and tapered crystals respectively. Dead-time was set to 10 $\mu$ s. . . . .	125
3.14	Illustration of the seventh grade polynomial curves adjusted (continuous lines) to the NECR (red squares) and True count rate (black triangles) values obtained from the simulations of the scanner based on cuboid crystals using the mouse-like phantom. . . . .	126
3.15	NECR according to NEMA standards for tapered and cuboid systems for mouse-like phantom. . . . .	127
3.16	Axial sensitivity profile at radial center for scanners based on tapered and cuboid crystals . . . . .	129
3.17	Profiles in (a) axial and (b) transverse direction through the centre of the of the sensitivity map discretized in voxels of $2 \times 2 \times 0.712 \text{ mm}^3$ for SSRB and SPAN1 axial rebinning policies and for both crystal geometries. . . . .	130
3.18	Sensitivity map based on Monte Carlo simulation of an homogeneous cylinder covering the entire FoV. (a) and (b) show the sensitivity map using SSRB policy for cuboid and tapered geometry respectively and (c) shows the subtraction of transverse sensitivity map for tapered and cuboid geometry. (d) and (e) show the sensitivity map using SPAN1 policy and (f) shows the subtraction. . . . .	132
3.19	Sensitivity map based on Monte Carlo simulation of an homogeneous cylinder covering the entire FoV using SSRB (a-c) for cuboid geometry and (d-f) for tapered geometry applying different thresholds to the image so that all the pixels with a value below the threshold are represented by white color. (a,d) show the sensitivity map without any threshold, (b,e) with a threshold value of 1% and (c,f) with a threshold value of 1.8% . . . . .	133

---

R.1	Detector empleado en las mediada. Se muestra en (a) en la parte inferior de la imagen los cristales con reflector especular y en la parte superior los cristales pintados de blanco, en (b) la matriz de SiPMs y en (c) el cristal centelleador pintado de blanco acoplado al SiPM. . . . .	143
R.2	Geometría (no a escala) del dispositivo experimental para la determinación de la posición. A la izquierda se muestra la configuración para las medidas de resolución transversal y a la derecha la de resolución en DoI. . . . .	144
R.3	Contornos a media altura y a un décimo de altura de las proyecciones X-Y de las DPIR para las cuatro posiciones de la fuente: (a,b) para el cristal de 5 mm de grosor y (c,d) para el cristal de 10 mm de grosor respectivamente. . . . .	147
R.4	(a,c) Proyección Y-Z de la DPIR y (b,d) la distribución del error de DoI para los cristales de 5 y 10 mm de grosor respectivamente. Los datos fueron adquiridos con una fuente colimada incidiendo con un ángulo de $45^\circ$ sobre la superficie. El haz incide con la dirección creciente de la coordenada z. . . . .	148
R.5	NECR obtenido siguiendo las indicaciones del NEMA para ambas geometrías para el caso de un maniquí tipo ratón con un tiempo muerto en (a) de $10 \mu s$ y en (b) de $64 \mu s$ . . . . .	154
R.6	Perfil de la sensibilidad axial en la posición central en el plano transaxial para ambas configuraciones. . . . .	154
R.7	Mapa de sensibilidad basado en simulaciones Monte Carlo de un cilindro homogéneo que cubre todo el campo de visión del escáner utilizando la política SSRB de rebineado axial para (a) el escáner basado en cristales trapezoidales y (b) el escáner basado en cristales cúbicos. Se muestra en (c) la resta del mapa de sensibilidad basado en cristales trapezoidales menos el correspondiente a cuboides. . . . .	155



# List of tables

1.1	Properties of the most commonly isotopes used for PET . . . . .	8
1.2	Properties of common inorganic scintillator materials used in PET. As otherwise mentioned, data is taken from [22]. . . . .	19
1.3	Properties of photodetectors taken from[27]. . . . .	21
2.1	Optical interfaces defined in the simulations. The rest of the interfaces were defined as dielectric-dielectric surface, following Snell equations with specular reflections. . . . .	65
2.2	Light distribution models. Relationship between the contribution of virtual sources ( $A_{0VS}$ ) and direct light ( $A_0$ ). . . . .	73
2.3	Average resolution of the four reconstructed positions obtained fitting the profile through the maximum in X and Y directions for the 5 mm thick white painted LYSO crystal. . . . .	74
2.4	Average resolution of the four reconstructed positions obtained fitting the profile through the maximum in X and Y directions for the 10 mm thick white painted LYSO crystal. . . . .	74
2.5	$\epsilon_{r,Position}$ is the relative error of the position of the centre of the contour of the DRIP for the corner position. . . . .	75
2.6	$l_{45^\circ}^{TM}$ and $l_{45^\circ+90^\circ}^{TM}$ are the projections along $45^\circ$ and its perpendicular of the contour at TM of the DRIP for the corner position. . . . .	76
2.7	Average resolution of the four reconstructed positions obtained fitting the profile through the maximum in X and Y directions for the 5 mm and the 10 mm thick white painted LYSO crystal. . . . .	79
2.8	Difference between the estimated interaction position and the gamma-ray source location in (X,Y). . . . .	80
2.9	Total DoI resolution and bias for the validated simulation for an entry position of the beam of 4.75 mm with different values of the AR. . . . .	84

2.10	Total DoI error and bias for the validated simulation with different reflectors. DoI error and bias was obtained from a Gaussian fit, while FWHM and FWTM of the DoI error distribution was obtained by linear interpolation. . . . .	86
2.11	Characteristics of the systems. In some of the cited works the size of the beam has been subtracted from the results (subtracted) and in others the results obtained have not been corrected by the size of the beam which is unknown (non-subtracted). For the rest the results obtained have not been corrected by the size of the beam but the size of the beam was reported and it is shown in the table. . . . .	91
2.12	Results obtained with developed systems. . . . .	91
3.1	The XY and XZ views of the cd tapered crystals in their local reference system. The origin of the coordinate system is located at the centre of the crystal. . . . .	104
3.2	Projections of the interaction position from Monte Carlo information (ground-truth) for cuboid and tapered crystals in the first row, projections of interaction position estimation using VS0 model and using VS1 model in the second and third row respectively for both cuboid and tapered crystals. . . . .	105
3.3	Percentage of interactions located at the entrance of the crystal ( $N_{entrance}$ ) for both geometries of the crystal using different models. . . . .	106
3.4	Projections of the interaction position from Monte Carlo information for cuboid and tapered crystals in the first row, projections of interaction position estimation using VS0 model and using VS1 model in the second and third row respectively for both cuboid and tapered crystals. . . . .	106
3.5	Projections of the interaction position estimation using VS0 and VS1 model to estimate X and Y coordinates and obtaining DoI from Monte Carlo information from cuboid geometry. . . . .	108



- 3.6 The impact of position estimation artefacts on the reconstructed images. First column shows the positions inside the crystal of the two endpoints for each LoR and the second and third column show the image reconstruction of these LoR using BP and FBP algorithms respectively. The reconstructed images represent all the coincidences (using SSRB and a slice thickness of the axial FoV size) in a FoV of 50.2 mm×50.2 mm with a voxel size of 0.2 mm×0.2 mm. A source located at the center of the scanner has been simulated and the ground-truth and the estimated LoRs have been processed in first and second row respectively. Another source located 15 mm away from the center of the scanner has been simulated and the ground-truth and the estimated LoRs have been processed in third and fourth row respectively. 110
- 3.7 Image Reconstruction of ground-truth interaction position for a source located at the center of the scanner and for a source located 15 mm away from the center, first and second row respectively. First column shows the positions inside the crystal of the two endpoints for each LoR and the second and third column the image reconstruction of these LoR using BP and FBP algorithms respectively. 150000 coincidences are processed for each source position. The reconstructed images represent all the coincidences (using SSRB and a slice thickness of the axial FoV size) in a FoV of 1.02 mm×1.02 mm with a voxel size of 0.02 mm×0.02 mm centred at the simulated source location. . 112
- 3.8 Resolution values reported according to NEMA at axial centre of both scanners. The image was reconstructed using FBP algorithm with SSRB. . . . 115
- 3.9 The response function in radial, tangential and axial directions from top to bottom and for from left to right the different radial offsets of the source (5,10,15,25) mm for the scanner based on tapered crystals. . . . . 116
- 3.10 The response function in radial, tangential and axial directions from top to bottom and for from left to right the different radial offsets of the source (5,10,15,25) mm for the scanner based on cuboid crystals. . . . . 117
- 3.11 Central slice of the reconstructed image and radial and tangential response functions for the source located at the center of the scanner (first row) and for the source located 5 mm from the center in the X-axis direction (second row). 118
- 3.12 Position of the maximum of the sum response function determined by a parabolic fit for both geometries. . . . . 118

3.13	Response function of radial and tangential direction for the spatial resolution measurements with the source located at 15 mm from the centre of the scanner. The first row shows the response function obtained using ideal interaction position within the crystal from Monte Carlo information, the second row using position reconstruction algorithm to estimate X and Y coordinates and using ideal Z from the information of the simulation and in the third column, using position reconstruction algorithm to obtained de 3D interaction position within the crystal. . . . .	120
3.14	Summary of Counting Rate results for Mouse-like phantom. . . . .	126
3.15	Summary of Counting Rate results for Rat-like phantom. . . . .	126
3.16	Summary of counting rate results for mouse-like phantom applying different DT values for both configurations. There is no peak up to $5200\mu\text{Ci}$ for $\text{DT}=1\ \mu\text{s}$ . . . . .	127
3.17	Sensitivity of complete axial FoV and peak detection efficiency. . . . .	129
3.18	Central slice of the reconstructed images of the homogeneous cylinder using ground-truth information for both geometries: cuboid crystals (first column) and tapered crystals (second column). First row shows the reconstructed images using FBP and second row using ML-EM and 5 iterations. . . . .	134
3.19	Central slice of the reconstructed images of the homogeneous cylinder using position determination method for both geometries: cuboid crystals (first column) and tapered crystals (second column). First row shows the reconstructed images using FBP and second row using ML-EM and 5 iterations.	135
R.1	Resolución media de las cuatro posiciones representativas en las direcciones X e Y para el cristal de 5 y 10 mm de grosor. . . . .	146
A.1	Values of the transformations applied to each detector head using the generic repeater that must be specified in GATE placements file. . . . .	168

# List of Abbreviations

## Roman Symbols

$Z$  Atomic number, The number of protons in an atom

$Z_{eff}$  Effective atomic number

## Acronyms / Abbreviations

3DRP 3D Retroprojection

APD Avalanche photodiode

CRF Coincidence Response Function

CRT Coincidence Resolution Time

CTW Coincidence Time Window

$DoI$  Depth of Interaction

ENF Excess Noise Factor

FORE Fourier Rebinning Algorithm

FoV Field of View

FSR Front Side Readout

FWHM Full Width at Half Maximum

LET Low Energy Threshold

$LoR$  Line of Response

LS Least Square

ML-EM Maximum Likelihood Expectation Maximization

NN Neural networks

OSEM Ordered Subsets Expectation Maximization

*PCB* Printed Circuit Board

PDE Photo-Detection Efficiency

*PET* Positron Emission Tomography

PMT Photomultiplier Tube

QE Quantum Efficiency

RD Maximum ring difference

SiPM Silicon Photomultiplier

SNR Signal to Noise Ratio

SR Singles Rate approximation

SSRB Single Slice Rebinning

*VoR* Volume of Response

# Introduction and Outline

Small animal preclinical scanners enable quantitative measurements of metabolic processes in vivo, labelling organic compounds with positron emitters. High spatial resolution and sensitivity are needed to provide an accurate estimation of the distribution and concentration of the radio-tracer within the body of the animal.

In the attempt to improve the performance of small animal scanners, detectors consisting of a combination of continuous crystals optically coupled to segmented photodetectors can provide higher efficiency than pixelated crystals and together with accurate interaction position estimation methods, high spatial resolution. In continuous crystals intrinsic spatial resolution is no longer limited to the size of the crystal. Depth of interaction (DoI) can also be estimated by the light distribution detected, avoiding parallax errors and leading to an improvement in spatial resolution of the system.

In the IRIS (Image Reconstruction, Instrumentation and Simulations for medical applications) group of IFIC the performance of a detector head based on a continuous crystal coupled to silicon photomultiplier arrays have been investigated with the aim of increasing the sensitivity with respect to the commonly used pixelated crystals in preclinical scanners while providing high resolution. To this end, in the first place the detector head has been characterized in the laboratory to assess the performance of this type of detectors in an imaging system. In this work, white crystals were chosen for the detectors in order to achieve the best energy and time resolution [1]. Since the main disadvantage of using continuous crystals is the difficulty to determine accurately the interaction position of the gamma-rays, the characterization was mainly focused on the position determination capability of the detector. The estimation of the interaction position was implemented using an analytical model of the light distribution including reflections on the facets of the crystal. The model of the light distribution was adapted to improve the results with our experimental data and tested at different positions of the crystal surface for different crystal thickness and different reflective materials. The intrinsic resolution obtained with the position estimation method used in this work, applied to experimental data, achieves submillimetric values and a good DoI resolution in comparison with other similar systems in the literature. In addition, a

PET prototype composed of two rotating detector heads to acquire tomographic data was assembled and employed to evaluate the imaging capability of the system.

In order to study more in detail the performance of the employed model of the light distribution, a Monte Carlo simulation of the detector head has been developed and validated through comparison with experimental data using the charge distribution as the main figure of merit. Those simulations have been employed to evaluate optimized geometries for the detector head with different aspect ratio and reflectors for the crystal.

Making use of the experience gained during the detector evaluation, detailed simulations were developed to study the performance of a full ring scanner. Besides the scanner based on cuboid crystals, a scanner based on tapered crystals was simulated with the aim of enhancing the sensitivity. Sensitivity may be increased in a full ring configuration in two ways: by using thicker crystals which allow increasing the probability of detection of gamma-rays or by increasing the solid angle coverage in a full ring system. The latter can be achieved by decreasing the ring diameter or by reducing the gaps between detectors in the ring. Increasing the thickness of the crystal or reducing ring diameter can cause larger parallax error degrading spatial resolution. Therefore, in this work, we have considered the increase of sensitivity by reducing the gaps between detectors in a ring by the use of tapered (in the transverse direction) continuous crystals. To evaluate the benefits of this geometry, two scanners with the same inner inner ring based on cuboid and on tapered crystals were simulated. The use of tapered crystals instead of cuboid crystals results in a tighter packing of the detector head in the ring geometry. The wedge shape gaps of the cuboid scanner are "filled" with scintillator material in the tapered configuration. By reducing the gaps, an increase in sensitivity is expected. However, the non-uniform geometry of the crystals makes position estimation more difficult, which can degrade spatial resolution.

The performance of the scanners was characterized following NEMA standardized protocol in order to compare them. Besides the well-known ML-EM algorithm, which is more accurate for scanners with gaps, a Filtered-Back-Projection algorithm was implemented to reconstructed the data taken with the simulated scanners as specified by NEMA. Since the main differences between scanners are expected to be in sensitivity, it was studied through two additional figures of merit. Then, in addition to the axial sensitivity measurements indicated by NEMA protocol, the sensitivity map from Monte Carlo information and the recovery of homogeneous regions were analysed for both scanners.

A significant average sensitivity gain over the entire axial FoV of 13.63% has been obtained with the tapered geometry, while similar performance of the spatial resolution has been proven. The activity at which NECR and True peak occur is smaller and the peak value is greater for tapered crystals than for cuboid crystals. Moreover, a higher degree of

homogeneity was obtained in the sensitivity map due to the tighter packing of the crystals, which reduces the gaps and results in a better recovery of homogeneous regions than for the cuboid configuration.

In conclusion, the detector presented in this thesis offers a combination of good spatial resolution, including DoI, without previous calibration needed, and high sensitivity. The imaging capability of the detector head has been assessed experimentally. Simulations of a full ring scanner have proven a significant increase of sensitivity with the use of tapered crystal without degrading spatial resolution in comparison with conventional cuboid geometry. PET technology has not reached its performance potential. Improvements can be made in terms of spatial resolution, sensitivity and image quality. This enhancement would be useful for example to detect earlier signs of cancer and to employ lower doses in diagnosis.

The work presented in this thesis consists of two parts: the detector head characterization which is mainly focused on position determination studies, and the performance characterization of a simulated full ring scanner based on tapered crystal with the aim of increasing the sensitivity and improving image quality.

A brief general introduction to PET is presented in chapter 1.

In chapter 2, the characterization of the detector head is explained. First, the characterization of the detector head based on continuous crystal and segmented photodetectors has been performed in terms of pedestal characterization, energy and time resolution. Then, position determination studies carried out, which are the main part of this chapter, are presented. They include simulation validation and studies of optimized geometries based on the developed simulation. Finally, the rotating system based on two rotating detector heads and its imaging capability are described.

Finally, in chapter 3, the comparison of the performance of two scanners with the same inner ring based on different geometries, cuboid and tapered crystals, is analysed. The performance of the interaction position estimation method applied to tapered crystals is assessed. The characterization following NEMA in terms of spatial resolution, count rates (NECR) and sensitivity is performed. Moreover, the sensitivity is studied through additional figures of merit to characterize more in detail the differences between scanners.

At the end of this manuscript we present the general conclusions of the thesis.





# Chapter 1

## Positron Emission Tomography

In this chapter a brief theoretical background necessary to follow the contents of this thesis is presented. The explanation includes the fundamentals of Positron Emission Tomography (PET) and the degradation effects caused either by physical effects as well as by the detection methods. Then, some notions about the detection system concentrating on the detectors based on continuous crystals coupled to segmented photodetectors, which are the focus of this thesis, are explained. After that, the data acquisition process in PET is described (mode, formats, sampling and reduction) and an overview of the most common image reconstruction algorithms is given. Finally, some insight in the Monte Carlo simulation tools is provided which have been extensively used in this thesis and general notions about NEMA NU-8 standard developed for the characterization of small animal PET scanners which have been followed in this thesis are also provided.

### 1.1 PET Basics

PET is a non invasive Nuclear Medicine imaging modality. Nuclear Medicine is based on the ability to trace a radioactive substance through the subject's body of study to provide a 3D map of a metabolic process. The radioactive substance employed is known as radiotracer, which is a chemical compound in which one or more atoms have been replaced by a radioisotope to obtain the information of its distribution in the body. In PET imaging, the tracer is labelled with a positron emitting radionuclide.

The positron, after losing most of its kinetic energy by inelastic collisions with atomic electrons of the tissue of the subject of study, combines with an electron decaying most commonly into two gamma rays travelling in almost opposite directions. This is commonly referred to as positron annihilation. The pair of detectors which gives a time coincidence detection of the two gamma-rays, defines a line of response (LoR) illustrated in figure 1.1.

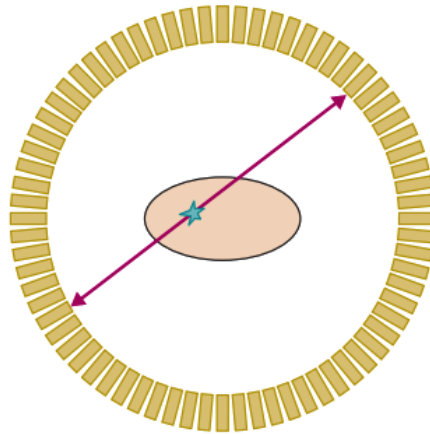


Figure 1.1 Illustration of an ideal LoR.

Measuring numerous LoRs the 3D-distribution of the radiotracer can be reconstructed by analytical or iterative methods. In the current clinical application, metabolic information from PET combined with structural information from CT (or even from MR) is becoming increasingly common. The high resolution structural information allows to locate accurately lesions indicated by PET.

## 1.2 PET Physics

### 1.2.1 Positron emission

A radioactive nucleus with an excess of either protons or neutrons (radionuclide) decays into an energetically more favoured state. The radio-tracers used in PET have an excess of protons and decay through positron emission along with a neutrino by turning a proton into a neutron. This process is also known as  $\beta^+$  decay and can be represented by equation (1.1).



The positron, which has the same mass as an electron but the opposite charge, can be emitted at a range of energies since the mass of the mother nucleus is distributed into the masses and kinetic energies of the different particles.

### 1.2.2 Annihilation

The positron emitted by the  $\beta^+$  decay will travel a certain distance in matter undergoing inelastic collisions with atomic electrons losing its kinetic energy. The net travelled distance

is known as the **positron range** and depends on the kinetic energy of the positron. When the positron comes nearly to rest, it combines with an electron (its antiparticle) and forms a hydrogen-like state called positronium (Ps). The state of the Ps prior to decay depends on the relative orientation of the spins of the electron and positron. If the total spin value is 0, singlet state, the state prior to decay would be para-positronium (p-Ps) and ortho-positronium (o-Ps) state if the total spin value is 1, triplet state. According to conservation laws, p-Ps state decays into an even number of photons and o-Ps state into an odd number of photons. The life-time of the p-Ps state is three orders of magnitude smaller than the life-time of the o-Ps, thus making even photon number decay much more common. Moreover, the probability decreases with the number of photons. Therefore, the most probable is the two-gamma decay mode which is the useful one for image reconstruction. The second most probable mode is the (4-gamma) decay mode which is already negligible having a branching ratio of  $1.49 \times 10^{-6}$  [2].

The law of conservation of energy and momentum in the rest frame of Ps for two-gamma decay mode requires that each photon carries half of the total energy equivalent to the Ps mass, 511 keV and that the two photons travel at 180 degrees from each other. However, if the momentum is non-zero at the time of annihilation there is a deviation from 180 degrees and the trajectories are not completely collinear.

### 1.2.3 Coincidence detection

The detection of the two back-to-back photons from the annihilation of the positron within a time coincidence window is called a coincidence detection. The line that connects the interaction positions in the two activated detectors is the Line of Response (LoR), when the detector finite size is considered we have a Volume of Response (VoR) also known as Tube of Response (ToR).

## 1.3 Image Effects

Ideally the LoR contains the emission point of the positron. However, due to the degradation effects caused by either the physical effects or by the coincidence detection method of the two back-to-back gamma-rays, the emission of the positron can be far away from the detected LoR degrading the image quality.

Table 1.1 Properties of the most commonly isotopes used for PET

Isotope	Half-life (min)	$E_{\beta}^{max}$ * (MeV)	$\bar{R}_{\beta}$ in soft tissue (mm)	FWHM in water * (mm)	FWTM in water * (mm)
$^{11}\text{C}$	20.3	0.970	1.52	0.188	1.86
$^{13}\text{N}$	9.97	1.19	2.05	0.282	2.53
$^{15}\text{O}$	2.03	1.72	3.28	0.501	4.14
$^{18}\text{F}$	109.8	0.635	0.83	0.102	1.03

\* Based on data from [4] .

### 1.3.1 Degradation caused by Physical Effects

Image quality in PET is degraded by the following physical factors: positron range, gamma-rays acollinearity, depth of interaction uncertainty within the scintillator crystal and detector size. These fundamental limits are described quantitatively in [3] together with potential methods to reduce the magnitude of their effects.

#### 1.3.1.1 Positron Range

The emitted positron in the  $\beta^+$  decay travels a short distance (from a few hundred micrometres to a few millimetres) before its annihilation that depends on its energy and the material through which it travels. The distance between the positron emission point and the annihilation point, is known as **positron range**. The quantity that directly degrades the spatial resolution is the **effective positron range**, that is defined as the component of the net positron displacement vector perpendicular to the LoR. The distribution of the x-coordinates of the net 3D positron displacement is characterized by a sharp peak with relatively broad tails, rather than a Gaussian function. Therefore, FWHM and FWTM should be given to characterize the distribution [4]. Table 1.1 shows the half-life, the maximum positron energy and the positron average range in soft tissue and the FWHM and FWTM of the distribution of the x-coordinates of the positron displacement vector for the most commonly used isotopes in PET.

#### 1.3.1.2 Acollinearity

The electron-positron system has non zero kinetic energy when it is annihilated in the laboratory frame. Therefore, to conserve energy and momentum, the annihilation photons travel at directions that deviate slightly from  $180^\circ$ . The maximum deviation from collinearity is  $\pm 0.25^\circ$  ( $0.5^\circ$  FWHM) [5]. Thus the ideal LoR does not intersect the emission point, and the deviation increases with the distance travelled by the photons before being detected. For

an annihilation taking place at the centre of the FoV, the relationship between the acollinearity error at the centre between two detectors ( $\Delta x$ ) and the deviation angle from acollinearity ( $\theta$ ) for small angles of deviation is  $\Delta X = R \sin(\theta/2) \sim \frac{R \cdot \theta}{2}$  as it can be deduced from figure 1.2. The angular deviation from acollinearity of  $0.5^\circ$  FWHM causes a Gaussian blurring profile at the centre of the scanner proportional to the diameter of the detector ring that can be expressed as:

$$\Delta X = 0.0044 \left( \frac{R}{mm} \right) FWHM, \quad (1.2)$$

where R is the radius of the ring.

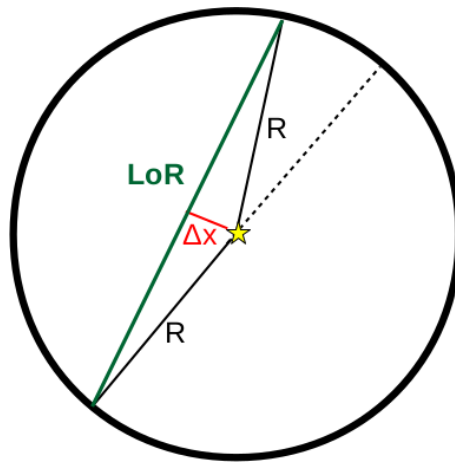


Figure 1.2 Relationship between the acollinearity and the angular deviation from collinearity and the radius of the scanner when the annihilation occurs at the centre of the scanner.

### 1.3.1.3 Depth of interaction

The uncertainty in the depth of interaction (DoI) of the gamma-ray within the detector crystal when the photon enters the detector at an oblique angle, produces an uncertainty in the determination of the LoR, therefore, an uncertainty in the annihilation point which degrades the spatial resolution.

The uncertainty increases as the incidence angle increases and annihilation takes place closer to the edges of the FoV. The resolution also degrades with the thickness of the crystal and is more pronounced for small ring diameters. This effect is illustrated in figure 1.3 and it is known as parallax error, also called radial elongation or radial astigmatism.

The uncertainty in the DoI within a crystal makes that the annihilation event could have occurred within the shaded volume defined by the two crystals that have been activated by the photons detected in time coincidence.

For ToRs outside the centre of the FoV, the effective width of the crystal ( $w'$ ) is increased due to its inclination with respect to the ToR. The effective width ( $w'$ ) is a factor  $\cos\theta + (x/w)\sin\theta$  larger than the 'real' width ( $w$ ) where  $x$  is the length of the crystal in the radial direction or the thickness of the crystal and  $\theta$  is the inclination angle of the crystal with respect to the ToR, (figure 1.3(b)).

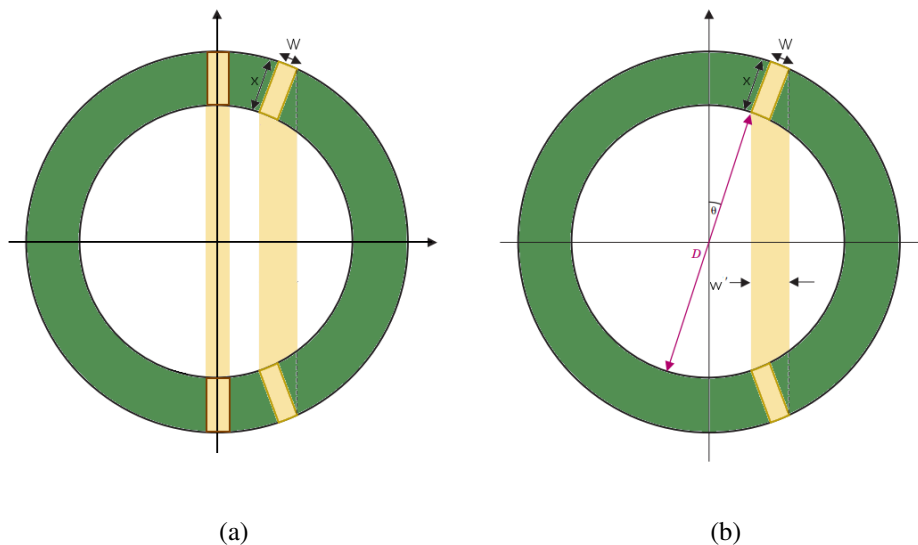


Figure 1.3 Parallax error caused by DoI uncertainty is shown for a vertical ToR close to the edge of the FoV, in (a) it is compared to the ToR defined by the opposite crystals in the centre of the scanner and in (b) its effective width ( $w'$ ) due to the inclination angle of the activated crystals with respect to it, is shown. The figure is based on [6].

Moreover, if the trajectory of the annihilation photon is not normal to the surface of the crystal it impinges upon, the photon may go through the crystal without interacting with it and then interact with another crystal. Then, the ToR would be assigned to the wrong crystal. This effect is more pronounced in pixelated crystals.

If the DoI within the crystal is determined, this blurring effect would be reduced or eliminated.

There exist different approaches to estimate the DoI. Some of them are to include extra hardware, for example using multi-layer structures with individual readout [7] or phoswich structures of two types of crystals with different decay [8] providing discrete DoI information. Pulse shape discrimination techniques have also demonstrated the capability of estimating the DoI information [9]. In continuous crystals, the light distribution has been used to estimate the DoI. Different options are read out of black painted crystals with an analog resistor network [10], estimation of the DoI using detectors on both sides of a black painted crystal

[11], fitting DoI based on parameters estimated from X-Y positions [12] and simultaneous estimation of all three coordinates without prior training [13].

#### 1.3.1.4 Detector size

In pixelated crystals in which the position of interaction within the crystal is not determined, the detector size is a dominant factor limiting the spatial resolution. Figure 1.4 shows in (a) a block of 64 pixelated scintillator crystals and in (b) a monolithic white painted crystal.

The coincidence response function (CRF) is the probability that a positron emitting point source, which is moved perpendicular to the ToR corresponding to a detector pair, is detected as a coincidence event. The effective width of the ToRs close to the edges of the FoV degrades the CRF.

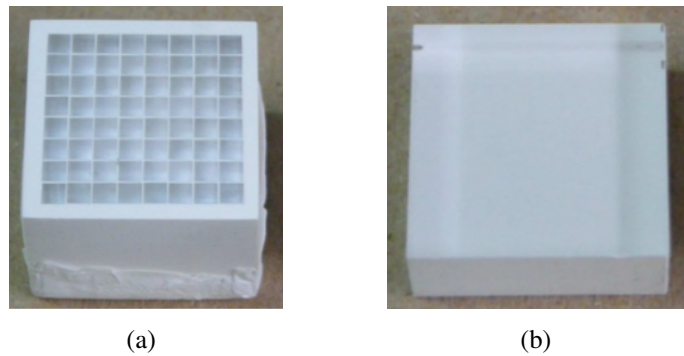


Figure 1.4 Scintillator crystals. In (a) a block of 64 pixelated crystals and in (b) monolithic white painted crystal.

**Pixelated scintillator crystal** Most clinical PET scanners use pixelated crystals. A pixelated crystal array is shown in figure 1.4(a). Ideally each pixelated crystal is coupled one-to-one to a photodetector element. However, in most of the cases, it is more practical to reduce the number of channels by reading the PET block detectors (matrix of pixelated crystals) by several photo-multiplier tubes. To this end, optical guides are employed or the matrix of pixels is generated by making saw cuts with different lengths filled with a reflective material to isolate the crystals. The different depths of the cuts are determined to share the generated light between the PMTs in order to obtain by a geometrical operation of the signals of the photodetectors X-Y coordinates of the interaction of the annihilation photon. These coordinates reflect which small crystal generates the light through an empirical look up table [14].

Intrinsic resolution of the opposing detector pair is determined by the small detector crystal size. The CRF for a 2D VoR connecting opposite identical crystals about the midpoint between them is a triangle whose FWHM is half the width of the detector element. As the source moves closer to one of the crystals the FWHM of the CRF increases and the function gets a trapezoidal shape until it becomes a rectangle with a FWHM equals the size of the crystal, see figure 1.5. For LoRs located away from the centre of the FoV, where the detector pairs are not directly facing each other, the shape of the CRF varies due to the effect of the depth of photon interaction in the detector and becomes asymmetric [15].

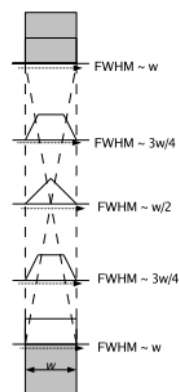


Figure 1.5 Intrinsic spatial resolution of a pair of face-to-face detectors. The figure is taken from [15]

**Monolithic scintillator crystals** Monolithic scintillator crystals consist of a continuous block through which the light can travel without constraints. The light distribution read by the photodetector contains information about the interaction position of the annihilation photon. The centre of the light distribution gives information about X-Y coordinates and the spread of the light distribution about the DoI (Z-coordinate). The intrinsic spatial resolution is determined by a position estimation algorithm. Similarly like in pixelated scintillators the CRF increases as the emission point moves away from the center of the FoV. If the intrinsic resolution of the method has a Gaussian shape, the CRF is also a Gaussian distribution. The best resolution is for the central position and the FWHM of the CRF is the intrinsic resolution divided by  $\sqrt{2}$ .

### 1.3.2 Degradation caused by Coincidence Detection Method

The quasi-simultaneous detection of the two annihilation photons by the detectors surrounding the subject of study is called time coincidence. The accuracy with which the detectors can



determine the simultaneous arrival of the two photons is called coincidence resolution time (CRT). Due to the fact that the time resolution is not perfect, a coincidence time window (CTW) must be defined to accept the coincidence events.

It is assumed that the annihilation point, which is quite close to the emission of the positron, is somewhere in the LoR defined by the two activated detectors. However, depending on the type of coincidence this is not a good assumption. There are four types of coincidence events: true, scatter, random and multiple coincidence as depicted in figure 1.6. A true coincidence is the detection of the two 511 keV photons coming from the same annihilation event within the CTW, if the detected photons have not previously interacted with the subject of study or with other part of the scanner. If at least one of the photons undergoes a Compton scattering inside the subject or in the system before being detected, we have a scattered coincidence. Random coincidences occur when two uncorrelated photons coming from different annihilation events are detected within the same CTW. Finally, if more than two photons are detected within the same CTW we have what is called a Multiple Coincidence. Therefore, only the LoR defined by the true events contains the annihilation point and provides correct information about the activity distribution being imaged.

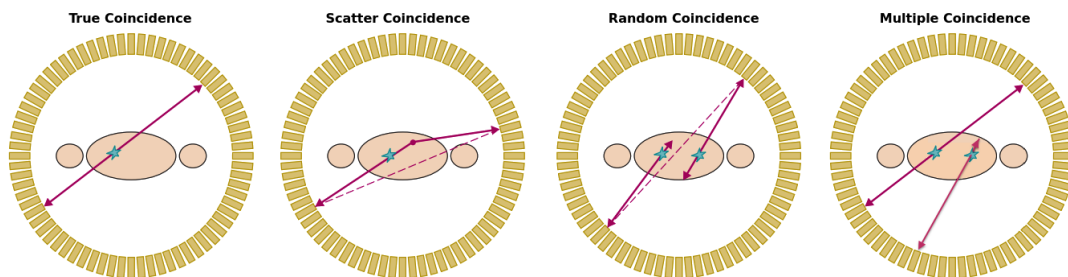


Figure 1.6 Types of coincidence events. From left to right: True, Scatter, Random, Multiple coincidences. The figure is based on [6].

Scattered events contribute to the degradation of the image reducing the contrast. This effect is more significant for large subjects. It is possible to distinguish scatter events from true events based on the energy deposition in the crystal. Scattered events can be eliminated if 511 keV photons are filtered due to the energy loss of the photon during the scatter process, but perfect energy resolution would be required. Moreover, we would lose 511 keV photons that interact in the crystal without depositing all the energy, losing sensitivity. PET systems usually employ a Low Energy Threshold (LET) about 350 keV to filter the scattered events.

Another source of degradation is random coincidences, which introduce statistical noise. There are several methods to estimate the contribution of the randoms to a given LoR. The most common method of correcting for random coincidences is called the delayed coincidence technique [16] also known as delayed Window (DW) method. The method

consists in delaying the signal of one detector by a time significantly greater than the CRT and extract coincidences between the delayed time signal in one detector and the non delayed signal in the other detector using the same sorter. When a coincidence is detected within the delayed time window it is necessarily a random because the correlations between the original signal and the delayed signal are broken. The main advantage of this method is that the estimated randoms are obtained using the same sorter as for coincidences with the same dead time properties. On the other hand, the estimated randoms by this method are quite noisy due to the relatively low statistics.

An alternative method for estimating random contribution is the singles rate approximation (SR) given by:

$$R_{randoms}^{SR} = 2\tau S_1 S_2, \quad (1.3)$$

where  $S_1$ , and  $S_2$  are the rates of the detected single photons in the considered two detectors and  $\tau$  the length of the CTW. This method assumes that the rate of true coincidences in which each detector is involved is negligible compared with the singles rate of the detector.

Equation (1.3) shows that the estimated random rate is proportional to the width of the CTW and increases as the square of the activity. Therefore, the rate of random events becomes important at high counting rate applications because the random rate increases as the square of the activity while the true coincidence rate increases linearly with the activity. Hence, the CTW should be kept as small as possible, taking into account the intrinsic CRT, to reduce random rate.

One of the advantages of this method, is that due to the high rate statistics of the detected single photons, it is characterized by lower statistical noise than DW method. As the main drawback, the SR method systematically overestimates the randoms rate [17]. Moreover, it does not take into account pile-up effects, when two or more events are detected inside the CTW opened by another event.

A method call Singles-Prompts (SP) has been proposed [18] that includes the information conveyed by prompt coincidences, models the pile-up and has the same structure as SR method to estimate the correct value for random rates.

CTW should also be kept as small as possible to reduce the detection of multiple coincidences and increase the detection of what may have been true coincidences.

Multiple coincidences refer to the case when more than two singles are detected in a coincidence event. This type of events are usually rejected because identifying which of the possible LoRs (if any) is the one which corresponds to the annihilation of the positron is non-trivial. There are several mechanisms that produce the detection of multiple coincidences illustrated in Figure 1.7. One annihilation event can produce a multiple coincidence when at least one of the annihilation photons undergoes inter-crystal scatter producing individual

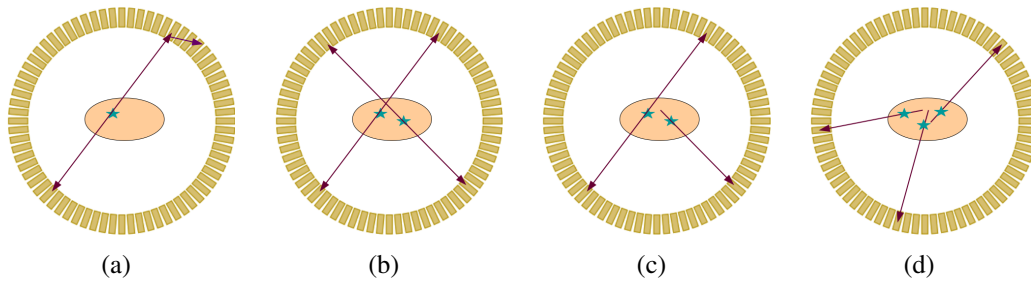


Figure 1.7 Illustration of the different types of multiple coincidences.

signals in different detectors, see figure 1.7(a). This type of events are not reduced by reducing the CTW length but increasing the LET of the energy window. Another possibility is the detection of more than one pair of correlated singles within the same CTW (figure 1.7(b)), or the detection of correlated singles together with one or more uncorrelated singles (figure 1.7(c)). Multiple coincidences can also be generated when three or more uncorrelated singles have been detected within the CTW which is known as random multiple coincidences (figure 1.7(d)).

## 1.4 PET Detectors

The detectors employed in PET imaging need to be designed for the efficient detection of the high energy annihilation gamma-rays. They rely on scintillator crystals coupled to photodetectors. The first step is the conversion of the gamma-rays into many optical photons of lower energy (few eV) and then this photons are converted into electrical signal by the photodetectors. This section introduces the basics involved in the detection process of annihilation photons and the most commonly used detectors (scintillators and photodetectors).

The main characteristics of a detector to be suitable for a PET system are good spatial resolution, high photoabsorption efficiency for annihilation photons and good energy and timing resolution.

The intrinsic spatial resolution is the ability of a detector to determine accurately the position interaction within the sensitive material and it is directly related with the image quality.

A higher photoabsorption leads to a higher fraction of photo-electrically absorbed photons; leads therefore, to a higher signal-to-noise ratio (SNR) in the images due to the smaller fraction of scattered events.

A good timing resolution allows to pair single detection into coincidences more accurately based on the detection time and to use a smaller CTW to reduce random coincidences.

A good energy resolution allows to discard unwanted events (scattered events) based on their energy deposition.

### 1.4.1 Scintillator crystal

There are two types of scintillators: organic and inorganic. Organic scintillators are composed of organic molecules with low effective atomic number ( $Z_{eff}$ ) and they are mainly used to track charged particles. For PET applications inorganic scintillators are a better choice due to their higher cross-section for stopping 511 keV photons and a light yield more proportional to the deposited energy than typically observed in organic scintillators [19]. Therefore, from now on we focus on inorganic scintillators.

#### 1.4.1.1 Scintillator process in inorganic scintillators

The scintillation process in inorganic scintillators depends on the energy states defined by the crystal lattice of the material. The crystals have a discrete structure of bands, Valence and Conduction band and the energy between them is called band gap. If the energy deposited in the crystal is above the band gap, an electron from the Valence band can jump to the Conduction band leaving a hole in the Valence band and thus, creating an electron-hole (e-h) pair.

In a pure crystal the band gap is void of electrons and its energy is usually above soft Ultra-Violet (UV). Moreover, the energy to activate an e-h pair would be the same as the light emission from the de-excitation of the electron from the Conduction to the Valence band so the crystal is not transparent to the scintillator light. Therefore, impurities are added to activate the crystal creating energy states within the band gap and enhancing the probability of visible photon emission during the de-excitation. Figure 1.8 shows the Valence and Conduction bands as well as the energy states created by the activator within the forbidden band gap. The emission occurs at activated sites giving rise to visible photons, the energy of which is smaller than the energy needed to activate an e-h pair.

There are three parts in the process of conversion from gamma ray to optical photons: excitation, thermal relaxation and photoemission. Each of the processes has a certain efficiency, so that only part of the energy deposited in the crystal by the gamma-ray is converted into low energy optical photons and another fraction of the energy is converted into thermal energy through phonons.

When a gamma ray interacts in the crystal it extracts a deeply bound electron and creates through a cascade of events a number of e-h pairs proportional to the energy deposited. At the end of the thermal process (through emission of phonons i.e. heat energy) in a pure

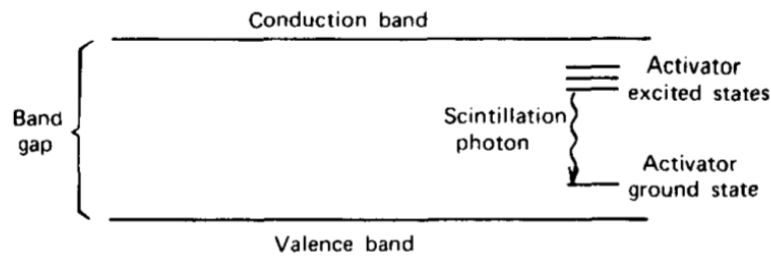


Figure 1.8 Energy band structures of an inorganic activated scintillator. The figure is from Knoll [19].

crystal the created holes have risen to the top of the Valence band and the electrons have dropped to the bottom of the Conduction band. All these processes happen in a very short time about  $10^{-12}$ s [20]. During the thermal relaxation phase, the holes ionize the activation sites [21]. An electron is captured by the impurity level close to Conduction band (energy difference between conduction band and impurity level of thermal agitation). So the activator is in an excited state and decays through the emission of the photon to the ground state of the activator just above the Valence band.

Due to the Stokes shift process the energy of the emitted photon is lower than the energy required to excite another impurity and the scintillator is transparent to its own light. Figure 1.9 depicts the Stokes effect for LSO scintillator with a  $Ce^{3+}$  luminescence centre. The configuration coordinate values of the lattice for the equilibrium position in 4f level are different from the values for equilibrium in 5d level; thus the emission and absorption for those transitions have different wavelength value. The decay of the excited activator state has a certain life time. The intensity of the scintillator light rises sharply to a maximum and decays exponentially depending on the lifetime (from a few tens of ns to a few hundred ns).

There is also a type of inorganic scintillator which does not rely on recombination centres. Bismuth Germanate (BGO) is an example of this kind of scintillator. It uses a transition state of the  $Bi^{3+}$  ion which has a relatively large shift between absorption and emission spectra.

#### 1.4.1.2 Properties of the ideal Scintillator for PET

Apart from being transparent to the wavelengths of its own emission spectra, there are some other properties that an ideal scintillator for PET application should have [19]. Some of the most important properties are a high light yield, high density, high Z number and fast decay. The light yield is the number of scintillation photons produced per unit of deposited energy in the crystal. It influences the detector's spatial, timing and energy resolution. The higher the light output the lower the statistical noise of the detected light intensity distribution in

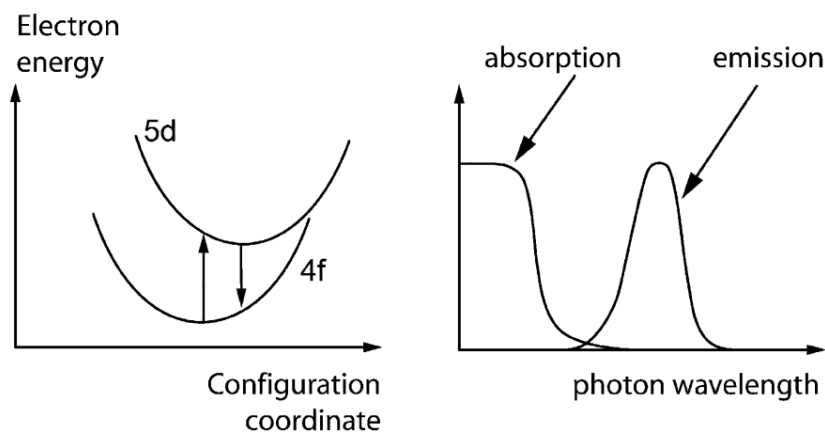


Figure 1.9 An example of Stokes effect for LSO scintillator with a  $Ce^{3+}$  luminescence centre taken from [20]. Left, the energy levels of the activator depending on the configuration of the lattice. Right, the emission and absorption spectra for the electron transitions shown in the left.

the surface of the crystal and the better the accuracy in determining the position interaction of the gamma ray. The energy resolution is also directly proportional to the light yield, and the better the energy resolution, the better the identification of scattered photons. The higher  $Z$  of the detector material, the higher the probability of the photon to interact within the crystal. Moreover, for a fixed energy of the gamma ray when  $Z$  increases, the probability of the photon of undergoing a photoelectric interaction instead of Compton interaction also increases. This is important because if all the energy is deposited in one single interaction the LoR is determined more precisely. The rise and decay time of the induced luminescence should be short to achieve a good time resolution and minimize dead time. The total energy of the low energy photons should be proportional to the deposited energy of the incoming particle. Such a conversion should be linear in the detection energy range. The emission wavelength of the scintillator should match the wavelength where the photodetector is most sensitive and the index of refraction of the scintillator should be near that of the photodetector to permit efficient coupling and maximize the light transmission. Moreover, it should be possible to manufacture it in large size and with no technological constraints (e.g hygroscopic or fragile) to be of interest as a practical detector. The properties of common inorganic scintillators used in PET systems are summarized in table 1.2.

One of the first choices for scintillator material was NaI (Tl) because of its high light yield. The main drawbacks were that it has a long decay time, low density (low stopping power) and it is hygroscopic and fragile which make it difficult to manipulate. In the 70s BGO crystal appears with a significantly better stopping power (higher density and larger

Table 1.2 Properties of common inorganic scintillator materials used in PET. As otherwise mentioned, data is taken from [22].

Properties	Scintillators				
	NaI (Tl)	BGO	GSO	LSO	LYSO(Ce) <sup>a</sup>
Density (g/cm <sup>3</sup> )	3.7	7.1	6.7	7.4	7.1
$Z_{eff}$	51	75	59	66	63
Lighth yield (ph/keV)	41	9	8	30	32
Decay time (ns)	230	300	60	40	40
Wavelength peak (nm)	410	480	440	420	420
Index of refraction	1.85	2.15	1.85	1.82	1.81
Hygroscopic	Y	N	N	N	N

<sup>a</sup> Data from Hilger Crystals. A dynasyl company.

atomic number) but with a poor light yield and decay time. It leads to a poor timing and energy resolution but good detector efficiency. In the 90s new scintillator materials were developed with silicates, particularly LSO. This scintillator has nearly the same stopping power as BGO, but it has a much larger light yield. Hence, LSO has become one of the most suitable scintillators for PET applications given its brightness and fast decay which lead to a good timing and energy resolution. However, due to the nonlinearities in the production of optical photons, the energy resolution is not as good as one might predict for its brightness [23]. One of the drawbacks of this scintillator is that it contains Lutetium, with a radioactive isotope <sup>176</sup>Lu (2.6% abundance) which decays via  $\beta^-$  with a half life of  $3.8 \cdot 10^8$  years. The energies of the main prompt gamma rays emitted from this nuclide are 88, 202, and 307 keV. In addition, the energy spectrum of internal LSO interactions shows a strong continuous background from internal beta decay. This contributes to a background count rate. However, the rate in coincidence mode is quite small so it can be used for PET imaging.

#### 1.4.1.3 Scintillator crystal surface: roughness and coating

The light transport in the crystal, and therefore the collected light distribution is dependent not only on the crystal geometry and bulk absorption and scattering of the material, but also on the surface roughness and coating. The crystal roughness (i.e., mechanically polished, chemically etched, or ground) and the reflector attached to the faces of the crystal (i.e., Teflon, ESR (Enhanced Specular Reflector) film, Lumirror,  $TiO_2$  paint, ...), and how it is attached (i.e., air-coupled or glued) influence the reflections on the surfaces of the crystal.

Different groups have developed codes to simulate the reflection in the crystal based on the properties of the crystal surfaces [24, 25].

### 1.4.2 Photodetector

The role of the photodetector is to transform the optical photons generated in the scintillator crystal into a detectable electrical signal proportional to the number of incident optical photons. A good photodetector for PET imaging should have a high Photo-Detection Efficiency (PDE), a high Quantum Efficiency (QE), high gain with low fluctuations, short response time (time jitter), should be compact and should be insensitive to temperature variations and to magnetic fields in order to be compatible with Magnetic Resonance imaging technique.

The QE is the percentage of the impinging photons that are converted into photoelectrons or electron-hole pairs, which strongly depends on the wavelength of the photons. The PDE is the photodetection efficiency which combines the probability to produce a photoelectron (QE) and produce a signal.

The gain is the multiplication factor of electrons or electron-hole pairs in the multiplication process needed to have a usable electrical signal. The fluctuations in the gain contribute to the noise. The spread in the distribution of the gains is given by the Excess Noise Factor (ENF) magnitude.

Time jitter reflects the variations of the time elapsed between the arrival of the photon and the output of the signal. A low time jitter allows a better timing resolution which is important for Time of flight PET or to use a smaller CTW.

Linearity of the response to incident radiation over a wide energy range is also important.

The compactness of the photodetectors allows to develop more complex systems, and Front Side Readout (FSR) of the scintillators placing the photodetectors in the front side of the crystal, in the inner part of the ring, so that the gamma-rays go first through the photodetector and then through the scintillator to generate optical photons.

Finally, the insensitivity of the detector to magnetic fields makes them suitable to develop a PET-MR hybrid system. Combining PET with MR, in a single gantry is technically more difficult than combining with CT and obtaining attenuation correction coefficients from MR is also more challenging [26]. However, due to the reduction of the dose to the patient and the superior soft tissue contrast of the MR the integration of PET with MR is an ongoing research topic.

There is not a detector which maximizes all the desired parameters. The majority of commercially available scanners uses Photomultiplier Tubes (PMT) as photodetector.



Table 1.3 Properties of photodetectors taken from[27].

Detector	Properties						
	PDE (%) in blue	Gain	ENF	Timing (ps) 10 ph.e	High voltage (V)	Compact	Insensitive to Magnetic Fields
PMT	20	$10^{6-7}$	1-1.5	100	1000-2000	No	No
APD	50	100-200	2 <sup>a</sup>	$\simeq 1000$	100-500	Yes	Yes
SiPM	12	$10^6$	1-1.5	30	25	Yes	Yes

<sup>a</sup> at 50 gain.

#### 1.4.2.1 Photomultiplier Tubes (PMTs)

In a PMT, optical photons enter the tube through a glass window transparent to the desired wavelengths. There is a photocathode on the back side of the window where the light interacts liberating photoelectrons that are accelerated and focused by an electric field to the first dynode. The efficiency of the conversion of scintillator light into electrons is given by the previously defined QE. The PDE is usually considered the same magnitude as QE in a PMT because the electron collection efficiency is supposed to be 1. The tube is composed of a series of dynodes in vacuum each set at higher voltage than the previous one for multiplication process of the photoelectrons. The last dynode is called anode. The anode is at ground potential and the cathode is at a negative potential around [500-2000] V. The electric signal is proportional to the incident light and it is collected in the anode.

The PMT has a high gain and low ENF. The main limitations of the PMTs are their low QE and their sensitivity to magnetic fields. Alternatives to the PMT are Avalanche photodiode (APD) and Geiger-Mode-APD (GM-APD), also called Silicon Photomultipliers (SiPM).

#### 1.4.2.2 Silicon Detectors

Semiconductor materials as silicon differ from insulators in the energy value of the gap band. Semiconductors have a lower energy band gap value than insulators. Therefore, at non zero temperatures the electrons can gain enough energy to promote to the conduction band creating an e-h pair. The missing electron in the valence band is called hole and is a positive charge carrier. Both carriers, electrons and holes, contribute to the conductivity. In a pure semiconductor the concentration of charge carriers of both types is the same. The number of carriers can be enhanced by adding impurities to the semiconductor. The process of adding impurities is called doping. There are two types of impurities: acceptor (p-type) and donor (n-type) impurities. The doped semiconductor is called extrinsic semiconductor

and depending on the doping the majority carriers are the electrons (donors) or the holes (acceptors).

This is illustrated for the case of Silicon intrinsic semiconductor in which each nucleus uses its four valence electrons to form four covalent bonds with its neighbours. In this case, atoms of group III, with 3 valence electrons as boron, are acceptors that contribute with holes; while atoms from group V, with 5 valence electrons as phosphorous are donors which contribute with negative carriers.

### PN Junction

A PN junction is fabricated by implanting impurities of the two types into a substrate of Silicon in two regions next to each other, creating regions of opposite doping type in contact. The free electrons of n-type diffuse towards the p-type regions and vice versa. When they reach the opposite doping type, they recombine creating a layer void of free carriers called depletion region (since the region is depleted of carriers). The ionized impurities produce an electric field which opposes to the diffusion. The drift current produced by the electric field sweeps holes from n-type to p-type region and vice versa (minority to majority carriers). The diffusion continues until the electric field is strong enough to reach the equilibrium so that drift and diffuse currents are equal and there is no net current flow. The potential across the depletion zone in thermal equilibrium is called the built-in potential, see figure 1.10. If an optical photon interacts in the depletion zone it has sufficient energy to create an e-h pair, the charges will be moved outside the depletion zone by the electric field and will contribute to the signal.

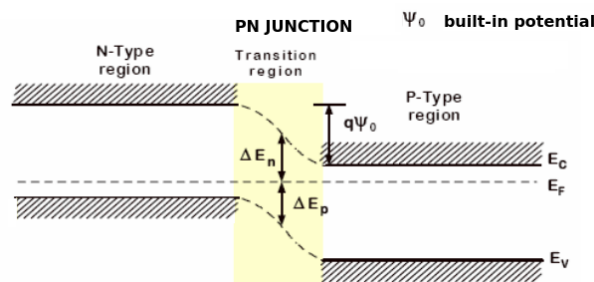


Figure 1.10 A PN junction in equilibrium where the Fermi level is constant along the system. The built-in potential along the depletion zone is depicted.

If an external voltage is applied, the PN junction works as a photodetector. Figure 1.11 shows schemes of the PN junctions with an external voltage applied. A **forward bias** corresponds to applying a positive voltage to the p-type region relative to the n-type region reducing the electrical field at the barrier. Therefore, diffusion current increases while drift

current decreases very slightly (almost the same) increasing the population of minority carriers and decreasing the depletion region width. On the other hand, if the junction is **reverse biased** the potential difference is increased at the junction and so does the depletion layer width and diffusion current decreases and the drift current dominates leading to a small net flow. Therefore, any e-h pair created in the depletion region will be swept out by the electric field, including an electrical signal.

A photodiode is a semiconductor detector consisting in a PN junction in a reverse biased mode.

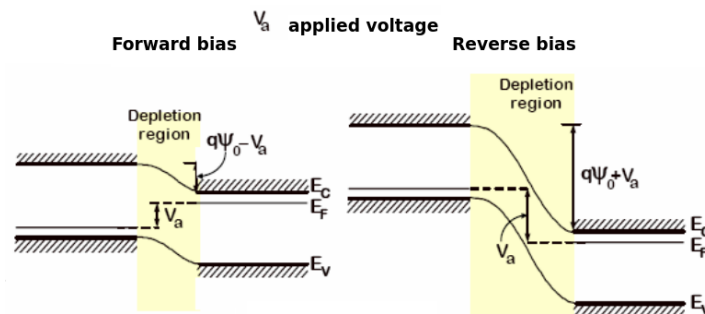


Figure 1.11 A PN junction with an external voltage ( $V_a$ ) applied.

If the reverse voltage is high enough the net current can rapidly increase and it is possible to reach the breakdown voltage. This effect can be related to tunneling effect called the Zener effect or to avalanche breakdown effect phenomena. Zener effect can only be observed in highly doped PN junctions in which the depletion region is short enough. When the depletion region is not so narrow the avalanche breakdown happens well before the Zener effect can be observed. The avalanche breakdown is explained more in detail below with the APD and SiPMs.

### Avalanche Photodiode (APD)

The APD is a PN photodiode designed to work at higher reverse bias voltage. The carriers created by the incident photons will be accelerated by the high electric field in the depleted region colliding with atoms and producing secondary carriers [28]. The collisions are produced repeatedly causing an avalanche multiplication effect resulting in an amplified signal. The factor of amplification is the gain and is only up to 1000. This is because the applied voltage is limited due to the fact that only electrons should contribute to the avalanche process. The holes should be collected before multiplication in order to have a signal proportional to the number of impinging photons. One of the main drawbacks

of these photodetectors is that the gain is strongly dependent of the applied voltage and the temperature. Moreover, the QE varies with the wavelength of the incident photon in a [60%-80%] range. The QE value is significantly higher than for PMTs. However, the ENF is worse, typically around 2 due to the higher statistical fluctuations in the multiplication process. The APD has high detection efficiency however the gain is low so they need low noise pre-amplifiers and the time resolution is also worse mainly influenced by a larger rise time than for PMTs [29] and by electronic noise. APDs have been used as an alternative photodetector to PMTs in some PET systems. Due to their compact size and insensitivity to magnetic fields, they have been successfully incorporated in the initial attempts to build PET-MR hybrid systems. However, the advantages of the APDs were not sufficient to overcome the widespread use of PMTs in PET scanners.

### **Geiger mode APD (GM-APD) or Silicon Photomultiplier (SiPM)**

An APD working in a reverse biased mode a few volts above the breakdown voltage is an APD working in Geiger Mode (GM-APD). In this operation mode, the electric field in the avalanche region is so high that the collected electrical signal is no longer proportional to the number of impinging photons and not only electrons are multiplied, but holes also generate secondary electrons. Therefore, an APD working in Geiger Mode behaves as a binary detector, which only indicates if the cell is excited or not independently of the number of impinging photons.

In order to have a detector whose electrical signal is proportional to the number of impinging photons, a matrix of small GM-APDs (known as micro-cells) is formed. The size of the micro-cells usually varies from  $25 \times 25 \mu m^2$  to  $100 \times 100 \mu m^2$ . The matrix of microcells, known as pixel, is the GM-APD detector which is commonly known as SiPM. The term SiPM is used from now on.

The signal of the SiPM pixel which is the sum of the signals from all the micro-cells is proportional to the number of impinging photons as long as the number of cells that form the SiPM is significantly larger than the total number of impinging photons. The gain of these detectors is about  $10^6$  and they have the ability to count single photons.

The PDE of a SiPM, described by equation (1.4) is given by three factors, where  $f_{geom}$  is the geometric efficiency and  $P_A$  is the avalanche breakdown efficiency. The geometric efficiency, also called fill factor, is defined as the ratio of sensitive to total area of the pixel [30] and reflects the dead spaces between and within the micro-cells in a pixel. The probability of initiating an avalanche ( $P_A$ ) is the probability of an e-h pair of creating an avalanche process.

It depends strongly on the bias voltage but also on the wavelength. The main limitation of the PDE is the fill factor.

$$PDE_{SiPM} = QE \cdot f_{geom} P_A \quad (1.4)$$

As the number of micro-cells in a pixel increases by decreasing the cell size, the dynamic range and the extent of the linearity increase but the gain and the fill factor decrease. The fill factor is reduced due to the increment of the dead regions of the series of quenching resistors to connect in parallel the GM-APDs in the pixel. The trade-off is between the dynamic range and the fill factor which reduces the PDE.

Some drawbacks of the SiPMs are dark rate and optical cross talk [31]. Dark count rate is the frequency in which the avalanche is triggered by thermally extracted carriers. SiPMs operated at room temperature have a typical dark rate value about 1 MHz for a  $1 \text{ mm}^2$  [31] which limits spatial and timing resolution performance in large area photodetectors [32]. The photons emitted by the hot carriers (electrons and holes) in an avalanche may travel to another cell of the pixel and initiate an avalanche there, which is called cross talk. As a result, more than one cell is fired by a single photon. This leads to non-linearities and additional noise.

### 1.4.3 Detector parameters

#### 1.4.3.1 Energy resolution

The energy resolution is an important property of a detector and represents the ability to distinguish between sources of similar energy and it can be characterized by its response to a mono-energetic radiation. In an ideal system the photopeak which corresponds to the full energy deposition of the mono-energetic radiation is a perfect  $\delta$ -peak, whereas in a non-ideal system, the detected peak is widened due to the finite energy resolution and its width represents the ability of the detector to resolve that energy. If the energy of two sources is separated more than one FWHM, then, the system can distinguish them. The energy resolution is given by the relative FWHM of the peak, see equation (1.5).

$$R = \frac{FWHM}{E} \quad (1.5)$$

### 1.4.3.2 Timing resolution

PET is based on the time coincidence detection of the quasi-simultaneous annihilation photons. Therefore, the ability to establish the difference in the time arrival of the two photons (CRT) is an important parameter as we have discussed in the introduction.

### 1.4.3.3 Spatial Resolution: pixelated and continuous crystals

The contribution of the detector to the spatial resolution of the systems is related to the accuracy with which the position interaction of the gamma-ray can be determined within the scintillator crystal. Scintillator crystals can be divided in two categories, pixelated and continuous crystals that have been previously described in section 1.3.1.4. In this thesis, in chapter 2, the spatial resolution in a continuous crystal employing a position interaction estimation algorithm based on an analytical model for the light distribution based on [13] will be discussed in detail.

In ideal pixelated crystals, no position algorithm is needed, the center of the pixel which generates the light is used as the interaction position. When a pixelated block is employed coordinates obtained from the signals of the PMTs are related to the center of one of the individual pixels through a look up table. Therefore, the position interaction is discrete and the maximum positioning error corresponds to half the width of a pixel. In order to determine DoI, extra hardware is needed. Several approaches have been employed like phoswich structures mentioned in section 1.3.1.3 providing discrete information and double readout of the crystal which employs the ratio of the amount of detected optical photons at opposite surfaces of the crystal to estimate DoI.

As it was explained in section 1.3.1.4 the collected light distribution in detectors based on continuous crystals contains information about the 3D interaction position. Continuous crystals coupled to finely segmented photodetectors that provide position information, together with an accurate interaction position determination algorithm, can improve simultaneously efficiency and spatial resolution. DoI information can be estimated from the light distribution without extra hardware which makes the system easier and cheaper to build, but a more complicated algorithm is needed to extract the information. The main disadvantage of continuous crystals is the difficulty to determine accurately the interaction position of the gamma-rays in the crystal which is strongly influenced by the position algorithm and detector properties and geometries. In particular when the interaction takes place close to the crystal edges, the light distribution is truncated and the position interaction is more difficult to estimate.

## 1.5 Overview of position estimation methods in monolithic crystals

The main disadvantage of continuous crystals is the difficulty to determine accurately the interaction position of the gamma-rays in the crystal, in particular when it takes place close to the crystal edges. Several groups have achieved good results in terms of spatial resolution and more specifically in terms of DoI accuracy. In some cases, the effect of the reflections is minimized by using black painted crystals or crystals with a large aspect ratio, at the cost of efficiency and degraded energy resolution. To improve this position determination, several approaches are employed with crystals painted white, black or black and white.

Statistical methods using Maximum Likelihood have proven to produce high spatial resolution [33]. However, the intensive computing calculations they required complicate their use for *real time* events acquisition and processing. Non-parametric pattern recognition methods based on training data sets, [34, 35] have shown to provide good results. As a part of recognition methods, Artificial Neural Networks have also been used for PET scanners [36] demonstrating high spatial resolution.

The main drawback in all the methods mentioned above is that they rely on a previous calibration process. This calibration is lengthy and many times it is impractical in a full scanner to create a proper data set. In addition, the calibration process must be followed every time the conditions change, for example due to temperature variations.

In order to avoid time-consuming calibrations, alternative methods based on simulation models [7] and theoretical models [10, 12, 13, 11] for the light distribution pattern have also been tested, demonstrating to provide high spatial resolution and small error near the edges of the crystals. Some of these methods also attempt to provide DoI information that is required to correct for parallax error, in particular towards the edges of the field-of-view of the scanners. In [10] black-painted crystals are read out with an analog resistor network. Some of the approaches are to include extra hardware, for example with three layers of crystals having discrete DoI [7] or detectors on both sides of a black painted crystal [11]. In [12] DoI is fitted based on parameters estimated from X-Y positions whereas in [13] all three coordinates are estimated simultaneously, without prior training. The latter method determines the 3D interaction position with only the information embedded in the signal of each event.

In this thesis, in chapter 2, we have mainly used white painted crystals in in order to achieve the best possible energy and timing resolution [1] and the position has been estimated using a position reconstruction method based on the analytical model developed in [13].

The different types of methods employed by several groups are briefly described below [37].

### 1.5.1 Anger Logic or Centre of Gravity

The Center of Gravity (CoG) is the simplest method for position determination. The interaction position is obtained as the weighted sum of the positions of the photodetector pixels where the weight are the pixel signals measured in each pixel. Usually a threshold is defined, and the pixels with a signal value below it are not considered in the calculation.

### 1.5.2 Statistical Methods based on precalibration process

These methods are based on the comparison of the detected light distribution for each event (with unknown position interaction) with a reference data set for which the interaction positions are known. Therefore, a precalibration is needed. Data sets are created for each coordinate measuring the light distribution for a grid of incidence positions of the beam on the front surface of the crystal. In each beam position a representative number of events is taken.

#### 1.5.2.1 Least Squares (LS) Criterion

Considering that the data set ( $R_i^{ref}$ ) has been measured for N reference positions of the beam denoted by the index i ( $i=1,2,\dots,N$ ), for each unknown event (k) we compute N distance values ( $LS_{k,i}$   $i=1,2,\dots,N$ ) according to:

$$LS_{k,i} = \sum_j (R_{k,j} - R_{i,j}^{ref})^2 \quad (1.6)$$

where the index j denotes the number of pixels in the photodetector and  $R_{k,j}$  is the response for the event k in the pixel j and  $R_{i,j}^{ref}$  is the response in the pixel j for the averaged reference data set for the beam position i.

The reference position of the beam associated with the smallest distance ( $LS_{k,i}$ ) is taken as the best estimate for the incidence position of the gamma-ray.

#### 1.5.2.2 Chi Square ( $\chi^2$ )

In  $\chi^2$  method the fluctuations on the response of each pixel for each beam position of the reference data set are also considered via the root mean square,  $\sigma_{i,j}$ .



The distance which should be minimized to obtain the estimation of the incidence photon is given by equation (1.7).

$$\chi_{k,i}^2 = \sum_j \left( \frac{R_{k,j} - R_{i,j}^{ref}}{\sigma_{i,j}} \right)^2 \quad (1.7)$$

### 1.5.2.3 Nearest Neighbours

The main difference for the first Nearest Neighbours and LS is that if a total of M events have been measured in the beam position i (i=1,2,...,N), in LS the averaged reference is computed and in first Nearest Neighbours the complete set of M events is the reference for that position. The impinging position is estimated by finding the beam position with the smallest LS value of the N×M calculated distances. Five Nearest Neighbours is a variant of first Nearest Neighbours in which the position is estimated with the mean of the 5 smallest LS lengths.

### 1.5.2.4 Maximum Likelihood (ML)

A likelihood is a probability density function of the form  $pr(g|\theta)$  where  $\theta$  denotes the vector of the parameters to be estimated and g the data vector [33]. ML estimate of the parameters maximizes the probability of the observed data with the probability model. Equation (1.8) shows this estimation rule.

$$\hat{\theta}_{ML} = \underset{\theta}{\operatorname{argmax}} \{pr(g|\theta)\} \quad (1.8)$$

One advantage of ML method is that is readily modified to incorporate prior information.

## 1.5.3 Neural networks (NN) based positining algorithms

Neural networks are computational architectures inspired by biological brain and are composed of weighted interconnections and interactions between their components called nodes or neurons. NN are characterized by a lack of explicit representation of knowledge; there are no symbols or values that directly correspond to classes of interest. Rather, knowledge is implicitly represented in the patterns of interactions between the network components [38]. The objective of NN is to fit a function that given as input the response of the pixels of a photodetector for an event, provides as output the sought after estimated position. The NN is trained, rather the interconnections weights between nodes are determined, by error minimization algorithms using the reference data set. The great advantage of NN over statistical methods is that, once they have been trained, they provide a straightforward position estimation while in statistical methods the comparison with all the reference measurements has to be done in

every new estimation [39]. Furthermore, the position is continuous over the crystal and it is not limited to the selected positions for the reference data like in statistical methods. On the other hand, the computational burden of the learning process is a disadvantage. Moreover, it is a black box learning approach where the relation between output and input parameters can not be interpreted.

#### 1.5.4 Analytical and theoretical models of the light distribution

Methods based on simulation models [7] and theoretical models [10, 12, 13, 11] for the light distribution pattern seek to avoid the required acquisition of reference data sets in Statistical and NN methods.

The position determination method employed in this work is based on a non-linear analytical model of the transport of the light developed in [13]. Modifications on the model from the original publication have been investigated in this thesis and are explained in detail in chapter 2. In this section the analytical model developed in [13] of the transport of the photons in the crystal and their reflection on the sides is described. The algorithm is based on the number of photons arriving to each pixel from a light source, which is the generation point of optical photons in the scintillator crystal, as a consequence of the energy deposition of the gamma-rays. The following equation describes the number of detected optical photons in pixel  $i$  ( $np_i$ ) by:

$$np_i = C_{est} + A_0\Omega(x, y, z) + A_0 \sum_j \Omega(x_j, y_j, z_j), \quad (1.9)$$

where  $A_0$  represents the total number of optical photons produced by the light source,  $\Omega(x, y, z)$  represents the solid angle subtended by pixel  $i$  from the light source located at  $(x, y, z)$  and  $C_{est}$  is a constant that represents the contribution of the reflected photons on the diffuse reflector around the crystal. The last two terms represent the number of photons impinging in pixel  $i$ .  $A_0\Omega(x, y, z)$  represents the number of photons impinging directly the pixel and  $A_0 \sum_j \Omega(x_j, y_j, z_j)$  the number of photons that are reflected in any of the five sides of the scintillator that are not coupled to the SiPM. This mirror-like internal reflections are modelled as if there was a virtual source at a symmetric position on the other side of each surface. Figure 1.12 represents the three contributions considered in the model.

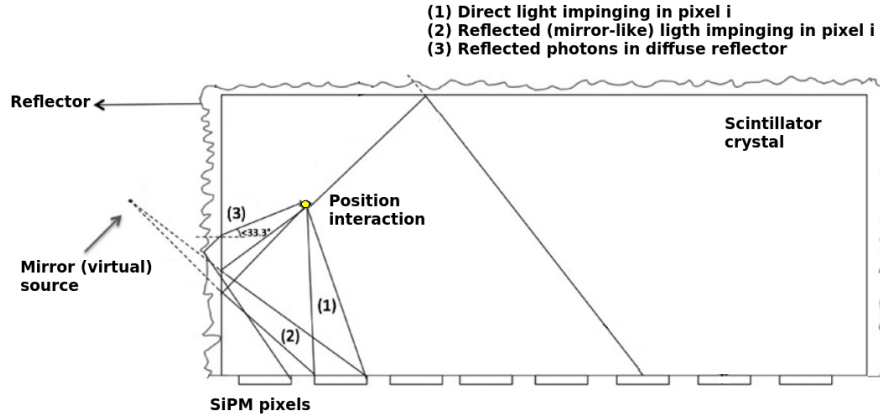


Figure 1.12 The analytical model for the light distribution and the representation of the three considered contributions to the detected light.

$$\begin{aligned}
 \Omega^{exact}(x, y, z) = & \arctan \left[ \frac{(x - (x_i - \frac{dx}{2})) \cdot (y - (y_i - \frac{dy}{2}))}{z \cdot \sqrt{(x - (x_i - \frac{dx}{2}))^2 + (y - (y_i - \frac{dy}{2}))^2 + z^2}} \right] \\
 & - \arctan \left[ \frac{(x - (x_i - \frac{dx}{2})) \cdot (y - (y_i + \frac{dy}{2}))}{z \cdot \sqrt{(x - (x_i - \frac{dx}{2}))^2 + (y - (y_i + \frac{dy}{2}))^2 + z^2}} \right] \\
 & + \arctan \left[ \frac{(x - (x_i + \frac{dx}{2})) \cdot (y - (y_i + \frac{dy}{2}))}{z \cdot \sqrt{(x - (x_i + \frac{dx}{2}))^2 + (y - (y_i + \frac{dy}{2}))^2 + z^2}} \right] \\
 & - \arctan \left[ \frac{(x - (x_i + \frac{dx}{2})) \cdot (y - (y_i - \frac{dy}{2}))}{z \cdot \sqrt{(x - (x_i + \frac{dx}{2}))^2 + (y - (y_i - \frac{dy}{2}))^2 + z^2}} \right] \\
 \Omega^{approx.}(x, y, z) = & dx \cdot dy \frac{z}{((x - x_i)^2 + (y - y_i)^2 + z^2)^{3/2}}
 \end{aligned} \tag{1.10a}$$

$$\tag{1.10b}$$

Exact and approximate solid angle based models described in [13] were evaluated. The expression for the exact solid angle subtended by a pixel with dimensions  $(dx, dy)$  at position  $(x_i, y_i)$  as seen from the interaction position  $(x, y, z)$  is given by equation (1.10a) and the expression for the approximate solid angle, based on the assumption that the distance from the interaction position to the centre of each pixel is large compared to the pixel size, is given by equation (1.10b). Both expressions were derived in [13] and no modifications have been done in this work.

The cost function is minimized with a LS procedure as shown in equation (1.11). Parameters  $x, y, z, C_{est}$  and  $A_0$  are estimated by fitting equation (1.9) to the normalized charge detected

by each pixel of the SiPM array. The fitting is performed iteratively using a non-linear least squares algorithm. The original method was based on an iterative trust-region-reflective optimization [40] implemented in a built-in Matlab function.

$$(\hat{x}, \hat{y}, \hat{z}, A_0, Cest) = \underset{(\hat{x}, \hat{y}, \hat{z}, A_0, Cest)}{\operatorname{argmin}} \sum_{n=1}^{n=64} (m_i - np_i)^2 \quad (1.11)$$

## 1.6 Data Acquisition in PET

In this section we will describe the 2D mode and 3D mode of collecting data in PET imaging to reconstruct the spatial distribution of a radiotracer. Moreover, data format and sampling employed for this thesis will be described.

### 1.6.1 Data acquisition mode: 2D and 3D PET

PET data are acquired and stored in different ways and the way that data are handled affects the noise in the resulting reconstructed image. There are two acquisition modes, 2D and fully 3D PET which are shown in figure 1.13. The nomenclature only specifies the type of acquired data, both acquisition modes lead to 3D images.

In 2D PET, LoRs through a specific imaging plane are considered and the volumetric image is reconstructed by repeating independently the 2D acquisition and reconstruction for multiple axial slices. In 2D acquisition mode interplane septa (lead or tungsten annuli) are placed between detector rings as it is shown in figure 1.13. Usually, the length of the septa is adjusted to accept not only the LoRs between detectors in the same ring but also between detectors in adjacent rings; so that, axial data can still be combined in cross planes. In 3D imaging both direct LoRs as well as LoRs lying in oblique planes that cross the direct plane are acquired. The advantage of not using septa is that any detector ring can be in coincidence with any other. Therefore, the sensitivity is substantially improved by a factor between 4 and 6 [42] and the statistical noise is also reduced. However, it has some disadvantages: more storage capability is needed so it is more computational intensive, more scattered events are included in the data and randoms from activity outside the FoV are also increased. Moreover, 3D reconstruction methods are needed which are more complicated and time consuming than 2D methods; thus, different methods of rebinning data (described in section 1.7.2) have been developed in order to reconstruct 3D data with 2D algorithms.

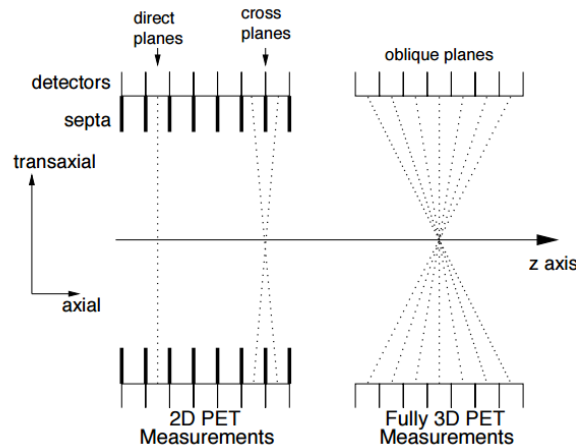


Figure 1.13 Comparison of 2D PET measurements and fully 3D. In 2D mode direct and cross planes (organized into direct planes) are collected, but in 3D mode all oblique planes are collected [41].

## 1.6.2 Data formats

Some of the most common data representation for PET acquisition are projections (sinograms or 2D parallel projections), histograms and list mode data. A sinogram is essentially a matrix where the number of events detected in each LoR are stored as a function of the radial distance from the LoR to the centre and the angle of orientation, while histograms store the number of events detected in each LoR index and list mode format is a list of detected events. List mode data can store events not only in coincidence but in single mode (single and coincidence list mode). In 2D PET, sinograms (1D parallel projections) are the most common data format. However, when more information about the event than the coordinates of the coincidence is recorded (i.e. energy, time), list mode format is more practical. Moreover, in list mode there is no resampling of the data, exact information of the event is stored. Usually, due to the large number of detectors involved in data acquisition, projections can not be as finely sampled.

In this thesis, from the point of view of the interaction position estimation single list mode data representations are of interest. Single list mode data are processed to obtain coincidence list mode data for time coincidence events and sinograms which are employed to reconstruct the image with ML-EM and FBP method respectively. Sinogram format is described more in detail below.

### 1.6.2.1 Line Integral Approximation and Sinograms

A LoR can be approximated as the line that connects two individual detector elements. When the finite size of the detector is considered, the column connecting the two detector elements is referred to as tube of response (ToR). If physical effects such as attenuation or scatter are not considered, the mean number of coincidence events detected in a LoR is proportional to the integral of the tracer concentration along that LoR.

$$n_{LoR} \propto \int_{LoR} f(\mathbf{x}) d\mathbf{x} \quad (1.12)$$

Coincidence data in each LoR are essentially line projections of the tracer distribution. The value  $p(x_r, \phi)$  is the line integral through the object,  $f(x, y)$ , at a particular angle ( $\phi$ ) and at a particular distance ( $x_r$ ) to the center of the scanner, see figure 1.14. These represent the intensity detected in the LoR defined by this orientation and distance; in other words, the number of coincidences detected between the detector pair associated with that LoR.

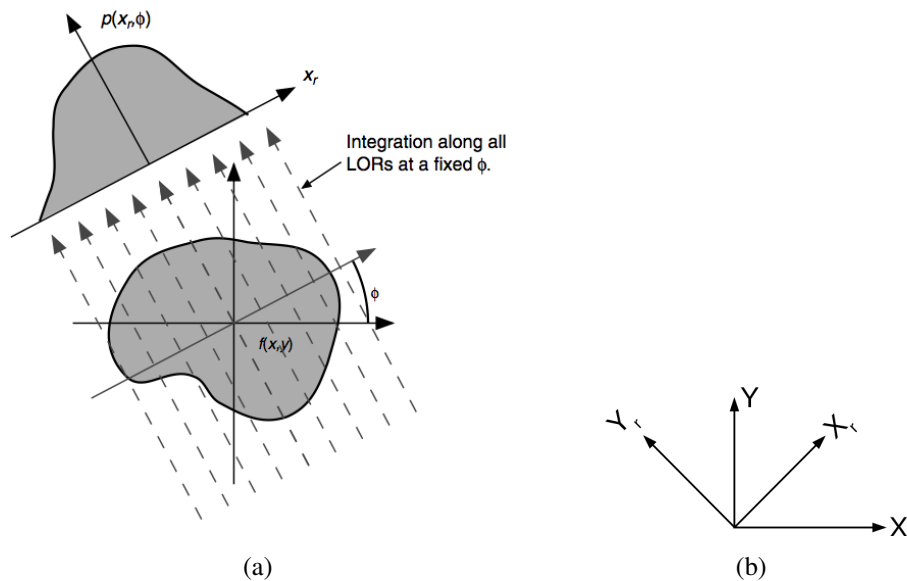


Figure 1.14 The projection  $p(x_r, \phi)$  obtained by the integration along parallel LoRs at an angle  $\phi$  [43].

The following equation represents the line integral of the object  $f(x, y)$  along the LoR and the set of integrals for the different values of  $x_r$  form the projection of the object for a fixed direction  $\phi$ , see figure 1.14.

$$p(x_r, \phi) = \int_{-\infty}^{\infty} f(x, y) dy_r = \int_{-\infty}^{\infty} f(\cos\phi x_r - \sin\phi y_r, \sin\phi x_r + \cos\phi y_r) dy_r \quad (1.13)$$

The 2D function,  $p(x_r, \phi)$ , composed of all the 1D projections for an angle value in  $[0, \pi]$  range is called sinogram. The name was coined by the Swedish scientist Paul Edholm in 1975 because the set of LoRs passing through a fixed point  $(x_0, y_0)$  are located along a sinusoid described by  $x_r = x_0 \cos \phi + y_0 \sin \phi$  [44]. Due to the linearity of equation (1.13), the sinogram of a more complicated object will consist of the overlapping of different sinusoids. As an illustration, figure 1.15 shows an object consisting of three circular regions with different activities and its sinogram where the overlapping of different sinusoids for the two rods can be clearly distinguished.

The line-integral transform of  $f(x, y)$  defined in equation (1.13) is called the X-ray transform and it can be demonstrated that the solution for  $f(x, y)$  is unique [45]. In 2D, the X-ray transform is equivalent to the Radon transform; thus, both terms are often used interchangeably. From now on, we refer to equation (1.13) as Radon transform whose name acknowledges the fact that the principles of this method of imaging were published by Johan Radon in 1917 [46]. The inverse of Radon transform can be computed to recover the object. However, its application is not straightforward and several methods, Filtered Back-Projection among others which will be described in detail in section 1.7.1, have been developed to recover the object.

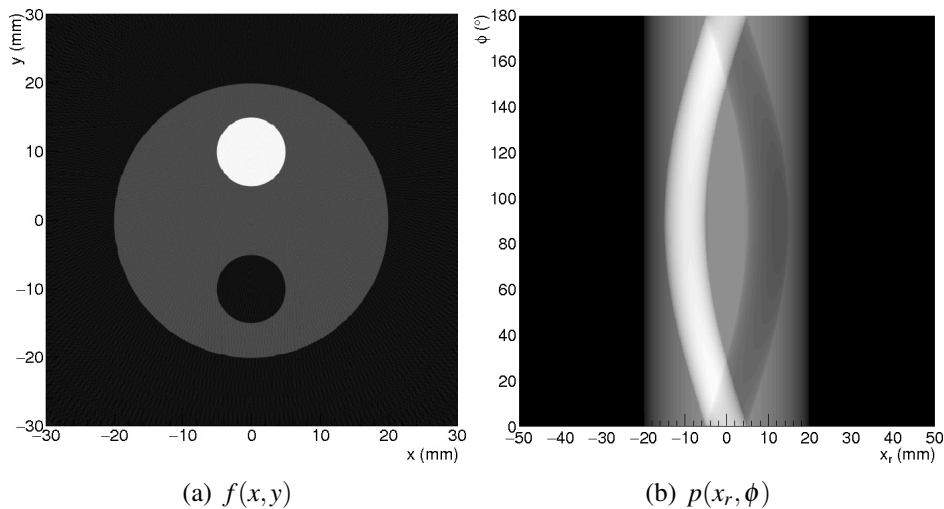


Figure 1.15 Left, a 2D object consisting of several circular regions of different activities. Right, the sinogram of that object.

### 1.6.3 Data sampling and reduction

There are different ways to combine the data to further reduce the noise in the acquired data and storage. Some approaches to undersampling the data are the averaging of contiguous

angular samples (mashing) or combining axially oblique projections (*span*). In the case of 3D PET data can be rebinned to resemble 2D data. Section 1.7.2.2 contains an overview of the different rebinning techniques. Moreover, in 3D PET the axial extent of allowable coincidences can be limited and it is characterized by the maximum Ring Difference (RD).

### 1.6.3.1 Angular Sampling

The combination of angular samples is known as mashing. Samples are reduced by a factor of  $2^m$  where  $m = 0, 1, 2, \dots$  is known as the mashing factor. Typically the initial number of angular samples ( $N_\phi$ ) is reduced to  $N'_\phi = N_\phi 2^{-m}$  with  $\Delta\phi' = \Delta\phi 2^m$ .

### 1.6.3.2 Axial Sampling

Axial sampling consists in compressing axially the oblique projections. In a multi-ring PET scanner in order to improve axial sampling and slice sensitivity, detectors are allowed to be in coincidence not only with opposite detectors in the same ring (direct LoRs) but with detectors in neighbouring rings (cross LoRs). The Michelogram is a grid combined with two axes, each one with the number of rings in the scanner, used to illustrate the amount of axial data combined and was devised by Christian Michel [47]. The detectors of one side are plotted in the X-axis and the detectors on the opposite side on the Y-axis. Then, allowable coincidences are marked by an asterisk in the cell that intersects the column and row associated with the two detector rings involved. When the data from the cells are combined into a single plane it is indicated by connecting the two cells with a line segment. Data in each cell of a Michelogram can be represented by a sinogram.

The term *span* is used to describe the extent of axial data combined [41]. The span is the sum of the number of cells in the Michelogram combined into an odd-numbered plane added to the number of cells combined into an even-numbered plane. Therefore, if only direct LoRs are used, the configuration is said to have a span of 1 and if the adjacent cross LoRs are considered is said to have a span of 3. Therefore, for a span of 3, if the scanner has  $n$  rings with an spacing  $d$  between centres, this will lead to  $n$  direct planes,  $n-1$  cross planes, so to a total of  $2n-1$  planes with a spacing of  $d/2$ . Besides, even-numbered (cross) planes will contain twice as many counts as odd-numbered (direct) planes since they combine the data from two cells in the Michelogram. Figure 1.16 based on [42] shows the axial sampling for a PET scanner of 16 ring with span 7 since odd-numbered planes combine 3 cells and even ones combine 4 cells in the Michelogram. Figure 1.16 A shows the LoRs taken into account in each plane, figure 1.16 B the Michelogram and figure 1.16 C the sinograms without plane efficiency corrections.



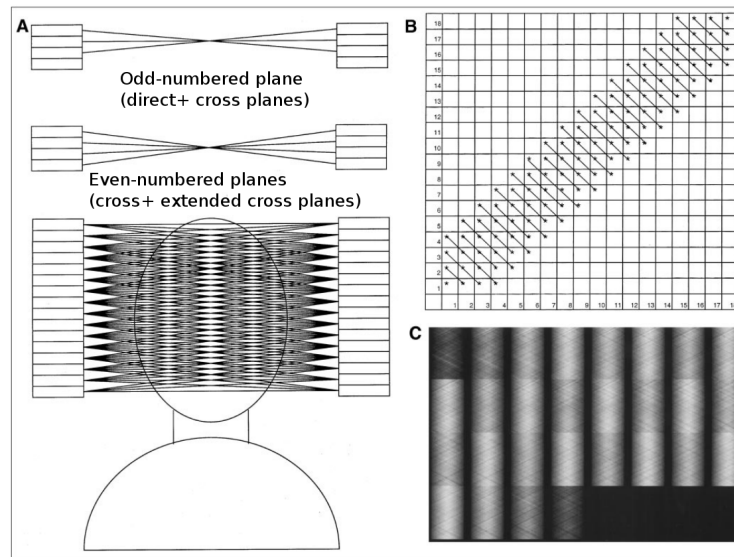


Figure 1.16 Illustration of a 2D PET acquisition with a span of 7. The figure is based on [42].

### 1.6.3.3 Maximum ring difference (RD)

The axial extent of allowable coincidences in 3D PET is characterized by the RD. The allowable cells in the Michelogram will be  $RD^2$ . In 3D mode, RD equals the total number of rings minus one, the sensitivity has the highest value for the central plane and decreases towards the edges. The axial sensitivity is a triangular function with the maximum in the middle. If coincidences are limited, the axial sensitivity has a central plateau of maximum sensitivity.

In 3D PET, as in 2D PET, several cells can be combined in the Michelograms. Therefore, 3D data acquisition can be characterized by span and RD values. Figure 1.17 shows the Michelograms for a 16 ring scanner with span of 7 in 2D acquisition mode and 3D acquisition mode (RD=15).

## 1.7 Image Reconstruction

In nuclear medicine, the goal is to reconstruct the unknown activity distribution in the subject of study (image  $\mathbf{f}$ ) having access only to the measured projections of the activity along different directions ( $\mathbf{p}$ ). One way to represent the imaging system is through a linear model where  $\mathbf{p}$  is the set of observations,  $\mathbf{H}$  is the system model,  $\mathbf{f}$  is the unknown image and  $\mathbf{n}$  stands for the error in the observations [41].

$$\mathbf{p} = \mathbf{H}\mathbf{f} + \mathbf{n} \quad (1.14)$$

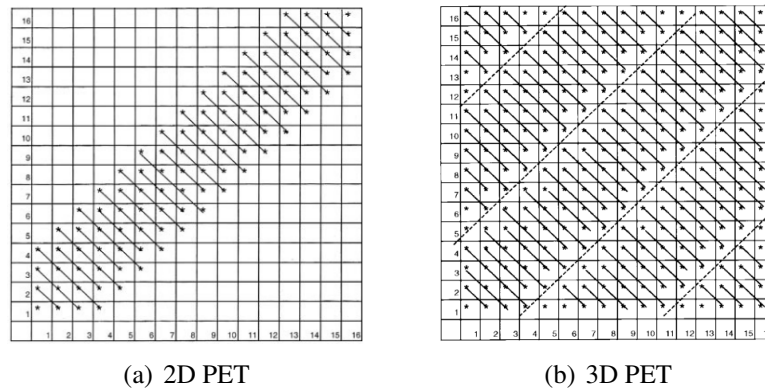


Figure 1.17 Michelograms for 16 ring scanner: (a) 2D PET with a span of 7 and (b) 3D PET with a span of 7 and a RD of 15.

Data values are intrinsically stochastic due to physical effects in PET imaging such as positron decay process and statistical nature of gamma-ray detection. However, data values are modeled either as deterministic or stochastic variables leading to two main groups of tomographic reconstruction methods: analytical and statistical methods.

Analytical reconstruction methods assume deterministic data values containing no statistical noise, which is not always accurate enough, in order to use explicit inversion formulas relatively practical and fast to compute. Analytical methods are based on the inverse of the Radon transform (equation (1.13)) which assumes that the number of detected coincidences in one LoR is proportional to the integral of the activity distribution along that LoR. Therefore, some important physical effects as attenuation of the radiation, scatter and detector size are not being considered. The main drawback is that these methods disregard noise structure and use an idealized system model  $\mathbf{H}$  which can lead to images with reduced resolution and poor noise structure [41].

Statistical methods are based on a more accurate description of the imaging process considering random noise, which makes impossible to find an exact solution for the image. Therefore, multiple steps (iterations) are needed to get an approximate solution for the final image constraining the solution with some form of regularization. These methods are known as statistical iterative reconstruction methods.

This section will give a brief overview of these two reconstruction methods and of the trade-offs between them in the scope of interest of this thesis.

### 1.7.1 2D Analytical Reconstruction Methods

The foundational relationship in analytical image reconstruction is the Central Slice theorem [41] also known as Central Section theorem or Fourier Slice theorem. For simplicity the deductions will be done for a 2D object.

#### The 2D central Slice Theorem

The Central Slice theorem says that the 1D Fourier transform of a parallel projection of an object described by  $f(x,y)$  equals a line of the 2D Fourier transform of such object through the center at the same angle as the projection angle [48].

Essentially the imaging device provides the measured projections  $p(x_r, \phi)$  for different angles  $\phi$ , see equation (1.13), where  $(x_r, y_r)$  is the rotated coordinate system.

$$\begin{bmatrix} x \\ y \end{bmatrix} = \begin{bmatrix} \cos\phi & -\sin\phi \\ \sin\phi & \cos\phi \end{bmatrix} \begin{bmatrix} x_r \\ y_r \end{bmatrix} \quad (1.15)$$

The 1D Fourier transform of a projection is given by

$$P(v_{x_r}, \phi) = F_1 \{p(x_r, \phi)\} = \int_{-\infty}^{\infty} p(x_r, \phi) e^{-i2\pi x_r v_{x_r}} dx_r \quad (1.16)$$

Replacing equation (1.13) and using coordinate transformation and differentiation we achieve the theorem, equation (1.17).

$$P(v_{x_r}, \phi) = \int_{-\infty}^{\infty} f(x,y) e^{-i2\pi(x\cos\phi+y\sin\phi)v_{x_r}} dx dy = F(v_{x_r}\cos\phi, v_{x_r}\sin\phi) \quad (1.17)$$

More concisely,

$$P(v_{x_r}, \phi) = F(v_x, v_y) \Big|_{\substack{v_x = v_{x_r} \cos \theta \\ v_y = v_{x_r} \sin \theta}} \quad (1.18)$$

Figure 1.18 shows a scheme of the 2D central slice theorem where  $F_1 \{ \}$  and  $F_2 \{ \}$  are the one and two-dimensional Fourier transform and  $v_x$  is the Fourier space conjugate of  $x$ . The theorem indicates that if we know the projections of the 2D slice of an object at angles  $0 \leq \phi \leq \pi$ , in a continuous framework, we can recover the object. In practice, angular sampled projections are recorded and therefore, the resolution of the reconstructed object could be degraded.

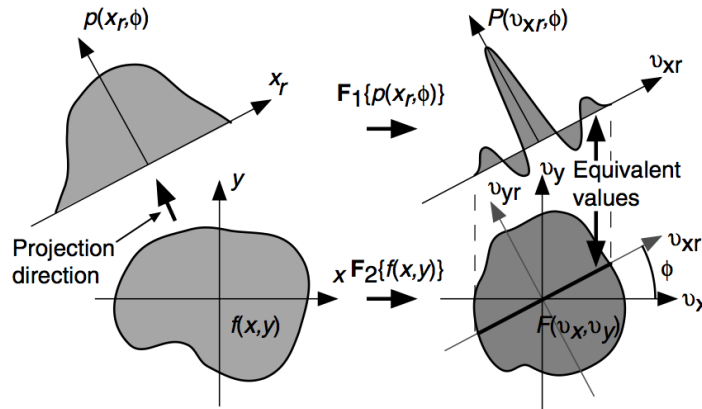


Figure 1.18 2D central section theorem, showing the equivalence between the 1D Fourier transform of the projection and the central section at the same angle through the 2D Fourier transform of the object [43].

**Back-Projection**

Since, in the process of forming the projection of an object through a LoR (particular direction), the knowledge of where within the LoR the value comes from is lost, a possible way to reconstruct the original distribution is to place the constant value of the projection along the whole LoR in the back-projection.

$$b(x,y) = \int_0^\pi d\phi p(x_r, \phi) \tag{1.19}$$

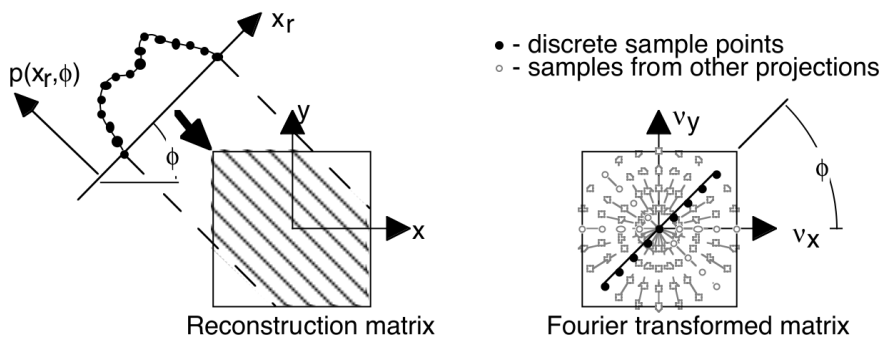


Figure 1.19 Left, an efficient manner of back-projecting in which for a given angle the value of the projection is back-propagated for each  $x_r$ . Right, the back-projection at a given angle is equivalent to placing the 1D transform of the projection into a line (array) representing  $F(v_x, v_y)$  at the same angle. The oversampling can be clearly seen in the right [47].

The straight back-projection of all the projections does not return the image due to the oversampling at the origin of the Fourier transform of the object which is filled with the 1D Fourier transform of the projections, as it can be seen in figure 1.19.

$$B(v_x, v_y) = F_2 \{b(x, y)\} = F(v_x, v_y) \frac{1}{\sqrt{v_x^2 + v_y^2}} = F(v_x, v_y)(1/v) \quad (1.20)$$

The Fourier transform of the back-projection of the data leads to the Fourier transform of the object but weighted by the factor,  $1/v$ , which reflects the need to compensate for the oversampling. The density of sample points is inversely proportional to the radial coordinate in the Fourier space. In order to obtain an artefact-free reconstructed object from the 2D inverse Fourier transform, projections must be filtered. Due to the Fourier Transform properties, the filtered projections,  $p_F(x_r, \phi)$ , can be obtained convolving the original projection at a given angle with the filter,  $h(x_r)$ , or multiplying by the filter in the Fourier space equation (1.21).

$$F_1 \{p(x_r, \phi) * h(x_r)\} = P(v_{x_r}, \phi)H(v_{x_r}) = P_F(v_{x_r}, \phi) \quad (1.21)$$

### Back-Projection Filtering (BPF)

One approach to obtain the original object is the BPF method. The projection data are first back-projected and then filtered in the frequency space and finally the inverse Fourier transform is done to obtain the image.

$$f(x, y) = F_2^{-1} \left\{ v F_2 \left\{ \int_0^\pi d\phi p(x_r, \phi) \right\} \right\} \quad (1.22)$$

One of the main disadvantages of this method is that the back-projection is computed first and this operation needs a larger matrix size than the size needed for the final result.

### Filtered Back-Projection (FBP)

The most common technique to reconstruct analytically the projections acquired in PET is a variant of BPF called FBP. So the projections are first filtered for each angle in the Fourier space and then the inverse Fourier of the filtered projections is back-projected in the image space. Equation (1.23) represents the FBP operation where  $|v_{x_r}|$  is the one dimensional ramp filter. One of the reason of the popularity of FBP method over BPF is that the ramp filter is applied to the measured projection; thus, the filtered projections only need to be

back-projected for a value of  $|x_r|$  smaller than the radius of the FoV which results in a smaller reconstruction matrix size.

$$f(x, y) = \int_0^\pi d\phi p_F(x_r, \phi) = \int_0^\pi d\phi \left[ \int_{-\infty}^{\infty} dv_{x_r} e^{2\pi i v_{x_r} x_r} |v_{x_r}| P(v_{x_r}, \phi) \right] \quad (1.23)$$

FBP algorithm can be deduced applying Central Slice Theorem as it is shown in equation (1.24).

$$\begin{aligned} f(x, y) &= \int_{-\infty}^{\infty} \int_{-\infty}^{\infty} dv_x dv_y F(v_x, v_y) e^{2\pi i v_x x} e^{2\pi i v_y y} \\ &= \int_0^{2\pi} d\phi \int_0^{\infty} dv v F(v \cos \phi, v \sin \phi) e^{i 2\pi v (x \cos \phi + y \sin \phi)} \\ &= \int_0^{2\pi} d\phi \int_0^{\infty} dv v P(v, \phi) e^{i 2\pi v x_r} \\ &= \int_0^\pi d\phi \int_{-\infty}^{\infty} dv |v| P(v, \phi) e^{i 2\pi v x_r} = \int_0^\pi d\phi p_F(x_r, \phi) \end{aligned} \quad (1.24)$$

An ideal sinogram for a phantom that consists of a circle of 20 mm radius with background activity with two equidistant rods of 5 mm radius, one hot (3 times more activity than the background) and the other cold (without any activity), was generated. Figure 1.20 shows, on the top, the ideal synthetically generated sinogram and its back-projection and on the bottom, the filtered sinogram and its back-projection. It can be seen that projections must be filtered in order to recover the object.

In general, FBP is an approximate solution to the Radon transform inversion due to the underlying assumptions that are not satisfied by the acquired data. FBP assumes continuous projections for all angles between  $(0, \pi)$  rad and noiseless data. Therefore, the exact solution is not possible due to the discrete sampling and the statistical noise in the measurements. Besides, the non-uniformity of the sampling and the missing angular projections can cause additional problems in the reconstruction of the image.

The discrete sampling ( $\Delta x_r$ ) limits the maximum frequency that can be recovered without aliasing artefacts. According to Shannon's sampling theorem, the maximum recoverable frequency is the Nyquist frequency ( $v_N = 1/2\Delta x_r$ ).

On the other hand, due to the presence of statistical noise in the measured projections, the Fourier transform of the projections is dominated by the noise above a certain frequency, the value of which depends on SNR. Moreover, ramp filter amplifies high-frequency components; therefore, amplifies the noise and degrades the SNR.

Therefore, a regularization is often required to constrain the solution to a physical acceptable value. The most common way of regularizing is via an apodizing window ( $W_H$ ), a

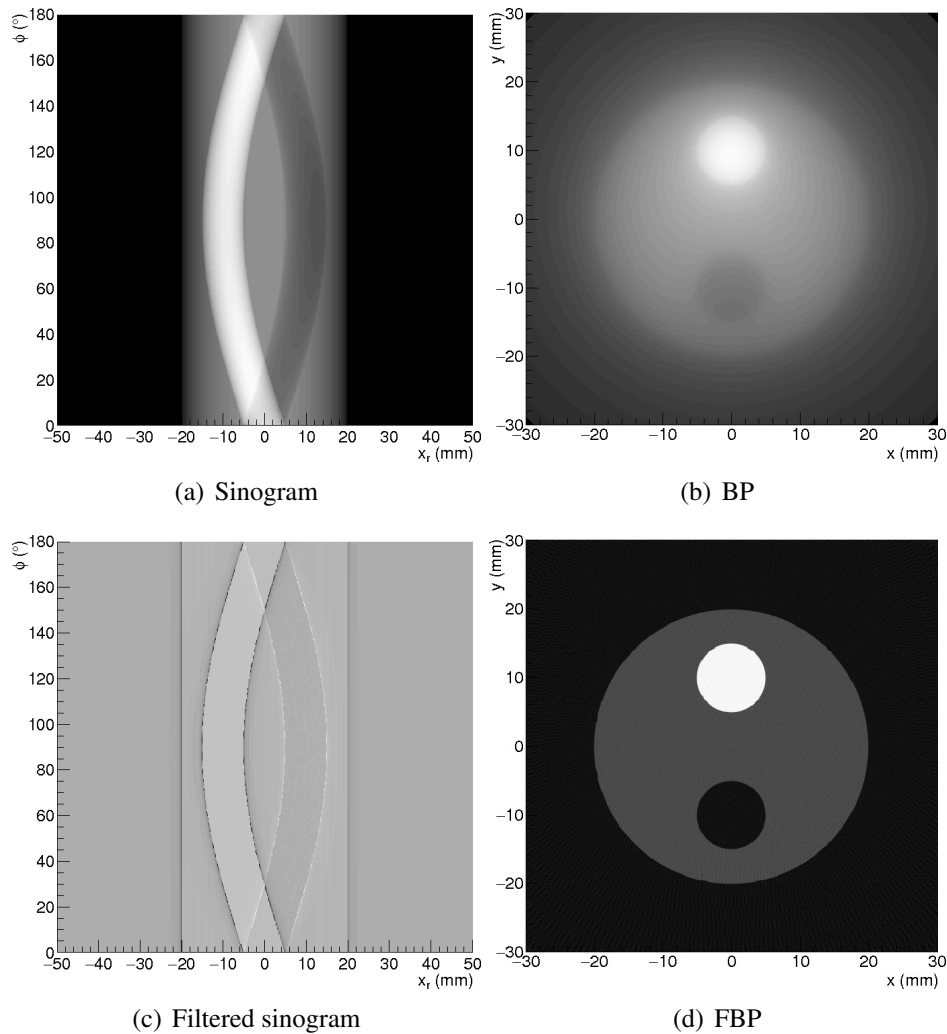


Figure 1.20 In the left, in (a) ideal synthetically generated sinogram for a hot and cold rod phantom and in (c) the corresponding filtered sinogram are shown. In the right, in (b) the back-projection of the sinogram and in (d) the back-projection of the filtered sinogram are presented.

smoothing function, which is applied to eliminate the contribution above a cut off frequency ( $v_c$ ). The election of  $W_H$  and  $v_c$  determines the noise-resolution trade-off and image noise structure. A typical apodizing function is the Hamming window, equation (1.25), where  $\alpha$  ( $0.5 \leq \alpha \leq 1.0$ ) controls the shape of the window and  $v_c < v_n$  controls the maximum frequency. Equation (1.26) represents the back-projection of the the regularized and filtered projections.

$$W_H(v_{xr}) = \begin{cases} \alpha + (1 - \alpha)\cos\left(\frac{\pi v_{xr}}{v_c}\right) & |v_{xr}| < v_c \\ 0 & |v_{xr}| \geq v_c \end{cases} \quad (1.25)$$

$$f(x, y) \approx \int_0^\pi F_1^{-1} \{W_H(v_{xr})|v_{xr}|P(v_{xr}, \phi)\} d\phi \quad (1.26)$$

There is not any regularization applied to the reconstructed images using FBP algorithm showed in this thesis. However, for the sake of completeness some regularization functions have been described in this section.

## 1.7.2 3D Analytical Reconstruction Methods

The difference between 3D and 2D image reconstruction from X-ray transform is the spatially-varying response and data redundancy due to the fact that only a single slice of data is required to reconstruct an image. The spatially-varying response is due to the differences in sensitivity along the axial direction of the scanner because of the finite axial extent of the scanner leading to truncated oblique projections. Standard FBP requires shift invariance. However, in 3D PET there are regions of missing data in oblique projections planes. Therefore, normal 3D FBP can not be applied without restricting the polar angular acceptance and the axial FoV.

### 1.7.2.1 3D reprojection algorithm (3DRP) 3D reconstruction method

3DRP algorithm [49] solved the problem of truncated oblique measured projection and is considered the standard “exact” 3D filtered back-projection method, an extension of the standard FBP. The algorithm consist in three steps. Firstly, a 3D image is formed with a 2D reconstruction of each transaxial slice using only direct planes. Secondly, the initial image is forward projected onto the regions of missing projection data, to estimate the unmeasured oblique projection. Finally, the final image is obtained with 3D FBP using the complete set of data, the new set and the original projection data.

The 3DRP method is computer intensive and slow compared to 2D reconstruction methods. Therefore, rebinning methods to reconstruct 3D data through 2D methods were developed.

### 1.7.2.2 Rebinning methods

Rebinning methods allow to create a set of 2-dimensional sinograms, one for each transaxial slice in which we divide the 3D FoV, sorting measured projections from 3D mode. Each rebinned sinogram can be reconstructed with a 2D image reconstruction method. Therefore, rebinning methods are not reconstruction methods but they are procedures for handling 3D data for the posterior reconstruction with 2D algorithms. Rebinning methods significantly



speed up 3D data reconstruction due to the reduced data, so the reconstruction is as fast as 2D reconstruction but retaining 3D mode sensitivity because all the LoRs are used. However, these methods produce statistical noise amplification and spatially varying distortion. The most common rebinning methods are briefly described below.

**Single-slice rebinning (SSRB)** SSRB algorithm [50] is the simplest rebinning algorithm for 3D PET. Rebinned sinograms are created averaging the oblique sinograms that intersect the direct plane at the center of the transaxial FoV. An oblique LoR is located in a parallel plane midway between the axial points of interaction of the two gammas in the two detectors in coincidence. The main limitation is that SSRB provides poor results when the reconstructed activity is not near the axis of the multi-ring scanner [51].

A rebinning method should be fast, accurate and as stable with respect to noise as a true 3D reconstruction method [47].

**Multi-slice Rebinning (MSRB)** MSRB is a rebinning method developed by [52]. Each oblique coincidence (LoR) increment several 2D sinograms instead of only the sinogram corresponding to the midway point between the axial positions of the coincidence as in SSRB.

The procedure is the following. The LoR is projected in  $z=0$  (central axial plane) and the standard values for the sinogram  $(x, \phi)$  are obtained. Then, an interval length centred in the projected LoR is defined and the  $z$  coordinates for this interval in the original LoR define the set of slices for which the sinogram is incremented in  $(x, \phi)$ . For each LoR the same increment is given for all slices in the range. However, for each LoR the increment is inversely proportional to the number of incremented sinograms. This method has a strong blurring in  $z$  direction which may be corrected by axial filtering operation either before or after 2D reconstruction of the slices.

MSRB is almost as computer intense as SSRB but it has better geometrical accuracy. The disadvantage is that when the 3D data is noise the results may become unstable [47].

**Fourier Rebinning (FORE)** FORE is an analytical factorization method in the 3D Fourier space [53] and is presented as the first order expression of an exact rebinning algorithm. FORE is based on taking the 2D Fourier transform of oblique sinograms.

The approximations are not valid at large aperture angles. However, it is accurate and stable in the presence of noise for axial apertures at least up to 35 degrees [54]. It speeds up the reconstruction in comparison with 3DRP reconstruction but less than SSRB and can not

be performed online. Moreover, FORE uses the Fourier Transform so it can not be applied to list mode data.

### 1.7.3 Iterative Reconstruction Methods

Iterative algorithms are based on minimizing or maximizing a target function through consecutive steps (iterations) that improve the estimation of the image. The main advantage of this methods is the possibility to model the statistical nature of the data and the physical processes involved in the data acquisition process such as positron range, non-collinearity, attenuation, scatter, inter-crystal scatter among others. Moreover, different a priori information can also be incorporated. However, more accurate descriptions lead to more processing time. Five basic components can be identified in iterative methods: image model, data model, system model, objective function, optimization algorithm [48].

**Image model** The object is represented as a discretized image, which can be expressed as a linear combination of a finite number  $J$  of basis functions  $b_i(x,y,x)$ .

$$f(x,y,z) \approx \sum f_i b_i(x,y,x) \quad (1.27)$$

Most common choice for the basis elements are voxels, although other functions such as 'blobs' [55], and 'natural' pixels [56] can be found in the literature. The goal of image reconstruction is to find the coefficient values  $f_i$  for the  $J$  elements of the basis.

Usually  $f(x,y,z)$  is considered to have deterministic values (classic scheme). However a more accurate framework (Bayesian framework) can be considered where  $f(x,y,z)$  is considered a random vector with a probability called the prior that allows to include previous information from the image.

**Data model** Data model describes the probability distribution of the measurement around the expected mean values. Usually Poisson model is employed to describe the statistical nature of the data because photon emission and detection obey this probability distribution. If data model is characterized by Poisson distribution and  $\vec{g}$  represents the measured vector data, the probability of measuring  $g_i$  counts is given by:

$$P(g_i|f) = \frac{\bar{g}_i^{g_i} e^{-\bar{g}_i}}{g_i!} \quad (1.28)$$

where index  $i$  could denote the LoR index and  $g_i$  the number of detected coincidences in that LoR.

If  $g_i$  is high enough, Gaussian model represents a good approximation where the probability of measuring  $g_i$  counts is given by:

$$P(g_i|f) = \frac{1}{\sqrt{2\pi}\sigma_i} \frac{e^{-(g_i-\bar{g}_i)^2}}{2\sigma_i^2} \quad (1.29)$$

where the variance of each LoR can be approximated by the noisy  $g_i$  counts.

**System model** The system model matrix ( $H$ ) relates the image ( $\vec{f}$ ) with the measured data ( $\vec{g}$ ) as it can be seen in

$$\bar{g}_i = \sum_{j=0}^{J-1} H_{ij} f_j \quad (1.30)$$

represents the forward projection. The elements of the matrix ( $H_{ij}$ ) represent the probability of detecting the positron emission produced in voxel  $j$  in the LoR  $i$ . If the size of the measurement vector is  $I$ , the size of the system matrix is  $I \times J$ , which is a large matrix of the order of trillions for 3D PET high resolution systems [57] and its computation is costly. The difficulties regarding the size can be overcome taking into account the high degree of sparsity of the matrix and system symmetries. The calculation of  $H$  is difficult. It can include physical linear effects such as attenuation, scatter, detector response and blurring. The three basic methodologies in descending order of accuracy to accomplish the system matrix are: empirical, Monte Carlo and analytical methodologies [58].

The inverse problem (obtaining  $\vec{f}$  from  $\vec{g}$ ) is ill posed except for the highly unrealistic case when  $H$  is a well behaved invertible matrix.

**Objective or Cost function** The cost function depends on the image and measured data,  $\Phi(f, g)$  and gives measure of how well an image agrees with the measured data. The cost function can also include a regularization term which adds some constraints to the reconstructed image.

Some of the most common cost functions are Maximum a Posteriori (MAP) Criterion, Maximum Likelihood (ML) and Least Squares Criterion. The most common approach is the ML in which we choose an estimate of the object which provides greatest value for the probability ( $P(\vec{g}|\vec{f})$ ) of obtaining the observed data. The ML can be considered as a particular case of Maximum a Posteriori (MAP) Criterion where the prior (function that reflects the assumptions about image properties) is a constant. On the other hand, Least Squares Criterion seeks to minimize the difference in terms of Euclidean norm of the measured data and the forward-projected image.

Some of these cost functions have been explained in Position Reconstruction statistical methods in section 1.5.

**Optimization algorithm** Optimization algorithms are the methods employed to optimize the cost function and achieve the desired solution. Numerous algorithms have been proposed from the gradient-based algorithms to the most commonly used Expectation Maximization (EM) and ordered subsets expectation Maximization (OSEM).

Figure 1.21 shows a flow diagram with the common elements of the iterative process for the optimization of the image. The process begins with an initial estimation of the unknown image ( $\hat{f}^{(0)}$ ). Normally it is a uniform estimation, same value for all the voxels. The next step is the Forward Projection into the measurement space of the estimation, which yields a set of measurement values  $\hat{g}^{(0)} = H\hat{f}^{(0)}$  which would be expected if  $\hat{f}^{(0)}$  was the unknown image. A comparison of the estimated projections with the measured projection follows, resulting in a set of weights accounting for the difference between projections that are back-projected into the image space. The previous estimate is modified with these weights to create a new estimate  $\hat{f}^{(1)}$ . Each loop to update the last estimated image is one iteration. Often a large number of iterations is needed to reach convergence to the unknown image. Commonly algorithms are terminated due to the increase in the noise with the iterations. When the process is terminated the final estimate is called the final image.

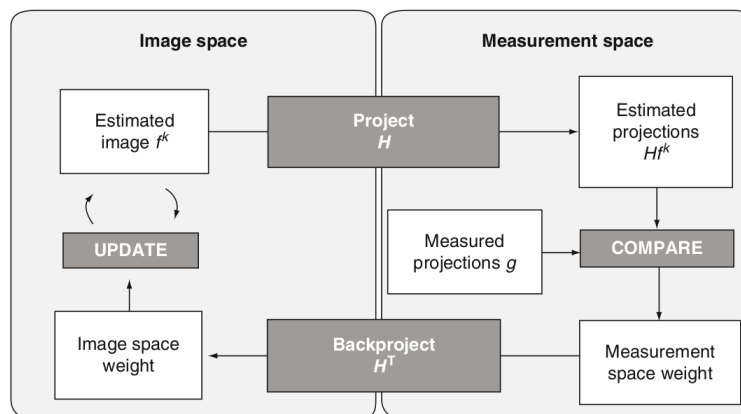


Figure 1.21 Flow diagram to represent iterative process of optimizations. Figure from [48]

### 1.7.3.1 Maximum Likelihood Expectation Maximization (ML-EM)

The ML-EM is the standard iterative algorithm in PET imaging and the basis for most of the statistical reconstruction methods. It was introduced to this field by Shepp and Vardi in 1982 [59]. It is based on the maximization of the logarithm of the Poisson likelihood cost function

(ML) using expectation maximization (EM) optimizing algorithm. ML-EM applied to PET image reconstruction (or to any linear inversion problem with Poisson noise [60]) leads to equation (1.31) where  $\hat{f}_j^{(k+1)}$  is the next estimate of voxel  $j$  based on the previous estimate  $\hat{f}_j^{(k)}$ .

$$\hat{f}_j^{(k+1)} = \frac{\hat{f}_j^{(k)}}{s_j} \sum_l \frac{g_l}{\sum_w H_{lw} \hat{f}_w^{(k)}} H_{lj} \quad (1.31a)$$

$$s_j = \sum_l H_{lj} \quad (1.31b)$$

The term  $\hat{g}_l^{(k)} = \sum_w H_{lw} \hat{f}_w^{(k)}$  corresponds to the forward projection in the measurement space of the last image estimate. The quotient  $g_l / \hat{g}_l^{(k)}$  expresses the comparison between the measured data ( $g_l$ ) and the data we would have measured if the image was  $\hat{f}_j^{(k)}$  and the normalization term  $s_j$  describes the sensitivity of the system for an emission originated in voxel  $j$ .

The main advantages of ML-EM over other statistical methods are that its convergence is guaranteed, the formula is simple and data are described with a realistic statistical model. However, the convergence is slow and the image noise increases with each iteration due to the statistical noise present in the measurements.

ML-EM usually requires approximately 20-50 iterations to reach an acceptable solution [41]. In each iteration one forward projection and one back-projection are needed. Therefore, the computation time is considerably bigger than for FBP but leads to a potentially more accurate reconstruction.

### 1.7.3.2 Ordered Subsets Expectation Maximization (OSEM)

OSEM was introduced in 1994 [61] to speed-up the reconstruction process of conventional ML-EM. The slight difference compared to ML-EM is that the entire data is divided into  $B$  subsets, see equation (1.32).

$$\hat{f}_j^{(k+1)} = \frac{\hat{f}_j^{(k)}}{\sum_{l' \in S_b} H_{l'j}} \sum_{l \in S_b} \frac{g_l}{\sum_w H_{lw} \hat{f}_w^{(k)}} H_{lj} \quad (1.32)$$

In each iteration the image will be updated as many times as the number of subsets in which the data are divided ( $B$  times). For example, during iteration ( $k$ ), the initial image for subset 2 will be the estimated image applying ML-EM to the first subset for the same iteration ( $k$ ).

In practice OSEM approaches ML solution roughly  $B$  times faster than ML-EM. However, it presents a formal disadvantage, while M-EM improves monotonically the solution, OSEM does not and it is not guaranteed to converge to ML solution. Often, this is not a serious problem. Furthermore, for the same bias level there is more image variance than using ML-EM. Therefore, an optimization of subsets and iteration number is required when the algorithm is applied to real (noisy) data.

## 1.8 Monte Carlo Simulations

Monte Carlo (MC) methods can be described as numerical calculation methods that use random sampling to solve problems involving stochastic processes. The name acknowledges the fact that the most famous center for playing games involving random numbers was Monte Carlo casino. Matter-radiation interactions were interpreted using cross sections as probabilities. The aim of Monte Carlo simulations is to create a model as similar as possible to the real system using random sampling of those probability density functions.

Radiation emission and interaction in radiation physics were not easily addressed using experimental or analytical approaches. On the other hand, Monte Carlo techniques accurately describe the physics by random sampling probability distributions and cross sections to estimate the interaction probability of the particles. Dedicated MC codes developed for emission tomography techniques usually suffer from limitations in terms of validation, accuracy and support.

The advantage of MC simulations is not only to model the performance of a real system, but it allows to measure quantities that are not possible in real systems like real random rate and also to turn off different effects such as positron acollinearity or attenuation of the photons.

GATE (the Geant4 Application for Tomographic Emission) [62], is one of the most extensively used MC package for Nuclear Medicine and Radiotherapy that combines the advantages of Geant4 package [63] which is a well validated package of high energy physics and specific tools dedicated to emission tomography. In this thesis, GATE MC toolkit has been used to simulate a PET detector head and different PET scanners.

## 1.9 NEMA NU-4 2008 Standard

The National Electrical Manufacturer Association (NEMA) is an organization which is responsible among other things for the development of protocols that aim to set a reference point to evaluate practical issues. These standards are created by ad-hoc committees which

---

include manufacturers as well as scientists. In this work, we focus on the standard developed to evaluate the performance of PET scanners dedicated to small animals, NEMA NU 4-2008, which was released in 2008. NEMA protocol establishes a set specifications and procedures to characterize the performance of PET systems in terms of spatial resolution, scatter fraction, count losses and random coincidence measurement, sensitivity and image quality for specific imaging tasks typical encountered in small laboratory animal imaging facilities.





# Chapter 2

## Detector Head Characterization

The detector head developed for small animal PET applications is composed of a continuous LYSO crystal coupled to a SiPM array. White crystals were chosen for the detectors in order to achieve the best energy and time resolution [1]. First, the detector head has been characterized. The operating parameters have been adjusted and different measurements have been undertaken to determine pedestal values, energy and time resolution. Then, position determination studies have been performed which are the main part of this chapter. Different crystal thicknesses and crystal coatings have been tested. In order to maximize the benefits of this detector, the performance of the light distribution model of the 3D position determination algorithm has been studied and the model has been adapted to match the experimental data. A Monte Carlo simulation of the detector head has been developed and validated through comparison with experimental data. X-Y and DoI resolution and bias have been estimated for experimental data and validated simulations. Moreover, DoI resolution and bias have been studied for optimized geometries using simulated data. Finally, the detectors have also been tested in a system consisting of two rotating heads that make it possible to acquire tomographic data.

### 2.1 Detector description

#### 2.1.1 Scintillator crystals

The detectors employed are made of  $12 \times 12 \text{ mm}^2$  Ce-doped LYSO continuous crystals coupled to a SiPM array. Two crystals from Hilger Crystals with 5 and 10 mm thickness have been tested. The crystals are polished and painted white in five faces, all but the one coupled to the photodetector. In addition, a crystal of size  $12 \times 12 \times 10 \text{ mm}^3$  covered with specular reflector from Proteus was also tested to evaluate the performance of the model with such a

reflector. Figure 2.1(a) shows 5 and 10 mm thick crystals painted in white and covered with specular reflector. Unless otherwise stated, the results presented refer to the white painted crystals.

### 2.1.2 SiPM array

Two SiPM arrays have been tested. Initially, a SiPM array developed at FBK-irst made of 64 SiPM elements in a common substrate with 1.4 mm x 1.5 mm pixels in a 1.5 mm pitch, [64] was tested. This detector has been employed to characterize the behaviour of the electronics board threshold and for the coincidence timing measurement. However, the bonds to read out the signal of some of the SiPM elements were damaged and the lack of signal from some elements of the SiPM array affected the performance of the detector and of the position reconstruction algorithm. Therefore, position characterization measurements were repeated with the same crystal coupled to a SiPM array from AdvanSiD. The SiPM array from AdvanSiD (model ASD-RGB1.5S-P-8x8A) is also composed of 8×8 pixels in a monolithic substrate, see figure 2.1(b). The pixels are 1.45×1.45 mm<sup>2</sup> in size in a 1.5 mm pitch. The SiPM array is connected to a custom-made printed circuit board (PCB) and biased through the backplane, see figure 2.1(c). SiPM elements have a spread of 100 mV in their breakdown voltage.

The breakdown voltage is temperature dependent. This affects to the gain, noise and PDE at specific applied bias voltage. Therefore, the ADC value of the position of the 511 keV annihilation photopeak varies during a day due to the temperature variations. Although the temperature in our laboratory could fluctuate up to four degrees Celsius during a day, no temperature corrections have been applied to the data since this work is focused on the position estimation measurements which are not highly dependent on this variations. Therefore, our efforts were not centered in temperature corrections.

### 2.1.3 Electronics

The detector is connected to a 64-channel MAROC2 (Multi-Anode ReadOut Chip) ASIC readout electronic test board from LAL-Orsay that is employed as data acquisition system [65, 1] together with a LabView software. The readout board is shown in figure 2.2 in the position determination set-up with the PCB connected to it.

The ASIC generates a trigger signal whenever any of the channels exceeds a previously defined threshold value (discriminator threshold). The discriminator threshold is set by an internal 10 bit Digital to Analog Converter (DAC1) [65]. The trigger signal is generated as the OR signal of all the 64 outputs of the channels. The trigger is sent to a TTL to NIM

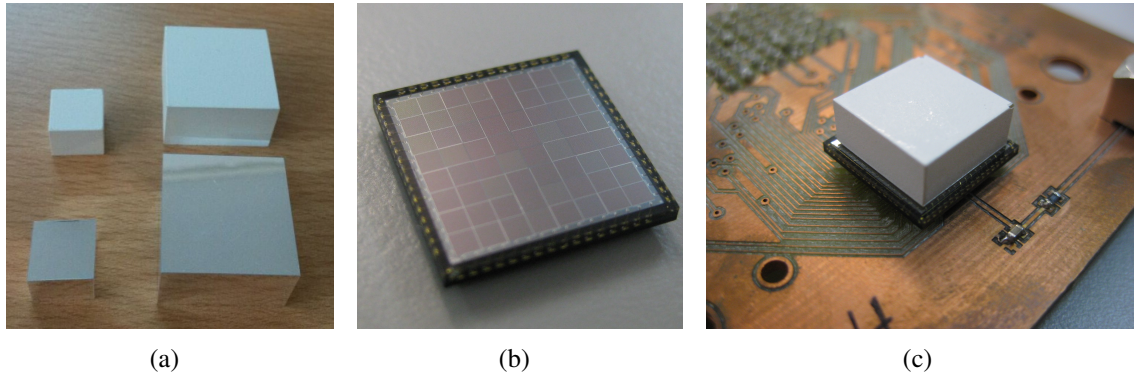


Figure 2.1 The detectors employed in the measurements: (a) several scintillator crystals with 5 and 10 mm thicknesses painted white and covered with a specular film, (b) the SiPM array from AdvanSiD and (c) 5 mm thick crystal coupled to the SiPM which is connected to the PCB.

converter to adapt the signal from the MAROC2 and the output is used to generate a HOLD signal of  $80 \mu\text{s}$  which is converted again to TTL and sent back to the board to read out the event detected in the SiPM. In singles mode whenever the trigger is generated, the event is registered and the ADC values of the detector channels for each event are stored in a text file.

In coincidence mode, the two detectors must trigger in time coincidence in order to register the event. Each detector is connected to a MAROC board and the width of the trigger signal from the MAROC is adjusted to 25 ns. A TTL to NIM converter is employed to adapt the trigger signal from the MAROC2. The output signal of the converter is used as input signal of the logic unit (CAEN 455) which is employed as a coincidence unit in AND mode. The first trigger opens a time coincidence window of 25 ns due to its width and the output of the logic module is one when a trigger in the other detector is generated before the coincidence window is closed. The coincidence signal is employed to generate a HOLD signal of  $80 \mu\text{s}$  which is converted to TTL and sent back to the two boards to read out the detected event.

#### 2.1.4 Position determination set-up

In order to study the position determination capabilities of the detector, it has to be tested with photons interacting in a given position. To this end, an electronically collimated  $^{22}\text{Na}$  point-like source was employed to restrict the interaction position of the photons in the crystal to a known position. A  $1 \times 1 \times 10 \text{ mm}^3$  LYSO crystal coupled to a  $1 \times 1 \text{ mm}^2$  SiPM was located orthogonally to the detector surface 30 mm away (figure 2.3(a)). This detector is operated in coincidence with the detector head for electronic collimation of the 511 keV

photons emitted by the source. The activity of the source was around 636 kBq confined to a 0.25 mm diameter spot and encapsulated in the centre of a 6 mm thick plastic disk. According to this geometry, the collimated photons traverse the crystal entrance surface in a region of approximately 0.21 mm diameter. The diameter of the spot close to the photodetector depends on the thickness of the crystal, being 0.39 mm and 0.56 mm for 5 mm and 10 mm thick crystal respectively. This value has not been subtracted from the results presented. The distance between the point source and the crystal entrance surface has been adjusted, within the mechanical constraints, to minimize the influence of the spot size in the resolution (section 2.4.1.1).

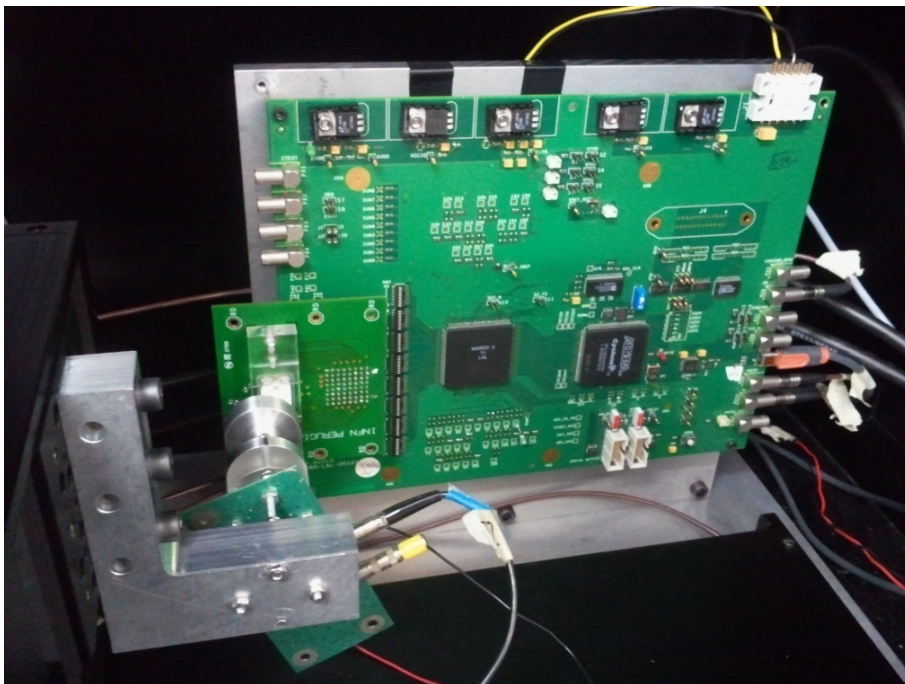


Figure 2.2 Experimental set-up for the position estimation.

A micrometre precision translation stage was used for positioning, considering relative distances with no absolute reference frame. The point closest to the centre was taken as a reference point for the rest of the measurements, keeping relative distances. Figure 2.2 shows the experimental set-up for position determination measurements. In the bottom left of the image, the set-up for the electronic collimation can be seen connected to the translation stage through an L-shaped structure located in front of the scintillator crystal. In the centre, the MAROC2 electronic board to which the detector is connected through a PCB is shown.

Data were taken for both crystal thickness in one quarter of the detector, at four representative positions to characterize the response over the surface. Given the detector symmetry, the performance in the other three quarters is expected to be similar. The nominal positions

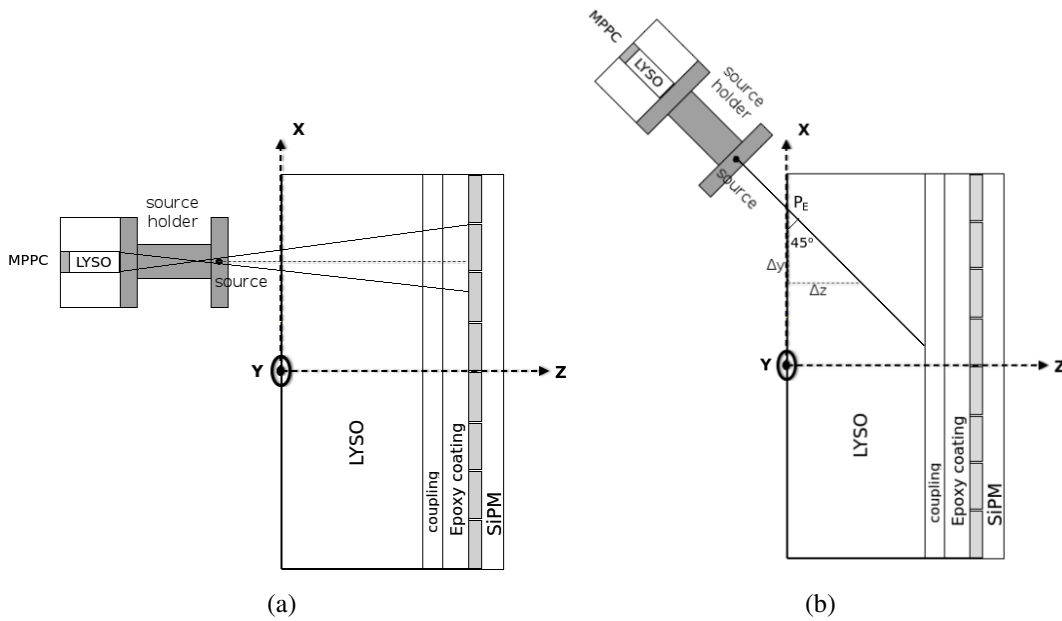


Figure 2.3 Geometry (not to scale) of the experimental set-up for interaction position determination. On the left the set-up for the transversal resolution and on the right DoI resolution set-up.

are one close to the centre (0.75,0.75) mm, another one close to the corner (3.75,3.75) mm, and two middle positions, (2.25,2.25) mm and (3.75,0.75) mm.

In addition, in order to have an estimation of the spatial resolution along the depth of the crystal, the collimated point source was placed so that the emitted gamma-rays imping in the detector at a  $45^\circ$  angle from the detector surface, as it was done in [13] (figure 2.3(b)). In this configuration, the interaction positions lie ideally in a  $45^\circ$  angle line inside the crystal and DoI has the same value as the displacement in the Y-axis from the entry position. The diameter of the spot at the entrance of the crystal was 0.42 mm.

## 2.2 Detector characterization

The adjustment of the operating parameters of the detector is needed to set the optimum measurement conditions. Several measurements have been done to characterize the detector. They include pedestals, characterization of the discriminator threshold, energy resolution measurements employing a  $^{22}\text{Na}$  source and time coincidence resolution measurements.

### 2.2.1 Pedestal measurement of the MAROC2

The stability of the pedestal values with the detector configuration has been studied. The pedestals are the ADC values stored for each channel by the MAROC2 when there is no signal. These values must be subtracted from the acquired data.

The pedestal value for each of the channels was measured using an external pulse as a trigger connected to the electronic board. ADC values stored in each channel were obtained for different configurations: from the electronic board and ASIC without detector (figure 2.4(a)), connecting the photodetector (SiPM) to the board without bias voltage (figure 2.4(b)), connecting the photodetector (SiPM) to the board and applying  $\sim 3$  V overvoltage bias (figure 2.4(c)) and connecting the whole detector (crystal+SiPM) to the board applying the same bias (figure 2.4(d)).

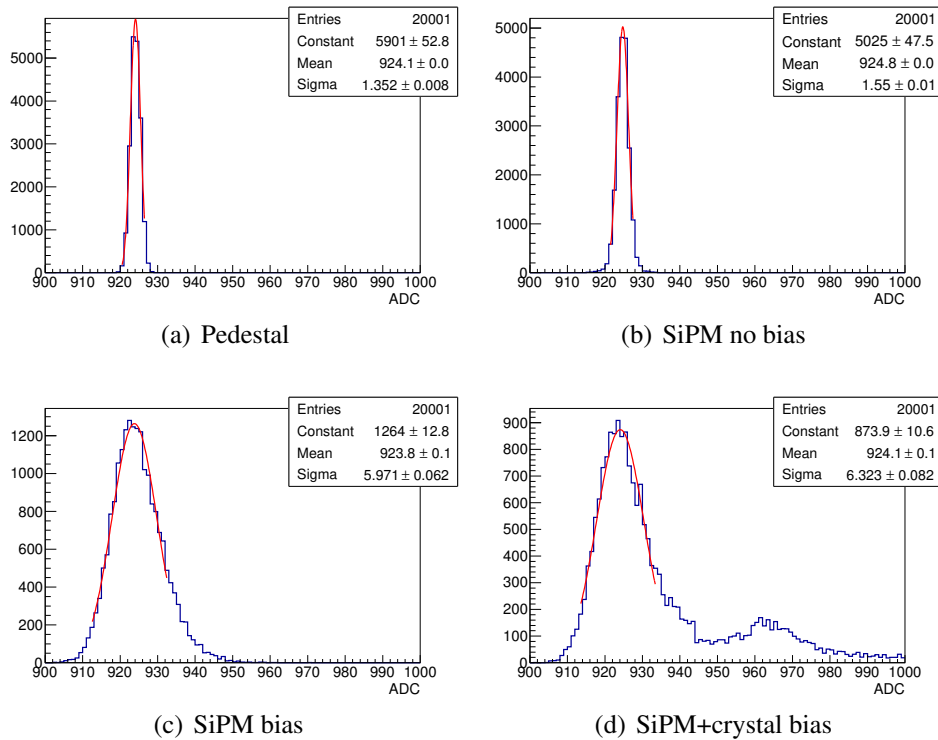


Figure 2.4 Measured pedestals (a) of the electronic board and ASIC, (b) with the SiPM connected to it without applying bias, (c) applying 3 V overvoltage bias and (d) obtained with the whole detector and 3 V overvoltage bias for one channel.

Figure 2.4 shows the typical distributions of the ADC values for one channel (number 32). The collected charge distribution was significantly spread out when the bias voltage was applied to the photodetector. The standard deviation ( $\sigma$ ) of the Gaussian fit to the distribution increases in a 285 %, from 1.55 ADC to 5.97 ADC, when bias is applied to the photodetector.

When the LYSO crystal is coupled to the SiPM an extra contribution from the intrinsic radioactivity of Lutetium can be seen in the charge distribution (see figure 2.4(d)). However, the mean of the Gaussian fit to the peak of the distribution of charge in the four configurations is equivalent. Thus, pedestal values for all channels have been obtained from the mean value of the Gaussian fit to the peak of the charge distribution of the first configuration where only readout board and ASIC were considered, given that this value does not fluctuate with the radiation detected by the photodetector. Figure 2.5(a) shows the pedestal values for each of the 64 channels and figure 2.5(b) shows the distribution of the pedestal values with a mean value of  $(925 \pm 7)$  ADC counts and a standard deviation of the mean of 0.9 ADC counts.

Pedestal values are subtracted to the data before any other data processing.

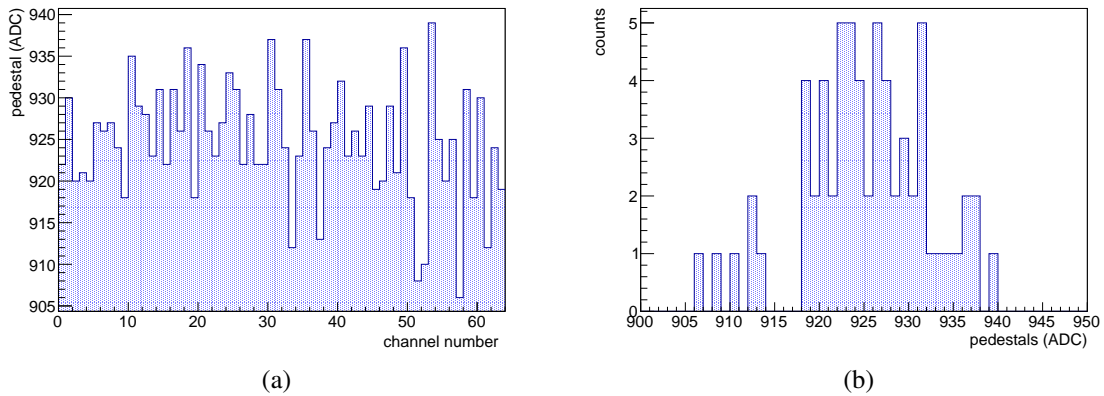


Figure 2.5 Distribution of the pedestals of the 64 channels of the detector.

## 2.2.2 Discriminator threshold of the MAROC2

A discriminator threshold must be applied to avoid triggering on the noise when there is no energy deposition of the annihilation photon in the detector. The threshold is not applied to the sum of the ADC values (total charge deposition) but to each channel individually. Therefore, the effect of the threshold in the energy spectrum and in the position reconstruction was studied to know which type of events were filtered when the threshold was increased. The performance of the threshold was studied with the detector in coincidence mode for different threshold (DAC1) values.

The distribution of the highest ADC value of the 64 detector channels in each coincidence event was obtained at different threshold values for the 5 and the 10 mm thick crystals and the results are shown in figure 2.6(a) and figure 2.6(b) respectively. Two arbitrary threshold values were selected. For a medium threshold value of 950 a.u., 24% of the events detected



with a low threshold (DAC1=800 a.u.) have been rejected using a 5 mm thick crystal, while using a 10 mm thick crystal 43% of the events have been rejected, which is an increase of rejected events of 79%. The percentage of rejected events for the same discriminator threshold is higher for 10 mm than for 5 mm thick crystal due to the more uniformly distributed charge of the events that interact far from the SiPM. Thus, the increment of the threshold affects more to the 10 mm thick crystal.

Figure 2.7(a) and figure 2.7(b) show the sum of the ADC value of the 64 channels (energy spectrum) using 5 and 10 mm thick crystals respectively for different values of the discriminator threshold. The vast majority of rejected events when the threshold is increased are photopeak events which have not deposited enough charge in any of the pixels of the photodetector to exceed the threshold.

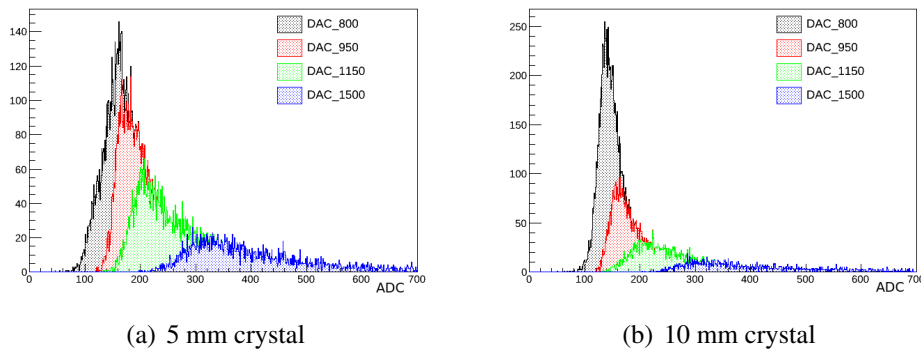


Figure 2.6 The distribution of the maximum intensity channel is shown in (a) and (b) for different DAC1 threshold values using 5 and 10 mm thick crystal respectively.

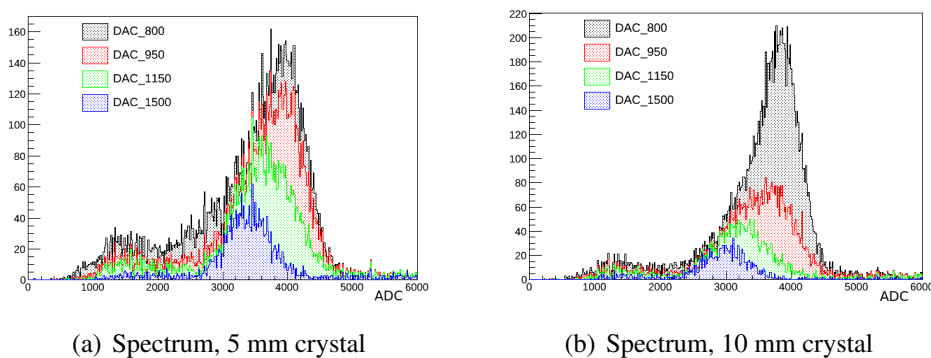


Figure 2.7 The measured spectra is shown in (a) and (b) and for different DAC1 threshold values using 5 and 10 mm thick crystal respectively.

The 10 mm thick crystal which is more sensitive to the variations of the threshold, was employed in coincidence with another detector in order to investigate more in detail the



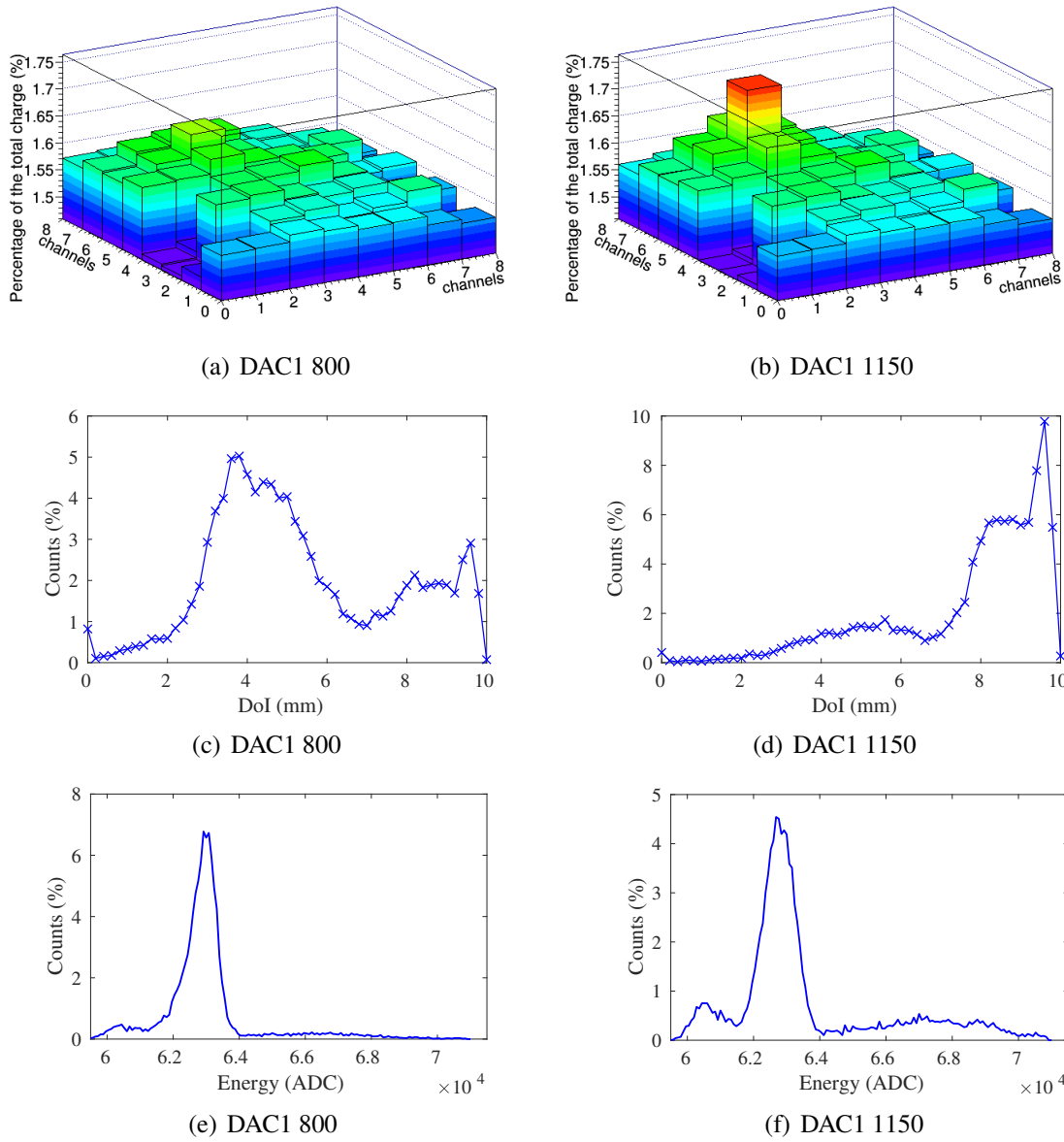


Figure 2.8 The effect of the DAC1 threshold in measurements. (a) and (b) show the percentage of the total charge distribution in each pixel, (c) and (d) show the estimated DoI distribution and (e) and (f) show the normalized energy spectrum applying a threshold value of 800 and 1150 (a.u.) respectively for 15000 events using an electronically collimated  $^{22}\text{Na}$  source.

distribution of accepted and rejected events with the threshold. Again, two arbitrary values were tested, a low threshold (DAC1 800 a.u.) high enough to avoid triggering on the noise and a high threshold (DAC1 1150 a.u.). Data were taken at a given interaction position employing the collimated  $^{22}\text{Na}$  source described in section 2.1.4. The percentage of the total charge distribution in each SiPM element, the estimated DoI distribution obtained with the

positioning algorithm that will be employed in the following sections and the normalized energy spectrum for those measurements are shown in figure 2.8. Figure 2.8(a) shows the percentage of the total charge detected in each SiPM applying the low threshold and figure 2.8(b) shows the distribution applying the high threshold value. For both threshold values, the location of the collimated source can be identified by the position of the pixel with the maximum value of the percentage of the detected charge. The maximum percentage of the detected charge is 5.7% and 10.9% above the mean value of all the pixels for DAC1 values of 800 and 1150 respectively. Applying the low threshold, (figure 2.8(a)) the total charge distribution is quite uniform due to the important percentage of events that interact in the first half of the crystal. On the other hand, in figure 2.8(b), all the events that interact far from the detector and produce uniform charge distribution where none of the pixels is above the threshold have been rejected resulting in a total charge distribution with a pixel with a significantly higher value. Therefore, the discriminator threshold is directly related with the DoI of the accepted events, given that increasing the threshold the events that interact far from the SiPM were rejected. Figure 2.8(c) and figure 2.8(d) show the distribution of detected events attending to the estimated DoI where for low threshold 32% of the events have been estimated in the 4 mm closer to the photodetector while this value rises to 79% of the events in the case of high threshold. In any case, figures 2.8(e) and 2.8(f) reveal that events with total energy deposition below the photopeak are included in both cases.

This is an undesired effect of applying an individual channel threshold to continuous crystals. This type of threshold is not good for our purposes because it is not possible to filter the Compton events and select only the photopeak without rejecting the events that interact far from the photodetector, thus eliminating DoI. Therefore, the acquisition threshold was set as low as possible to accept DoI while rejecting noise.

Applying the discussed criteria the threshold was set as low as possible to avoid triggering on the noise in order to accept the events interacting along the whole crystal in DoI direction. The same threshold value was applied for the measurement with 5 and 10 mm thick crystal.

### 2.2.3 Energy Resolution

Energy spectra have been obtained acquiring data in singles mode with the MAROC2 electronics board and filling a histogram with the sum of the ADC values for all channels for each event. An energy spectrum is shown in figure 2.9(a). The two photopeaks of  $^{22}\text{Na}$  (511 keV which correspond to one of the annihilation photons and 1275 keV) were fitted to a Gaussian distribution to calibrate the energy spectrum assuming linearity (assessed previously to this work), see figure 2.9(b). The energy resolution obtained for the overall

detector (crystal, SiPM, MAROC) at 511 keV photopeak was between 26% and 33%. The energy resolution is far from the values achievable with this type of detectors.

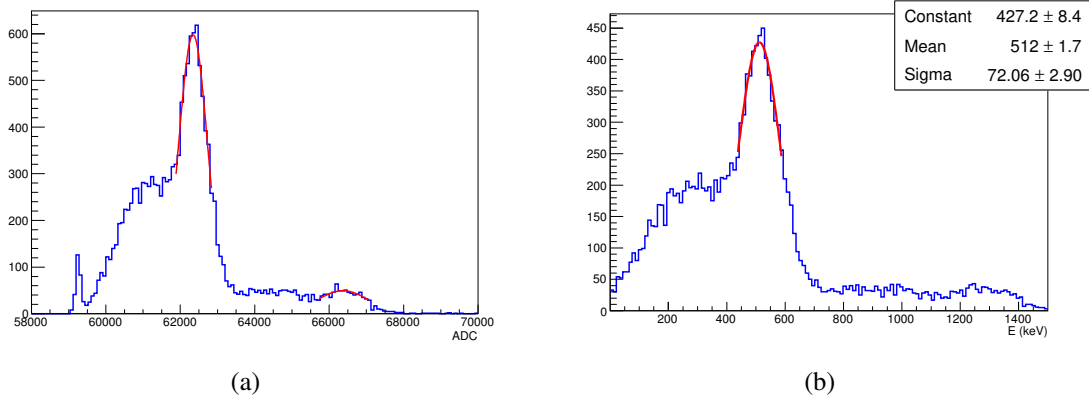


Figure 2.9  $^{22}\text{Na}$  spectra using 10 mm thick crystal measured with MAROC2 readout board. Energy spectrum in ADC units without pedestal subtraction is shown in (a) and the calibrated energy spectrum in keV units is shown in (b).

Values of 16% FWHM at 511 keV have been obtained with this set-up and FBK-irst photodetectors [1]. Temperature variations affect the energy resolution. There are fluctuations in the mean ADC value that correspond to the photopeak due to the temperature variations in the laboratory which degrade energy resolution. Besides, energy resolution depends on the employed crystal. In this work, no attempt to improve the energy resolution has been made, since these values does not influence significantly position determination studies.

## 2.2.4 Time Resolution

The time resolution study was performed in coincidence experiments with two detector heads, employing the 511 keV annihilation photons of a low activity  $^{22}\text{Na}$  source. A  $^{22}\text{Na}$  point-like source was located equidistantly from the two detector heads, so that the annihilation photons coming from the same event ideally arrive simultaneously to both detectors.

The measurement was carried out with a LeCroy WavePro 940 oscilloscope employing three channels: two channels for the trigger of the MAROC2 of each detector and the third one for the coincidence signal. The coincidence signal was used as external trigger for the oscilloscope to obtain the temporal difference of the arrival of the signal of the two detectors when there is a coincidence event. A schematic of the set-up is shown in figure 2.10.

A resolution of  $\text{FWHM}_{\text{coincidence}} = (12.8 \pm 0.2)$  ns was obtained from a Gaussian fit (see figure 2.11). Assuming both detectors have the same characteristics, the timing corresponding to a single detector was about  $(9.1 \pm 0.2)$  ns.

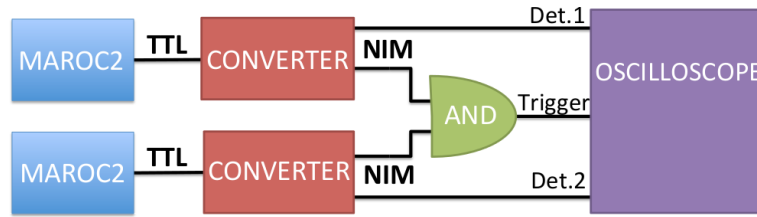


Figure 2.10 Schematic of the set-up for time resolution measurement.

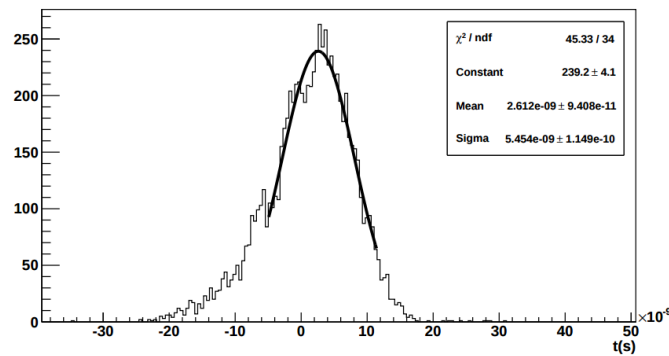


Figure 2.11 Coincidence resolution time measurement with a  $^{22}\text{Na}$  point-like source.

## 2.3 Monte Carlo Simulations

Monte Carlo simulations of the SiPM array combined with the monolithic crystal based on GATE v6.1 have been carried out including the generation of optical photons in the crystal in order to reproduce the experimental data.

A mono-energetic 511 keV point-like source with an opening emission angle of  $1.005^\circ$  was simulated yielding the same spot size ( $\sim 0.21$  mm diameter) on the crystal surface as in the experimental data. The detector has been simulated with the same geometry as the experimental set-up (figure 2.3). From the source to the SiPM matrix we have: the LYSO crystal, the optical grease used to optically couple the SiPM matrix to the crystal (0.4 mm thick) and the epoxy coating (0.3 mm thick) of the SiPM matrix. Some real values of the parameters of the detector (crystal surface reflectivity and roughness, reflector characteristics, optical glue thickness, etc.) are unknown. Those parameters have been adjusted to reproduce the light distribution in the crystal.

Although 5 and 10 mm thick crystals have slightly different properties and thus the experimental results have small variations, we have decided to select a set of parameters for the simulations that matches well all the measurements instead of aiming at a perfect match with different parameters in each case, with the aim of extrapolating the results to other geometries. Section 2.3.1 describes the parameters needed to reproduce the simulation.

### 2.3.1 Properties of materials and surfaces included in the simulations

Some of the properties of the crystal are given by the manufacturer: density ( $7.1 \text{ g/cm}^3$ ), absolute light yield (32000 phot/MeV), decay constant (40 ns) and emission peak (420 nm). The index of refraction was set as a function of wavelength [66]. Intrinsic energy resolution was also defined. LYSO:Ce intrinsic energy resolution of  $\frac{\Delta E}{E} = 9\%$  for 511 keV [67, 68], corresponding to a 4.90 scale factor was simulated. The optical absorption length determined from the measured transmission spectrum of a  $20 \times 10 \times 20 \text{ mm}^3$  LYSO:Ce crystal in [67] was included in the simulations. The scattering length [69] is only significant below 420 nm and in the range of 1 to 2 m. In the non-fluorescent region scattering length is three orders of magnitude larger than the crystal dimension, so it has a negligible effect. The natural radioactivity of  $^{176}\text{Lu}$  has not been included in the simulations because it has a minor impact on the collected charge distribution. The optical grease (Rhodorsil Paste 7) has a refractive index  $n = 1.41$  [70]. The SiPM is coated with EPOTEK-301-2 optical glue with a refractive index for the emission peak of LYSO of approximately 1.59 [71]. The thickness of the coating is  $(300 \pm 50) \mu\text{m}$  and the thickness of the silicon die is  $(375 \pm 150) \mu\text{m}$  according to the manufacturer.

Table 2.1 summarizes the characteristics of the optical surfaces employed in the simulations. The LYSO-air surface has been simulated with the attribute *ground-back-painted* with a reflectivity value of 98% corresponding to a white crystal. In the case of the ground-back-painted surface, the next volume (paint layer) is considered to be the reflector. The surface between LYSO and the reflector was polished with a very low level of roughness due to micro-facet surfaces with normal vectors following a Gaussian distribution with  $\sigma=0.1^\circ$ . The paint layer reflects photons assuming Lambertian reflection. The reflected photons reach a micro-facet where they can again be reflected or refracted and there we have defined 70% of the reflections to be diffuse reflections and 30% specular reflections to match the experimental data.

Table 2.1 Optical interfaces defined in the simulations. The rest of the interfaces were defined as dielectric-dielectric surface, following Snell equations with specular reflections.

Optical interface	Type	Finish	Reflectivity (%)
LYSO-air	dielectric-dielectric	groundbackpainted	98
pixel-SiPM	dielectric-metal	polished	-
pixel-Epoxy	dielectric-metal	polished	-

### 2.3.2 Properties of the SiPM array performance

The optical photons that interact in the sensitive elements of the SiPM array are considered for data analysis. After the simulation process, some SiPM parameters were included. The photon detection efficiency (PDE) of the SiPM was considered to be 16%, which is in the range specified by the manufacturer. AdvanSiD data sheet specified a PDE of 18% at 420 nm, 5 V overvoltage and 20°C temperature. Operational parameters are  $\sim 3$  V overvoltage in a temperature range between 23°C and 27°C.

### 2.3.3 Simulation validation

The simulation depends on many parameters, the actual values of which are not always known. In our case, crystal surface reflectivity and roughness, reflector characteristics and optical glue thickness among others must be specified to model the system. A complete systematic validation of the simulated data would require the selection of one set of parameters for the simulation that matches all the sets of data (measurements with different crystal thickness, with different positions of the beam, with differently manufactured crystals ...) and a figure of merit to study the agreement between simulated and experimental data. The optimization of so many parameters simultaneously for different situations would require a deep study that is far beyond the scope of this work. Thus, we have validated our simulation adapting the unknown values of the parameters of the simulations to have a good agreement with the light distribution measured in the photodetector, which determines the position determination accuracy.

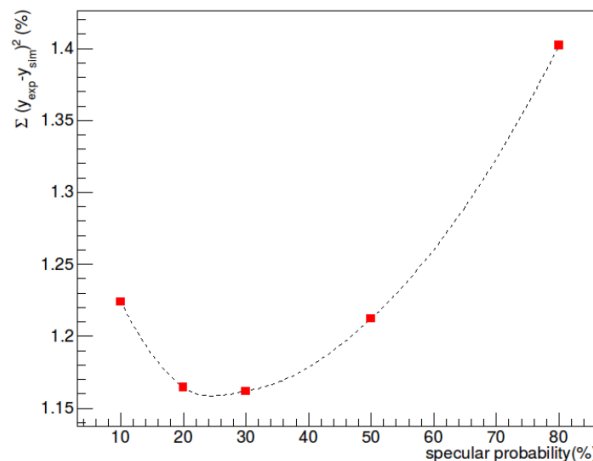


Figure 2.12 Agreement between the percentage of the total detected mean charge distribution for experimental and simulated data for different values of the probability of having specular reflections using 5 mm thick crystal and the beam located in the central position

The quadratic sum of the differences between the percentage of the total mean charge detected in each SiPM for experimental and simulated data was employed as a figure of merit to study the variation of the light distribution with the unknown parameters. The study was carried out for some representative cases. One of these cases is represented in section 2.3.3, which shows the result of calculating this figure of merit for different values of the probability of having specular reflections in the simulated crystal-air surface for the 5 mm thick crystal with the beam located at the central position in section 2.3.3. The agreement was better for a probability of 30% of having specular reflections than for the rest of studied values.

The parameters described in section 2.3.1 were the ones adjusted in the simulations. Some of the SiPM parameters have not been considered in the simulations such as nonuniform gain, dark counts or gain and PDE shifts due to temperature variations.

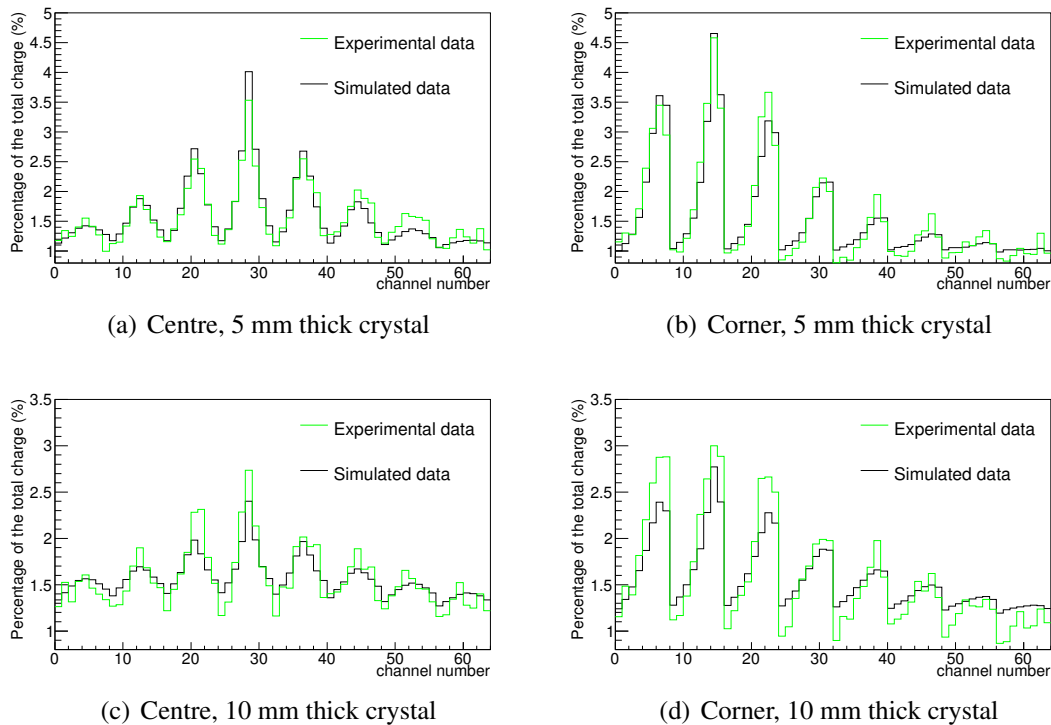


Figure 2.13 Comparison of the simulated (black) and experimental (green) normalized charge accumulation for two position, central position and the one close to the edge, for 5 and 10 mm thick crystals.

Simulations were performed placing the collimated source at the four different positions of one quarter of the detector, corresponding to the nominal experimental positions (section 2.1.4). The set of simulation parameters which better reproduces the experimental results has been selected (see section 2.3.1). The histograms shown in figure 2.13 represent the

percentage of the total mean charge detected in each SiPM element, for all events collected. Results are shown for two positions, the central position, and the one close to the corner. The charge distribution for both beam positions are shown in figure 2.13(a) and figure 2.13(b) for the 5 mm thick white painted crystal. The same results are shown for the 10 mm thick crystal in figure 2.13(c) and figure 2.13(d) with a good agreement for both crystals.

As a consequence of not having simulated all parameters, some detector characteristics such as the spatial resolution (section 2.4.5) and energy resolution obtained with simulated data are better than with experimental data. The difference in the resulting energy resolution is mainly due to the temperature variations during experimental data acquisition. The energy resolution at 511 keV for simulated data is  $\sim 10\%$  FWHM, whereas for experimental data is significantly higher. Nevertheless, these parameters do not affect significantly the performance of the position determination algorithm and the validated simulations allow us to study the response of the detector with different geometries and thickness and also to estimate realistically the performance of the detector with different reflectors (section 2.4.6).

The exact match of all the characterization parameters, that would require a much deeper study, is not sought in this thesis, which aims at a comparative study of different geometries and situations. Thus, the parameters of the simulation have not been exactly adapted to reproduce the numerical value of experimental spatial resolution, since in this thesis simulations have only been employed to compare between different configurations.

## 2.4 Position Determination

Position determination constitutes the main part of the detector characterization studies. The position determination method employed in this work [13] is based on the model described in section 1.5.4. The estimation of the direct light arriving to each pixel is based on the solid angle subtended by it from the light source and the contribution of internal reflections is based on the the solid angle subtended by it from the location of virtual sources.

The differences in X-Y spatial resolution using approximate and exact solid angle models were found to be negligible. Therefore, the approximate solid angle model was employed to determine X-Y positions because it is faster to compute. However, in the case of the DoI determination there are differences between the results of the two models in the events placed one millimetre close to the photodetector in the Y-Z projection. For this reason, the results in section 2.4.4 were obtained employing the exact solid angle model.

Modifications on the model have been investigated considering separately the contribution of real and virtual sources using different parameters with the aim of adapting it to obtain the



best possible results with our experimental data. The contribution of virtual sources has been modified or eliminated to adapt the model to the experimental case. In the equation:

$$np_i = C_{est} + A_0\Omega(x, y, z) + A_{0VS} \sum_j \Omega(x_j, y_j, z_j), \quad (2.1)$$

different options have been investigated:

- **VS0 model:** when there is no contribution of virtual sources  $A_{0VS}=0$ .
- **VS1 model:** when the weight for direct light and for the reflections has the same value  $A_0=A_{0VS}$  (original model).
- **Independent VS1 model:** when both parameters ( $A_0, A_{0VS}$ ) are determined independently.
- **Independent VS1\* model:** In addition, this model discards the events with a weight value for the reflected light  $A_{0VS}$  with respect to weight value of the direct light  $A_0$  bigger than a defined acceptance limit (AL),  $\frac{A_{0VS}}{A_0} \geq AL$ .

In order to speed-up the process and have a more flexible code, easier to integrate with the data analysis and image reconstruction, we implemented the algorithm in C++. A Levenberg-Marquardt optimizer was used from the ALGLIB libraries, [72]. The computation time using a core Intel (R) Core (TM) 2 Quad CPU Q6700 @ 2.66 GHz is about 126 events/s for experimental data and 207 events/s for simulated data using a detector of 64 pixels. The difference is due to the preprocessing of experimental data. The estimated interaction positions located just in the surfaces of the crystal which correspond to the boundary conditions of the optimization algorithm were rejected in this chapter.

The outcome of the analysis is a 3D distribution of the reconstructed interaction positions (DRIP) for each experimental or simulated interaction position under study. In order to compare the results, contours of the DRIP at different heights (half maximum (HM) and tenth maximum (TM)), profiles through the maximum of the distribution and XY or YZ projections have been studied. The contours have been mainly employed to study the shape of the distributions and X and Y profiles through the maximum of the DRIP to study the spatial resolution. The profiles are fitted with a Gaussian function or a Lorentzian function given by:

$$L(x) = \frac{1}{\pi} \frac{\frac{1}{2}\Gamma}{(x - x_0)^2 + (\frac{1}{2}\Gamma)^2}, \quad (2.2)$$

where  $x_0$  is the mean value and  $\Gamma$  is the FWHM of the distribution.

The work carried out includes previous studies that have been performed to determine the optimum experimental conditions for position determination measurements and for a better understanding of the model. Experimental and simulated results for X,Y and DoI resolution and bias have been obtained. The results are presented in section 2.4.3, 2.4.4 and 2.4.2.

### 2.4.1 Previous studies

The experimental conditions were determined by studying the optimum range for the distance from the collimated source to the crystal. In addition, in order to better understand the model response, the contribution of real and virtual sources to the model was analysed and studied in two ways: applying the method to different simulated behaviours for the reflections of the optical photons in the crystal surface and also to experimental data with diffuse and specular crystal reflectors. Finally, the parameters of the model that produce the best possible results with our experimental data with white painted crystals were determined to be applied in the data analysis presented in the following sections.

#### 2.4.1.1 Optimization of the distance from the source to the crystal surface

In order to determine the optimum distance from the collimated source to the crystal surface, position determination measurements with the source at different distances were performed employing the model for the estimation of the interaction position. The shorter distance at which the source could be positioned from the crystal was around 3 mm because of the thickness of its encapsulation. X and Y profiles through the maximum of the DRIP were fitted with a Gaussian distribution and the value of the FWHM for each distance is shown in Figure 2.14. An appropriate working range was found for a distance between 4.7 and 6.7 mm. All position determination measurements were taken at the centre of that range, corresponding to a distance of 5.7 mm.

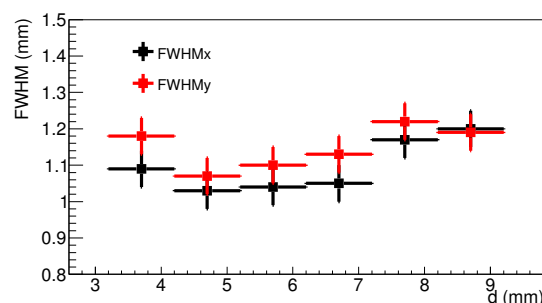


Figure 2.14 Resolution (FWHM) for a central point at different distances.

### 2.4.1.2 Effect of the VS0 and VS1 models on simulated diffuse and specular reflectors

In order to determine the applicability of the models VS0 and VS1, simulations with ideal specular and diffuse reflector have been performed and the model response has been studied.

The interaction position under study has been selected close to the crystal corner in (3.75,3.75) mm, to better study the effect of the reflections. The DRIP is obtained for 15000 events.

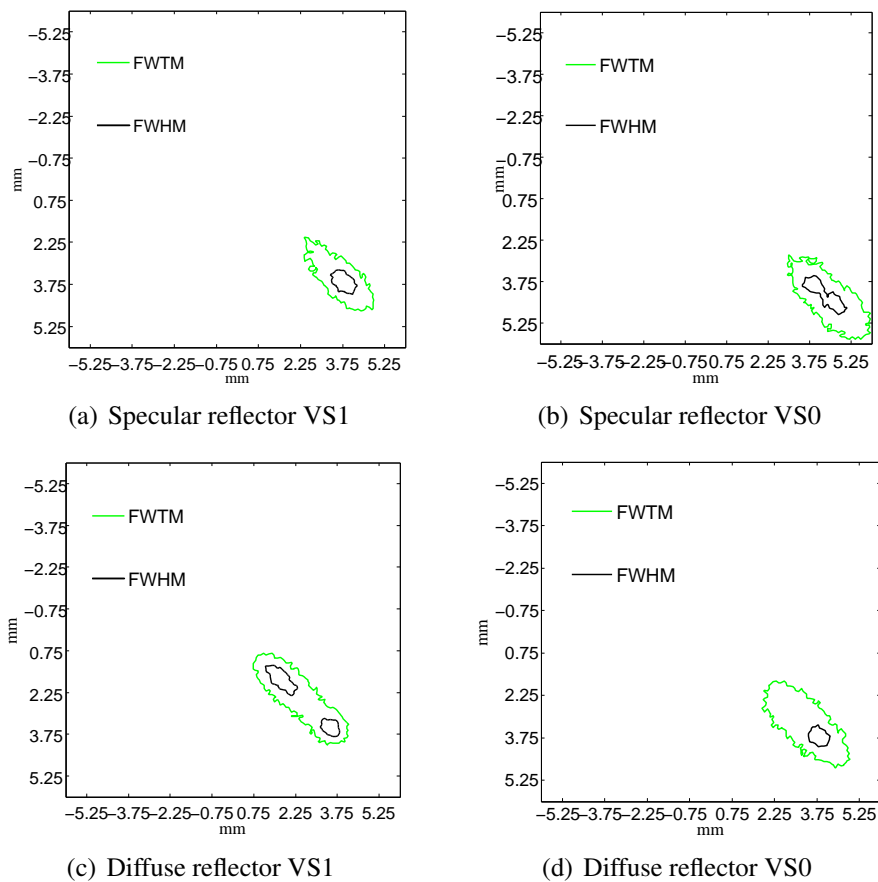


Figure 2.15 X-Y contours of the DRIPs at HM and at TM for simulations with ideal specular reflector and diffuse reflector. On the left modelling specular reflections with the same weight as the direct light (VS1) and on the right without modelling reflections (VS0).

Figure 2.15 shows the X-Y contours of the DRIP at HM and at TM. Figure 2.15(a) and figure 2.15(b) show the contours for the simulated ideal 100% specular reflector using the two models in the reconstruction algorithm: with virtual sources having the same weight as the direct light (VS1), and without considering virtual sources (VS0). Figure 2.15(c) and figure 2.15(d) show the same results for simulated 100% diffuse reflector. Even though there is an elongation towards the centre of the crystal in all cases, it can be observed that

when reflections are specular, modelling mirror-like reflections improves spatial resolution. However, if reflections are not purely specular, the results are more accurate using VS0 than VS1 model.

### 2.4.1.3 Comparison of the model performance with experimental data using diffuse and specular reflectors

The data taken with the 10 mm thick crystal with specular reflector are compared to the 10 mm thick white painted crystal in order to explore experimentally if the model performs better with specular reflectors than with painted crystals. Figure 2.16 shows the comparison of the contour plots of the DRIP at HM and at TM for the source located near the edge for the crystal with specular reflector (black) and the white painted crystal (red). The performance of the specular reflector crystal was slightly better when the specular reflections are included in the model, but there is no significant improvement in the results and the behaviour is very similar to the white painted crystal.

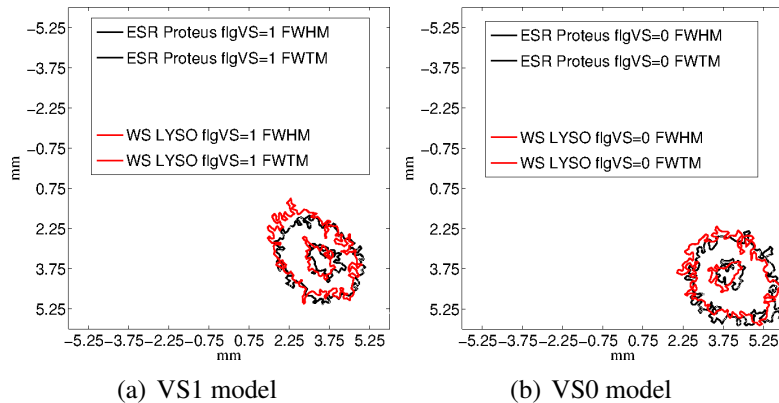


Figure 2.16 X-Y contours at HM and at TM for experimental data for specular reflector and white painted (diffuse reflector) 10 mm thick crystals.

### 2.4.1.4 Parameter selection for Position Reconstruction algorithm in experimental data with white painted crystals

The spatial resolution of the detector has been studied with the four models to evaluate if including mirror-like reflections improves or degrades the accuracy in position estimation in experimental data with white painted crystals. Table 2.2 summarizes the four different models employed, described in section 2.4.

Table 2.2 Light distribution models. Relationship between the contribution of virtual sources ( $A_{0VS}$ ) and direct light ( $A_0$ ).

	Models			
	VS0	VS1	Independent VS1	Independent VS1*
Relation between $A_{0VS}$ and $A_0$	$A_{0VS} = 0$	$A_{0VS} = A_0$	no relation	no relation
Rejected events	no rejection	no rejection	no rejection	$\frac{A_{0VS}}{A_0} > AL$

The resolution, center (centroid) position and shape of the contours of the DRIP have been studied in order to select the parameters of the model that better match the experimental data.

Figure 2.17 shows an X-profile for the central point for 10 mm thick crystal using VS0 model fitted with a Gaussian and a Lorentzian function. The Lorentzian function fits better the shape of the distribution. The FWHM is 1.20 mm fitting the peak with a Gaussian function and 0.94 mm fitting it with a Lorentzian function.

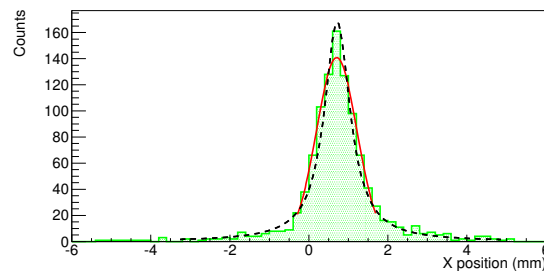


Figure 2.17 Fit of a profile through the maximum of the reconstructed interaction position distribution for a 10 mm thick crystal with a Gaussian function (solid line) and with a Lorentzian function (dashed line).

### Effect of virtual sources in experimental data

Table 2.3 and table 2.4 show the average FWHM and standard deviation for the four different positions of the source in one quarter of the crystal, for 5 and 10 mm thick crystals respectively. The FWHM was obtained by fitting the X and Y profiles of the DRIP with Gaussian and Lorentzian functions. It can be observed that for both crystals the result is slightly better with the model including specular virtual sources, VS1.

Table 2.3 Average resolution of the four reconstructed positions obtained fitting the profile through the maximum in X and Y directions for the 5 mm thick white painted LYSO crystal.

mm	$\overline{FWHM}_x^{Gauss}$	$\overline{FWHM}_y^{Gauss}$	$\overline{FWHM}_x^{Lor}$	$\overline{FWHM}_y^{Lor}$
VS1	0.89±0.03	0.94±0.03	0.75±0.03	0.80±0.03
VS0	1.06±0.03	1.01±0.03	0.85±0.06	0.89±0.06

Table 2.4 Average resolution of the four reconstructed positions obtained fitting the profile through the maximum in X and Y directions for the 10 mm thick white painted LYSO crystal.

mm	$\overline{FWHM}_x^{Gauss}$	$\overline{FWHM}_y^{Gauss}$	$\overline{FWHM}_x^{Lor}$	$\overline{FWHM}_y^{Lor}$
VS1	1.22±0.05	1.36±0.05	1.0±0.1	1.2±0.1
VS0	1.30±0.05	1.29±0.05	1.1±0.1	1.1±0.1

### Effect of Acceptance Limit (AL) for Independent VS1\* with experimental data

The effect of the AL for Independent VS1\* has been studied. To this end, the contours at HM and TM of the DRIP have been studied for different AL values of  $A_{0VS}/A_0$ . Figure 2.18 shows the contours for different values of the AL ( $(\frac{A_{0VS}}{A_0})_{AL} = \{2, 0.9, 0.5, 0.1\}$ ) and without rejecting any events for experimental data obtained at the interaction position located near the edge with the 10 mm thick crystal. The main difference is in the size of the contours at TM, which decreases with the AL. The behaviour of the size of the contour at HM is not monotonic with the AL. The contour size at HM is larger when the value of the AL is above 0.5 and the size is smaller when the value is below 0.5 than when all the data is taken into account (Independent VS1). However, there were not significant changes below an AL of 0.5.

A trade-off between the best performance in terms of smaller contours at TM (figure 2.18(b)) and the percentage of accepted events was obtained for an AL of  $\frac{A_{0VS}}{A_0}$  close to 0.5.

### Effect of the models on the bias and shape of the contours

The deviation of the center (centroid) of the DRIP contours from the interaction position of the beam in X-Y plane is known as X-Y bias. Due to the lack of an absolute reference frame for experimental data, X-Y bias has been studied analysing the relative distance between the centroid of the contours of two interaction positions, the central and the corner

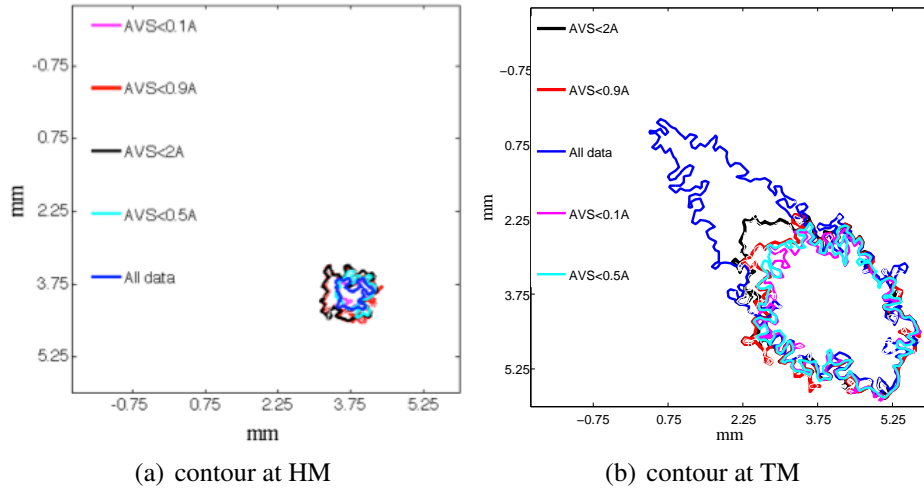


Figure 2.18 X-Y contours at HM and at TM of the DRIP for experimental data (beam located at the corner position) and different values of AL.

positions, after checking that the central position does not change significantly with the different models.

Figure 2.19 shows the X-Y contours at HM and at TM of the DRIP for the corner position and the TM for the central position (dashed line), employing the four different models for the light distribution. It can be observed that the X-Y distribution for VS1 model was misplaced (biased) towards the centre whereas for VS0 model it was slightly positioned towards the corner of the crystal.

We know the real value of the distance between those two points in X and Y directions (3 mm in both directions) and we calculate the relative error ( $\epsilon_{r,Position}$ ) for each model (see table 2.5). The relative error in the position for VS1 was more than two times larger than for VS0.

Table 2.5  $\epsilon_{r,Position}$  is the relative error of the position of the centre of the contour of the DRIP for the corner position.

(x,y)	VS1	VS0	Independent VS1	Independent VS1*
$\epsilon_{r,Position}^{HM}$ (%)	(-9,-8)	(-1,2)	(0,2)	(1,2)
$\epsilon_{r,Position}^{TM}$ (%)	(-21,-17)	(4,5)	(-16,-16)	(8,9)

In addition, the shape of the DRIP was studied for the corner position of the 10 mm thick crystal, for which the influence of the reflections in the charge distribution is more important. The shape of the contour at TM was characterized by the projections along the direction of the elongation ( $l_{45^\circ+90^\circ}$ ) and its perpendicular direction ( $l_{45^\circ}$ ), the two diagonals (figure

2.19(a). Table 2.6 shows  $l_{45^\circ}$ ,  $l_{45^\circ+90^\circ}$  of the X-Y contours for the corner position and the ratio of the TM values ( $(\frac{l_{45^\circ}}{l_{45^\circ+90^\circ}})^{TM}$ ) which represents the asymmetry of the shape.

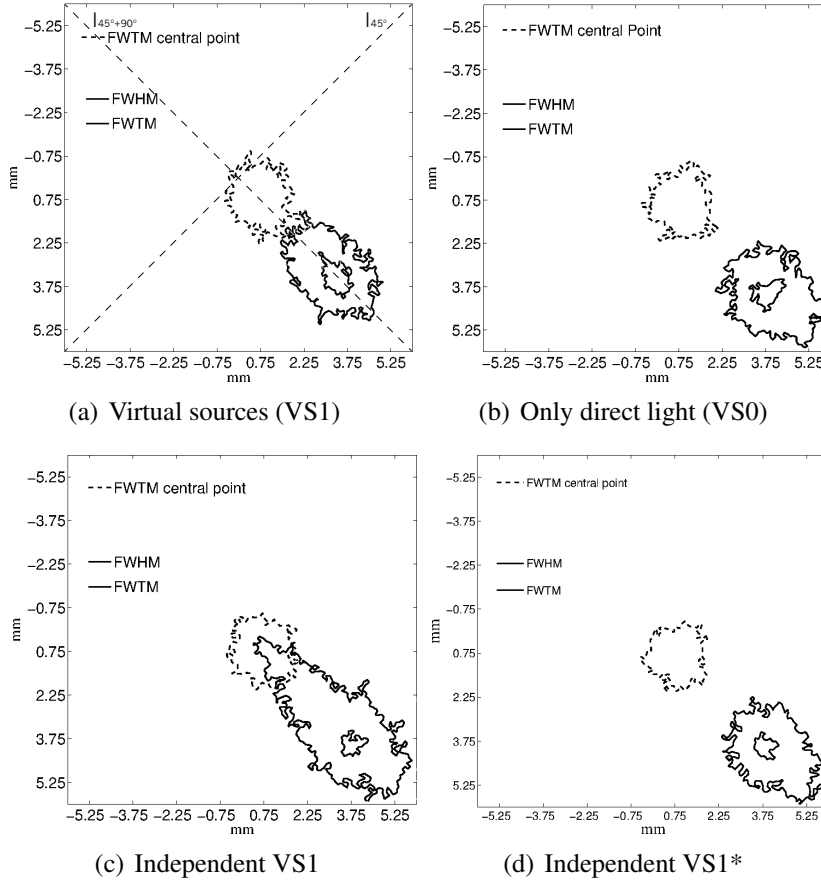


Figure 2.19 X-Y contours of the DRIP at HM and at TM for different models.

Table 2.6  $l_{45^\circ}^{TM}$  and  $l_{45^\circ+90^\circ}^{TM}$  are the projections along  $45^\circ$  and its perpendicular of the contour at TM of the DRIP for the corner position.

(x,y)	VS1	VS0	Independent VS1	Independent VS1*
$l_{45^\circ}^{TM}$ (mm)	3.3	3.6	3.8	3.1
$l_{45^\circ+90^\circ}^{TM}$ (mm)	4.5	4.3	7.5	4.3
$(\frac{l_{45^\circ}}{l_{45^\circ+90^\circ}})^{TM}$	0.73	0.84	0.51	0.72

Asymmetries of the contours for VS0 model are less pronounced than for VS1 as it can be seen by the value of the ratio of the projections, which is closer to 1.

Considering the previous results, we conclude that position determination in our case is more accurate when specular reflections are not included for experimental data reconstruction.



The best performance for the experimental data is obtained without modelling reflections VS0 or modelling reflections independently and discarding the events with a weight value for specular reflections above half of the weight value for direct light (Independent VS1\*). However, the latter discards about 48% of the recorded events. So experimental data were reconstructed with VS0 model.

### **Effect of the models in z**

Although the DoI will be studied in detail in section 2.4.4 and section 2.4.5, the effect of the different models has also been checked. The elongation of the XY contour depends also on the z of the interaction position.

The DRIP of the source located in the corner of the 10 mm thick crystal was also represented by its projections into the X-Y and Y-Z plane within the crystal in figure 2.20 using VS0 and VS1 model. The grid represents the size of the pixels of the SiPM and the Z-coordinate increases towards the SiPM. The DRIP for the measurements taken with this beam position would be ideally distributed within the grid lines that represent the pixel centred at (3.75,3.75)mm. Figure 2.20(a) and figure 2.20(b) show the X-Y and Y-Z projections respectively using VS1 model. It can be observed that the events reconstructed far from the SiPM are mispositioned towards the centre of the crystal. On the other hand, figure 2.20(c) and figure 2.20(d) show the X-Y and Y-Z projections respectively using VS0 model where in X-Y projection mostly all the events are estimated within the corresponding pixel and in Y-Z projection. Although the real DoI value is unknown for each event, the DoI distribution of the events can be observed reasonably distributed along the thickness of the crystal.

### **Model selection**

The best spatial resolution results were obtained using VS1. However, a lower bias was obtained at the edges without considering reflections (VS0). An overestimation of the reflections (VS1) misplaced the position towards the centre of the crystal, while eliminating reflections from the model (VS0) misplaced slightly the position towards the corner. The smaller misplacement using VS0 model means that the predominant contribution in the light pattern came from the direct light.

Given the results of the previous test, in the following sections, VS0 model has been selected and will be employed to reconstruct experimental data and also simulated data unless otherwise stated.

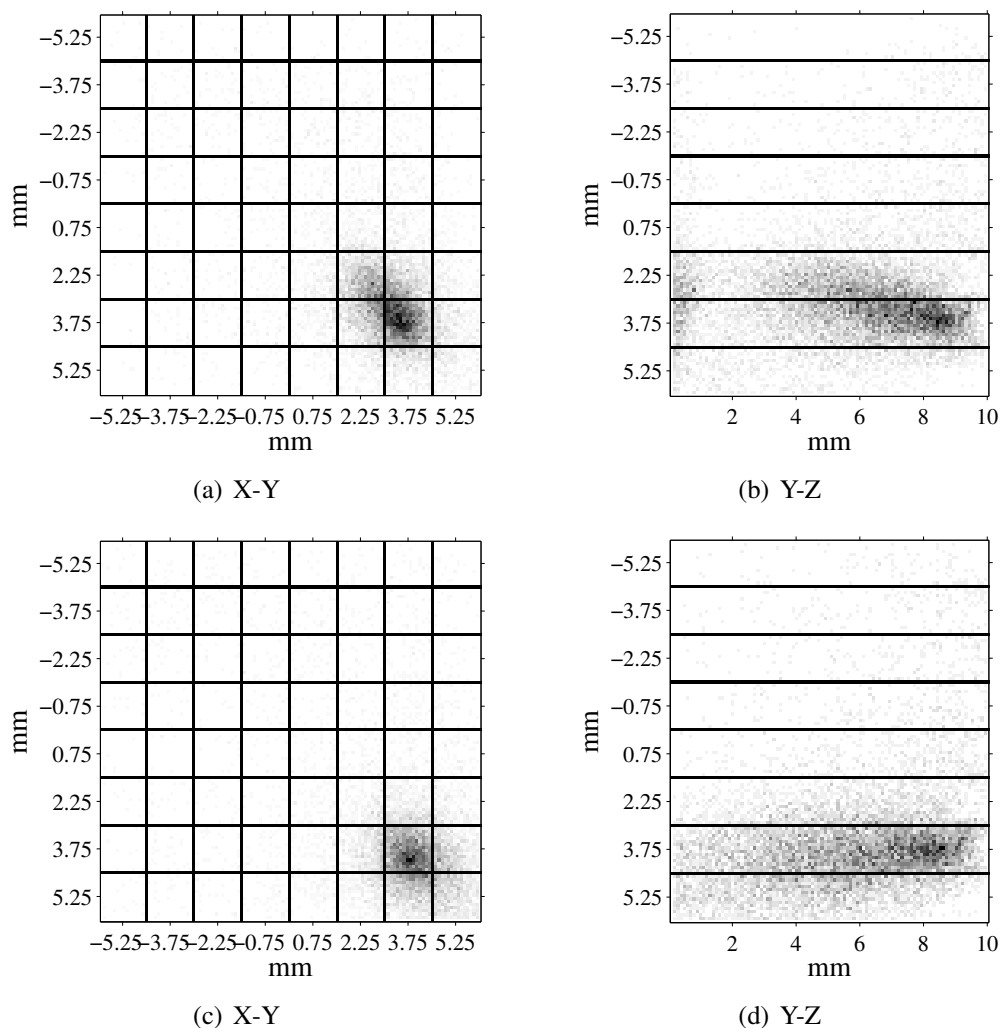


Figure 2.20 X-Y and Y-Z projection of the interaction position distribution for the position located at the edge of 10 mm thick crystal are shown in (a) and (b) respectively applying VS0 model and in (c) and (d) applying VS1 model. The Z-coordinate increases towards the SiPM.

## 2.4.2 Determination of X-Y resolution

Once the parameters of the position estimation model that better match the experimental data have been determined, the X-Y spatial resolution characterization of the 5 and 10 mm thick detectors was studied for the four positions over the surface.

The FWHM was obtained in each case by fitting the profile through the maximum of the DRIPs in X and Y directions with Gaussian and Lorentzian functions. Table 2.7 shows the summary of the average FWHM in X and Y direction of the four representative positions over the surface of the crystal described in section 2.1.4 for 5 and 10 mm thick crystals.

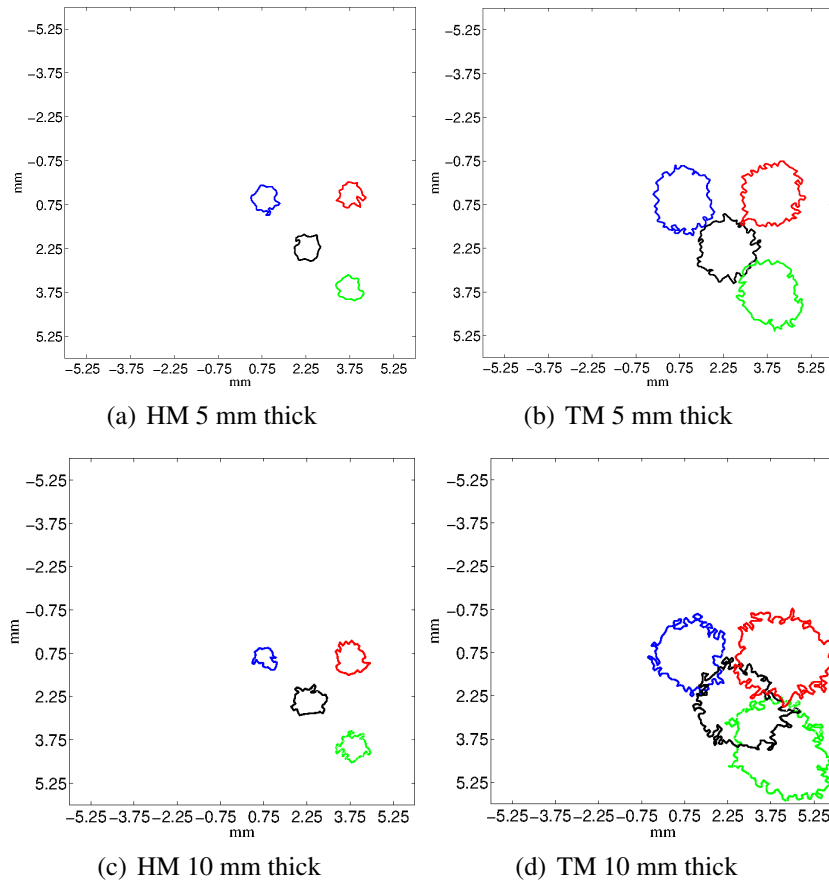


Figure 2.21 Contours at HM and at TM of the X-Y projections of the distributions of the reconstructed position interactions for a point-like source in four different positions for the 5 mm thick crystal ((a),(b)) and for the 10 mm thick crystal ((c),(d)) and VS0 model.

Table 2.7 Average resolution of the four reconstructed positions obtained fitting the profile through the maximum in X and Y directions for the 5 mm and the 10 mm thick white painted LYSO crystal.

mm	$\overline{FWHM}_x^{Gauss}$	$\overline{FWHM}_y^{Gauss}$	$\overline{FWHM}_x^{Lor}$	$\overline{FWHM}_y^{Lor}$
5 mm thick crystal	$1.06 \pm 0.03$	$1.01 \pm 0.03$	$0.85 \pm 0.06$	$0.89 \pm 0.06$
10 mm thick crystal	$1.30 \pm 0.05$	$1.29 \pm 0.05$	$1.1 \pm 0.1$	$1.1 \pm 0.1$

Figure 2.21 shows the contours of the DRIP at HM and at TM in the X-Y plane for each of the four positions of the source for the 5 and 10 mm thick crystal.

### 2.4.3 X-Y bias determination with simulated data

Due to the lack of an absolute reference frame in the experimental data and in order to better characterize the effect of the bias without other types of distortion, validated simulations have been used to study the X-Y bias of the position determination method in the four reference positions. Table 2.8 shows the difference between the X-Y estimated interaction position and the gamma-ray source location set in the simulation for 5 and 10 mm thick crystal. It can be observed that the estimated position is slightly misplaced towards the edge of the crystal. The bias increases gradually towards the edge. The central position is biased around 0.1 mm while the position close to the edge is biased around 0.2 mm in both directions.

The bias of the position determination method for simulated data is almost negligible in the centre of the crystal and remains small even for the worst case.

Table 2.8 Difference between the estimated interaction position and the gamma-ray source location in (X,Y).

$\Delta\text{Pos}$ (mm)	Source location (X,Y)(mm)			
	(0.75,0.75)	(2.25,2.25)	(3.75,3.75)	(3.75,0.75)
5 mm thick	(0.08,0.08)	(0.17,0.12)	(0.19,0.19)	(0.43,0.05)
10 mm thick	(0.08,0.09)	(0.14,0.12)	(0.15,0.17)	(0.34,0.12)

### 2.4.4 DoI resolution and Bias for experimental data

Due to the geometry of the PCB at which the photodetector is connected and the position determination set-up, there is no possible configuration for side irradiation with the collimated source. Therefore, the real DoI position can not be known.

An estimate of the DoI resolution was obtained through a consistency check, employing the source-detector configuration described in figure 2.3(b). In this configuration, the emitted gamma-rays imping in the detector at a  $45^\circ$  angle from the detector surface, so that the displacement in Y-axis from the entry position is equivalent to the DoI value. Following this approach, the DoI error distribution was computed as the difference of the reconstructed DoI position and the reconstructed transversal displacement ( $\text{DoI} - \Delta y$ ) for all the events. DoI resolution was defined as the FWHM of the distribution and DoI bias as the mean of the DoI error distribution fitted with a Gaussian function. However, the error distribution is not Gaussian and FWHM and FWTM values have been also estimated by linear interpolation between adjacent pixels. DoI bias, which has been considered here as the mean of ( $\text{DoI} - \Delta y$ ) distribution, is influenced by the uncertainty on the mean incidence position of the beam in

Y-axis. Thus, bias was studied only for simulated data, where the beam incidence position was perfectly defined.

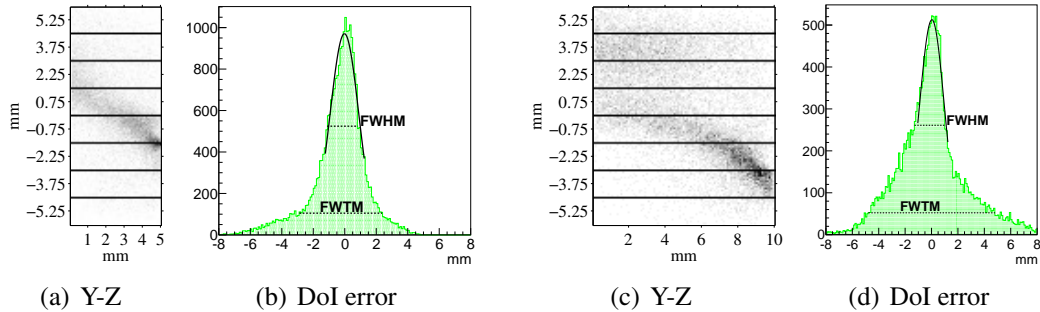


Figure 2.22 Y-Z projection of the reconstructed position distribution (a,c) and DoI error distribution (b,d) for 5 and 10 mm thick crystals respectively. Data were acquired with a collimated point source incident on the detector surface at a  $45^\circ$  angle.

Figure 2.22 shows the Y-Z projections (a,c) and DoI error distribution (b,d) of the estimated interaction position distribution for 5 and 10 mm thick crystals respectively. The FWHM of the error distribution for 5 mm thick crystal is  $(2.12 \pm 0.05)$  mm whereas for 10 mm thick crystal it is  $(2.19 \pm 0.05)$  mm. The FWHM and FWTM values estimated by linear interpolation are 2.0 and 5.3 mm respectively for 5 mm thick crystal and 2.3 and 9.6 mm respectively for 10 mm thick crystal. The large FWTM for the 10 mm thick crystal is caused by the events that interact far from the photodetector, most of which are mispositioned.

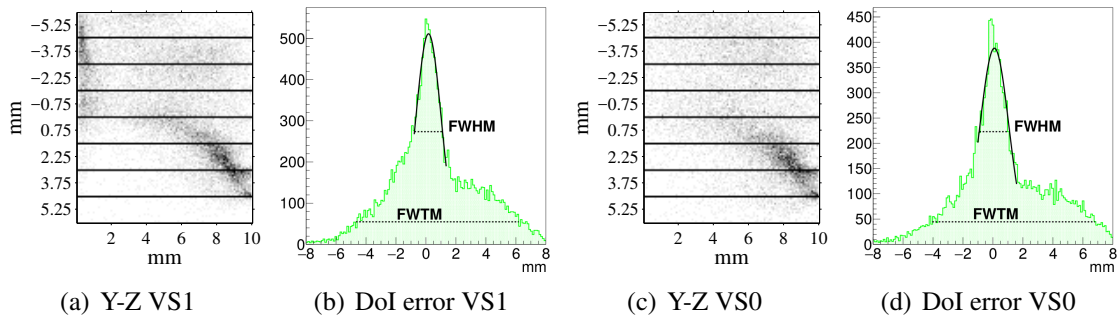


Figure 2.23 Y-Z projection of the reconstructed position distribution (a,c) and DoI error distribution (b,d) for 10 mm thick crystal with specular reflector using VS0 and VS1 respectively. Data were acquired with a collimated point source incident on the detector surface at a  $45^\circ$  angle.

The results obtained with the 10 mm thick crystal with specular reflector are very similar to the 10 mm white painted crystal (figure 2.23). The DoI resolution obtained for specular reflector is  $(1.98 \pm 0.05)$  mm for the model including specular reflections (VS1) and

( $2.21 \pm 0.05$ ) mm not including them (VS0). The FWHM and FWTM values estimated by linear interpolation are 2.0 and 10.9 mm respectively for VS1 model and 2.2 and 10.9 mm respectively for VS0 model.

### 2.4.5 DoI resolution and bias for validated simulations.

DoI resolution and bias were analysed for validated simulations and compared to experimental data. As in experimental data, a collimated point source incident on the detector surface at a  $45^\circ$  angle was simulated. The FWHM of the error distribution for the 5 mm thick crystal is ( $1.04 \pm 0.01$ ) mm whereas for the 10 mm thick crystal it is ( $1.53 \pm 0.04$ ) mm. The FWHM and FWTM values of the error distribution estimated by linear interpolation are 1.0 and 2.2 mm respectively for the 5 mm thick crystal and 1.6 and 6.5 mm respectively for the 10 mm thick crystal. In the simulations, as well as in the experimental data (figure 2.24), the DoI information is better determined for the events occurred in the five millimetres closest to the photodetector in our system.

The behaviour of the DoI error distribution and the Y-Z projection of the DRIP for simulations is in quite good agreement with experimental data. Therefore, in the following section the validated simulation will be employed to study alternative geometries of the detectors.

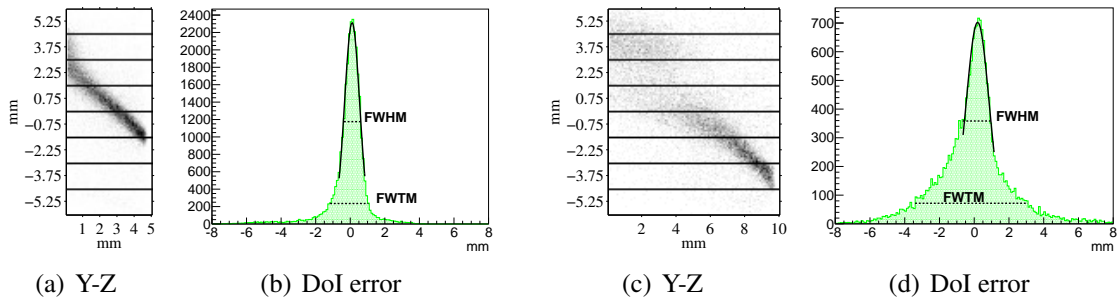


Figure 2.24 Y-Z projection of the reconstructed position distribution (a,c) and DoI error distribution (b,d) for 5 and 10 mm thick crystals respectively.

### 2.4.6 DoI resolution and bias for simulated optimized geometries

In thick crystals, the charge distribution of the events that interact far from the photodetector is quite uniform due to the strong interference of the diffuse reflections of the optical photons on the sides of the crystal. The light distribution is rather homogeneous and it does not contain position information [73].

This can be seen in figure 2.25, which shows the charge distribution of two simulated events in which the gamma-ray is photo-absorbed at different depths along the crystal for the 10 mm thick crystal with the beam located at the central position. Figure 2.25(a) shows the charge distribution when the gamma-ray interacted at the centre of the crystal and figure 2.25(b) when it interacted at a distance of one millimetre from the photodetector. It can be seen that when the gamma-ray interacts farther from the photodetector the charge distribution is more homogeneous and contains less position information.

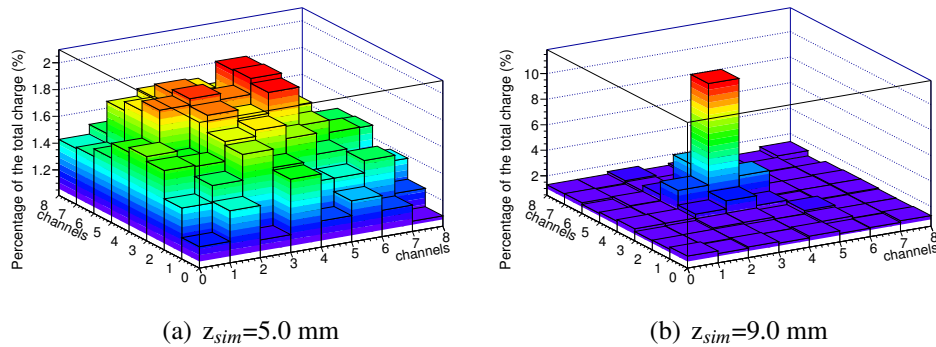


Figure 2.25 The charge distribution of different events that have interacted at different depths along the crystal: (a) 5 mm and (b) 1 mm from the photodetector using validated simulations of the 10 mm thick crystal.

The Aspect Ratio (AR, ratio of length of the side of the detector to thickness) and the surface treatment of the crystal are the main parameters that influence the impact of the reflections on the light distribution. The simulation study presented in [73] concluded that a larger AR produces less light interferences in the light distribution than smaller AR.

In the following sections (section 2.4.6.1 and section 2.4.6.2), the influence of the AR for the diffuse reflector employed in the validated simulation and the influence of different reflectors for an AR of 1.2 on the DoI estimation error has been studied.

#### 2.4.6.1 Aspect Ratio of the Scintillator

The DoI error was studied employing the validated simulations for different values of the crystal AR. The number of SiPM pixels is the same (64) for the three cases but the pitch is 1.5 mm, 2.2 mm and 3.0 mm and the gaps 0.05 mm, 0.20 mm and 0.10 mm respectively. The entry position of the beam is the same for all cases, 4.75 mm from the centre of the crystal. Y-Z projections of DRIP are shown in figure 2.26 and values of DoI resolution and bias are shown in table 2.9. DoI resolution is equivalent for the three cases but the bias decreases when the AR increases.

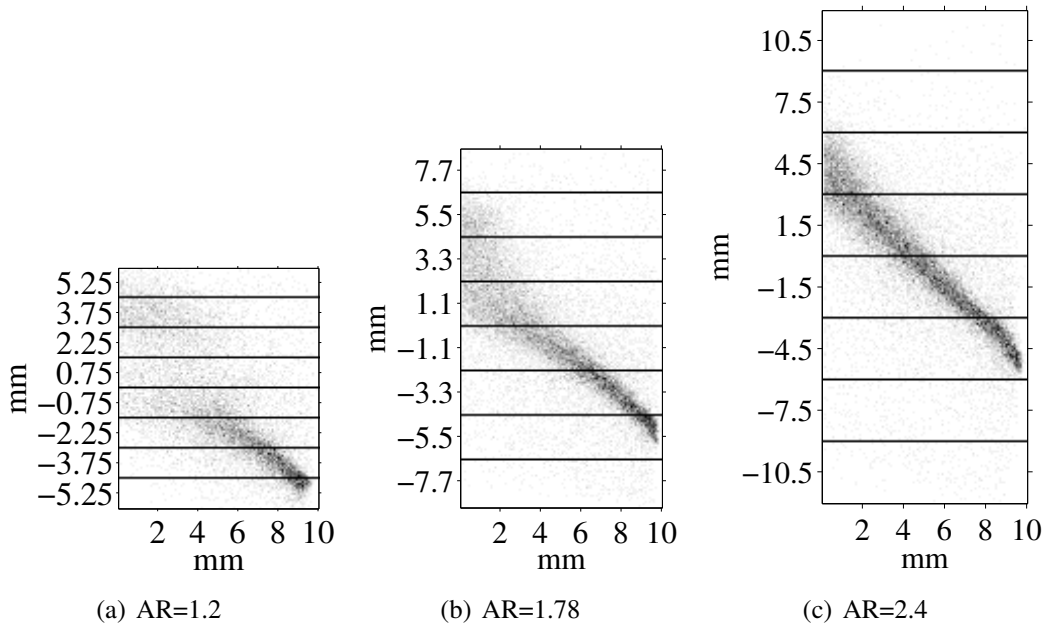


Figure 2.26 Y-Z projection of the reconstructed position distribution for the validated simulation with 10 mm thick crystal and different value of the AR, (a) AR=1.2, (b) AR=1.78 and (c) AR=2.4.

Table 2.9 Total DoI resolution and bias for the validated simulation for an entry position of the beam of 4.75 mm with different values of the AR.

AR	1.20	1.45	2.40
DoI resolution (mm)	$1.70 \pm 0.04$	$1.65 \pm 0.03$	$1.65 \pm 0.02$
bias (mm)	$-0.68 \pm 0.01$	$-0.47 \pm 0.01$	$-0.31 \pm 0.01$

In order to compare the results of the crystals with the same thickness and different AR, the events were divided in five sections of 2 mm according to the real DoI interaction position, the z coordinate value given by the simulation. The section that is closer to the crystal entrance is referred to as section 1 (green line) and the section that is closer to the photodetector is referred to as section 5 (red line). Figure 2.27 shows the DoI error distribution for the defined five sections. DoI can be recovered and the DoI error distribution can be fitted by a Gaussian function in the first two sections for AR=1.20 and over the whole crystal for AR=2.40 (see figure 2.27). Figure 2.28 shows the DoI bias and resolution values in different sections of the crystal, 2 mm thick each. For AR=1.2 the DoI error distribution in the sections located far from the SiPM does not have Gaussian shape and the estimated FWHM from a Gaussian fit to the distribution is above 2.4 mm.



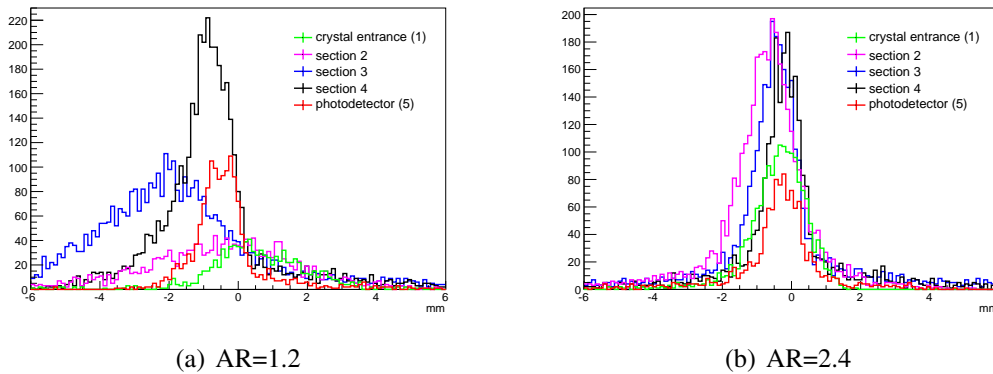


Figure 2.27 DoI distribution errors by sections (a) for AR=1.2 and (b) for AR=2.4.

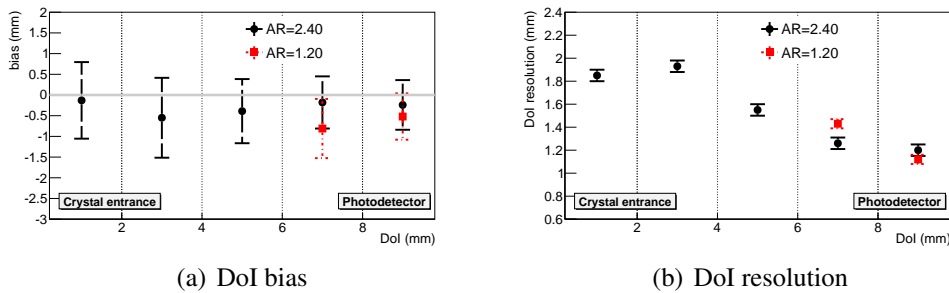


Figure 2.28 (a) DoI bias and resolution (error bar) by sections and (b) DoI resolution by DoI sections.

DoI accuracy depends on the gamma-ray position interaction along the crystal thickness. DoI error is lower for interactions close to the photodetectors, therefore placing the photodetector in the crystal front surface for the incidence radiation (FSR) can provide better spatial resolution [74].

Reflections highly influence the light distribution, in particular near the edges of the crystal or when event occurs far from the photodetector. This effect is more pronounced for crystals with smaller AR where the reflections play a more important role and should be also taken into account in the model.

### 2.4.6.2 Effect of reflector type on DoI

The DoI error was studied employing simulations with different coatings for the crystal. Three different reflectors were studied, the mixed reflector of the validated simulation matching the experimental data (ground-back-painted reflector with a 30% of specular reflections and 70% of diffuse reflections), an ideal specular reflector and a totally diffuse reflector (100%

diffuse reflections). The last two reflectors were the same reflectors that were studied in section 2.4.1.2.

Section 2.4.1.2 showed that for purely specular reflectors, including reflections in the model for positron determination results in a more accurate position estimation. However, when the behaviour of the reflections was not perfectly specular it was more accurate to reconstruct the interaction position with the VS0 model. The latter has been tested with simulated and experimental data. Therefore, in this section, simulations with diffuse reflector were reconstructed using VS0 model and the simulation with ideal specular reflector was reconstructed using both models to verify that VS1 was more accurate.

Table 2.10 shows the total DoI error and bias obtained for simulations with totally diffuse reflector and mixed reflector using the VS0 model for position determination and also for ideal specular reflector using VS0 and VS1 model. The DoI error distribution does not have a perfect Gaussian shape; therefore, the FWHM and FWTM values obtained from linear interpolation are also shown in table 2.10. It can be seen from the FWTM values that except for the 100% specular reflector reconstructed with the VS1 model, the total DoI error distributions have large tails. The FWHM of the total DoI error and the bias are smaller for the mixed reflector than for the diffuse reflector, while the interpolated FWTM is larger for the mixed reflector. The FWHM of the DoI error distribution for the specular reflector is 14% smaller and the FWTM is around 42% smaller using VS1 model than using VS0 model. The total DoI error is more accurate for the ideal specular reflector using VS1 method (smaller bias) and the DoI resolution is better than using VS0.

Table 2.10 Total DoI error and bias for the validated simulation with different reflectors. DoI error and bias was obtained from a Gaussian fit, while FWHM and FWTM of the DoI error distribution was obtained by linear interpolation.

AR=1.2	100 % diffuse VS0	Validated VS0	100% specular VS1	100% specular VS0
Error* (mm)	2.08±0.03	1.70±0.04	1.36±0.02	1.78±0.03
bias (mm)	-0.93±0.01	-0.68±0.01	0.20±0.01	-0.50 ±0.01
FWHM (mm)	2.01	1.76	1.32	1.53
FWTM (mm)	6.67	7.68	3.44	5.91

\* Error value (FWHM) was obtained from a Gaussian fit.

In order to compare the performance of both models for specular reflector, the DoI error and bias have also been analysed for each crystal section (figure 2.29 and figure 2.30). Using the VS1 model, the DoI error of each section of the crystal can be fitted by a Gaussian function with a value of FWHM below 1.6 mm and an absolute value of the bias below 0.5 mm. On the other hand, using VS0 the DoI error can be fitted by a Gaussian function

only in the three sections closest to the SiPM, (see figure 2.29). For the rest of the sections, the estimated FWHM value from a Gaussian fit was above 2.3 mm. In terms of bias and resolution of the DoI error distribution, the results are equivalent for the two sections closer to the photodetector (section 4 and section 5). For farther sections, DoI resolution degrades significantly. Therefore, analysing the DoI error by sections we have verified that using VS1 model was more accurate for an ideal specular reflector than the VS0 model.

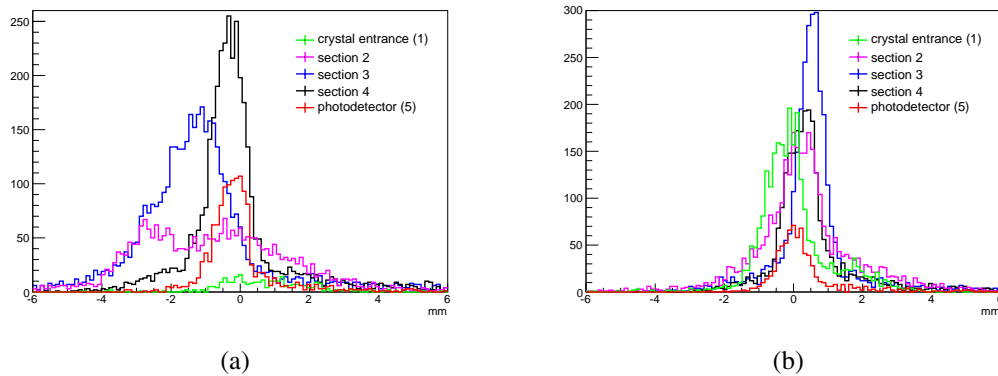


Figure 2.29 DoI distribution errors by sections for ideal specular reflector (a) using VS0 model and (b) VS1 model.

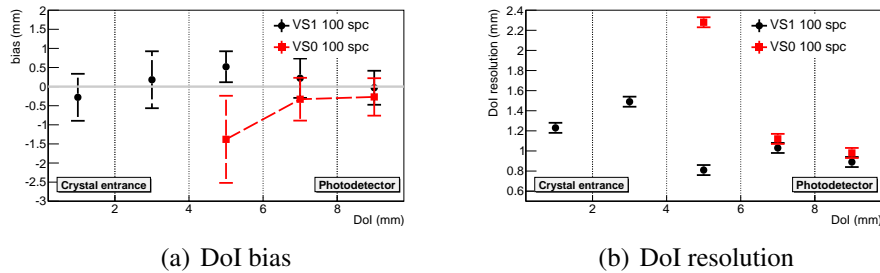


Figure 2.30 (a) DoI bias and FWHM (error bar) and (b) DoI resolution by DoI sections for 100% specular reflector using VS1 model and VS0 model.

The Y-Z projections of the reconstructed interaction position distribution for (a) the diffuse reflector, (b) the mixed reflector and (c) the ideal specular reflector, the latter reconstructed with VS1 model, can be seen in figure 2.31. Figure 2.32 shows DoI error and bias for each section of the crystal for the three different types of reflectors. The values were obtained by fitting a Gaussian function to the distributions, although those sections far from the SiPM do not have Gaussian shape.

DoI error has a smaller bias for the ideal specular reflector and the DoI resolution is better than for diffuse reflectors. There are only slight differences between diffuse reflectors.

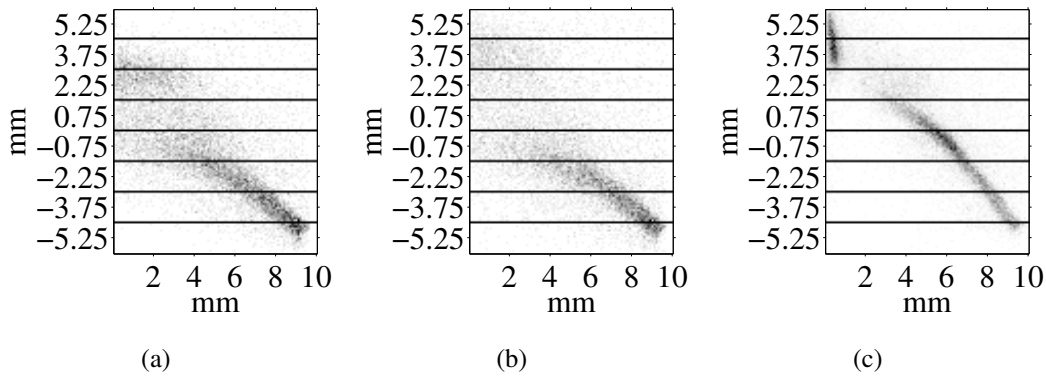


Figure 2.31 Y-Z (DoI) projection of the reconstructed position distribution (a) for the 100% diffuse reflector using VS0 model, (b) for mixed reflector using VS0 model and (c) for 100% specular reflector using VS1 model.

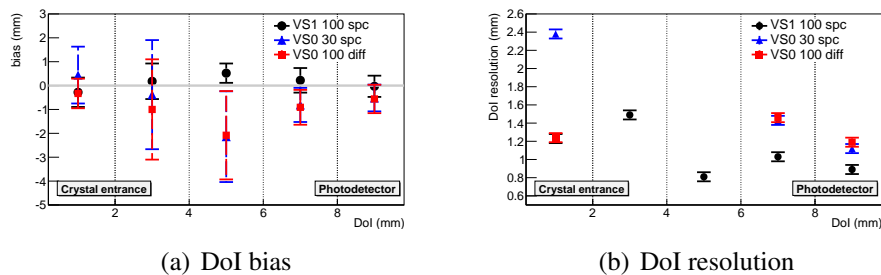


Figure 2.32 (a) DoI bias and FWHM (error bar) and (b) DoI resolution by DoI sections for different reflectors. The shape of the DoI error distribution of last three sections for diffuse reflector and for validated simulation is not Gaussian, the distributions have large tails.

## 2.5 Two head PET prototype

The imaging capability of the detector head and the performance of the position determination method were tested in a PET prototype developed at IFIC. The prototype consists of two detector heads attached to a motorized rotation stage to acquire tomographic data. Figure 2.33 shows the PET prototype where the two detector heads can be seen attached to a methacrylate frame and the source holder between them.

Data were taken placing the detectors at six angular positions from  $0^\circ$  to  $150^\circ$  in steps of  $30^\circ$  covering a FoV of  $12\text{ mm} \times 12\text{ mm} \times 12\text{ mm}$ . 3D coordinates of the estimated interaction

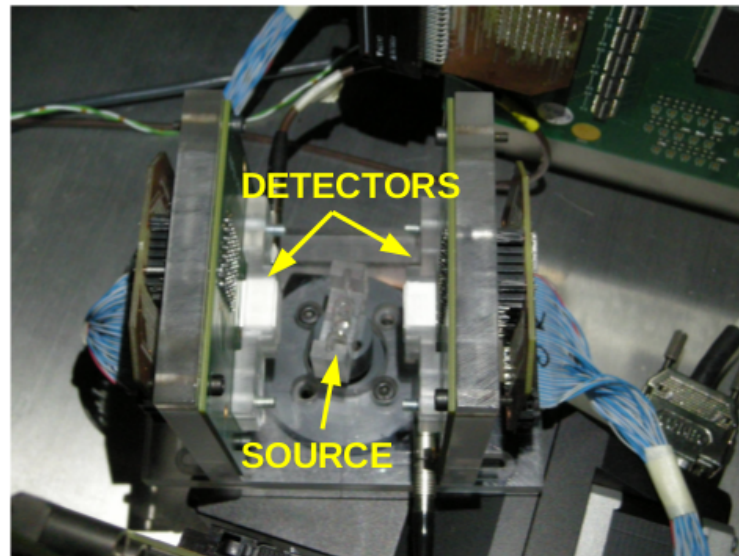


Figure 2.33 The PET prototype developed at IFIC.

position were stored in coincidence list-mode format and employed as data input for the image reconstruction algorithm.

The image reconstruction was performed using ML-EM with a called Simulated One-Pass List mode (SOPL) algorithm adapted to this detector that was explained in [64]. The implementation of this code is not a part of this thesis.

Figure 2.34 shows the transverse, sagittal and coronal planes of the reconstructed image of the data acquired with two point sources of 1 mm nominal diameter. The reconstructed FoV is  $12\text{ mm} \times 12\text{ mm} \times 12\text{ mm}$  with a voxel size of  $0.1\text{ mm} \times 0.1\text{ mm} \times 0.1\text{ mm}$ .

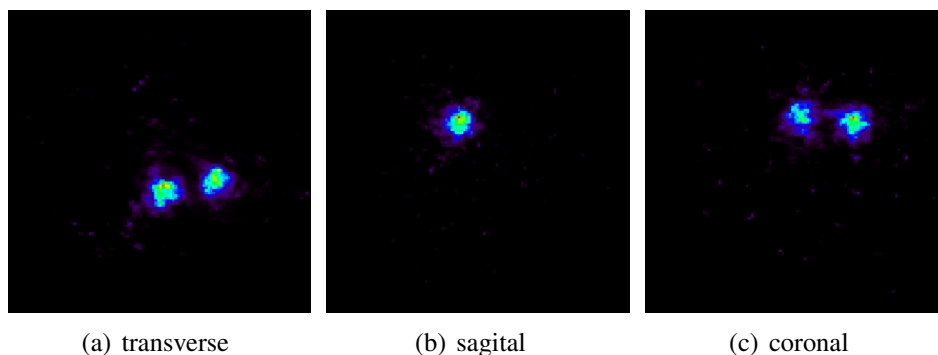


Figure 2.34 (a) Transverse, (b) coronal and (c) sagittal plane of the reconstructed image of two  $^{22}\text{Na}$  point sources of 1 mm nominal diameter with the prototype.

Images of  $^{22}\text{Na}$  point sources of 0.25 mm nominal diameter were reconstructed with submillimeter spatial resolution [64], assessing the imaging capability of the detector head employing continuous crystals.

## 2.6 Conclusions

The method developed in [13] has been modified and studied further in detail applying it to both experimental data and simulations. The model has been adapted to our data in a simple way to obtain the most accurate positioning and the best spatial resolution possible leaving the physical implications and necessary modifications of the model for future studies. The original model considers specular reflections on the sides of the crystal with the same weight as the direct light. For purely specular reflections, including such reflections improves the results. However, it has been shown that if the reflections behaviour is not perfectly specular it is better to limit the influence of the internal reflections (Independent VS1\*) or even eliminate such reflections in the model (VS0). The model for the reflections should be revised and modified for a non-specular behaviour. The test carried out experimentally with specular crystals did not yield the results expected and further tests in this sense are foreseen.

For our white painted crystals the results obtained applying VS0 and VS1 model have been compared and VS0 has shown more accurate results. Average transversal spatial resolutions over the detector surface (centre and edges) of 0.9 mm FWHM for the 5 mm thick white crystal and 1.2 mm FWHM for the 10 mm thick white crystal were measured. An experimental DoI resolution of 2 mm FWHM for both crystals was obtained using VS0 model considering interactions along the whole crystal thickness. The influence of the beam size was not subtracted from the results.

The comparison of the results obtained by different groups is difficult due to the significant differences in the detectors and measurement conditions. The latest published results with the most similar set-ups comprised of continuous crystals and multi-pixel photosensors for PET have been summarized in table 2.11 (characteristics of the system) and 2.12 (spatial resolution obtained). Our results with the 10 mm thick crystal are very good when compared to other systems, even without considering the unfavourable AR.

Validated simulations developed in this work allowed us to explore the performance of different crystal AR, keeping the same thickness and the same number of pixels in the photodetector. Increasing the AR, DoI accuracy was improved while keeping the same DoI resolution.

The impact of multiple interaction events, that cause light distribution overlapping and therefore a wrong interaction position determination, is a matter of study. Multiple

Table 2.11 Characteristics of the systems. In some of the cited works the size of the beam has been subtracted from the results (subtracted) and in others the results obtained have not been corrected by the size of the beam which is unknown (non-subtracted). For the rest the results obtained have not been corrected by the size of the beam but the size of the beam was reported and it is shown in the table.

Reference	Beam (mm FWHM)	Crystal (mm <sup>3</sup> )	Coating	Photodetector
[75]	1.00	20x10x10	Teflon	APD
[12]	0.52 0.65	50x50x8	black (edges) white (top)	MAPMT
[74]	0.54	13.2x13.2x10	PTFE	FSR SiPM
[76]	subtracted	42x42x10	black resin	MAPMT
[13]	1.20	20x20x10	Teflon	APD
[77]	subtracted	tprd bottom 18.5x21.4x10	White	APD
[11]	non-subtracted	20x20x10	black	2-SiPMs
[78]	0.5 <sup>a</sup>	24x24x10	Teflon	dSiPMs
[79]	non-subtracted	32x32x2	black (edges) white (top)	dSiPMs

<sup>a</sup> diameter.

Table 2.12 Results obtained with developed systems.

Reference	Thickness (mm)	AR	Pitch (mm)	XY (mm FWHM)	DoI (mm FWHM)
[75]	10	(2,1)	2.3	1.7	Entrance point
[12]	8	6.25	5.8	centre 1.06 edges 1.27	3.24
[74]	10	1.32	3.3	<1.6	Entrance point
[76]	10	4.20	5.8	mean 3.4 min. 1.3	mean 4.9 min. 1.9
[13]	10	2.00	2.3	(X) 1.85 (Y) 2.5	3.4
[77]	10	(1.85,2.14)	2.3	centre 2.1 edges 2.7	Entrance point
[11]	10	2.00	4.0	(X) 1.95 (Y) 1.76	4.7 <sup>a</sup>
[78]	10	2.40	4.0	mean 1	-
[79]	2	16	4.0	mean 0.54	-

<sup>a</sup> A standard deviation of (2-3) mm was reported. Conversion to FWHM was done assuming a Gaussian distribution.

interactions of the 511 keV photons in the crystal produce a degradation in the transversal and DoI resolution [80]. Moreover, the experimental data employed in this study could improve by controlling the temperature and reducing the amount of random coincidences and background events.

The validated simulations are able to reproduce the qualitative behaviour of the experimental data. However, the values of the the spatial and energy resolution are significantly smaller for simulated data than for experimental data. Since, in this work, the aim of developing simulations is to investigate and understand more in detail the performance of the light distribution model to improve the estimation of the interaction position, the quantitative values of the spatial resolution of the simulated data are not of the primary interest. Some aspects that have not been taken into account in the simulations as the influence of temperature variations in the laboratory could degrade the response of the detectors degrading the resolution values.



# Chapter 3

## Simulation Study of a Full Ring Prototype

The two main parameters to maximize in the performance of the PET scanner are sensitivity and spatial resolution. The use of continuous crystals [34, 81, 10, 7, 75, 12, 33, 1, 13, 35, 77, 82, 11, 78, 79] can increase sensitivity compared to pixelated ones maximizing the active volume by eliminating insensitive areas in the detector crystal. Sensitivity may also be increased: by using thicker crystals which allow increasing the probability of detection of gamma-rays or by increasing the solid angle coverage in a full ring system.

In the previous chapter, the characterization of a detector head based on continuous crystals coupled to SiPMs has been performed. The studies were mainly focused on the position determination capability of the detector. To evaluate more in detail the performance of the position determination algorithm and the light distribution within the crystal, Monte Carlo simulations of the detector head were developed and validated through experimental data. Making use of the experience gained during detector evaluation, detailed simulations of a full ring geometry have been performed in this chapter. The performance of two simulated PET systems of same ring diameter but with different crystal geometries, cuboid and tapered, have been compared following NEMA NU 4-2008. Since an improvement of sensitivity is expected in tapered configuration, due to the tighter packing of the detectors, additional figures of merit have been employed to evaluate it.

The 3D interaction position of gamma-rays in the crystal is estimated using an analytical model of the light distribution [13] that was previously validated with experimental data using cuboid crystals [83]. The performance of the position estimation method applied to tapered crystals has been assessed. Image reconstruction was implemented with Filtered Back-Projection (FBP) as indicated by NEMA standard. In addition, in order to have a better

estimation of the future performance, some images have also been reconstructed using a conventional ML-EM.

## 3.1 Simulated Full Ring scanners

Monte Carlo simulations of two scanners based on cuboid and tapered crystals were developed with the same dimensions to isolate the impact on the performance of the scanner due to the crystal geometry. Firstly, geometrical characteristics of the scanners were designed. Once the geometry was defined, the validated Monte Carlo simulation of the detector head was adapted to this new geometry and to the full ring system. Finally, the signal generated in the Monte Carlo simulation was post-processed and blurred to generate time coincidences between different detector heads.

### 3.1.1 Geometry of the simulated scanners

Two different scanners were designed with the same inner ring, same gap between contiguous heads ( $l_{gap}$ ), same crystal thickness ( $d_{crystal}$ ) and same size of the crystal external face ( $l_{SiPM}$ ), see figure 3.1. The detector head of the scanners consists of an LYSO continuous crystal coupled to an  $8 \times 8$ -pixel SiPM array. The photodetector characteristics were based on the  $8 \times 8$  SiPM matrix (TSV, Through Silicon Via, model S13361-2050AE-08) from Hamamatsu. The active area of each pixel of the array is  $2.0 \text{ mm} \times 2.0 \text{ mm}$  in a  $2.2 \text{ mm}$  pitch resulting in a SiPM size ( $l_{SiPM}$ ) of  $17.8 \text{ mm}$ . For designing the scanner we took  $l_{SiPM}$  as a constrain, a fixed quantity which corresponds to the side of the external square section of the crystal (Back Side Readout of the crystals).

Taking into account that  $l_{SiPM}$  is a fixed parameter which corresponds to the purchased detectors, equation (3.1a) shows the value of the inner ring of the scanner for cuboid crystals ( $R_{inner}^{cub}$ ) as a function of the minimum value of the gap between detector heads ( $l_{gap}$ ) and the number of detector heads of the scanner ( $N_{Detectors}^{cub}$ ). Equation (3.1b) shows the value of the inner ring of the scanner for tapered crystal ( $R_{inner}^{tprd}$ ) as a function of  $l_{gap}$ , the number

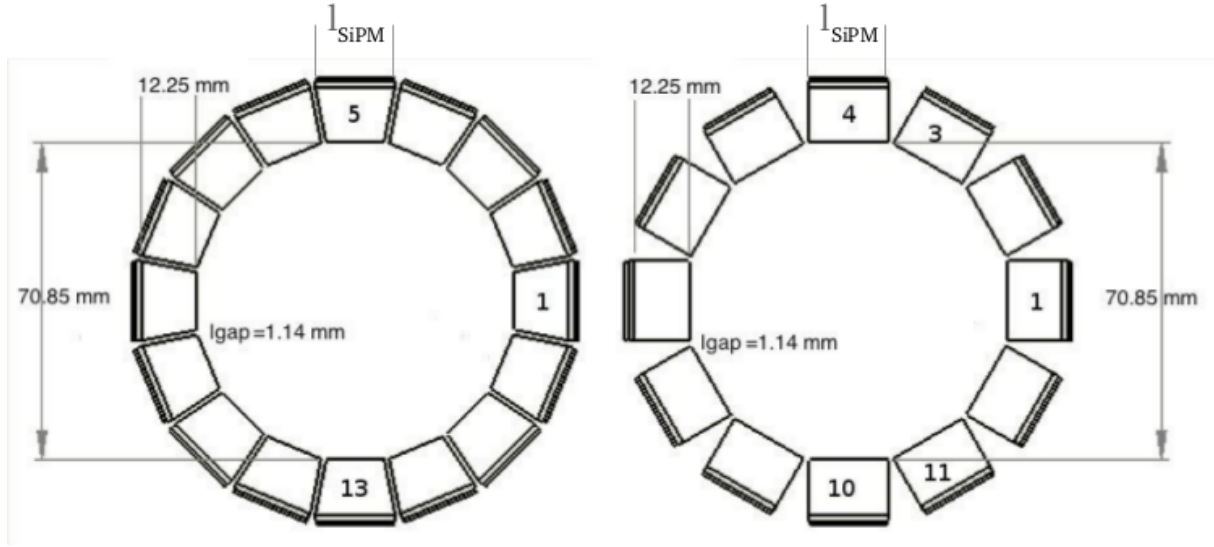


Figure 3.1 Scanner geometries. Left: scanner based on 16 tapered crystals. Right: equivalent scanner based on 12 cuboid crystals.

of detectors of the scanner ( $N_{Detectors}^{tprd}$ ) and the thickness of the crystal ( $d_{crystal}$ ). It is worth mentioning that only for tapered geometry, the inner radius is a function of  $d_{crystal}$ .

$$R_{inner}^{cub}(N_{Detectors}^{cub}, l_{gap}) = \frac{l_{SiPM}}{2 \tan\left(\frac{\pi}{N_{Detectors}^{cub}}\right)} + \frac{l_{gap}}{2 \sin\left(\frac{\pi}{N_{Detectors}^{cub}}\right)} \quad (3.1a)$$

$$R_{inner}^{tprd}(N_{Detectors}^{tprd}, l_{gap}, d_{crystal}) = \frac{l_{SiPM}}{2 \tan\left(\frac{\pi}{N_{Detectors}^{tprd}}\right)} + \frac{l_{gap}}{2 \sin\left(\frac{\pi}{N_{Detectors}^{tprd}}\right)} - d_{crystal} \quad (3.1b)$$

The minimum value of  $l_{gap}$  for a realistic design of a full ring geometry was estimated to be about 1 mm. Moreover, a small  $R_{inner}$  of around 70 mm was desired so that the system could be also used as PET-MR insert. Taking into account the above constrains and following equation (3.1) to obtain the same value of the  $R_{inner}$  and  $l_{gap}$  for both scanners, 12 detector heads were needed for cuboid crystals and 16 detector heads for tapered geometry. Figure 3.2 shows the possible range of values for  $R_{inner}$  and  $l_{gap}$  for different  $d_{crystal}$ . A  $d_{crystal}$  of 12.25 mm was chosen to have a small realistic value for  $l_{gap}$  resulting in a scanner of an  $R_{inner}$  of 70.85 mm and  $l_{gap}$  of 1.14 mm. The two simulated scanners are shown in figure 3.1 in the same scale, where tighter packing for scanner based on tapered crystals can be clearly seen.

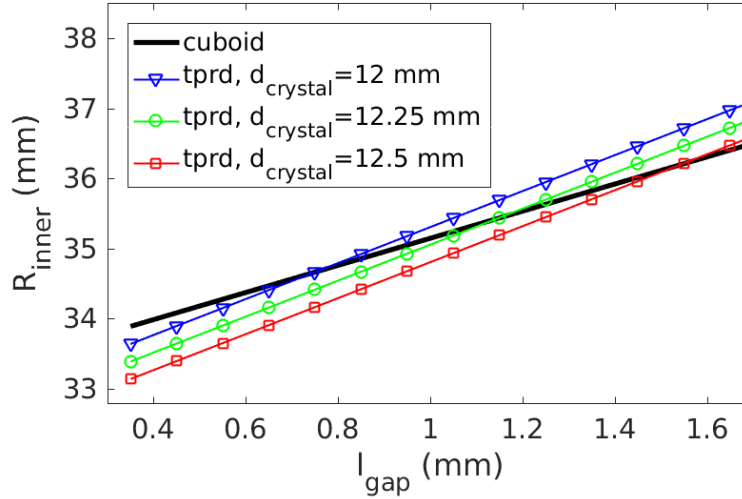


Figure 3.2 Inner ring of the scanner as a function of the  $l_{gap}$  for cuboid system and for tapered system for different thickness of the crystal.

The scanner based on tapered crystals can be viewed as the scanner with cuboid crystals where the gaps between contiguous detector heads have been "filled" with scintillator material.

### 3.1.2 Monte Carlo simulation

The detailed Monte Carlo simulation of the detector head developed for cuboid crystals described in section 2.3 was adapted to simulate the geometry of both systems, cuboid and tapered, including the generation of optical photons in the crystal. Validated Monte Carlo simulations of the detector head were performed using GATE v6.1 version. However, this version does not work properly when ion sources are simulated, producing inconsistent values of timestamps of the detected signals. Ion sources were required to characterize the performance of the scanners following NEMA standard and timestamp was needed to analyse time coincidences. Therefore, full ring simulations were performed using a newer version of the GATE toolkit (GATE v7.0 version), where this feature was corrected, [84].

#### 3.1.2.1 Material and Surfaces properties

Material properties employed in the simulations were described in section 2.3.1. In this chapter intrinsic activity of  $^{176}\text{Lu}$  of the LYSO crystal was also included because the presence of natural radioactivity of the scintillator could generate additional coincidences. LYSO

crystals contain a fraction of  $^{176}\text{Lu}$  (2.6% abundance), a natural radioactive element with a half life of  $3.8 \times 10^{10}$  years.

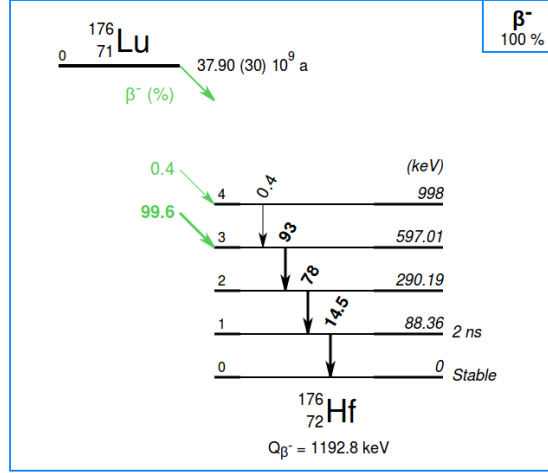


Figure 3.3  $^{176}\text{Lu}$  decay scheme to  $^{176}\text{Hf}$  source:larawebfree.

Figure 3.3 shows the decay scheme of  $^{176}\text{Lu}$  which after  $\beta^-$  emission is left in an excited state of  $^{176}\text{Hf}$ . The energies of the main prompt gamma-rays emitted in the decay to the ground state of  $^{176}\text{Hf}$  are 88 keV, 202 keV, and 307 keV. In addition the maximum energy deposition of the electron of the most probable (99.6%) beta decay is 596 keV, which overlaps with the 511 keV gamma-rays emitted from annihilation of the positron of PET radiotracers. Following [85, 86], we took the following LYSO crystal composition  $\text{Lu}_{2(1-x)}\text{Y}_{2x}\text{SiO}_5$ ,  $x \approx 0.1$ . The activity per unit volume of LYSO, has been obtained by using the following equation reported in [87]:

$$R = f \cdot n_{\text{Lu}} \frac{\rho_{\text{LYSO}} N_A}{M_{\text{LYSO}}} (1 - e^{-\frac{\ln 2}{T_{1/2}}}) \simeq f \cdot n_{\text{Lu}} \frac{\rho_{\text{LYSO}} N_A}{M_{\text{LYSO}}} \frac{\ln 2}{T_{1/2}}, \quad (3.2)$$

where the number of moles of Lu per LYSO mole is  $n_{\text{Lu}} = 1.8$ , the abundance of  $^{176}\text{Lu}$  is  $f = 0.026$ , the LYSO molar mass is  $M_{\text{LYSO}} = 440.8$  g/mole,  $N_A$  is the number of Avogadro and the density of LYSO is  $\rho_{\text{LYSO}} = 7.1$  g/cm<sup>3</sup> leading to a value of density of activity of 263 Bq/cm<sup>3</sup> for LYSO crystal.

A technical detail is in order, GATE toolkit has not the option to simulate the shape of the sources with tapered geometry. However, for the components of the scanner (detector heads) tapered geometry is available. Therefore, the intrinsic radioactivity of LYSO is simulated using  $^{176}\text{Lu}$  ion sources with box shape volumes for both geometries of the scanner. For cuboid configuration, the volume and the location of  $^{176}\text{Lu}$  ion sources is the same as for the scintillator crystals.

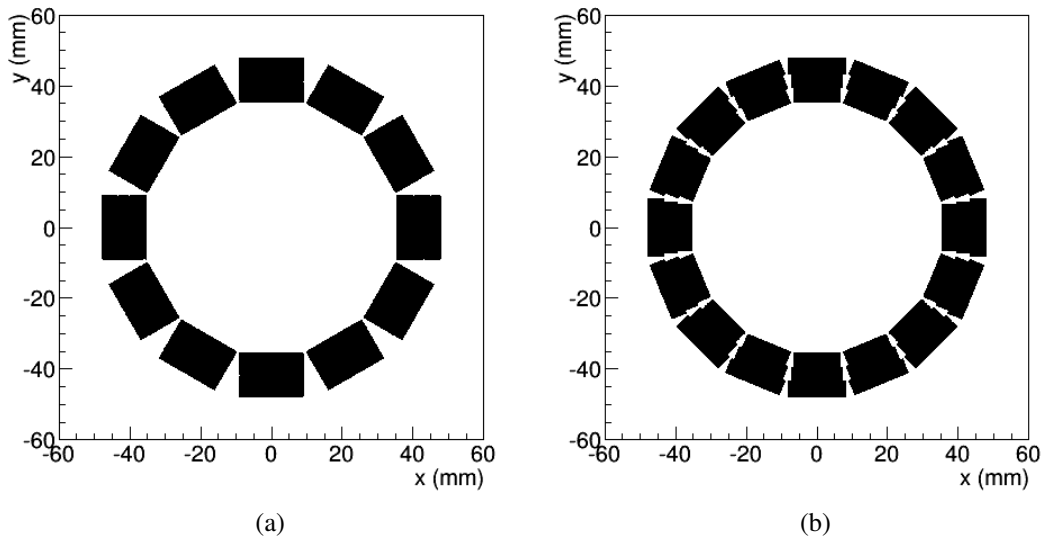


Figure 3.4 Volumes of the sources of the Monte Carlo simulations to simulate the natural radioactivity of LYSO crystals. Left, simulated volumes for cuboid configuration. Right, simulated volumes for tapered configuration.

In order to simulate the natural radioactivity of a tapered scintillator crystal three box shape volumes were employed which cover 94.7% of the volume of the crystal, see figure 3.4(b). The activity per unit volume of each of the boxes was increased by a factor of  $(\frac{1}{0.947})$  so that the total activity simulated per tapered crystal was correct. Figure 3.4 shows the volume of the sources employed to simulate the natural radioactivity of the scintillator crystals that composed the systems.

An acquisition for both scanners, without any source apart from the natural radioactivity of LYSO, was simulated in order to check the simulation of intrinsic radioactivity. Figure 3.5 shows the spectrum collected from the signal of each detector head in a full ring in singles mode. Figure 3.5(a) and Figure 3.5(b) show respectively the energy spectrum for ideal energy resolution and for a post-processed energy blurring of 12% at 511 keV which is the energy resolution value that will be applied in the rest of the chapter. In figure 3.5(a) 202 and 307 keV prompt gamma-rays can be clearly seen and the sum peak of them. In addition 88 keV prompt gamma-ray can be distinguished and with similar detected number of counts the deposited energy by the X-rays emitted in the shell transitions of the electrons of Lutetium. The peaks around 54 keV are produced by electron transitions from L-shell to K-shell, while the peaks around 63 keV are produced by transitions from M to K-shell. The maximum energy value in the spectrum in singles mode without any source is around 1.2 MeV which is the expected value according to the  $^{176}\text{Lu}$  decay scheme which corresponds

to the 597 keV energy sum of the three prompt gammas and the maximum energy deposition of the electron of the  $\beta$  decay (596 keV). Due to the finite energy resolution, in figure 3.5(b) neither 88 keV prompt gamma nor the energies that correspond to the shell transitions nor the sum peak of the prompt gammas can be distinguished in the energy spectrum.

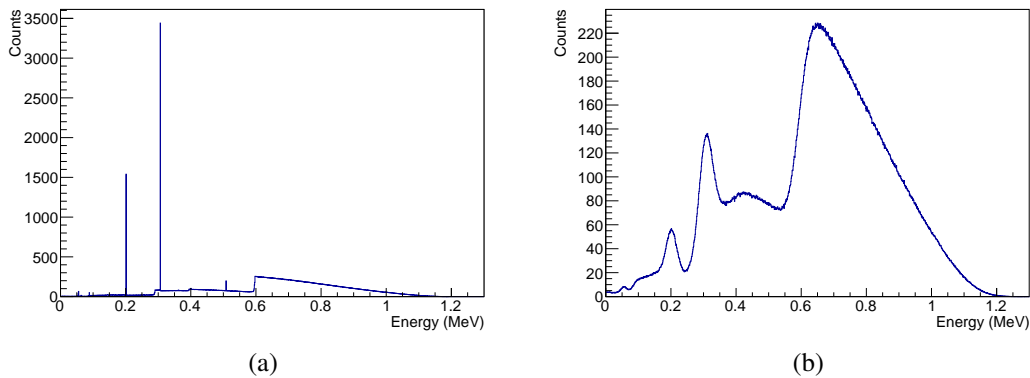


Figure 3.5 Spectrum of the Lutetium natural radioactivity in singles mode in the full ring geometry: (a) for ideal energy resolution and (b) for an energy resolution of 12% at 511 keV.

### 3.1.2.2 Scanner Geometry implementation

The definition of the geometry of the system is hierarchical in GATE. The main volume is the scanner. There are several predefined structures for PET systems. The predefined generic PETscanner hierarchy has been selected to build the system, because it is to our knowledge the only structure which has not any restriction to the shape of the components (sector, module, layers...) of the scanner; thus, it is compatible with tapered geometry. The shape of the components of the commonly used hierarchy known as cylindricalPET is restricted to a box shape. The PETscanner has the possibility to attach its components to 5 different levels. The scanner consists of one ring which is composed of several detector heads (level1), inside which smaller elements are inserted (level2). The shape of the scanner is cylindrical in order to allow the allocation of phantoms in the centre of the FoV.

The components of the detector heads are the same as the ones described in section 2.3. The size of the components (pixel and SiPM size, crystal dimension and thickness) has been adapted to the dimensions described in section 3.1.1.

Another technical detail we have faced is the difficulty in constructing a scanner with a cylindrical shape based on tapered crystals. The construction of a full ring with cuboid crystals is straightforward. GATE has a ring repeater which replicates a volume the number of times selected about a circumference. There is an autorotation option which places the

heads in a correct orientation. Figure 3.6 shows the use of a ring-repeater for cuboid crystals from GATE user's guide. Figure 3.6(a) shows the performance of the repeater when the autorotation option is disabled and figure 3.6(b) when the autorotation option is enabled.

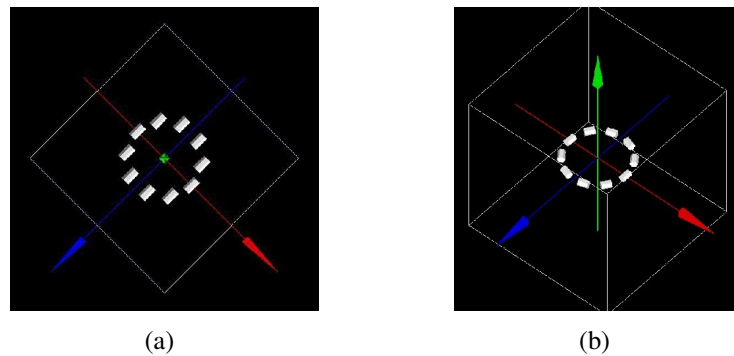


Figure 3.6 Ring Repeater. Images from GATE user's guide.

However, for tapered crystals in a scanner with a cylindrical geometry the autorotation option of the ring-repeater does not work as expected. By default, the orientation of a cylindrical volume in GATE is with the symmetry axis along the Z-axis. The default orientation of the creation of a tapered volume with respect to the global reference system in GATE is shown in figure 3.7. When the tapered volume (crystal) is located inside a cylindrical volume (scanner) its default orientation with respect to the symmetry axis of the cylinder is the same as the orientation with respect to Z-axis shown in figure 3.7(a). Therefore, due to the default orientation of the creation of a tapered volume either the tapered crystal or the scanner must be rotated with respect to the default orientation to construct the system; thus, resulting in an undesired behaviour of the autorotation command.

Figure 3.8(a) shows the behaviour of the ring-repeater with autorotation option enabled applied to a tapered crystal (red) which has been previously rotated 90 degrees around Y-axis and located along X-axis. The orientation of the repeated crystals is not correct for the construction of a ring. This feature of the autorotation command has been tested constructing a scanner with a box shape where the default orientation for the tapered volumes can be maintained. Figure 3.8(b) and figure 3.8(c) show a scanner with a box shape (blue). In figure 3.8(b) the tapered crystal (red) has been rotated 90 degrees around Y-axis before applying the repeater in order to construct a scanner with the axial direction along Z-axis and the mis-behaviour of the autorotation command is clearly visible, while in figure 3.8(c) the default orientation of tapered crystals has been maintained constructing a scanner with the axial direction along X-axis and the autorotation command of the ring-repeater works properly.



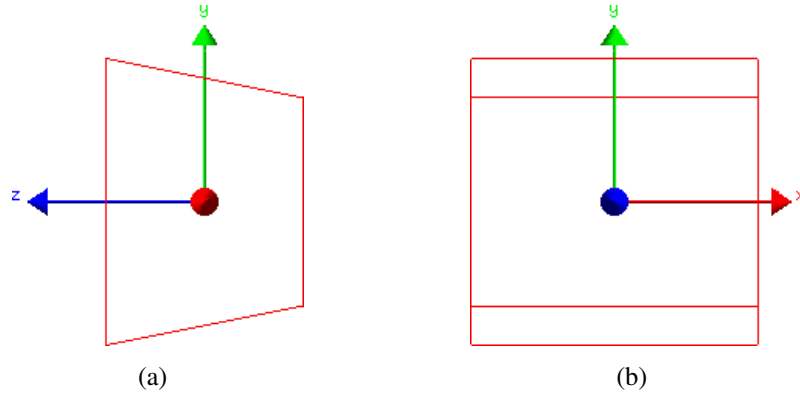


Figure 3.7 Illustration of the default orientation of the creation of a tapered volume in GATE with respect to the global reference system. Figure (a) shows the view of a tapered crystal from X-axis and figure (b) from Z-axis.

However, if a scanner with a box shape is simulated, phantoms can not be located in the centre of the FoV without overlapping with the scanner since they are at the same hierarchical level in the structure of the system as the scanner. Figure 3.8(b) and figure 3.8(c) show the overlapping of the phantom (yellow circle) and the scanner volume (blue box).

Therefore, in order to be able to simulate a PETscanner with a cylindrical shape based on tapered crystals it was necessary to employ the generic-repeater specifying a list of rotations and translations for each detector head of the scanner in a placements extension file. Due to the default orientation of the creation of tapered geometry with respect to the symmetry axis of the scanner, each module has been rotated twice. Firstly, it was rotated 90 degrees around Y-axis and secondly, it was rotated around Z-axis, and angle ( $\theta''_{n_i}$ ) given by:

$$\theta''_{n_i} = \frac{(n_i - 1) \cdot 360}{N_{sectors}}, \quad n_i = 1, \dots, N_{sectors}, \quad (3.3)$$

which depends on the detector head number ( $n_i$ ) and the total number of detectors that composed the scanner ( $N_{sectors}$ ), see figure 3.1.

For each detector head only one rotation angle and axis and one translation can be specified. Therefore, the product of two rotations must be calculated. The mathematical operations to deduce the expressions for the total rotation angle and axis for each detector are described in Appendix A. The list of transformations applied to each detector using the global reference system located at the centre of the FoV of the scanner are also shown in table A.1. Figure 3.8(d) shows the generic repeater applied to each tapered crystal in a cylindrical scanner aligned along Z-axis.

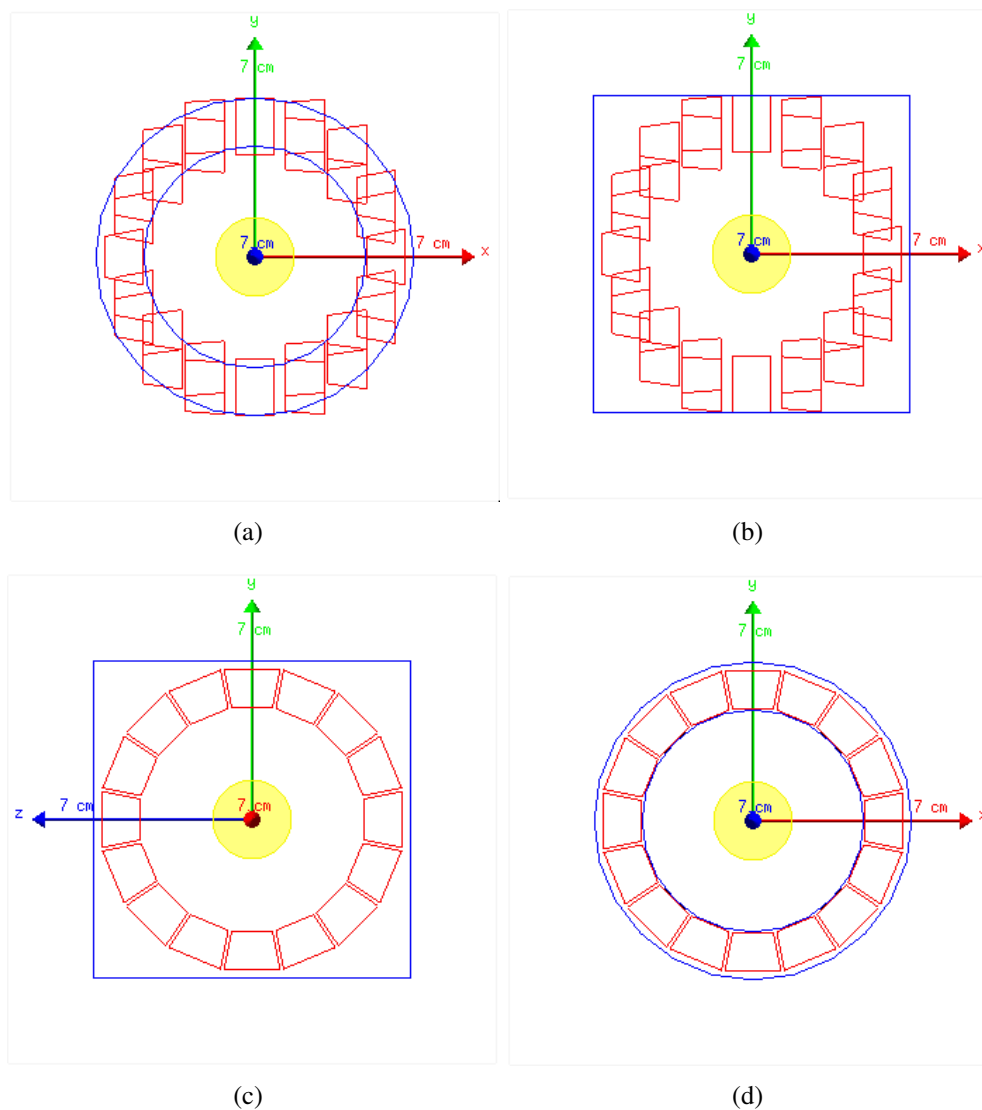


Figure 3.8 Illustration of the use of the ring-repeater with autorotation option enabled applied to tapered crystals in different configurations and illustration of the use of generic repeater. In (a) the ring-repeater is applied to re-orientated tapered crystals in a cylindrical scanner orientated along Z-axis (default orientation), in (b) is applied to tapered crystals re-orientated as in figure (a) in a scanner with box shape, in (c) it is applied to tapered crystals (default orientation) in a scanner with box shape and in (d) the generic repeater has been used to position each of the crystal in a cylindrical scanner along Z-axis.

### 3.1.2.3 Sources and phantoms

The shape of the scanner is important to be cylindrical in order to add the volume of the simulated phantoms in the FoV of the scanner, which will be at the same hierarchical level as the phantom, without overlap. Several phantoms with different sources have been employed

for the characterization of the performance of the scanner. The characteristics of each of them will be explained in detail in the corresponding sections.

### 3.1.3 Digitizer and Coincidence sorter

GATE digitizer module was employed to read out the ideal detected single events. Ideal single events were post-processed (blurred and filtered) to generate coincidences by using home-made software. Energy blurring was set to 12% at 511 keV and only those events within an energy window of [450,700] keV were accepted. Coincidence Resolution Time (CRT) was set to 1 ns FWHM and Time Coincidence Window (TCW) was defined as  $2\sigma_{CRT}$ , so it was set to 851 ps. Geometrically non-meaningful coincidences were not analysed. To this end, a sector difference of the two detected singles greater than 2 was required. Multiple coincidences were discarded except for their contribution to dead-time losses. Non-paralyzable coincidence dead-time was simulated only in section 3.4.2 (Scatter Fraction, Count Losses and Random Coincidences), where different values were investigated.

## 3.2 Performance study of the Position Estimation method when applied to a Full ring

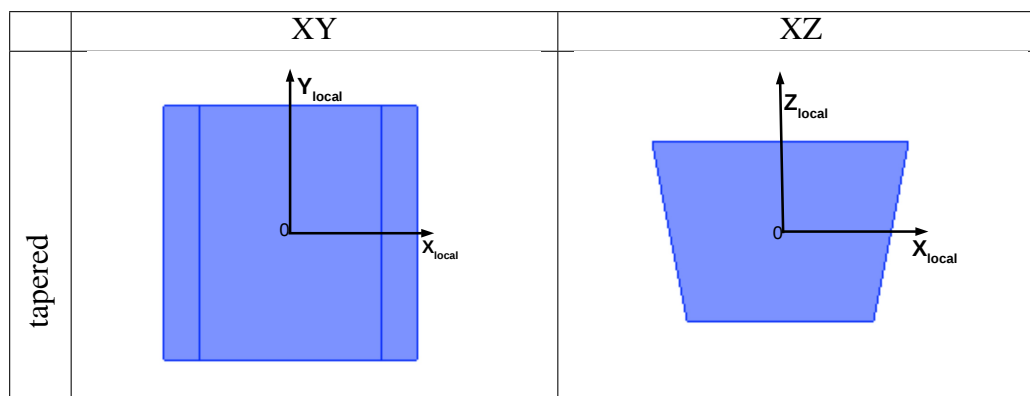
The position determination method employed in this thesis is based on a non-linear analytical model of the transport of the photons in the crystal and their reflection on the sides [13] and it was explained in detail in section 2.4. In the previous chapter, the different modifications of the model were tested in a position determination set-up using a collimated beam and a detector head based on cuboid crystals, see figure 2.3. Simulations were validated with experimental data and VS0 model was employed for the estimation of the interaction position in cuboid crystals because it was more accurate than the other models due to the mismatch between specular modelled reflections and experimental ones.

Here, we want to apply this method to estimate the position interaction of detected gamma-rays in time coincidence (3.1.3), which have been emitted isotropically from a source located in the FoV of a scanner based on different geometries: cuboid and tapered. The fact that now two photons are detected in coincidence in a full ring geometry implies a different distribution of the interaction positions in a detector head from the one studied previously. This distribution induces LoR misalignments, which in terms, will produce additional artefacts in the consequent reconstructed images. These artefacts will be studied in this section especially with respect to their impact in the spatial resolution.

In order to gain a first estimation of the performance of the models when using a full ring geometry, a point-like source (0.1 mm of diameter) emitting 511 keV mono-energetic back-to-back gamma-rays has been simulated in the centre of the scanner. The interaction position of the post-processed coincidences (3.1.3) has been obtained from Monte Carlo information (ground-truth<sup>1</sup>) and in addition estimated by using different models (VS0 and VS1 model).

The position estimation algorithm has been for the first time applied to tapered geometry. The light distribution models have been revised to take into account the new geometry of the crystal. VS0 model has been applied without making any modification since it only considers the direct light arriving to each pixel based on the solid angle subtended by it from the light source. However, since VS1 model employs virtual sources which must be located at the symmetric position of the interaction position estimation on the other side of the five surfaces of the crystal to model mirror-like reflections, it must be adapted to take into account the slope of the two of the five sides of the tapered crystal to correctly obtain their position.

Table 3.1 The XY and XZ views of the cd tapered crystals in their local reference system. The origin of the coordinate system is located at the centre of the crystal.

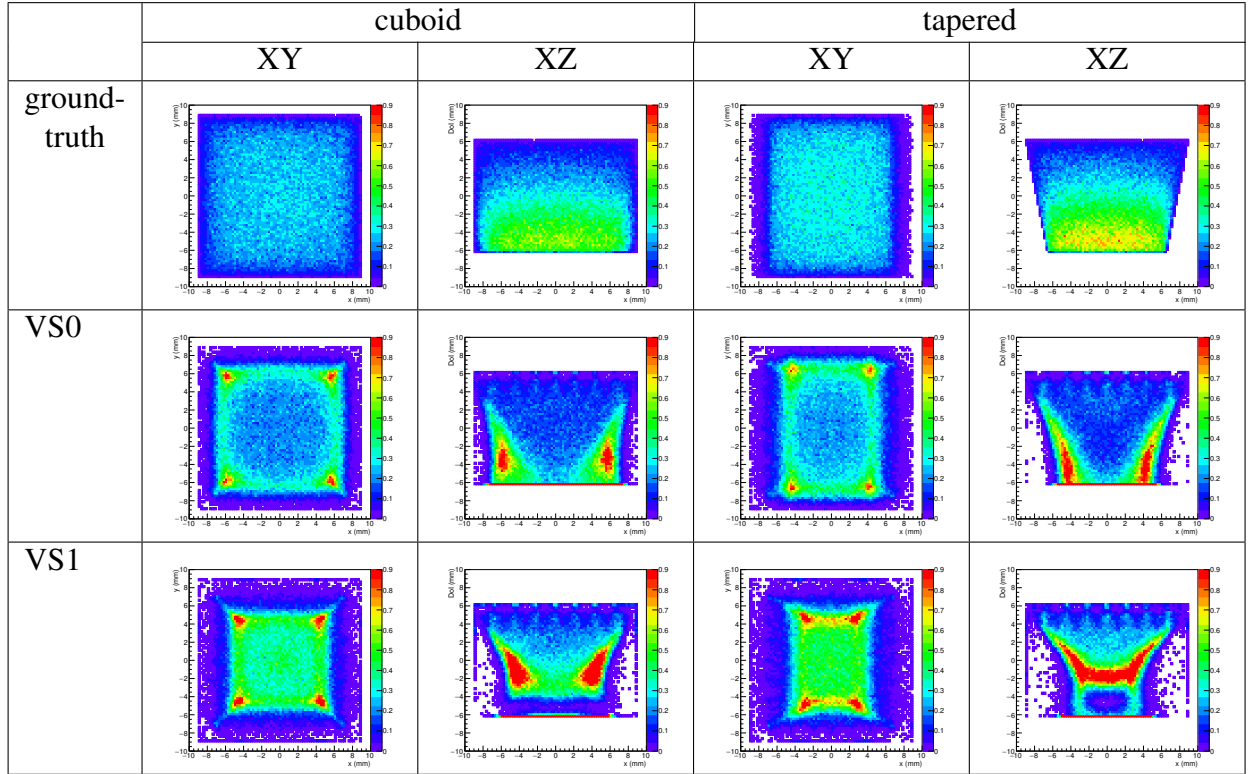


The interaction position distribution of all the detected coincidences in the scanner has been studied in the local reference coordinate system of the detector heads to analyse them simultaneously, since the source was located at the centre of the scanner. Table 3.1 shows the XY and XZ views of the tapered crystal geometries in their local reference system where the origin of the system is located at the centre of the crystals. XY planes correspond to the planes of the crystals that are facing the centre of the scanner, which are perpendicular to the radial direction while XZ planes contain radial and tangential directions.

Table 3.2 shows the projections on the XY and XZ planes of the interaction position of  $10^5$  post-processed coincidences in the local reference coordinate system of the crystals

<sup>1</sup>By ground-truth we will understand the singles of each crystal as provided by GATE

Table 3.2 Projections of the interaction position from Monte Carlo information (ground-truth) for cuboid and tapered crystals in the first row, projections of interaction position estimation using VS0 model and using VS1 model in the second and third row respectively for both cuboid and tapered crystals.



for tapered and cuboid geometries. The first row of the table 3.2 shows the projections of the interaction position from the Monte Carlo information (ground-truth) while the second and the third row show the projections of the interaction position estimation using VS0 and VS1 model respectively. The voxel size of the projections (table 3.2, table 3.4, table 3.5) is  $0.25 \text{ mm} \times 0.25 \text{ mm}$  and the color scale is in a range between zero and 0.09%. Those voxels whose value is above 0.09% are represented with the same color as those with a value of 0.09%. This scale has been selected because an important percentage of the estimated interactions are accumulated at the entrance of the crystal (lower part of the distribution XZ). This accumulation of events is visible as a horizontal red line in the XZ plane for VS0 and VS1 model. The values of the percentages of those accumulations for both geometries of the crystal using different models are shown in table 3.3.

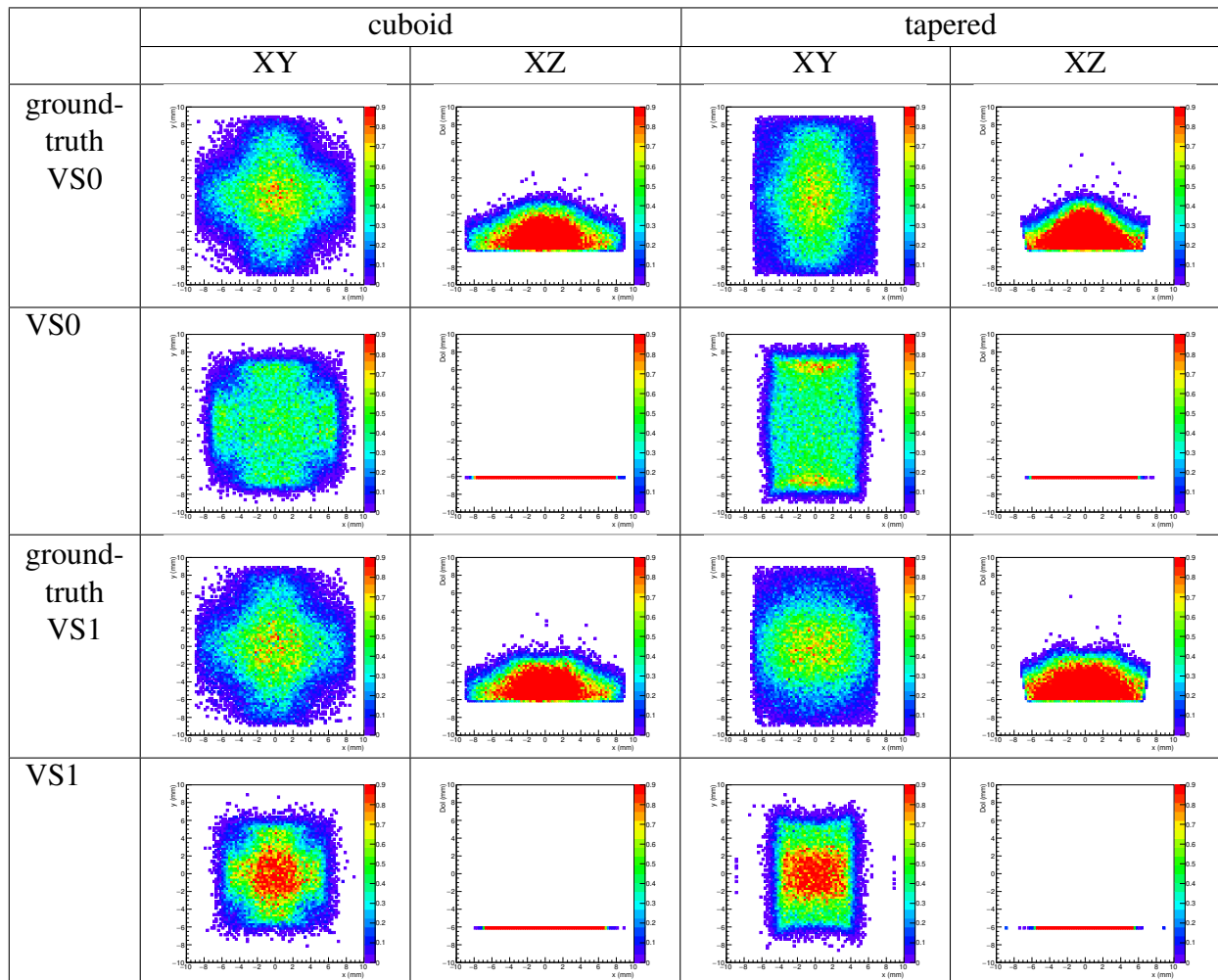
The red line at the entrance of the crystal in projections on the XZ plane using both models is saturated in order to be able to visualize the pattern of the position estimation distribution in the rest of the crystal. The distribution for VS0 and VS1 model shows an

Table 3.3 Percentage of interactions located at the entrance of the crystal ( $N_{entrance}$ ) for both geometries of the crystal using different models.

	VS0+cub	VS0+tprd	VS1+cub	VS1+tprd
$N_{entrance}$ (%)	25.92	31.85	21.37	26.93

accumulation of the events close to the edges of the crystal. Whereas in the first half of the crystal ( $z_{local} < 0$ ) close to the centre ( $|x| < 4$  mm), there is less density of estimated interactions comparing to the ground-truth. This effect is more pronounced for VS1 model where the percentage of positioned events in the first two millimetres far from the SiPM is one order of magnitude below the value of the ground-truth, see table 3.2.

Table 3.4 Projections of the interaction position from Monte Carlo information for cuboid and tapered crystals in the first row, projections of interaction position estimation using VS0 model and using VS1 model in the second and third row respectively for both cuboid and tapered crystals.



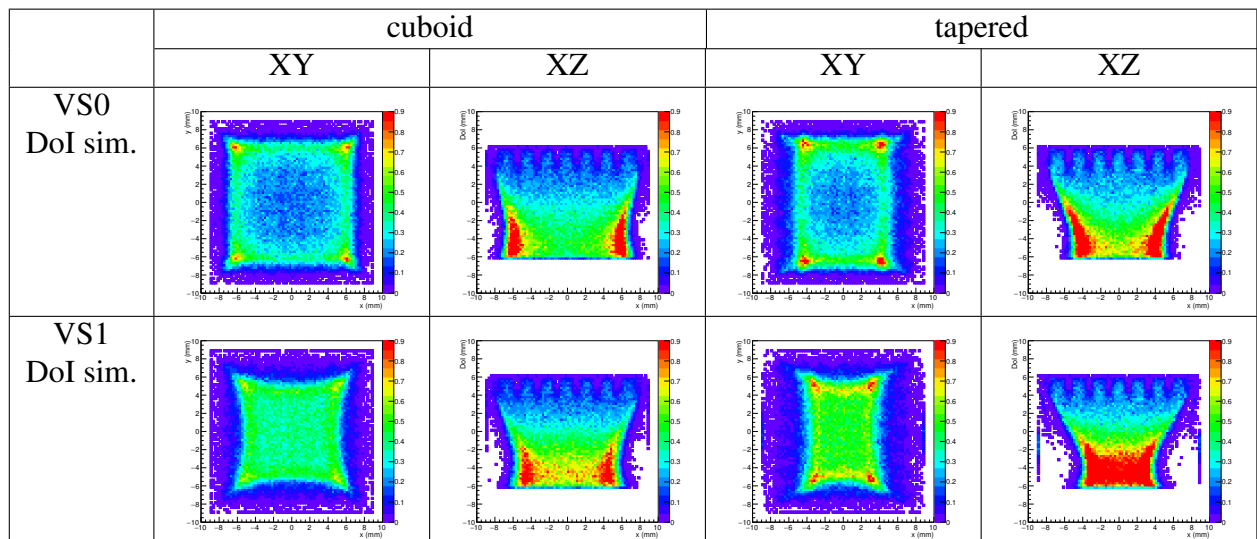
In order to study the mispositioning of the non-negligible percentage of events that have been located just in the entrance of the crystal by the different models, the XY and XZ projections of their estimated interaction position have been compared with the real interaction positions obtained from Monte Carlo simulations. Table 3.4 shows that most of the events located at the entrance of the crystal correspond to ground-truth interactions in the first millimetres of the crystal. The estimated positions of those events are located at the entrance surface of the crystal, producing those areas in the first half of the crystal, previously discussed, where the percentage of estimated events is significantly smaller than the corresponding to the ground-truth. For the algorithm, those events are difficult to position with accuracy because they interact far from the SiPM producing quite uniform collected charge distribution as we saw in chapter 2. However, table 3.4 shows that the estimated position distribution is not so different from the correct position distribution; thus, those coincidences contain information of the activity located in the FoV which can be used for the image reconstruction

The interaction position of the events that the optimization algorithm can not determine, is generally located at the boundary conditions of the algorithm which are the surfaces of the crystal. Those events whose DoI (z coordinate) is difficult to estimate due to the uniformity of the charge distribution are located at the boundary surface coinciding with the entrance of the crystal as it was shown in table 3.4. In table 3.2 some interaction position can also be seen located in the boundary conditions coinciding with the lateral surfaces of the crystal. For both crystal geometries the applied boundary conditions are the six surfaces of the cuboid crystal of  $17.8 \text{ mm} \times 17.8 \text{ mm} \times 12.25 \text{ mm}$ . For the cuboid crystals, these are the correct boundary conditions. However, for tapered crystals the boundary conditions depend on the estimated z coordinate which complicates the implementation in the optimization algorithm. Since the percentage of events that are not located within the real volume of the tapered crystal is negligible, the boundary conditions of the cuboid crystals have been employed for both geometries.

Since the main artefacts identified in the estimated interaction position distribution seem to come from the difficulty in estimating DoI of the events that interact far from the SiPM, the performance of the algorithm has been studied in the unrealistic scenario where only X and Y-coordinates are estimated from the charge distribution having DoI information from the Monte Carlo simulation, see table 3.5. The performance of both models improves, resulting in a more homogeneous estimated interaction position distributions. The improvement is more pronounced for VS1 model where the recovered distribution is more uniform than for VS0 where the accumulation of events at the edges is more noticeable and the regions in the first half of the crystal with significantly smaller percentage of estimated events have disappeared.

However, VS1 still locates towards the centre of the crystal the events interacting close to the four lateral surfaces of the crystal.

Table 3.5 Projections of the interaction position estimation using VS0 and VS1 model to estimate X and Y coordinates and obtaining DoI from Monte Carlo information from cuboid geometry.



In this section it has been appreciated that when all three spatial coordinates are estimated the performance of VS0 model is closer to the ground-truth than the performance of VS1 model, see table 3.2. The studied region with smaller percentage of estimated events comparing with the ground-truth is more pronounced for VS1 model than for VS0 model. Moreover, the deviation of the events that interact far from the photodetector close to the edges of the crystal towards the centre is larger for VS1 model than for VS0 model. Therefore, from now on VS0 model will be employed for the estimation of the 3D interaction position in both geometries of the crystals.

### 3.3 Image Reconstruction

In this study, two image reconstruction algorithms have been implemented: FBP and ML-EM. These methods are affected by the mispositioning of the interaction position estimation; thus, the impact of these artefacts on the reconstructed image has been analysed.



### 3.3.1 Image Reconstruction methods

The use of FBP for image reconstruction was prescribed by NEMA standard for the characterization of the scanner. A 2D FBP algorithm was implemented in C++ with a ramp filter at the Nyquist frequency applied in the Fourier Domain. Radix-2 Fast Fourier Transform (FFT) routines for real data from gsl libraries [88] were used to compute the Fourier transform. These routines use the Cooley-Tukey algorithm to compute in-place FFTs for lengths of arrays (number of bins of each angular projection in the generated sinogram) that are a power of 2. Two policies of axial rebinning to sort data were used: *span* of 1 (SPAN1) where only direct Lines of Response (LoR) were considered, i.e. lines contained within one slice, and Single Slice Rebinning (SSRB) [89] where all LoRs were considered.

Moreover, the well-known ML-EM method based only on geometrical considerations was implemented. ML-EM is a more accurate algorithm for scanners with gaps. Systems with gaps do not typically employ FBP algorithm because the degradation of the resolution and artefacts introduced by the rebinning of the acquired LoRs onto sinograms with regular spacing.

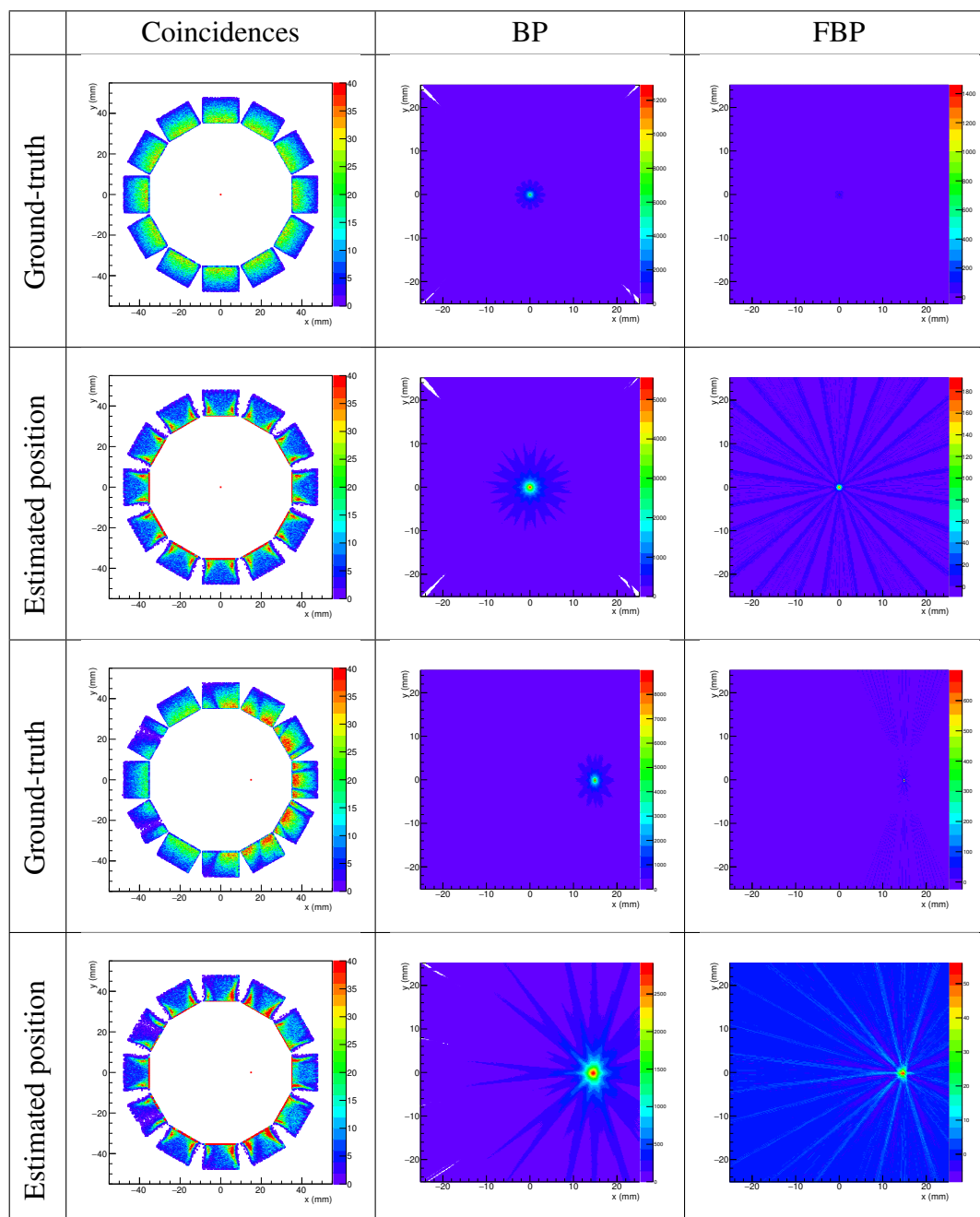
### 3.3.2 Impact of the Position Estimation artefacts in the image reconstruction

In this section, the artefacts induced by the position estimation algorithm in the reconstructed image using FBP have been studied to be able to identify during the characterization of the scanner following NEMA the features coming from the mispositioning of the interaction position estimation. The scanner based on cuboid crystals was employed to study the artefacts of the reconstructed image because they are easier to identify due to the smaller number of detectors that form the scanner. The influence of the gaps for this geometry is also more important than for tapered geometry.

The main effect from the mispositioning of the interaction position which produces artefacts in the image reconstruction was the accumulation of estimated interaction positions towards the edges of the crystal, see XZ projection in table 3.2.

Table 3.6 shows in the first column the distribution of the positions inside the crystal of the two endpoints for each LoR and the image reconstruction of these LoR using BP and FBP algorithms in the second and third column respectively. The reconstructed images represent a transverse FoV of 50.2 mm  $\times$  50.2 mm with a voxel size of 0.2 mm  $\times$  0.2 mm, the employed axial rebinning policy is SSRB and the slice thickness corresponds to the total axial FoV.

Table 3.6 The impact of position estimation artefacts on the reconstructed images. First column shows the positions inside the crystal of the two endpoints for each LoR and the second and third column show the image reconstruction of these LoR using BP and FBP algorithms respectively. The reconstructed images represent all the coincidences (using SSRB and a slice thickness of the axial FoV size) in a FoV of  $50.2\text{ mm} \times 50.2\text{ mm}$  with a voxel size of  $0.2\text{ mm} \times 0.2\text{ mm}$ . A source located at the center of the scanner has been simulated and the ground-truth and the estimated LoRs have been processed in first and second row respectively. Another source located 15 mm away from the center of the scanner has been simulated and the ground-truth and the estimated LoRs have been processed in third and fourth row respectively.

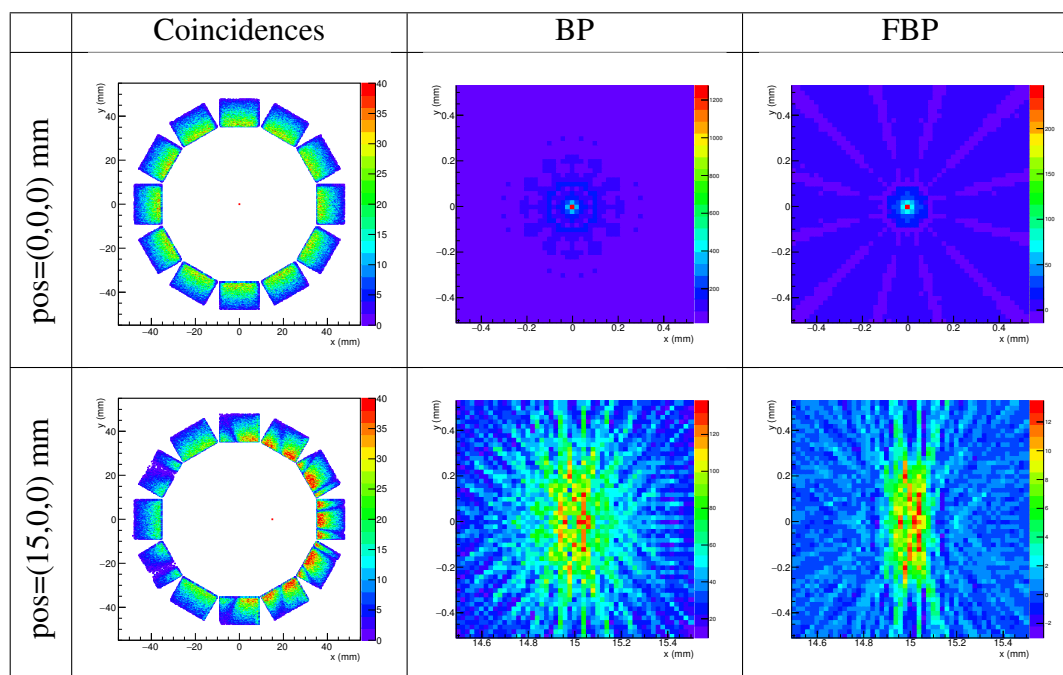


These images have been analysed for a source located at the centre of the scanner (0,0,0) and a source located in (15,0,0) mm, at a radial offset of 15 mm, using the real interaction position (ground-truth) obtained from Monte Carlo information and using the estimated LoRs, see table 3.6. In the first column, the location of the sources in the FoV was represented by a red dot together with the two endpoints for each of the 150000 analysed LoRs. In order to visualize the structures around the voxel of maximum intensity, the maximum color scale value (red) for the representation of the interaction positions in the scanner was set to 40 interactions located within the same voxel of a size of 0.34 mm. Therefore, when there are more than 40 interactions, the voxel is represented by the same color as if there were only 40 interactions. The red line at the entrance of the crystals of the scanner, shown when interaction positions are estimated (second and fourth column), is saturated in order to visualize the distribution of the interaction positions in the rest of the crystal, as it was discussed in 3.2.

Reconstructed images for the source located at the centre of the scanner using the ground-truth are shown in the first row of table 3.6. BP image shows small streak artefacts where 12 regions of smaller quantity of intersecting LoRs can be seen corresponding to the gaps between adjacent detectors in the ring. Whereas FBP image shows a high intensity voxel with an almost imperceptible weak (one order of magnitude smaller) structure around that can not be clearly distinguished due to the size of the voxel. When the LoRs were estimated by the interaction position estimation algorithm (second row) the spatial resolution of the image was significantly degraded. The reconstructed image using FBP shows streak artefacts where the 12 gaps between the detectors can be appreciated. Moreover, close to the regions corresponding to the gaps peak structures appear: 24 peaks in total which correspond to the accumulation of the estimated interaction position in the edges of the crystal. In the image obtained using FBP, after applying the ramp filter, the artefacts are more noticeable and the 24 equidistant lines coming from the edges of the 12 detectors that compose the scanner can be clearly seen crossing the FoV through the centre where the source is located.

Reconstructed images for the source located with a radial offset of 15 mm using the ground-truth (third column) show a slightly degraded resolution in comparison with the source located at the centre of the scanner. BP image shows a streak artefact, but due to the asymmetries it is more difficult to identify the effect of the 12 gaps between adjacent detectors. FBP image shows a high intensity voxel with two adjacent voxels in the tangential direction with smaller intensity and a weaker structure around can be seen. When the LoRs were estimated (fourth column), the artefacts coming from the positioning are stronger and the resolution is degraded in comparison with the source located at the centre.

Table 3.7 Image Reconstruction of ground-truth interaction position for a source located at the center of the scanner and for a source located 15 mm away from the center, first and second row respectively. First column shows the positions inside the crystal of the two endpoints for each LoR and the second and third column the image reconstruction of these LoR using BP and FBP algorithms respectively. 150000 coincidences are processed for each source position. The reconstructed images represent all the coincidences (using SSRB and a slice thickness of the axial FoV size) in a FoV of  $1.02\text{ mm} \times 1.02\text{ mm}$  with a voxel size of  $0.02\text{ mm} \times 0.02\text{ mm}$  centred at the simulated source location.



In order to analyse the effects produced by the gaps (without taking into account the artefacts produced by the mispositioning of the interactions in the scanner), the reconstructed images using the ground-truth have been analysed with a smaller voxel size of  $0.02\text{ mm}$  and smaller FoV. Table 3.7 shows the reconstructed images for a FoV of  $1.02\text{ mm} \times 1.02\text{ mm}$  centered in the location of the simulated source. When the source is located at the centre (first row) the effect of the 12 gaps between detectors is clearly visible in both reconstructed images (BP and FBP) with a high intensity pixel one order of magnitude above the rest of the voxels. However, when the radial offset of the source is 15 mm, the resolution is degraded. For the point of view of NEMA characterization, it is important to note that, the degradation is greater in the tangential direction, and the contribution of the gaps is difficult to identify due to the asymmetry.

The predominant artefacts on the reconstructed image from the estimated LoRs using FBP seem to come from the mispositioning of the interaction position estimation method

which accumulates interactions close to the edges of the crystal. Since when the source is located at the centre of the scanner, 24 equidistant lines from the centre to the edges of the crystals can be clearly seen. The degradation on the reconstructed images produced by the gaps of the scanner, which share the same geometrical symmetries, is added to it.

The main difference, comparing the reconstruction using ground-truth and the interaction position estimation method for the determination of the LoRs, is the degradation in the spatial resolution of the reconstructed image. We will not go deeper here, since the spatial resolution of the image will be studied in detail in section 3.4.1 following NEMA standard where the results for the scanners based on both geometries were compared.

### 3.4 Comparison of the performance of the scanners

A characterization of the performance of the scanners has been done following NEMA NU 4-2008 standard [90] and the results obtained for both scanner geometries, cuboid and tapered, have been compared.

As specified by NEMA, spatial resolution of the scanners has been analysed reconstructing point-like sources at different radial offsets with FBP algorithm. This is why the influence of the artefacts of the interaction position estimation algorithm and the influence of the gaps on the results have been analysed in the previous section. Besides, Scatter Fraction (SF), count losses and random coincidence measurements have been performed to study the ability of the scanners to measure high activity sources with accuracy and to estimate the optimal conditions to achieve the best image quality through the NECR value.

The most important parameter for this study is the sensitivity, since a significant improvement of the sensitivity is expected for the tapered geometry due to the tighter packing of the crystals in the scanner. The expected increase on the sensitivity will allow radiation dose reduction without reducing the quality of the image. On the other hand, due to the smaller influence of the gaps, the recovery of homogeneous regions will be better without correcting for the inhomogeneities and the incomplete set of angular projections.

Since the sensitivity of the scanner is so important, apart from the axial sensitivity measurement proposed by NEMA standard, it has been studied through another two figures of merit: a sensitivity map obtained from Monte Carlo simulation and the reconstruction of homogeneous regions.

### 3.4.1 Spatial Resolution

Spatial resolution of the scanner can be defined as the minimum distance at which two point-like sources can be distinguished by the scanner after reconstruction. Following NEMA, spatial resolution was measured using a 1 MBq spherical  $^{22}\text{Na}$  source of 0.1 mm diameter size embedded in a 1 cm<sup>3</sup> plastic cube. The whole set of points (5, 10, 15 and 25 mm radial distances from the centre in X-axis direction) at axial centre of the scanner were simulated using a  $^{22}\text{Na}$  source according to NEMA standard, see figure 3.9.

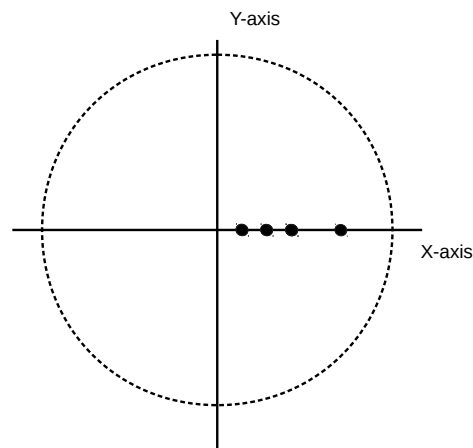


Figure 3.9 Schematics of the positioning of the sources for spatial resolution measurements in transaxial plane. The dashed line represent the inner radius of the scanner and the points the positions of the sources at 5 mm, 10 mm, 15 mm and 25 mm from the center of the scanner. The size of the sources is not to scale.

As indicated by NEMA, image reconstruction was implemented using 2D FBP algorithm and SSRB rebinning algorithm without smoothing filters. The resolution was measured along different directions: radial and tangential directions in the transaxial plane and axial direction (Z-axis). Due to the location of the sources, X-axis corresponds to the radial direction and Y-axis to the tangential direction. The sampling in the transaxial plane was set to 0.2 mm and the plane thickness of the reconstruction, axial sampling, was set to 0.4 mm. A thicker plane will result in smoother profiles. Each measurement had more than  $10^5$  prompt counts as NEMA specifies.

According to NEMA standard, the response function in each direction (radial, tangential and axial) was formed by summing to the profile the parallel one-dimensional profiles in the

other two orthogonal directions within two times the FWHM of that direction. The FWHM and FWTM were determined by linear interpolation between adjacent pixels at half and tenth of the maximum of the response function. The maximum was determined by a parabolic fit using the peak and its two nearest neighbouring points. FWHM and FWTM of the response function of the four locations of the source specified in NEMA standard were reported as a measurement of spatial resolution of the system.

Table 3.8 Resolution values reported according to NEMA at axial centre of both scanners. The image was reconstructed using FBP algorithm with SSRB.

Reconstructed image pixel size (mm): 0.2								
Slice thickness (mm): 0.4								
cuboid crystals								
	5 mm <sup>a</sup>		10 mm <sup>b</sup>		15 mm		25 mm	
	FWHM	FWTM	FWHM	FWTM	FWHM	FWTM	FWHM	FWTM
Radial	1.22	2.64	1.08	1.97	1.37	2.22	1.33	3.07
Tangential	1.04	2.68	1.68	4.98	1.39	4.15	1.49	4.32
Axial	1.18	2.35	1.44	3.13	2.55	3.92	2.87	5.32
tapered crystals								
	5 mm <sup>a</sup>		10 mm <sup>b</sup>		15 mm		25 mm	
	FWHM	FWTM	FWHM	FWTM	FWHM	FWTM	FWHM	FWTM
Radial	1.29	2.36	1.08	2.23	1.13	2.02	1.41	2.59
Tangential	1.13	2.91	1.49	3.34	1.20	3.47	1.38	5.67
Axial	1.26	2.43	1.50	3.08	2.96	4.42	2.81	5.91

<sup>a</sup> There is a more pronounced artefact along radial direction which produces worse radial resolution (more visible for cuboid scanner).

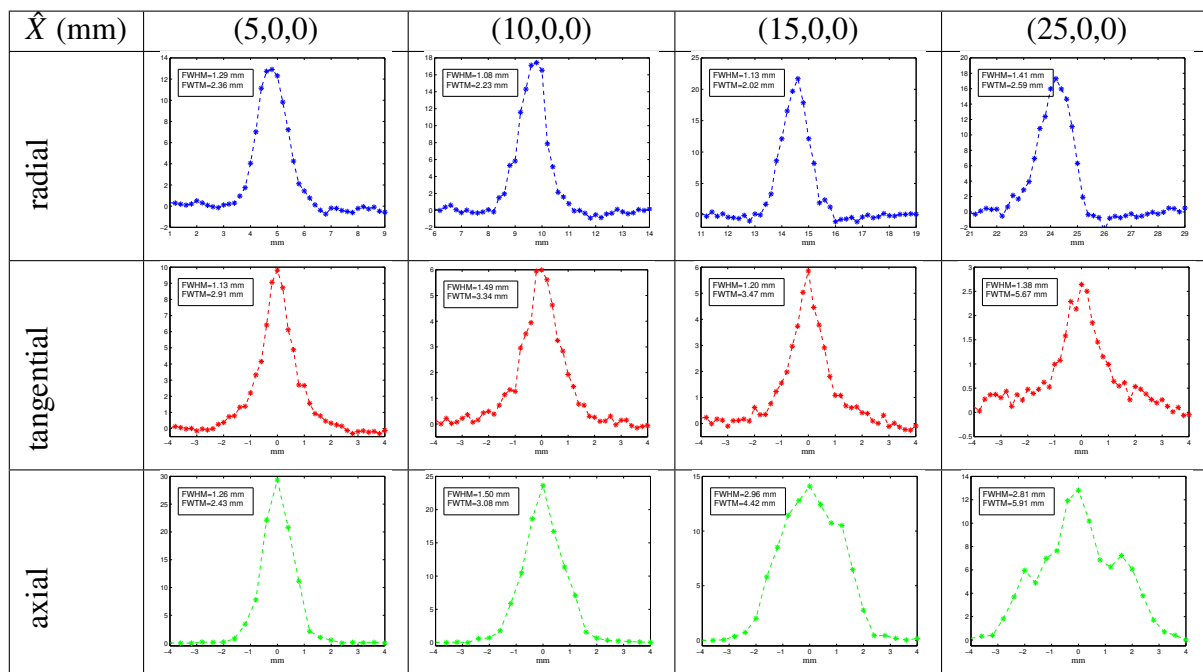
<sup>b</sup> The source in position  $x=10$  mm for the scanner based on cuboid crystals is located in the gap between two detector heads.

The spatial resolution for both geometries, cuboid and tapered crystals, at axial centre of the scanner using a  $^{22}\text{Na}$  source is shown in table 3.8. The response profiles obtained in the three orthogonal directions are shown in table 3.9 and table 3.10 for tapered and cuboid crystals respectively.

In general, as the radial offset is increased, spatial resolution profiles in all directions are degraded. The degradation in the tangential and axial direction is more significant than in radial direction. There are some exceptions that do not obey the tendencies described that have been analysed below.

The radial resolution value of the first source position located at (5,0,0) mm is worse than the value of the source located 10 mm and 15 mm away from the centre for cuboid and tapered scanners. Moreover, only for the scanner based on cuboid geometry, the FWTM

Table 3.9 The response function in radial, tangential and axial directions from top to bottom and for from left to right the different radial offsets of the source (5,10,15,25) mm for the scanner based on tapered crystals.



of the sum response for this position in the radial direction is approximately equivalent to the FWTM of the response function in the tangential direction. For the rest of the analysed situations the FWTM of the tangential direction is significantly greater than the FWTM of the radial direction. This anomalous outcome is due to an artefact in the image reconstruction for this source location that degrades the radial resolution and is more prominent for cuboid geometry. Table 3.11 shows the central slice of the reconstructed image of 0.4 mm slice thickness obtained with FBP and SSRB rebinning policy (first column) and radial and tangential response functions (second and third column respectively) for a source located at the centre of the scanner (first row) and for the same source located 5 mm away from the centre in the X-axis direction (second row) for the scanner based on cuboid crystals. The radial and tangential response functions for the source located at the centre of the FoV have equivalent resolution values (FWHM and FWTM) and that symmetry can be observed in the reconstructed image. However, for the source located 5 mm away from the centre (second row) an artefact can be clearly seen with the shape of a small horizontal line from the source location towards the centre of scanner, with a value above the the background in the reconstructed image using FBP (first column). This artefact degrades the resolution of the radial response function. For this position, significant asymmetries can be seen between the resolution of the radial and tangential response functions. The artefacts of the reconstructed



Table 3.10 The response function in radial, tangential and axial directions from top to bottom and for from left to right the different radial offsets of the source (5,10,15,25) mm for the scanner based on cuboid crystals.

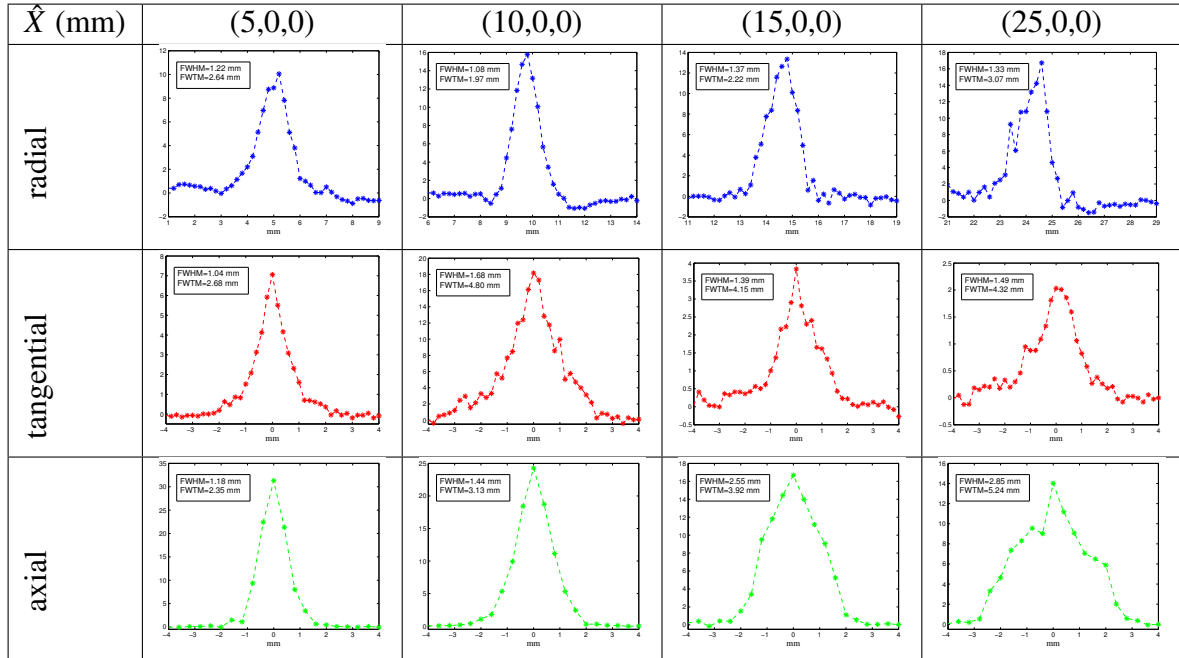


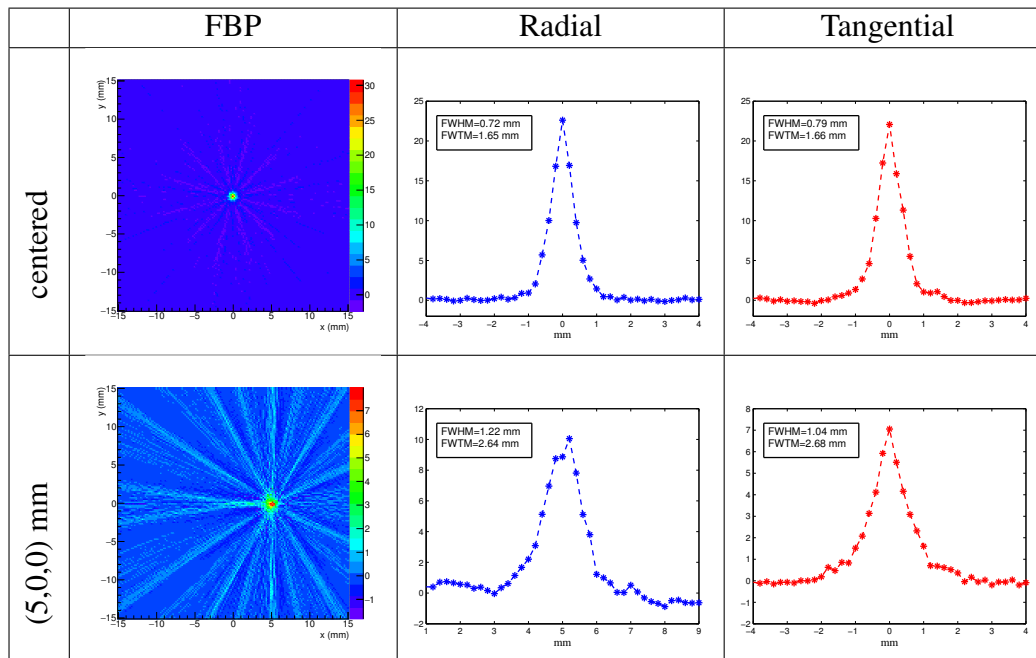
image when the source is located at the center of the scanner affect in the same way to radial and tangential resolution without changing the shape of the reconstructed source. However, this is not the case when the source is located in any other position as for NEMA spatial resolution characterization.

The second position of the source represents another singularity. The position  $x=10$  mm in cuboid geometry is located just in the gap between 3-4 and 10-11 detectors, see figure 3.1. The tangential resolution in terms of FWHM and FWTM for the second position in cuboid geometry is worse than for the rest of positions including those positions at higher value of the radial offset. On the other hand, for tapered geometry in that position there is a small fluctuation only in the FWHM value that degrades the resolution in terms of FWHM but not in FWTM.

However, for cuboid geometry, the impact of the artefacts is more important and the response functions are less smooth than for tapered geometry, see table 3.10 and table 3.9.

The position of the maximum of the response function in tangential and axial directions is equivalent to the location of the sources for both scanners. However, the position of the maximum of the response function in radial direction is slightly biased towards the centre of the scanner for the sources with the greatest radial offset. For cuboid geometry, the source with a radial offset of 25 mm is slightly biased ( $0.4 \pm 0.2$  mm) towards the centre of the

Table 3.11 Central slice of the reconstructed image and radial and tangential response functions for the source located at the center of the scanner (first row) and for the source located 5 mm from the center in the X-axis direction (second row).



scanner while for tapered geometry the sources with a radial offset of 15 and 25 mm are biased towards the centre of the scanner  $0.4 \pm 0.2$  mm and  $0.8 \pm 0.2$  mm respectively. The maximum is determined by identifying the bin with the maximum value as well as by a parabolic fit as specified by NEMA, see table 3.12.

Table 3.12 Position of the maximum of the sum response function determined by a parabolic fit for both geometries.

$(x,y,z)^{nominal}$	(5,0,0) mm	(10,0,0) mm	(15,0,0) mm	(25,0,0) mm
Maximum: bin position ( $\pm 0.2, \pm 0.2, \pm 0.4$ ) mm				
cuboid	(5.2,0.0,0.0)	(9.8,0.0,0.0)	(14.8,0.0,0.0)	(24.6,0.2,0.0)
tapered	(4.8,0.0,0.0)	(9.8,0.0,0.0)	(14.6,0.0,0.0)	(24.2,0.0,0.0)
Maximum: parabolic fit (mm)				
cuboid	(5.17,-0.02,-0.01)	(9.74,0.04,0.01)	(14.74,0.00,-0.02)	(24.56,0.10,0.06)
tapered	(4.74,-0.02,-0.02)	(9.75,-0.08,-0.03)	(14.57,-0.02,-0.02)	(24.20,0.05,-0.10)

Figure 3.10 compares the transversal and coronal central slices of the superimposed reconstructed images of the four positions of the point-like sources along radial direction using FBP algorithm applied to a FoV of  $60.2 \text{ mm} \times 60.2 \text{ mm} \times 18 \text{ mm}$  with a voxel size of  $0.2 \text{ mm} \times 0.2 \text{ mm} \times 0.4 \text{ mm}$  for tapered and cuboid geometry. Figure 3.10(a) and figure 3.10(b)

show the transversal central section of 0.4 mm thickness with a voxel size of  $0.2\text{ mm} \times 0.2\text{ mm}$  for tapered and cuboid geometries respectively. Figure 3.10(c) and figure 3.10(c) show the coronal central section of 0.2 mm thickness with a voxel size of  $0.2\text{ mm} \times 0.4\text{ mm}$  for tapered and cuboid geometries respectively. The artefacts in the image reconstruction can be seen for both geometries; however, they are more pronounced in cuboid geometry and the point-like sources are more blurred. Some artefacts have the shape of vertical crosses in the transverse plane which produce long tails in tangential sum response functions. This is the reason behind the discussed asymmetry between the FWTM value of the radial and tangential sum response functions. The sum response in the tangential direction was formed by summing to its profile the parallel one-dimensional profiles in radial and in axial directions. The summed profiles in radial direction contain high values far from the source location due to the cross artefacts that contribute to the long tails of the sum response function.

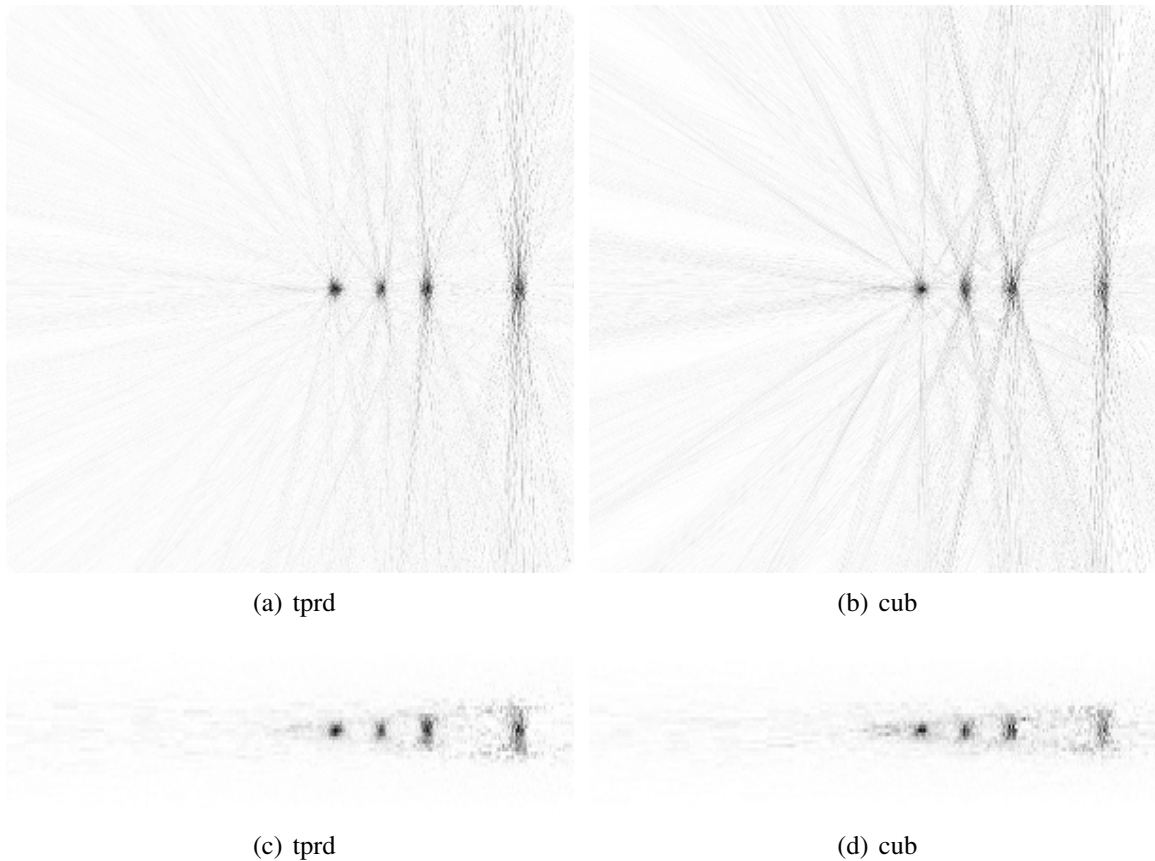


Figure 3.10 Transversal and coronal central slices of the superposition of the reconstructed images of the 4 positions of the point-like sources using FBP algorithm applied to a FoV of  $60.2\text{ mm} \times 60.2\text{ mm} \times 18\text{ mm}$  with a voxel size of  $0.2\text{ mm} \times 0.2\text{ mm} \times 0.4\text{ mm}$  for tapered (a,c) and cuboid (b,d) geometry.

The artefacts produced in the reconstructed image either by the gaps between crystals or by the position estimation algorithm, which share similar pattern, highly depend on the geometry and on the number of detectors of the scanner and on the location of the reconstructed source which make resolution quite unstable across the transaxial FoV. Therefore, the reconstructed image of a source located at the same global position for both scanners might present quite different artefacts mainly due to the different number of detector heads that compose the scanners, as it was analysed for the second location of the source (10,0) mm.

Table 3.13 Response function of radial and tangential direction for the spatial resolution measurements with the source located at 15 mm from the centre of the scanner. The first row shows the response function obtained using ideal interaction position within the crystal from Monte Carlo information, the second row using position reconstruction algorithm to estimate X and Y coordinates and using ideal Z from the information of the simulation and in the third column, using position reconstruction algorithm to obtained de 3D interaction position within the crystal.

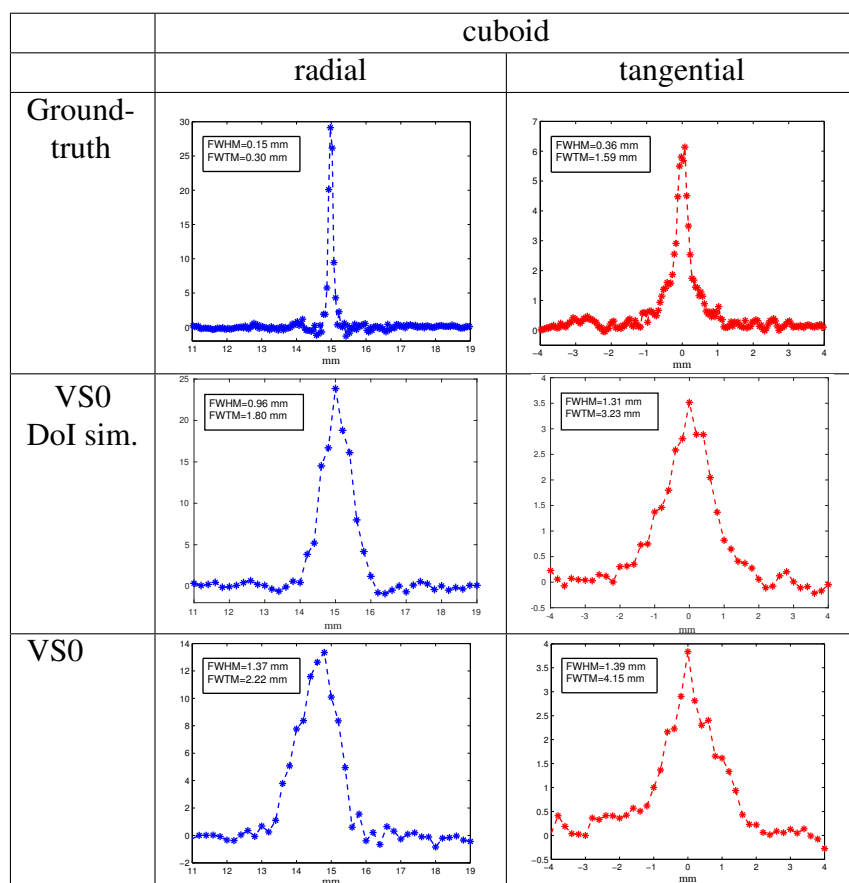


Table 3.13 shows the radial and tangential response function for the spatial resolution measurements with the source located 15 mm away from the center of the scanner, obtaining the estimated position of the interaction of the gamma-rays through different methods. The

first row shows the response function obtained using ideal interaction position from Monte Carlo information, the second row, reconstructing the X and Y coordinates using VS0 model and using ideal Z information from the simulation, and in the third column, using position reconstruction algorithm to estimate the 3D interaction position within the crystal. It can be seen that comparing the cases in which all 3-coordinates or only X and Y are estimated, the response functions are less smooth, the spatial resolution in radial direction is degraded and the position of the centre of the response function is slightly biased towards the centre of the scanner when DoI is also estimated. The resolution in the tangential direction is worse than in the radial direction and the tails, represented by the FWTM value, are longer in the tangential direction already in the reconstructed image from ground-truth data where only gaps between detectors are contributing to the artefacts. The estimation of the interaction position degrades the resolution maintaining the same behaviour and producing less smooth sum response functions.

In general, we can conclude that there are no significant differences in the spatial resolution values obtained in terms of FWHM and FWTM of the response function along the different positions of the transaxial FoV between cuboid and tapered crystals. Although for cuboid geometry the impact of the artefacts is more important and the response functions are less smooth than for tapered geometry producing more unstable resolution values across the transverse FoV and more blurred images.

### **3.4.2 Scatter Fraction, Count Losses, and Random Coincidence Measurements**

The measurements of count losses and random coincidence rates express the ability of a positron emission tomograph to measure highly radioactive sources with accuracy (4.1, 2nd paragraph NEMA-NU). Following NEMA protocol count rate performances (scatter, random, true, total rate and Peak Noise Effective Counting Rate (NECR)) and Scatter Fraction (SF) were calculated and compared for both scanners. Due to the various sizes of animals used in preclinical PET studies, NEMA proposes three different phantoms to simulate the size of a mouse, a rat and a monkey. The inner ring of the simulated scanner only allows us to study the mouse-like and rat-like phantoms defined in NEMA standard. The mouse-like phantom is made of a solid cylinder composed of high density polyethylene ( $0.96 \text{ g/cm}^3$ ), 70 mm long and 25 mm in diameter. A cylindrical hole (3.2 mm diameter) is simulated drilled parallel to the central axis at a radial distance of 10 mm. The rat-like phantom has similar geometry but with larger dimensions to simulate the geometry of a rat. The cylinder of the rat-like phantom has a diameter of 50 mm and a length of 150 mm with a cylindrical hole of the

same diameter as in the mouse-like phantom but located at a radial distance of 17.5 mm. The test phantom line source is a fillable section 10 mm shorter than the cylindrical phantoms with a diameter which fits the 3.2 mm hole. The line source was simulated filled with water and  $^{18}\text{F}$  ion source without considering its decay. Different simulations were performed for each fixed value of the total activity of the line source from 5 to 5000  $\mu\text{Ci}$ .

NEMA protocol establishes a set of steps and rules to analyse the sinograms acquired in each measurement. Figure 3.11 shows the main operations (apply a mask, align and sum angular projections) applied to the acquired prompt sinograms for the case of mouse-like phantom and the scanner based on cuboid crystals. Firstly, a mask which sets to zero the value of all the pixels of the coincidence sinogram (applying SSRB policy) that are farther than 8 mm from the edges of the phantom is applied, figure 3.11(b). Then, the angular projections are shifted so that the maximum value of the projection is aligned with the central pixel of the sinogram, see figure 3.11(c). After alignment, a sum projection is produced for each radial offset, see 3.11(d). The total number of prompt events ( $C_{Total,i,j}$ ) in the sinogram (true, scattered and random events) is calculated summing up all the counts of the sum projection for each axial slice (i) and for each measured activity (j). The total number of scatter and random events ( $C_{r+s,i,j}$ ) has been estimated following a set of mathematical operations applied to the sum projection which are described in detail in NEMA protocol. The remaining counts in the sum projection ( $C_{True,i,j}=C_{Total,i,j}-C_{r+s,i,j}$ ) are considered the true coincidences of each axial slice.

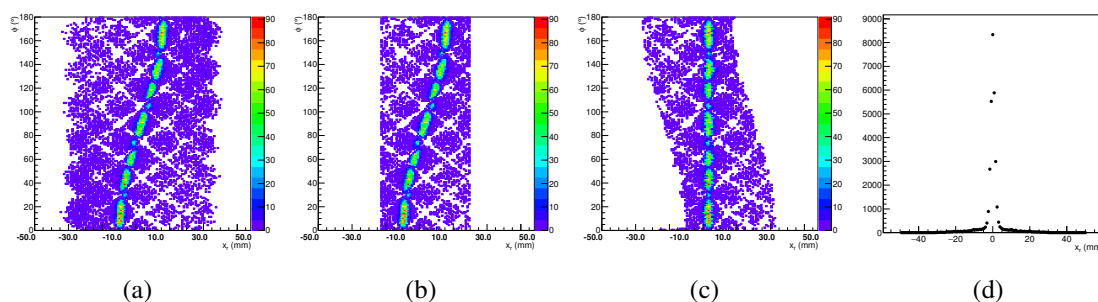


Figure 3.11 Operations applied to sinograms according to NEMA to obtain total counts, true counts and scatter plus random counts for each acquisition and each slice. The collected sinogram (a), the sinogram with the mask applied (b), the aligned sinogram (c) and the sum projection (d) for cuboid configuration and mouse-like phantom are shown.

The Scatter Fraction (SF) of a scanner is defined as the ratio between the number of scattered events over all the measured prompt events, provided that the random rate is negligible. SF was calculated only with the measured activities in which the fraction of randoms to the trues is less than 1%. SF was computed following the equation (3.4) where

$j'$  represents the acquisition for activities in which random event rates are below 1%. For those acquisitions, it is assumed that  $C_{r+s,i,j'}$  consists of scattered event counts and  $C_{Total,i,j'}$  represents the true and scattered events. Therefore, computing the fraction of these two quantities estimated from prompt sinograms over the low activity acquisitions the SF was obtained.

$$SF = \frac{\sum_i \sum_{j'} C_{r+s,i,j'}}{\sum_i \sum_{j'} C_{Total,i,j'}} \quad (3.4)$$

The total event rate was computed as the fraction of the sum for all the axial slices (i) of the total counts ( $C_{Total,i,j}$ ) for each measured activity (j) divided by the acquisition time as it is shown in equation (3.5). The true event count rate was computed as the sum of the true counts for all the slices divided by the acquisition time, equation (3.6)

$$R_{Total,j} = \frac{\sum_i C_{Total,i,j}}{T_{acq,j}} \quad (3.5)$$

$$R_{True,j} = \frac{\sum_i (C_{Total,i,j} - C_{r+s,i,j})}{T_{acq,j}} \quad (3.6)$$

The random event rate ( $R_{random,j}$ ) was computed as a function of total rate, true rate and SF following equation (3.7).

$$R_{Random,j} = R_{Total,j} - \frac{R_{True,j}}{1 - SF} \quad (3.7)$$

Finally the rate of scattered counts is computed following equation (3.8) where  $R_{intrinsic}$  is the intrinsic true count rate. Intrinsic radiation from the natural radioactivity of the scintillator contributes to a background single event rate. In addition, intrinsic radioactivity may also give rise to true coincidences when due to the  $\beta^-$  decay of the Lutetium the energy of the electron is locally deposited and one of the emitted gamma-rays from the decay is detected in another detector head which is referred to as intrinsic true count. Intrinsic true count Rate ( $R_i$ ) value was measured simulating the mouse and rat-like phantom filled with non-radioactive water. Background single event rate from Lutetium of about 4.5 kcps for an energy window of [450,700] keV was measured. This background single event rate may contribute to the random coincidence rate. However the intrinsic true rate measured for a window of [450,700] keV and without considering contiguous coincidences (geometrical conditions) was less than 0.05 cps. Therefore, no corrections have been made for the intrinsic true rate.

$$R_{scatter,j} = R_{Total,j} - R_{True,j} - R_{Random,j} - R_{intrinsic} \quad (3.8)$$

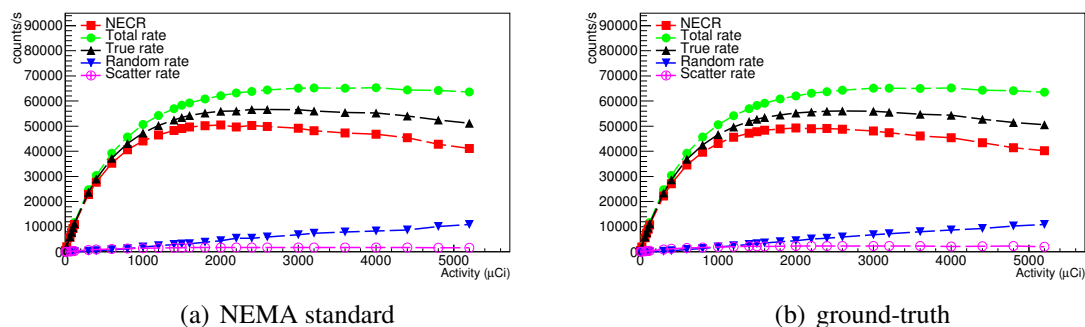


Figure 3.12 Count rate capability for the full ring based on cuboid crystals with a coincidence dead-time of  $10 \mu\text{s}$ . (a) shows the count rates estimated following NEMA standard and (b) represents ground-truth count rates obtained from Monte Carlo information.

The NECR can now be computed as a function of true, scatter and random rates using the following equation:

$$NECR_j = \frac{T_j^2}{T_j + S_j + R_j} \quad (3.9)$$

NECR represent the effective performance of the counting system and takes into account the statistical noise introduced by scatter and random coincidences. It is considered to be a surrogate indicator of the final image quality since it provides an estimation of the quality of the measured data [18]. Therefore, the performance of the scanners will be compared through NECR value.

In this section, unless otherwise stated, a non-paralyzable coincidence dead-time of  $10 \mu\text{s}$  was simulated.

Count rates obtained following NEMA standard, see figure 3.12(a), were compared to the ground-truth where random, true and scatter rates were obtained from Monte Carlo information, see figure 3.12(b), applying the same mask that was applied in NEMA standard to the sinograms. There is a good agreement between the estimation of the count rate following NEMA protocol and the count rates obtained from Monte Carlo information after applying the mask. The application of the mask decreases the rate of random coincidences.

Figure 3.13 shows total, random, true, scatter and NEC rates as a function of the total activity for the mouse and rat-like phantom according to NEMA for an energy window of [450-700] keV, a TCW of 851 ps and a coincidence dead-time of  $10 \mu\text{s}$ . Count rate aspects of both system geometries for the mouse and rat-like phantom were summarized in table 3.14 and in table 3.15 respectively. For mouse-like phantom the NECR peak occurs at 2.1 mCi with a value of 50.4 keps while for tapered crystal it occurs at 1.9 mCi with a value of 53.5 keps. For rat-like phantom the NECR peak occurs at 2.9 mCi with a value



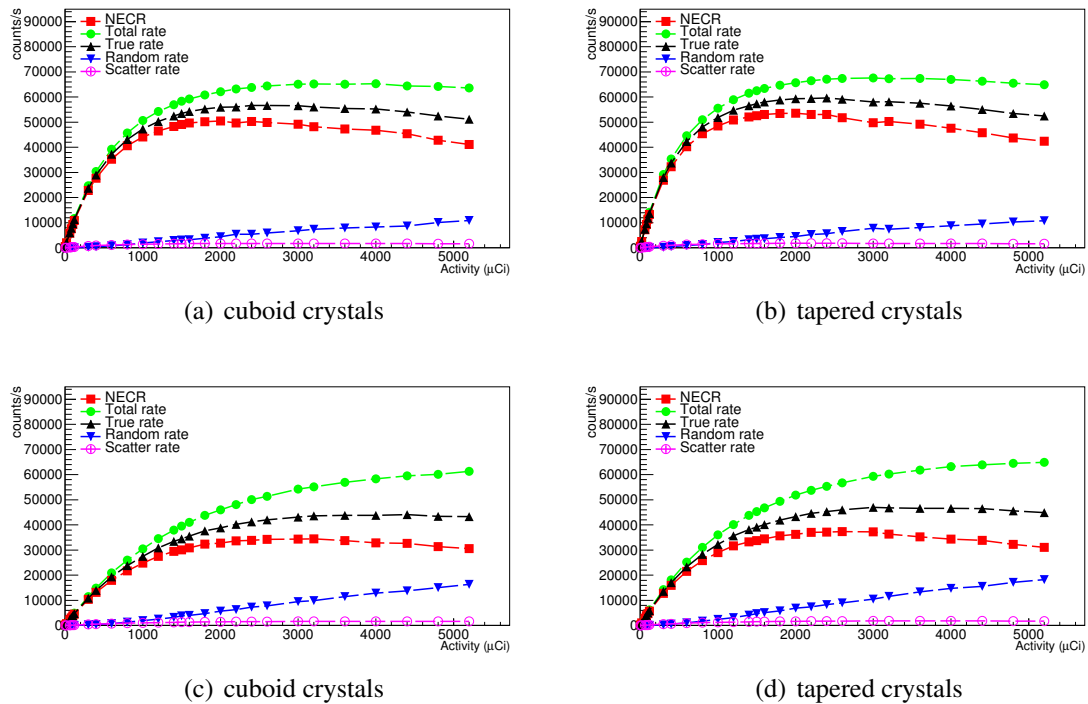


Figure 3.13 Count rate capability using: (a,b) the mouse-like phantom and (c,d) the rat-like phantom for the system based on cuboid and tapered crystals respectively. Dead-time was set to 10  $\mu$ s.

of 34.4 kcps while for tapered crystal it occurs at 2.6 mCi with a value of 37.2 kcps. In summary, for mouse-like phantom the activity at which NECR peak occurs is 7.4% smaller and the NECR peak value is 6.2% greater for tapered crystals than for cuboid crystals and for rat-like phantom the activity at which NECR peak occurs is 9.4% smaller and the peak value is 8.1% greater for tapered crystals. The same trend can be observed for the true peak. The peaks of the true and NEC rate curves were obtained by fitting those count rate values above 80% of the maximum count rate value obtained from the set of simulated activities to a polynomial of seventh degree. Figure 3.14 illustrates the good agreement of the fitted curves with the rate values obtained from the simulations for the scanner based on cuboid crystals using the mouse-like phantom. The fitted curves are represented with a continuous line and the NECR and True rate values with red square and black triangular markers respectively.

The differences of the SF between the two scanner for the same phantom are negligible. On the other hand, the SF of the rat-like phantom is greater than the SF from the mouse-like phantom as it was expected due to the larger volume of the phantom which increase the scatter inside the object of study. The peak of the curves occurs at higher activities for rat-like phantom but the rate values are smaller than for mouse-like phantom.

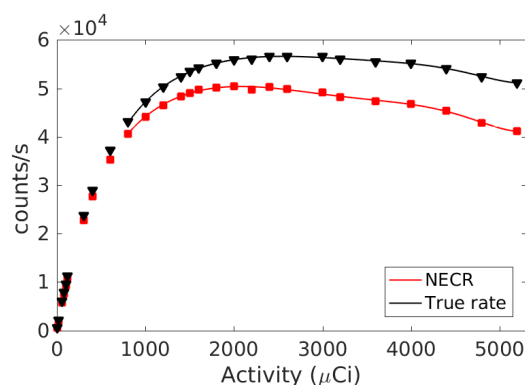


Figure 3.14 Illustration of the seventh grade polynomial curves adjusted (continuous lines) to the NECR (red squares) and True count rate (black triangles) values obtained from the simulations of the scanner based on cuboid crystals using the mouse-like phantom.

Table 3.14 Summary of Counting Rate results for Mouse-like phantom.

System	Energy window (keV)	TCW (ns)	DT ( $\mu$ s)	Mouse Phantom				
				peak NECR (kcps)	Activity ( $\mu$ Ci)	peak True (kcps)	Activity ( $\mu$ Ci)	SF (%)
cuboid	450-700	0.851	10	50.4	2090	56.6	2500	3.04
tapered	450-700	0.851	10	53.5	1936	59.6	2241	2.98

Table 3.15 Summary of Counting Rate results for Rat-like phantom.

System	Energy window (keV)	TCW (ns)	DT ( $\mu$ s)	Rat Phantom				
				peak NECR (kcps)	Activity ( $\mu$ Ci)	peak True (kcps)	Activity ( $\mu$ Ci)	SF (%)
cuboid	450-700	0.851	10	34.4	2865	44.0	3960	3.63
tapered	450-700	0.851	10	37.2	2595	46.9	3365	3.71

In order to complete the study of the counting capabilities of our scanner, count rates have also been studied for different coincidence dead-time values of  $1 \mu$ s,  $10 \mu$ s and  $64 \mu$ s. Coincidence dead-time of  $64 \mu$ s was chosen to be studied because it is the coincidence dead-time value that our prototype already has which corresponds with  $1 \mu$ s dead-time for each channel,  $10 \mu$ s was selected as a realistic achievable value for our system and  $1 \mu$ s is in

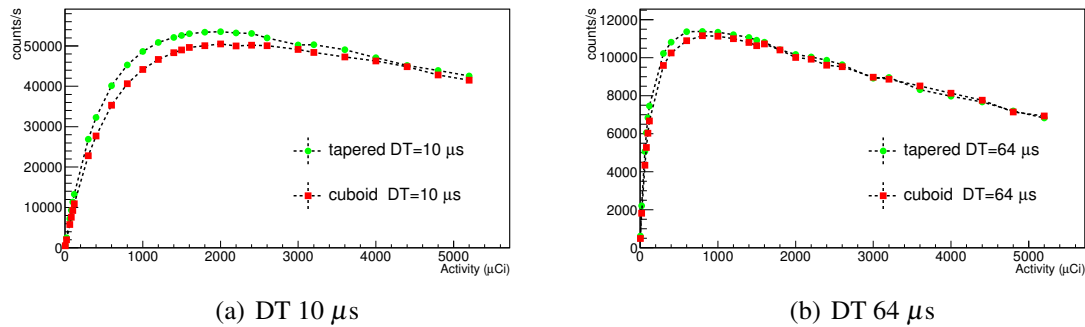


Figure 3.15 NECR according to NEMA standards for tapered and cuboid systems for mouse-like phantom.

the same order of magnitude of the effective dead-time employed for commercial scanners [91].

For the dead-time value of  $1 \mu\text{s}$  there is not a peak within the range of studied activities in the simulated scanners. In figure 3.15 NECR as a function of activity is compared between tapered and cuboid system applying a  $10 \mu\text{s}$  and a  $64 \mu\text{s}$  coincidence dead-time values using the mouse-like phantom. Count rate for the tapered system is always higher than for the cuboid system. As the dead-time increases the peak occurs at smaller activities and the curves decrease faster for activities above the activity at which the peak occurs. The activity at which the NECR peak occurs is reduced to a 41.2% and the count rate value to a 22.2% for cuboid crystals while for tapered crystals the activity is reduced to 38.8% and the count rate to a 21.3% when the dead-time is increased from 10 to  $64 \mu\text{s}$ .

Table 3.16 Summary of counting rate results for mouse-like phantom applying different DT values for both configurations. There is no peak up to  $5200 \mu\text{Ci}$  for  $\text{DT}=1 \mu\text{s}$ .

System	DT ( $\mu\text{s}$ )	peak NECR (kcps)	Activity ( $\mu\text{Ci}$ )	peak True (kcps)	Activity ( $\mu\text{Ci}$ )
cuboid	10	50.4	2090	56.6	2500
tapered	10	53.5	1936	59.6	2241
cuboid	64	11.2	862	11.9	998
tapered	64	11.4	756	12.2	900

The general shape of the count rate curves is similar for both geometries. NECR have a linear range with the activity at least up to  $200 \mu\text{Ci}$  which is below the NECR peak. The linear range is reduced as the dead-time increases. For both phantoms, the activity at which peak occurs for NECR and True counts is smaller for tapered crystals than for cuboid crystals

and the peak value is greater. Therefore, for tapered crystal the estimated quality of the measured data is better than for cuboid crystals and the optimum conditions occur at lower activities.

### 3.4.3 Sensitivity

Sensitivity is the part of this study that has been analysed in more detail. It is the most important and complete part since enhancing the sensitivity is the main goal when replacing cuboid crystals by tapered crystals.

According to that, the sensitivity was studied through two additional figures of merit beside the axial sensitivity measurement specified in NEMA standard. The employed figures of merit were: a sensitivity map obtained by using Monte Carlo simulations and the reconstruction without sensitivity correction of an homogeneous cylinder covering almost all the FoV, which results in a sensitivity estimation of the system.

#### 3.4.3.1 NEMA sensitivity

Sensitivity was obtained according to NEMA standard [90]. A  $^{22}\text{Na}$  point-like source with an active diameter of 0.1 mm and 1 MBq activity embedded in a 1 cm<sup>3</sup> plastic cube was simulated in the center of the FoV. The source is stepped through the axial FoV of the scanner. The step size, identical to the reconstructed plane thickness, was set to 0.712 mm (25 source positions within the 17.8 mm axial FoV). In this case, optical photons were not included in the simulations because they are expected to have no effect when counting the number of detected coincidences and they highly increase computational time. For each detected gamma-ray, the simulation of optical photons will be necessary if the light distribution over the photodetector is important.

We report values of absolute sensitivity (taking into account the branching ratio of  $^{22}\text{Na}$ ) for all axial source positions and the total absolute sensitivity obtained as the average absolute sensitivity over the entire axial FoV. NEMA standard recommends to report the absolute sensitivity value for mouse and rat lengths (70 mm and 150 mm respectively). Since the axial FoV of the studied scanners is smaller than 70 mm, the reported total absolute sensitivity is equivalent to those recommended quantities.

The sensitivity axial profile for both scanners is shown in figure 3.16, sensitivity is maximum at axial center and decreases towards the edges.

Table 3.17 shows the sensitivity at the center of the scanner and the average sensitivity over the entire axial FoV for both geometries of the system. The sensitivity at the centre of the scanner for cuboid crystals was found to be 2.29% and for the tapered crystals was found

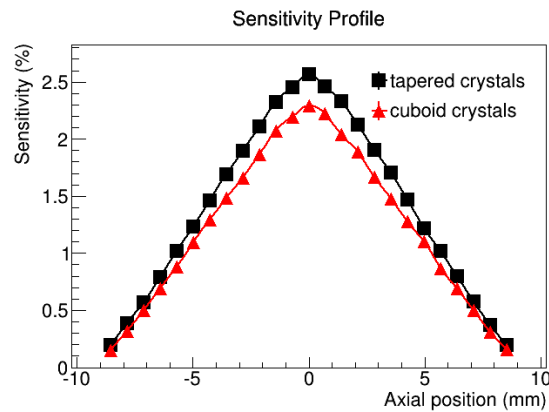


Figure 3.16 Axial sensitivity profile at radial center for scanners based on tapered and cuboid crystals

to be 2.56%, an increase of 11.79% was achieved. The average sensitivity over the entire axial FoV for the scanner with cuboid crystals was 1.23% and 1.39% for tapered crystals. An increase of 13.63% on the average sensitivity was achieved.

Geometrical efficiency taking into account the solid angle covered by the inner surface of the crystals that composed the scanners is the same for both configurations. However, the volume of the gaps between contiguous crystals is significantly higher for the cuboid geometry. The scanner based on tapered crystals can be seen as if the intermodule wedge shape gaps in cuboid configuration were filled with sensitive scintillator material producing an increase of intrinsic efficiency; thus, and increase of sensitivity. The scanner composed of tapered crystals has 15.08% more volume of scintillator material than the one composed of cuboid crystals, as expected this increase of sensitive material is in agreement with a rough estimation of the increase in sensitivity.

Table 3.17 Sensitivity of complete axial FoV and peak detection efficiency.

System	Energy window (keV)	Axial length (cm)	Total sensitivity (%)	Peak detection efficiency (%)
cuboid	450-700	1.78	1.23	2.29
tapered	450-700	1.78	1.39	2.56

### 3.4.3.2 Sensitivity Map

Another possible way to characterize sensitivity is to obtain the sensitivity map. The value of a pixel of the sensitivity map is defined as the probability of detecting an annihilation event emitted from that pixel by any detector pair of the scanner. The sensitivity has been obtained

through Monte Carlo simulations. To this end, a homogeneous cylinder source filled with an activity of 1 MBq (approximately  $27\mu\text{Ci}$ ) covering the entire FoV has been simulated. In this study, we focus on the main components of the sensitivity map, i.e. the geometrical coverage and intrinsic efficiency. According to this, 511 keV back-to-back gammas have been simulated ignoring positron range and acollinearity. Neither intrinsic activity of the Lutetium nor the generation of optical photons within the crystal were included in the simulations. Optical photons are important when the distribution of the light in the SiPM generated by a detected gamma-ray is important. For counting the number of detected gamma-rays, though, that degree of detail in the simulations is unnecessary and highly increases the computational time.

Following the definition, the sensitivity map was generated by recording the emission positions of the events detected as true coincidences from the information of the MC simulation. The value of each voxel of the sensitivity image corresponds to the fraction of the detected true coincidence counts emitted within that voxel by the expected annihilation events within that voxel taking into account the volume of the voxel and the density of the simulated activity. The FoV is discretized in voxels of  $2 \times 2 \times 0.712 \text{ mm}^3$  so that the axial sensitivity has the same sampling in both figures of merit.

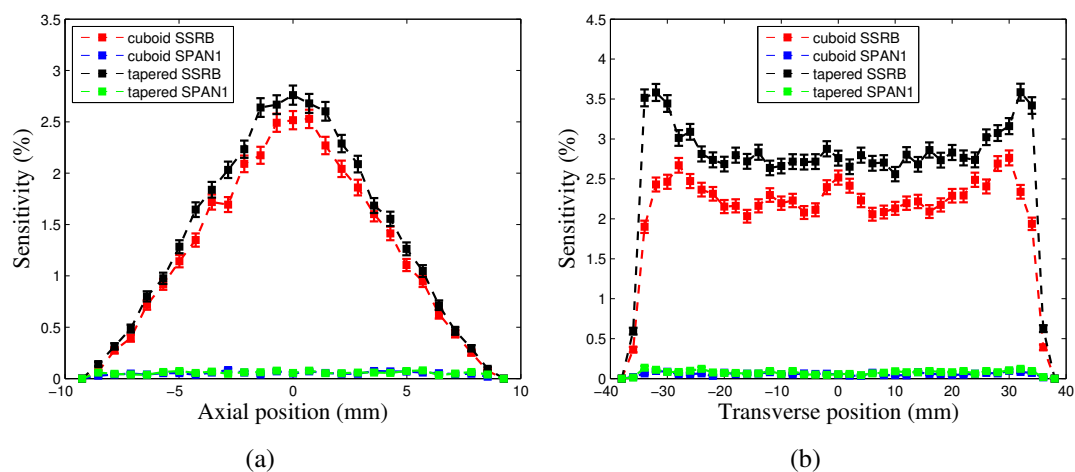


Figure 3.17 Profiles in (a) axial and (b) transverse direction through the centre of the of the sensitivity map discretized in voxels of  $2 \times 2 \times 0.712 \text{ mm}^3$  for SSRB and SPAN1 axial rebinning policies and for both crystal geometries.

Axial profiles and transverse profiles through the centre of the sensitivity image were generated to compare the sensitivity for both geometries and axial rebinning policies. Figure 3.17(a) shows the axial profile through the Z-axis of symmetry and figure 3.17(b) shows the transverse profiles through the centre of the image. The axial profile shape was uniform

for SPAN1 and had a peak at the center of the axial FoV for SSRB having the same shape as the axial sensitivity profile obtained following NEMA standard. The axial sensitivity profiles, with a maximum value at the center, are in accordance with geometric considerations based on the number of LoRs inside the FoV when the point source is stepped in the axial direction and SSRB policy is applied. However, if only direct LoRs are considered, the axial sensitivity profile is approximately uniform. The sensitivity value for the peak in cuboid geometry is  $(2.53 \pm 0.09)\%$  while the peak value for tapered geometry is  $(2.76 \pm 0.09)\%$ . The values obtained from the sensitivity map are greater than the values obtained from the axial sensitivity study following NEMA standard. Preliminary studies, strongly suggest that the difference is due to the plastic cube that surrounds the source in section 3.4.3.1. It is present to ensure the annihilation of the positrons but it also attenuates the emitted gamma-rays. If a back-to-back source of 511 keV is employed inside the plastic cube, the value of the peak for cuboid crystals is 2.35%. This value increases to 2.62% when the plastic cube is removed; which is in closer agreement with the value obtained for the sensitivity map,  $(2.53 \pm 0.09)\%$ . Differences between both configurations can be appreciated in transverse profiles shown in figure 3.17(b). Using SPAN1 the sensitivity was reduced by 97% compared to SSRB policy.

The value of the pixels of the sensitivity image increases towards the edge of the FoV, the increment of the value of the edges is greater for tapered geometry. Besides, irregular structures can be seen in the profiles near the centre for cuboid geometry.

In order to study more in detail these structures, the transverse sensitivity image at the centre of the scanner has been obtained.

The sensitivity image from Monte Carlo simulation of the transverse central slice section of 0.712 mm thickness and 1 mm  $\times$  1 mm voxel size for both systems and different axial rebinning policies (SSRB and SPAN1) are shown in figure 3.18. Figure 3.18(a) shows the transverse sensitivity image for tapered geometry, figure 3.18(b) for cuboid geometry and figure 3.18(c) the subtraction of the transverse sensitivity image for tapered and cuboid geometry all of them using SSRB policy. The same data were processed using SPAN1 axial rebinning policy. The transverse sensitivity image for tapered crystals is shown in figure 3.18(d), for cuboid crystals in figure 3.18(e) and the subtraction is shown in figure 3.18(f) using SPAN1 policy. Using SSRB policy, 12 loop structures connected to a concentric circumference can be seen in the transverse sensitivity image using cuboid geometry (figure 3.18(b)). These structures are produced by the gaps between the 12 contiguous detectors that compose the scanner based on cuboid crystals. However, the transverse sensitivity image for scanners based on tapered crystal is barely uniform in the centre of the FoV due to the tighter packing of the 16 detectors that compose the scanner. As expected from geometrical arguments, the transversal profiles of the sensitivity map have higher values towards the edges of the

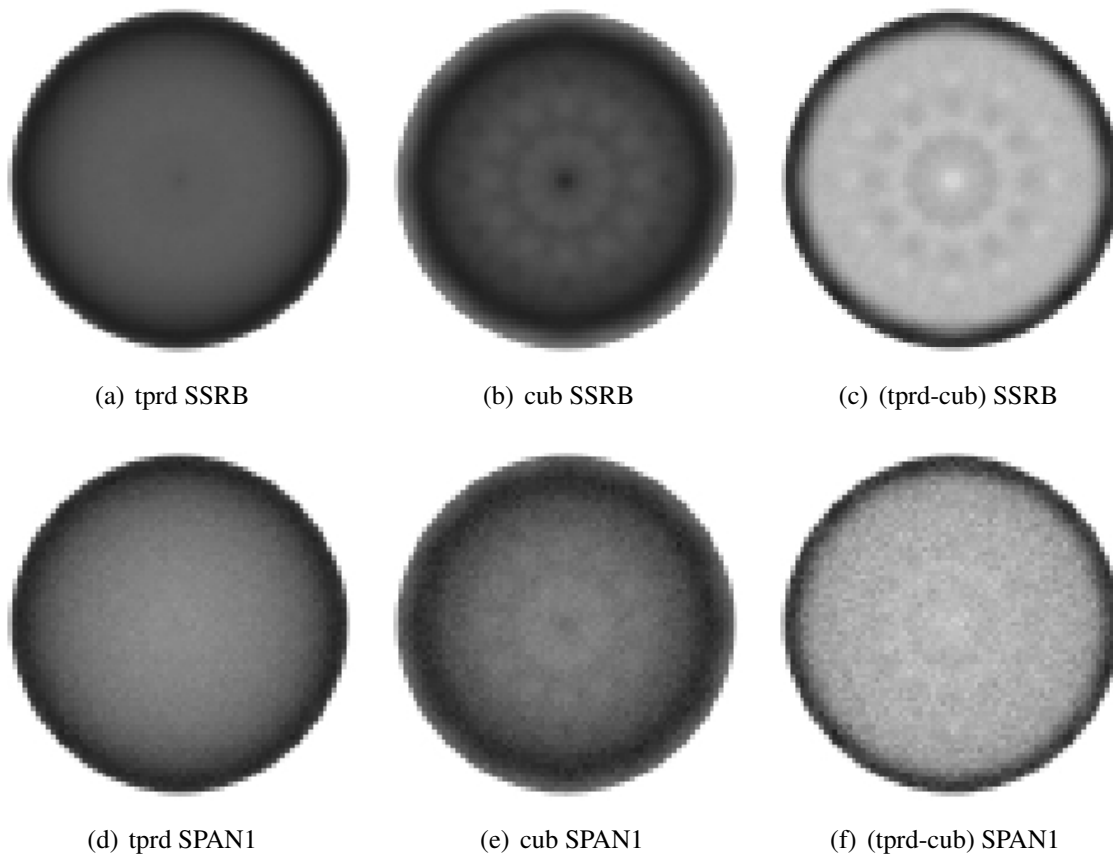


Figure 3.18 Sensitivity map based on Monte Carlo simulation of an homogeneous cylinder covering the entire FoV. (a) and (b) show the sensitivity map using SSRB policy for cuboid and tapered geometry respectively and (c) shows the subtraction of transverse sensitivity map for tapered and cuboid geometry. (d) and (e) show the sensitivity map using SPAN1 policy and (f) shows the subtraction.

FOV, see for instance [92], since gamma-rays emitted from the edges of the FoV have higher probability of detection due to the larger crystal intersection length of the LoRs that are not perpendicular to the crystal front side. Using SPAN1 policy the same 12 loop structures can be appreciated for cuboid crystals while for tapered crystals the image is barely uniform in the centre of the FoV. The data analysed with both axial rebinning policies are the same. Therefore, 97% less coincidences were analysed using SPAN1 policy leading to noisier images.

Figure 3.19 shows the sensitivity map for the cuboid and tapered geometry applying SSRB policy and different thresholds to the color scale of the image in order to visualize better the artefacts of the image. Applying a threshold value of 1.8% to the white/black linear color scale, which means that the pixels with a value below 1.8% are represented with white



color, the artefacts for the scanner based on cuboid crystals are more noticeable while for the scanner based on tapered crystal the image is still barely uniform in the centre.

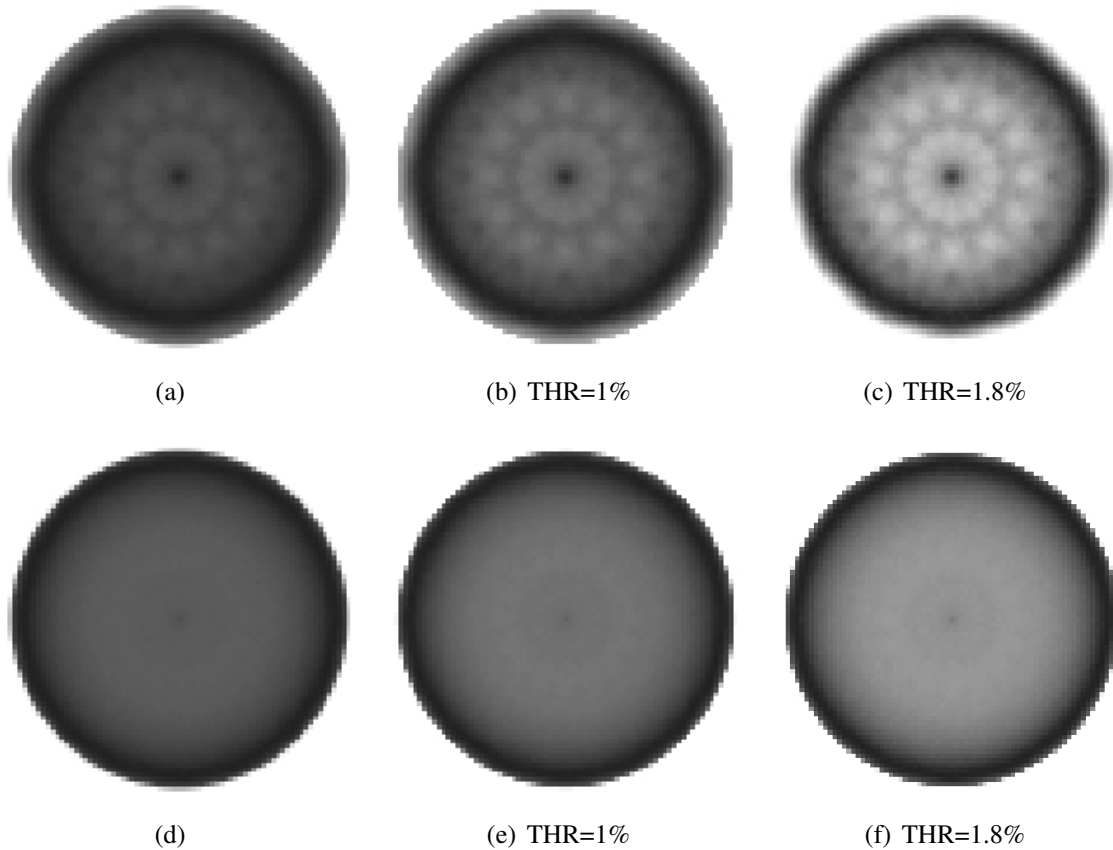


Figure 3.19 Sensitivity map based on Monte Carlo simulation of an homogeneous cylinder covering the entire FoV using SSRB (a-c) for cuboid geometry and (d-f) for tapered geometry applying different thresholds to the image so that all the pixels with a value below the threshold are represented by white color. (a,d) show the sensitivity map without any threshold, (b,e) with a threshold value of 1% and (c,f) with a threshold value of 1.8%

### 3.4.3.3 Image Reconstruction of Homogeneous regions

Finally, the sensitivity of the scanners has been studied and compared from the point of view of the reconstruction. The sensitivity estimation of the system was pursued by the reconstruction of homogeneous regions without sensitivity compensation in the image reconstruction algorithm. To this end, a uniform cylinder of 30 mm radius and height equal to the length of the axial FoV, filled with an activity of 1 MBq of 511 keV back-to-back gammas was simulated. The simulations include optical photons to reconstruct the image using the

LoRs obtained from the interaction position determination method (VS0) as well as the LoRs obtained from the ground-truth.

Table 3.18 Central slice of the reconstructed images of the homogeneous cylinder using ground-truth information for both geometries: cuboid crystals (first column) and tapered crystals (second column). First row shows the reconstructed images using FBP and second row using ML-EM and 5 iterations.

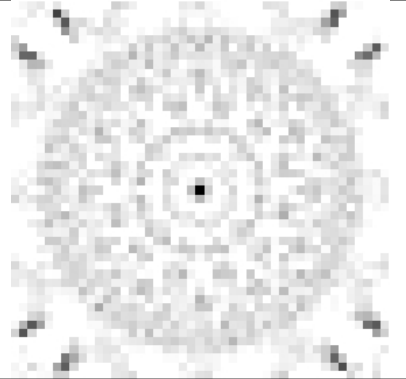
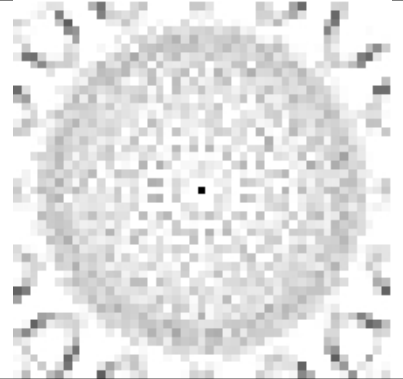
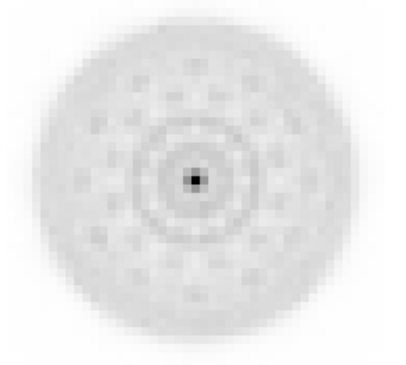
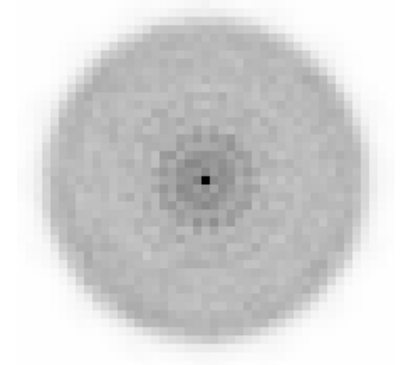
Ground-truth		
	cuboid	tapered
FBP		
ML-EM		

Images have been reconstructed with FBP and ML-EM algorithm using a voxel size of  $1.5 \times 1.5 \times 3.0 \text{ mm}^3$ . FBP is expected to be more sensitive to the inhomogeneities of the sensitivity due to the gaps. On the other hand, ML-EM images could be compensated by sensitivity. A more homogeneous sensitivity map, should allow us to better recover homogeneous regions. To investigate this, only true coincidences were analysed.

Table 3.18 shows the central slice of the reconstructed images using FBP (first row) and ML-EM with 5 iterations (second row) using ground-truth information for the interaction position for both geometries: cuboid crystals (first column) and tapered crystals (second column). The structures of the sensitivity map studied in section 3.4.3.2 are reproduced for both methods and both geometries using ground-truth. For the scanner based on cuboid crystals, the 12 loop structure studied in the sensitivity map is clearly visible while for tapered

geometry the recovered image is barely uniform due to the smaller gaps between detectors. The images were reconstructed with the same simulated time for both methods. However, while the statistical level is enough for ML-EM to produce an acceptable image, it is still too low for FBP.

Table 3.19 Central slice of the reconstructed images of the homogeneous cylinder using position determination method for both geometries: cuboid crystals (first column) and tapered crystals (second column). First row shows the reconstructed images using FBP and second row using ML-EM and 5 iterations.

Estimated interaction position		
	cuboid	tapered
FBP		
ML-EM		

The same simulated data have been reconstructed using the position determination algorithm to estimate the LoRs. Table 3.19 shows the central slice of the reconstructed images using FBP (first row) and ML-EM with 5 iterations (second row) for both geometries: cuboid crystals (first column) and tapered crystals (second column). In all the reconstructed images, artefacts with the shape of concentric rings can be identified as the result of the artefacts produced by the position determination method (VS0) and the gaps between detector heads. The artefacts produced by the position determination method modify significantly the structures of the sensitivity produced by the gaps. However, both artefacts share the same symmetries making difficult to disentangle their contribution. In any case, the artefacts are

again more visible for cuboid scanner than for tapered scanner when interaction position is estimated.

Only SSRB policy was employed due to the low number of coincidences accepted in SPAN1 policy resulting in images with poorer statistics and the computational cost of the simulations with optical photons.

The scanner based on tapered crystals produces a better recovery of homogeneous regions than the scanner based on cuboid crystals when there is no sensitivity correction employing FBP and ML-EM algorithm.

### 3.5 Discussion

The two main parameters to maximize in the performance of PET scanners are the sensitivity and spatial resolution. A scanner based on tapered crystals has been simulated with the same inner ring and dimensions as a scanner based on cuboid crystals to increase the sensitivity by a tighter packing of the detectors, “filling” the wedge shape gaps of the cuboid scanner with scintillator material. In order to compare the performance of both scanners and evaluate the enhancement of sensitivity, detailed Monte Carlo simulations have been performed. The characterization of the performance of the scanners has been done following NEMA standard protocol which recommends to employ FBP algorithm for image reconstruction.

Since the accuracy in the estimation of the interaction position in continuous crystal affects significantly the quality of the reconstructed image, the interaction position performance has been studied for both geometries in a full ring configuration. The employed method, VS0, has shown similarly good performance for both geometries. The performance of VS0 model in which internal reflections are not modelled seems to be closer to the ground-truth than the performance of VS1 model where specular reflections are modelled. This is in agreement with previous studies of position determination in which VS0 model showed more accurate results. The performance of the interaction position estimation method for both scanners presents two different patterns. On the one hand, an important percentage of the events that interact close to the entrance of the crystal are biased and located just in the entrance surface of the crystal. On the other hand, the method tends to accumulate more events in regions close to the corners of the crystals for both geometries which produces clearly visible artefacts in the image reconstruction using FBP. The artefacts produced by the mispositioning of the method share the same symmetries that the artefacts produced by the gaps making difficult to disentangle their contribution in the reconstructed image.

The spatial resolution of the reconstructed image is degraded significantly by the interaction position estimation with respect to ground truth. The spatial resolution performance

evaluation obtained following NEMA standard is similar for both scanners. However, for cuboid geometry the impact of the artefacts is more important than for tapered geometry producing more unstable resolution values across the transverse FoV and more blurred images. Our results show that, despite the difficulties introduced by the slanted faces of the tapered crystals, the spatial resolution is at least as good as for cuboid geometry.

Another aspect of the performance of the scanner that has been evaluated is the SF and count rates performance. The SF and the shape of the count rate curves is similar for both scanners. For both phantoms the activity at which NECR and True peak occurs is smaller and the peak value is greater for tapered crystals than for cuboid crystals. For mouse-like phantom the activity at which NECR occurs is 7.4% smaller and the NECR peak value is 6.2% greater for tapered crystals than for cuboid crystals and for rat-like phantom the activity at which NECR peak occurs is 9.4% smaller and the peak value is 8.1% greater for tapered crystals. Therefore, for tapered configuration the estimated quality of the measured data is better than for cuboid configuration and the optimum conditions occur at lower activities.

Finally, sensitivity which is the most important aspect of the comparison due to the expected significant increase for tapered scanner, has been studied through three different figures of merit. Firstly, the axial sensitivity following NEMA standard has been evaluated for both scanners. An average sensitivity gain over the entire axial FoV of 13.63% and an increase of 11.79% in the sensitivity at the centre of the scanner were achieved by using transaxial tapered crystals which is in the same order of the increment of the scintillator material in the scanner (15.08%). Sensitivity has also been studied through the sensitivity map obtained from the Monte Carlo information. In the scanner based on cuboid crystals, loop-like structures due to the gaps between detector modules are clearly visible in the transverse plane of the sensitivity map, while for the scanner based on tapered crystals these artefacts are barely visible due to the tighter packing of the detectors in the ring. A higher degree of homogeneity was obtained in the sensitivity map with the scanner based on tapered crystals. Finally, the evaluation of the sensitivity was completed with the study of the recovery of homogeneous regions. The scanner based on tapered crystals produces a better recovery of homogeneous regions than the scanner based on cuboid crystals either employing FBP algorithm or ML-EM without sensitivity compensation. The same variations/structures observed in the sensitivity map for cuboid configuration were reproduced in the reconstruction of a homogeneous cylinder when ground-truth was employed for interaction position. Whereas, when interaction position was estimated using VS0, the artefacts coming from the position determination method are added to those structures.

### **3.6 Conclusions**

In summary, the performance of a scanner based on tapered crystals has been studied and compared with the performance of a scanner based on cuboid crystals. An average sensitivity gain over the entire axial FoV of 13.63% has been obtained with tapered geometry, while similar performance of the spatial resolution has been proven. For both phantoms the activity at which NECR and True peak occurs is smaller and the peak value is greater for tapered crystals than for cuboid crystals. Moreover, a higher degree of homogeneity was obtained in the sensitivity map due to the tighter packing of the crystals, which reduces the gaps and results in a better recovery of homogeneous regions than for cuboid configuration.

# Conclusions

Continuous crystals have shown to be an interesting alternative to increase sensitivity without degrading the spatial resolution. The main challenge in the use of continuous crystals is the estimation of the 3D interaction position of the gamma-rays within the crystal; hence, accurate position estimation methods are needed.

One of the goals of this thesis is to develop a high resolution detector head based on white painted crystals coupled to silicon photomultipliers. To this end, the analytical model of the light distribution developed by [13] to estimate the interaction position in continuous crystals has been modified and further studied in detail applying it to both experimental and simulated data. While the original model takes into account specular reflections on the sides of the crystal with the same weight as the direct light, we have shown that if the behaviour of the reflections is not purely specular it is better to limit the influence of the internal reflections or even eliminate such reflections in the model. The model has been adapted to our data to obtain the most accurate positioning and the best spatial resolution leaving the physical implications and necessary modifications of the model for future studies. The model for the reflections should be revised and modified for a non specular behaviour.

For our detector head based on white painted crystals, the estimation of the interaction position when reflections are not included was more accurate. An average transversal resolution over the detector surface (centre and edges) of 0.9 mm FWHM for 5 mm thick white crystal and 1.2 mm FWHM for 10 mm thick white crystal were measured and a DoI resolution of 2 mm FWHM. The results obtained with the 10 mm thick crystal are very good when compared with other systems even considering the unfavourable aspect ratio (AR) of our detector. The validated simulation, developed to characterize the positioning in the detector head, allow us to explore different characteristics of the detectors and showed that duplicating the value of the AR of our detector, DoI accuracy improves significantly.

Making use of the experience gained during the characterization of the detector head, detailed simulations of a full ring geometry were developed to study the imaging capability of the detector head. Since the sensitivity is one of the main parameters to maximize in the performance of a PET scanner, tapered crystals have been investigated as an alternative

geometry to the commonly used cuboid crystals to increase the solid angle coverage of the scanner by reducing the wedge-shaped gaps between contiguous crystals. The performance of both scanners has been assessed following NEMA standard and compared. Since enhancing sensitivity is the main goal when using tapered geometry, it was analysed in more detail through two additional figures of merit. Besides the axial sensitivity measurement specified by NEMA, a sensitivity map and the reconstruction of homogeneous regions without sensitivity compensation were investigated. An average sensitivity gain over the entire axial FoV of 13.63% has been obtained with tapered geometry, while similar performance of the spatial resolution has been proven. For both phantoms the activity at which NECR and True peak occur is smaller and the peak value is greater for tapered crystals than for cuboid crystals. Moreover, a higher degree of homogeneity was obtained in the sensitivity map due to the tighter packing of the crystals which reduce the gaps and results in a better recovery of homogeneous regions than for cuboid configuration.

In conclusion, this thesis has shown a high resolution performance of a detector head based on continuous crystal coupled to SiPM using an analytical model for the light distribution. The imaging capability of this detector head has been proven in a preliminary prototype based on two rotating heads. In order to enhance the sensitivity in the full ring configuration by increasing the solid angle coverage, the performance of a simulated scanner based on tapered crystals has been studied and compared to a scanner based on cuboid crystals with the same dimensions. The results have shown a significant increase of sensitivity and a better recovery of homogeneous regions due to the tighter packing of the detector heads while maintaining spatial resolution.

The use of continuous crystals is gaining interest, and they are already being employed in commercial systems such as Albira (Oncovision/Bruker) or  $\beta$ -cube (Molecubes). The good results obtained in this work imply a significant step forward towards the enhancement of the performance of continuous crystals for PET applications.



# Resumen

## Introducción

La tomografía por emisión de positrones (PET, por sus siglas en inglés) es una técnica de Medicina Nuclear que permite obtener de manera no invasiva imágenes funcionales “*in vivo*” marcando un compuesto orgánico con un emisor de positrones. Los tomógrafos PET requieren un alta resolución espacial y sensibilidad para estimar con precisión la distribución del radiotrazador en el animal.

Frente a los bloques pixelados comúnmente utilizados en PET, los detectores que consisten en la combinación de cristales continuos acoplados a fotodetectores segmentados pueden ofrecer una mayor eficiencia y una alta resolución espacial. Esta última depende de la precisión de los algoritmos de determinación de la posición de interacción de los fotones en el cristal. Una de las ventajas de los cristales continuos es que la resolución intrínseca ya no está limitada al tamaño del cristal. Por otro lado, a partir de la distribución de la luz de cada evento detectado se puede estimar la profundidad de interacción reduciendo así los errores de paralaje mejorando la resolución espacial del sistema.

En esta tesis se ha investigado el uso de detectores compuestos por cristales continuos acoplados a fotomultiplicadores de silicio (SiPMs), un tipo de detector segmentado, con el objetivo de aumentar la sensibilidad respecto a los cristales pixelados usados más comúnmente en los escáneres comerciales. Para ello, en primer lugar se ha caracterizado el comportamiento de una cabeza detectora basada en cristales continuos acoplada a SiPMs en el laboratorio para evaluar el comportamiento de este tipo de detector en un sistema de imagen. Debido a que el principal inconveniente del uso de cristales continuos es la determinación de la posición de interacción en el cristal, la caracterización ha incluido un estudio detallado del posicionamiento de dicha interacción. El método para la determinación de la posición que se ha investigado en este trabajo, se basa en un modelo analítico para la distribución de la luz que tiene en cuenta las reflexiones en las paredes del cristal. Para ahondar en el comportamiento del modelo, además de aplicarlo a datos experimentales, se han desarrollado simulaciones de la cabeza detectora que han sido validadas con datos experimentales

para estudiar la respuesta del método en distintas situaciones y con geometrías alternativas. Basándonos en estas simulaciones y en el conocimiento adquirido en la caracterización de la cabeza detectora, se han desarrollado simulaciones de anillo completo. Además del escáner convencional basado en cristales cuboides, se ha implementado un anillo basado en cristales trapezoidales con el mismo radio interno con el objetivo de aumentar la sensibilidad del escáner. La configuración basada en cristales trapezoidales se puede entender como un anillo de cristales cuboides en el que en los huecos en forma de cuña que existen entre detectores contiguos hay también material centelleador. La caracterización de ambos escáneres se ha llevado a cabo a partir del protocolo estandarizado NEMA. Se ha puesto especial interés en caracterizar la sensibilidad. Es por ello que se han utilizado figuras de mérito adicionales para caracterizar las diferencias entre las dos configuraciones.

## Caracterización de la cabeza detectora

En primer lugar, se ha realizado una caracterización de la cabeza detectora desarrollada basada en cristales centelleadores (de LYSO) continuos acoplados a SiPMs. El cristal empleado tiene una sección de  $12 \times 12 \text{ mm}^2$  y se han estudiado dos grosores distintos, 5 y 10 mm. Los cristales empleados son cristales de Hilger Crystals pulidos y pintados de blanco en cinco de sus caras, todas menos la que se acopla al fotodetector. Además, se han puesto a prueba cristales de Proteus con reflector especular. La figura R.1(a) muestra en la parte superior los cristales centelleadores pintados de blanco y en la inferior aquellos con reflector especular. Salvo que se especifique lo contrario, todas las medidas mostradas se han realizado con los cristales pintados de blanco. El fotodetector usado es una matriz de SiPMs de AdvanSiD (modelo ASD-RGB1.5S-P-8x8A) compuesta por  $8 \times 8$  píxeles en un sustrato monolítico, véase la figura R.1(b). La figura R.1(c) muestra el cristal centelleador pintado de blanco de 5 mm de grosor acoplado al SiPM.

Para realizar las medidas con los detectores, en primer lugar, se han escogido las condiciones de trabajo. Se ha caracterizado el valor de los pedestales y el valor del umbral para la adquisición de datos. A continuación, se ha caracterizado la respuesta del detector en términos de resolución energética y resolución temporal. Debido a que la mayor dificultad en el uso de esta tecnología es el correcto posicionamiento de la interacción de los fotones en el cristal centelleador, la caracterización se ha centrado principalmente en estudios de posicionamiento.

Para realizar los estudios de posicionamiento, se ha empleado una fuente de  $^{22}\text{Na}$  colimada electrónicamente para limitar la posición de la interacción de los fotones a una posición conocida. Los datos se han tomado en cuatro posiciones representativas de uno de los

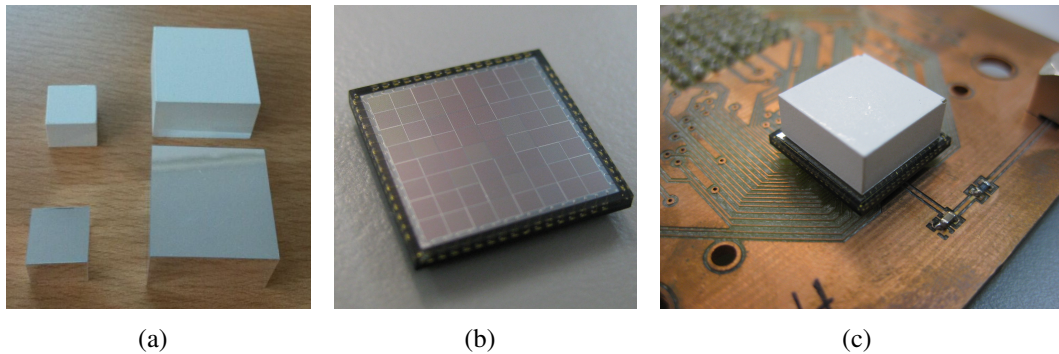


Figura R.1 Detector empleado en las mediada. Se muestra en (a) en la parte inferior de la imagen los cristales con reflector especular y en la parte superior los cristales pintados de blanco, en (b) la matriz de SiPMs y en (c) el cristal centelleador pintado de blanco acoplado al SiPM.

cuadrantes del detector con el objetivo de caracterizar la respuesta en toda su superficie. Las posiciones nominales escogidas son las siguientes: una cerca del centro (0.75,0.75) mm, otra cerca de la esquina (3.75,3.75) mm y dos posiciones intermedias (2.25,2.25) mm y (3.75,0.75) mm.

Además, para tener una estimación de la resolución a lo largo de la profundidad del cristal, la fuente colimada se ha colocado de manera que los fotones detectados en coincidencia incidan con una inclinación de  $45^\circ$ . De este modo, idealmente la profundidad de interacción tiene el mismo valor que el desplazamiento en el eje Y desde la posición de entrada del haz. La figura R.2 muestra un esquema de la geometría del dispositivo para los estudios de determinación de la posición. La figura R.2(a) muestra el dispositivo orientado para la toma de medidas de resolución transversal, mientras que la figura R.2(b) muestra la configuración del dispositivo para las medidas de resolución en DoI.

El diámetro del haz en la entrada del cristal es de 0.21 mm para medidas de posicionamiento transversal, mientras que para las medidas de DoI es de 0.42 mm. En ninguno de los resultados mostrados se ha sustraído el valor del diámetro del haz.

Se han realizado simulaciones Monte Carlo de la cabeza detectora, con un haz colimado de fotones mono-energéticos de 511 keV con el mismo diámetro en la entrada del cristal que en las medidas experimentales, situando la fuente en las cuatro posiciones de referencia para los dos grosores de cristal estudiados. El valor de los parámetros (reflectividad, rugosidad de la superficie del cristal, características del reflector, grosor de la grasa óptica,...) cuyo valor real no se dispone, se ha seleccionado en las simulaciones de tal manera que reproduzcan el conjunto de las medidas realizadas en lugar de apuntar a una reproducción perfecta con distintos parámetros para cada una de las medidas. Debido a que el método de posicionamiento

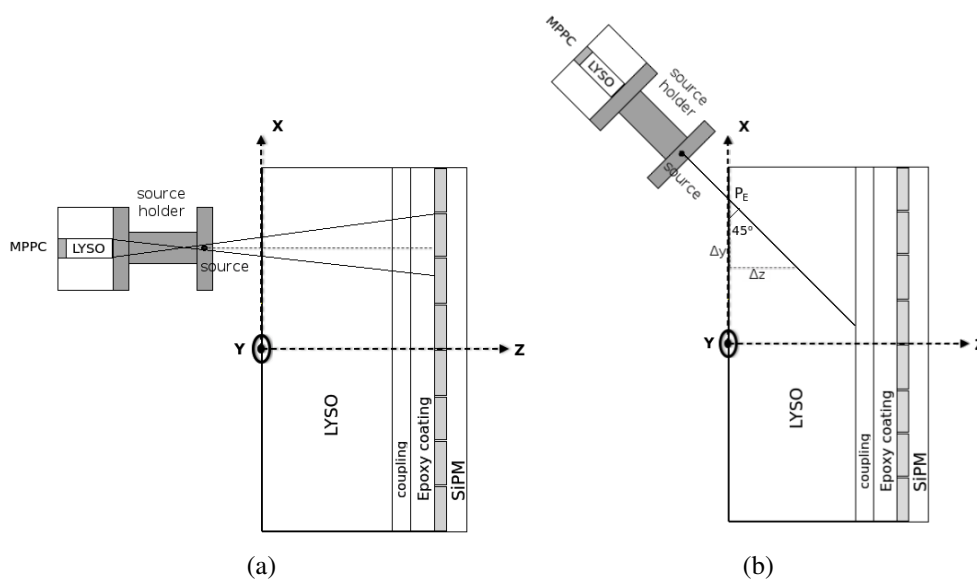


Figura R.2 Geometría (no a escala) del dispositivo experimental para la determinación de la posición. A la izquierda se muestra la configuración para las medidas de resolución transversal y a la derecha la de resolución en DoI.

se basa en la distribución de luz medida en el fotodetector, la figura de mérito utilizada para la validación de las simulaciones es el porcentaje de la carga total media medida en cada uno de los SiPMs.

Se han realizado diversos estudios previos a las medidas para la resolución experimental con el objetivo de obtener las condiciones óptimas para realizar las medidas de determinación de la posición y entender el modelo de la distribución de la luz empleado en mayor profundidad. Para ello, en primer lugar, se ha realizado un estudio para obtener el rango de trabajo óptimo para la distancia entre el colimador y el cristal centelleador. Por otro lado se han estudiado variaciones del modelo para entenderlo en mayor profundidad y obtener los mejores resultados posibles con los datos experimentales.

El algoritmo empleado para la determinación de la posición se basa en un modelo analítico de la propagación de la luz en el cristal centelleador, [13]. El modelo tiene en cuenta la luz que llega a cada pixel directamente desde la fuente de luz (punto en el que se generan los fotones ópticos), y a través de las reflexiones en las paredes del cristal. Las reflexiones internas se modelan a través de la creación de fuentes virtuales que se sitúan en posiciones simétricas respecto cada una de las paredes del cristal. En el modelo original se considera el mismo valor para el peso de las contribuciones de la fuente directa y las fuentes virtuales. La estimación de la luz directa que llega a cada píxel se basa en el ángulo sólido subtendido por

éste desde la fuente de luz y la contribución de las reflexiones internas se basa en el ángulo sólido subtendido por el pixel desde la posición de la fuente virtual.

En este trabajo se han investigado modificaciones en el modelo considerando separadamente la contribución de ambas fuentes usando distintos parámetros. La siguiente ecuación describe el número de fotones ópticos detectados en cada píxel a la que se le ha añadido un parámetro adicional respecto al modelo original para considerar el peso de las fuentes virtuales ( $A_{0VS}$ ):

$$np_i = C_{est} + A_0\Omega(x,y,z) + A_{0VS} \sum_j \Omega(x_j,y_j,z_j), \quad (\text{R.10})$$

donde  $C_{est}$  es una constante que representa la contribución de los fotones ópticos reflejados en el reflector difuso del cristal,  $A_0$  representa el número total de fotones ópticos producidos por la fuente de luz y  $\Omega(x,y,z)$  el ángulo sólido subtendido por el pixel  $i$  desde la fuente de luz localizada en  $(x,y,z)$ . Los últimos dos términos de la ecuación ( $A_0\Omega(x,y,z)$  y  $A_{0VS} \sum_j \Omega(x_j,y_j,z_j)$ ), representan respectivamente el número de fotones ópticos que alcanzan el pixel  $i$  de manera directa y tras ser reflejados en las caras del cristal centelleador que no están acopladas al SiPM. Se han investigado las siguiente opciones:

- **modelo VS0:** cuando no se consideran fuentes virtuales  $A_{0VS}=0$ .
- **modelo VS1:** cuando el peso de la luz directa y de las reflexiones internas tiene el mismo valor  $A_0=A_{0VS}$  (modelo original).
- **modelo VS1 Independiente:** cuando ambos parámetros ( $A_0, A_{0VS}$ ) son determinados independientemente.
- **modelo VS1\* Independiente:** Además este modelo desecha aquellos eventos con un peso para la luz reflejada respecto a la luz directa mayor que un límite de aceptación (AL) definido,  $\frac{A_{0VS}}{A_0} \geq AL$ .

Los distintos modelos se han aplicado a simulaciones y a datos experimentales con diferentes tipos de reflectores, especulares y difusos, para una mejor comprensión de la respuesta de los modelos. Por otro lado, se ha estudiado la respuesta de los diferentes modelos aplicándolos a los datos experimentales con los cristales pintados de blanco. De los estudios realizados se concluye que la determinación de la posición para nuestro caso es más precisa cuando las reflexiones especulares no son contempladas (VS0). La mejor respuesta del modelo para las medidas con los datos se obtienen sin modelar las reflexiones (VS0) o modelándolas independientemente y descartando aquellos eventos con un peso para las reflexiones por encima de la mitad del peso de la luz directa (modelo VS1\* Independiente).

Sin embargo, este último desecha más del 48% de los eventos reconstruidos por lo que los datos se han reconstruido utilizando el modelo VS0.

Una vez fijado el modelo a utilizar, se ha estudiado la resolución espacial del detector a partir de las cuatro posiciones representativas para los cristales de 5 y 10 mm de grosor. La anchura a media altura, abreviada FWHM (del inglés Full Width at Half Maximum), ha sido obtenida ajustando mediante funciones Gaussianas y Lorentzianas los perfiles en torno a al máximo de la distribución de las posiciones de interacción reconstruidas (DPIR, en adelante) en las direcciones X e Y. La tabla R.1 muestra la resolución media en ambas direcciones de los 4 puntos representativos sobre las superficie del cristal para los cristales de 5 y 10 mm de grosor.

Tabla R.1 Resolución media de las cuatro posiciones representativas en las direcciones X e Y para el cristal de 5 y 10 mm de grosor.

mm	$\overline{FWHM}_x^{Gauss}$	$\overline{FWHM}_y^{Gauss}$	$\overline{FWHM}_x^{Lor}$	$\overline{FWHM}_y^{Lor}$
5 mm de grosor	1.06±0.03	1.01±0.03	0.85±0.06	0.89±0.06
10 mm de grosor	1.30±0.05	1.29±0.05	1.1±0.1	1.1±0.1

Los valores de FWHM obtenidos mediante ajustes a funciones Gaussianas son en torno a 1.0 mm y 1.3 mm para los cristales de 5 y 10 mm de grosor respectivamente. Los valores obtenidos mediante funciones Lorentzianas son ligeramente inferiores en torno a 0.9 y 1.1 mm respectivamente. La figura R.3 muestra los contornos a mitad de altura y a un décimo de altura de la DPIR para cada una de las cuatro posiciones de la fuente para el cristal de 5 y 10 mm de grosor.

Debido a la configuración del sistema de determinación de la posición, no hay una posible configuración que permita hacer incidir el haz lateralmente. Por lo tanto, la posición real de la DoI es desconocida. Una estimación de la DoI se ha obtenido mediante un comprobación de coherencia, utilizando la configuración descrita en la figura R.2(b). En esta configuración, los rayos gamma emitidos por la fuente colimada inciden con una inclinación de 45° respecto a la superficie del cristal de modo que el desplazamiento en el eje Y respecto a la posición de entrada idealmente es equivalente al valor de DoI. Siguiendo esta aproximación, la distribución del error de la DoI ha sido calculada como la diferencia entre la DoI y el desplazamiento transversal reconstruido ( $DoI - \Delta y$ ) para todos los eventos. La resolución de DoI ha sido definida como la FWHM de la distribución del error y el sesgo de la DoI como la media de la distribución del error ajustada mediante una función Gaussiana. Sin embargo,

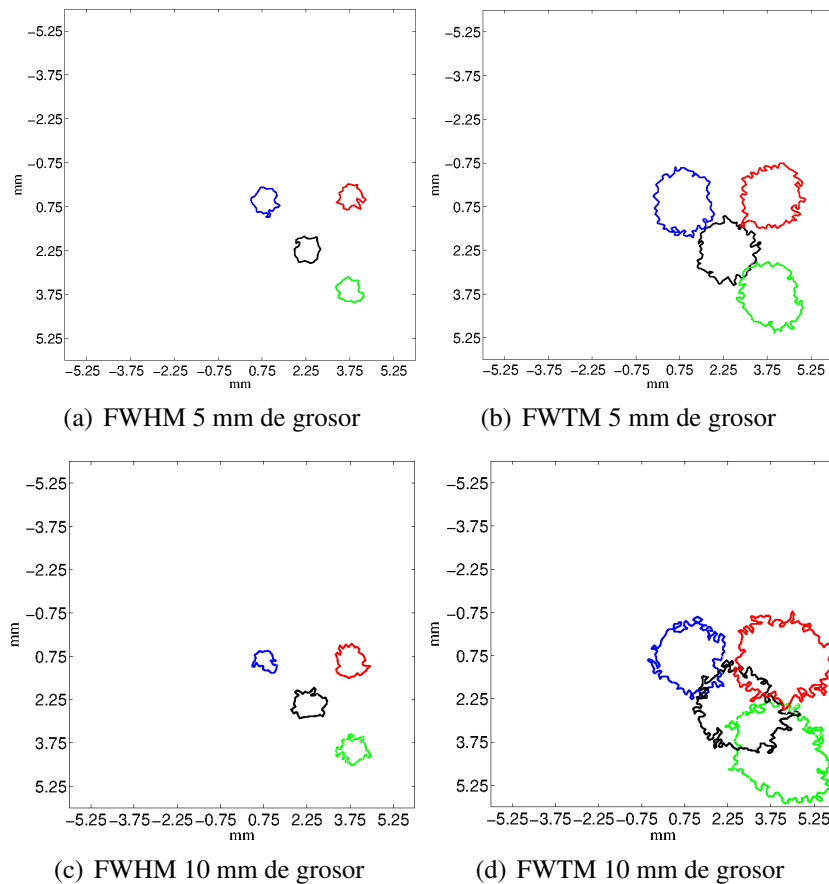


Figura R.3 Contornos a media altura y a un décimo de altura de las proyecciones X-Y de las DPIR para las cuatro posiciones de la fuente: (a,b) para el cristal de 5 mm de grosor y (c,d) para el cristal de 10 mm de grosor respectivamente.

las distribuciones del error de DoI a menudo no corresponden con una función Gaussiana por sus largas colas por lo que se han estimado también los valores de FWHM y FWTM mediante interpolación lineal.

La Figura R.4 muestra las proyecciones Y-Z (a,c) y la distribución del error de DoI (b,d) de la DPIR para los cristales de 5 y 10 mm de grosor respectivamente. La FWHM de la distribución de error para el cristal de 5 mm es  $(2.12 \pm 0.05)$  mm mientras que para el cristal de 10 mm de grosor es  $(2.19 \pm 0.05)$  mm. Los valores de FWHM y FWTM estimados mediante interpolación lineal son 2.0 y 5.3 mm respectivamente para el cristal de 5 mm de grosor y 2.3 y 9.6 mm respectivamente par el cristal de 10 mm de grosor. Sin embargo, para el cristal de 10 mm de grosor, la coordenada z correspondiente a la profundidad del cristal se estima correctamente sólo en la parte del cristal más cercana al fotodetector, como se puede observar en la figura R.4(c).

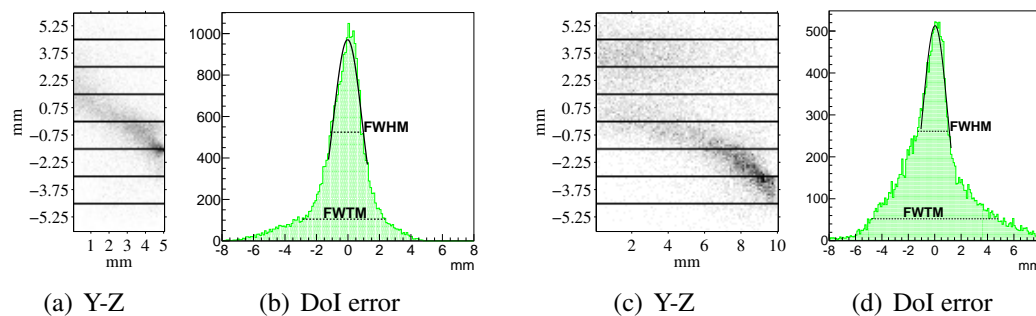


Figura R.4 (a,c) Proyección Y-Z de la DPIP y (b,d) la distribución del error de DoI para los cristales de 5 y 10 mm de grosor respectivamente. Los datos fueron adquiridos con una fuente colimada incidiendo con un ángulo de  $45^\circ$  sobre la superficie. El haz incide con la dirección creciente de la coordenada z.

La distribución de carga detectada de los eventos que interaccionan lejos del SiPM puede ser bastante uniforme en cristales gruesos e incluso perder la información de la posición de interacción debido a la influencia que tienen las reflexiones que sufren los fotones ópticos en las paredes del cristal. Este efecto se vuelve importante cuando la razón de la longitud del lado de la sección del cristal y su grosor, abreviada AR (del inglés Aspect Ratio), es menor de un determinado valor. Además del AR, el tipo de reflexiones (especulares o difusas) que sufren los fotones en las paredes del cristal es uno de los principales componentes que influyen en el impacto que tienen las reflexiones sobre la distribución de luz. Las simulaciones validadas se han empleado para estudiar la influencia de estos dos aspectos.

La influencia del AR se ha estudiado utilizando las simulaciones validadas de nuestro detector experimental con un reflector con una alta componente difusa (70%) y un AR de 1.20 y comparando los resultados obtenidos con simulaciones de dos detectores equivalentes pero con AR mayor, de 1.78 y 2.40, manteniendo el valor del grosor del cristal en 10 mm. Los resultados en cuanto a resolución de DoI son equivalentes para los tres casos. Sin embargo, el sesgo se reduce con el aumento del AR. La resolución se mantiene porque se determina a partir de la FWHM de la distribución total del error de DoI. Sin embargo, para el caso de los AR menores las distribuciones del error de DoI tienen largas colas que están relacionadas con el hecho de que los eventos que interaccionan cerca de la entrada del cristal, alejados del SiPM, se posicionan incorrectamente. Analizando el cristal por secciones de dos milímetros se observa que para el AR de 2.4 la DoI se recupera en toda la profundidad del cristal y el error de DoI se puede ajustar mediante una función Gaussiana en todas las secciones del cristal, mientras que para el AR de 1.20 solamente sucede esto en las dos primeras secciones.

La influencia del tipo de reflector del cristal se ha estudiado a partir de las simulaciones con un AR de 1.20 con diferentes reflectores: un reflector totalmente difuso, otro mixto



como el empleado en las simulaciones validadas con datos experimentales y otro totalmente especular. A partir de dichas simulaciones se observa que el sesgo y la resolución de DoI es mejor para el caso del reflector totalmente especular que para aquellos con componentes difusas. Por otro lado, las diferencias entre los dos reflectores difusos estudiados son mínimas.

## **Caracterización de un escáner de anillo completo basado en simulaciones**

En un escáner PET, como se ha comentado con anterioridad, los principales parámetros a maximizar son la resolución espacial y la sensibilidad. En la sección anterior se ha realizado una caracterización centrada principalmente en el posicionamiento de la interacción de los rayos gamma en el cristal de una cabeza detectora para PET basada en cristales continuos donde se realizaron simulaciones Monte Carlo del sistema que fueron validadas con datos experimentales. Estos estudios estaban principalmente dirigidos a obtener una buena resolución espacial. En esta sección, se hará uso de la experiencia y conocimientos adquiridos para realizar una simulación detallada de la geometría de un anillo completo. En este caso uno de nuestros principales objetivos es aumentar la sensibilidad por lo que se van a diseñar dos escáneres de las mismas dimensiones basados en dos geometrías de cristales distintas: cuboides y trapezoidales. La idea fundamental que nos lleva a considerar la construcción de un anillo basado en cristales trapezoidales es la de que haya también material centelleador en los huecos en forma de cuña que existen entre cristales contiguos en la configuración convencional basada en cristales cuboides. La caracterización de la respuesta de ambos escáneres se ha realizado basándose en el protocolo NEMA-NU para su posterior comparativa. Debido al aumento de sensibilidad esperado en la configuración trapezoidal, además de la figura de mérito recomendada por el protocolo NEMA para estudiar la sensibilidad axial, se han empleado varias figuras de mérito adicionales para evaluar las diferencias desde diferentes puntos de vista.

Para poder realizar la caracterización se ha evaluado el comportamiento del método de posicionamiento en la configuración de un anillo completo y su aplicación a cristales trapezoidales. Para reconstruir las imágenes se ha implementado el método FBP, tal y como requiere el NEMA, así como el método ML-EM.

### **Simulaciones**

Basándonos en las simulaciones de una cabeza detectora validadas en la primera parte de este trabajo, se han desarrollado simulaciones detalladas de anillo completo para ambas geo-

metrías (cristales cuboides y trapezoidales) en las que además se ha incluido la radiactividad natural del LYSO. Los anillos se han diseñado de manera que tengan el mismo diámetro interno de valor 70.85 mm, con una separación mínima entre cristales contiguos de 1.14 mm y un grosor de los cristales de 12.25 mm. Para ello, el escáner basado en cristales cuboides está formado por 12 cabezas detectoras mientras que el basado en cristales trapezoidales está formado por 16 cabezas detectoras. Las dimensiones del fotodetector simulado están basadas en la matriz de  $8 \times 8$  píxeles (TSV, Through Silicon Via, modelo S13361-2050AE-08) de Hamamatsu. El área activa de cada píxel es de  $2.0 \text{ mm} \times 2.0 \text{ mm}$  en un pitch de 2.2 mm siendo el tamaño de la matriz de  $17.8 \text{ mm} \times 17.8 \text{ mm}$ .

La señal obtenida de las simulaciones en cada cabeza detectora ha sido posprocesada para incluir las resoluciones temporales y energéticas y filtrar los eventos que quedan fuera de una ventana energética de aceptación de [450,700] keV antes de realizar las coincidencias temporales entre la señal de los detectores. Se ha aplicado una resolución energética del 12% a 511 keV. La resolución temporal en coincidencias (CRT, por sus siglas en inglés) se ha fijado a 1 ns FWHM y la ventana temporal de coincidencias (TCW, por sus siglas en inglés) se ha definido como  $TCW = 2CRT_{\sigma}$ , siendo su valor de 851 ps. La condición geométrica se ha aplicado de tal manera que solamente han sido procesadas aquellas coincidencias cuyas señales individuales hayan sido detectadas en sectores que estén separados por dos o más de ellos. Las coincidencias múltiples no han sido consideradas salvo por su contribución al tiempo muerto.

## Posicionamiento de la interacción en un escáner

En la sección correspondiente a la caracterización de la cabeza detectora el método de posicionamiento ha sido puesto a prueba tanto para medidas experimentales de determinación de la posición como para simulaciones validadas, mostrando una respuesta superior al modelo VS0 que no contempla las reflexiones en las paredes del cristal. Sin embargo, en este caso se quiere aplicar el método de posicionamiento a otra configuración en la que la forma de la distribución de carga será distinta, puesto que ahora en vez de tener una fuente colimada electrónicamente dirigida a una posición concreta de un detector, tendremos fuentes situadas en el campo de visión del escáner que emiten isotrópamente y son detectadas en coincidencia temporal entre los distintos detectores que forman el anillo. Debido a que el incorrecto posicionamiento de las líneas de respuesta (LoRs, por sus siglas en inglés) puede producir artefactos en la reconstrucción de la imagen, se ha estudiado la respuesta de los métodos VS0 (sin considerar fuentes virtuales) y VS1 (considerando las fuentes virtuales como en el modelo original) en esta nueva configuración.

Con el objetivo de tener una estimación del comportamiento de los modelos, se simula una fuente de tipo puntual en el centro del escáner que emite fotones de 511 keV en la misma dirección y sentidos opuestos. Las posiciones de interacción reconstruidas se analizan en el sistema de referencia local de los detectores. Analizando las distribuciones se aprecian dos tipos de acumulaciones en ambos modelos: una justo en la superficie de entrada del cristal y otra en regiones localizadas a lo largo de las cuatro esquinas laterales de los cristales. La primera acumulación corresponde a una importante proporción de eventos (en torno al 21%-32% dependiendo del método y la geometría del cristal) que en la realidad han interactuado cerca de la superficie de entrada del cristal produciendo una distribución de carga bastante uniforme que dificulta su posicionamiento, por ello son reconstruidos justo en la superficie de entrada del cristal. El segundo tipo de acumulaciones corresponde a regiones a lo largo de las cuatro esquinas laterales de los cristales que forman el anillo, lo que se traduce en acumulaciones incorrectas de LoRs en el campo de visión del escáner que puede causar artefactos en la imagen reconstruida.

Los resultados muestran que la respuesta del modelo VS0, que en el capítulo anterior había demostrado ser más precisa que la del modelo VS1, aquí también se aproxima más a la distribución real (ground-truth, singles) de las posiciones de interacción obtenidas a partir de la información de la simulación Monte Carlo. Por lo tanto, este modelo es el que se ha utilizado en la comparativa entre escáneres.

## Reconstrucción de la imagen

Se ha implementado el método de la Retro-proyección Filtrada, abreviado FBP (del inglés Filtered Back-Projection), en 2D para la reconstrucción de las imágenes siguiendo las indicaciones del protocolo NEMA. Se han empleado dos políticas de rebineado axial para la reconstrucción de los datos adquiridos en 3D: SPAN1, donde sólo las LoR directas (LoRs contenidas en una única sección 2D) son consideradas y Single Slice Rebinning (SSRB) [89] en el que todas las LoRs son tenidas en cuenta. Además, se ha implementado el método ML-EM que es más flexible a la hora de incorporar efectos como los huecos entre detectores contiguos en un escáner.

Con el objetivo de analizar los posibles artefactos producidos en la reconstrucción de la imagen, se han empleado simulaciones de fuentes de tipo puntual en el centro del escáner y a 15 mm del centro.

La imagen obtenida a partir del método FBP para la fuente en el centro del escáner muestra 24 líneas equidistantes desde el centro del escáner a los bordes del cristal, lo que indica que los artefactos predominantes en dicha imagen provienen de la incorrecta estimación de la posición de interacción que acumula los eventos a lo largo de los bordes

laterales del cristal. El efecto en la reconstrucción de la imagen producido por los huecos entre detectores comparte la misma simetría espacial que los artefactos producidos por el método de posicionamiento, por lo que es difícil distinguirlos.

Las imágenes reconstruidas con la fuente situada a 15 mm del centro muestran una ligera degradación en la resolución respecto a la fuente situada en el centro. Cuando la imagen se reconstruye a partir de las LoRs estimadas, los artefactos en la imagen son más prominentes que para el caso de la fuente centrada. Sin embargo, son más difíciles de identificar con los artefactos del posicionamiento de los eventos o con los gaps debido a las asimetrías.

La principal diferencia entre las imágenes obtenidas a partir de LoRs reconstruidas con ground-truth o a partir de la estimación del punto de interacción es la degradación de la resolución espacial de la imagen. En esta sección no se profundizará más en este aspecto, ya que la resolución espacial se estudiará en detalle como parte de la caracterización de los escáneres siguiendo el protocolo NEMA.

## **Caracterización de la respuesta de los escáneres: cúbico y trapezoidales**

Una vez estudiada la respuesta del método de posicionamiento en la configuración de anillo completo tanto para cristales cuboides como para trapezoidales y su influencia en la imagen reconstruida, tenemos las herramientas para proceder con la caracterización de los escáneres. Los escáneres se han caracterizado siguiendo el protocolo NEMA NU 4-2008 [90] para su posterior comparativa.

De acuerdo con el protocolo NEMA se han evaluado distintos aspectos de la respuesta de un escáner. La resolución espacial se ha caracterizado mediante la reconstrucción de fuentes de tipo puntual situadas a distintas distancias radiales utilizando el método FBP. Con el objetivo de estudiar la habilidad de los escáneres de medir fuentes de alta actividad con precisión se han realizado medidas para estimar la fracción de dispersión (SF), la tasa de coincidencias aleatorias y la influencia del tiempo muerto. Además, para estimar las condiciones óptimas para la obtención de una imagen de calidad se ha estimado el valor del NECR. Por último, se ha evaluado la sensibilidad, que es el aspecto que mejor queremos evaluar, ya que la principal idea detrás de construir un anillo con cristales trapezoidales es la de aumentar significativamente su valor. Por ello, además de la medida propuesta por el protocolo para evaluar la sensibilidad axial, la sensibilidad se ha estudiado a través dos figuras de mérito adicionales: un mapa de sensibilidad obtenido a partir de la información de las simulaciones y la evaluación de la uniformidad en la reconstrucción de regiones homogéneas.

## Resolución espacial

En general, a medida que la fuente se desplaza radialmente, la resolución espacial en las tres direcciones espaciales se degrada y el máximo del perfil radial se desvía ligeramente hacia el centro del escáner.

Los valores de resolución obtenidos siguiendo el protocolo NEMA para las diferentes posiciones del campo de visión son equivalentes para ambos escáneres. Sin embargo, para la geometría con anillos cuboides, el impacto de los artefactos (en gran medida provenientes del método de posicionamiento) es más importante. Los perfiles obtenidos con cristales cuboides son menos suaves que para la configuración basada en cristales trapezoidales, produciendo una resolución más inestable a lo largo del campo de visión y unas imágenes más difuminadas.

## NECR

Se ha obtenido la tasa de cuentas totales, aleatorias, verdaderas, dispersadas y el NECR en función de la actividad para los maniquís tipo rata y ratón que se especifican en el protocolo NEMA, para una ventana energética de [450-700] keV, una TCW de 851 ps y un tiempo muerto en coincidencias de 10  $\mu$ s.

Para el caso del maniquí ratón el pico del NECR ocurre a 2.1 mCi con un valor de 50.4 kcps mientras que para el caso de cristales trapezoidales ocurre a 1.9 mCi con un valor de 53.5 kcps. Para el caso de la rata el pico del NECR ocurre a 2.9 mCi con un valor de 34.4 kcps para el caso de cristales cuboides, mientras que para cristales trapezoidales ocurre a 2.6 mCi con un valor de 37.2 kcps. En resumen, para el caso del maniquí tipo ratón la actividad a la cual ocurre el pico del NECR es 7.4% menor y el valor del pico es 6.2% mayor para la configuración basada en cristales trapezoidales que para la configuración basada en cristales cuboides y para el caso de la rata la actividad a la cual el pico NECR ocurre es 9.4% menor y el pico tiene un valor 8.1% mayor para los trapezoidales.

Los picos de las curvas de las tasa de cuentas suceden a actividades mayores para el maniquí tipo rata que para el tipo ratón y los valores de cuentas son menores. La fracción de dispersión para el maniquí tipo rata es mayor que la del tipo ratón como es de esperar debido al mayor tamaño del volumen del maniquí.

Al aumentar el tiempo muerto de 10 a 64  $\mu$ s se observa como la actividad a la cuál sucede el pico del NECR y su valor de la tasa de cuentas se reducen significativamente (figura R.5). Para el caso de cristales cuboides se reduce el valor de la actividad a un 41.2% y el valor de la tasa de cuentas a un 22.2%, mientras que para el caso de cristales trapezoidales se reduce la actividad a un 38.8% y el valor de la tasa de cuentas a un 21.3%. La tendencia observada

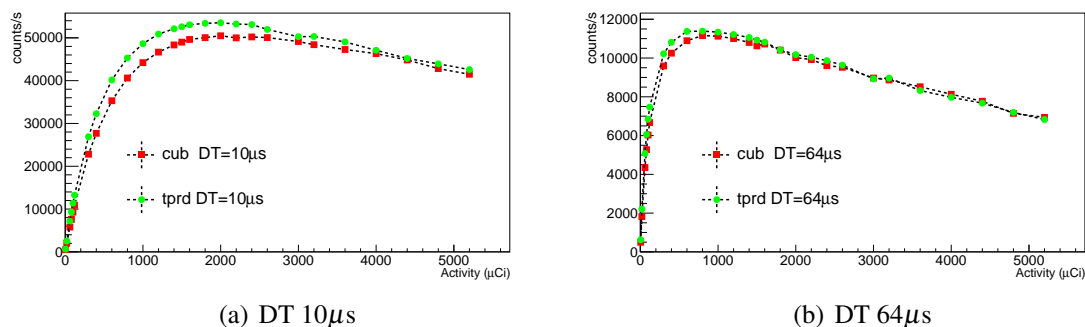


Figura R.5 NECR obtenido siguiendo las indicaciones del NEMA para ambas geometrías para el caso de un maniquí tipo ratón con un tiempo muerto en (a) de  $10\mu\text{s}$  y en (b) de  $64\mu\text{s}$ .

se mantiene, produciéndose el pico del NECR a actividades menores y con un valor de la tasa de cuentas mayor para el caso de cristales trapezoidales.

### Sensibilidad

A continuación, se resumen los resultados obtenidos a partir de las tres figuras de mérito empleadas para evaluar la sensibilidad.

**Sensibilidad axial** La sensibilidad obtenida en el centro del escáner siguiendo el protocolo NEMA ha sido de un 2.29% para cristales cuboides y de un 2.56% para cristales trapezoidales lo que corresponde a un aumento del 11.79% para el caso de cristales trapezoidales (figura R.6). La sensibilidad media sobre el campo de visión axial del escáner para la configuración basada en cristales cuboides es de 1.23% y de 1.39% para cristales trapezoidales lo que corresponde a un aumento del 13.63%.

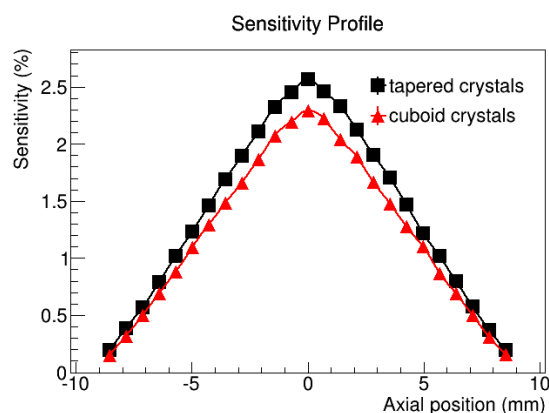


Figura R.6 Perfil de la sensibilidad axial en la posición central en el plano transaxial para ambas configuraciones.

**Mapa de sensibilidad** Otra posibilidad de caracterizar la sensibilidad es a partir de un mapa de sensibilidad utilizando la información de las simulaciones Monte Carlo. El valor de cada pixel del mapa de sensibilidad se define como la probabilidad de detectar un evento de aniquilación emitido desde dicho pixel por cualquier par de detectores del escáner.

En este estudio nos centramos en los principales componentes del mapa de sensibilidad, la cobertura geométrica y la eficiencia intrínseca de los cristales. Para ello, se ha desarrollado una simulación de un cilindro homogéneo de 1 MBq de actividad que emite rayos gamma de 511 keV en la misma dirección en sentidos opuestos sin incluir la actividad intrínseca del lutecio, ni los fotones ópticos. Solamente se han procesado la coincidencias verdaderas.

El valor de cada vóxel del mapa de sensibilidad se ha obtenido de la fracción de eventos detectados como coincidencias verdaderas que cumplen las condiciones de posprocesado (ventana energética, condiciones geométricas) que hayan sido emitidos desde ese vóxel dividido del valor esperado de eventos emitidos desde dicho vóxel teniendo en cuenta su volumen y la densidad de actividad simulada.

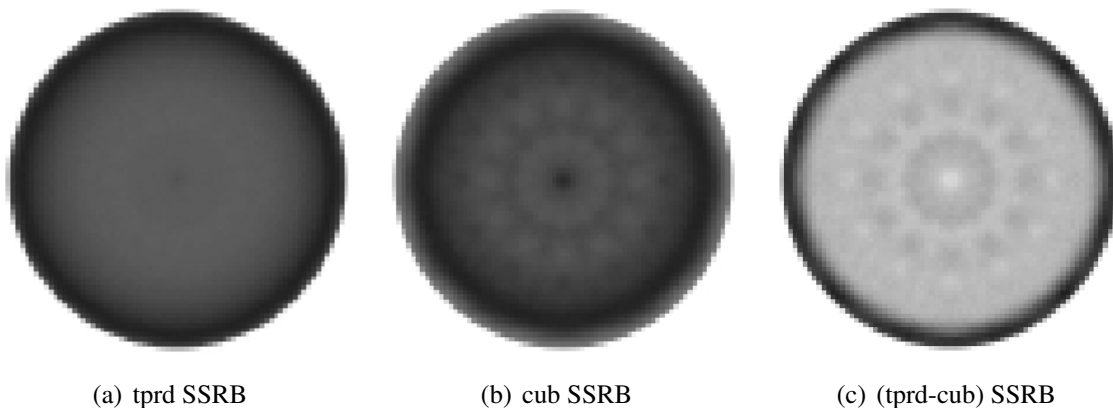


Figura R.7 Mapa de sensibilidad basado en simulaciones Monte Carlo de un cilindro homogéneo que cubre todo el campo de visión del escáner utilizando la política SSRB de rebineado axial para (a) el escáner basado en cristales trapezoidales y (b) el escáner basado en cristales cúbicos. Se muestra en (c) la resta del mapa de sensibilidad basado en cristales trapezoidales menos el correspondiente a cuboides.

La figura R.7 muestra las imágenes correspondientes a la sección central del mapa de sensibilidad con un vóxel de tamaño  $1 \times 1 \times 0.712 \text{ mm}^3$  para el escáner basado en cristales trapezoidales, para el escáner basado en cristales cuboides y la resta de ambos. El mapa de sensibilidad para los cristales trapezoidales (véase la figura R.7(a)) es prácticamente uniforme en el centro del escáner. Sin embargo, para el caso de cristales cuboides (véase la figura R.7(b)) se muestran 12 artefactos en forma de líneas conectadas a una circunferencia concéntrica con el escáner en la zona central. Estas estructuras son producidas por los 12

huecos entre los detectores contiguos que componen el anillo basado en cristales cuboides. Como es de esperar por argumentos geométricos, el valor del mapa de sensibilidad aumenta en los bordes de la sección transversal. Esto es debido a que los rayos gamma emitidos desde el borde del escáner tienen una mayor probabilidad de detección a causa de una mayor longitud de intersección con el cristal de las LoRs que no son perpendiculares a la superficie de entrada del cristal.

**Reconstrucción de regiones homogéneas** Por último se ha estudiado la sensibilidad desde el punto de vista de la reconstrucción de la imagen. Para ello, se ha simulado un cilindro homogéneo en el centro del escáner de 30 mm de radio de 1 MBq de actividad que emite fotones mono-energéticos de 511 keV en la misma dirección y sentidos opuestos. Debido a que nos centramos en la parte geométrica de la sensibilidad, tampoco se incluye la actividad natural del LYSO y además sólo son procesadas las coincidencias verdaderas para la reconstrucción de la imagen.

Las imágenes se han reconstruido tanto con FBP como con ML-EM y se han empleado tanto las posiciones de interacción ideales obtenidas de las simulaciones como las posiciones de interacción reconstruidas a partir del número de fotones ópticos detectados en los SiPMs. Las imágenes reconstruidas para el escáner basado en cristales cuboides con las posiciones ideales muestran claramente para ambos métodos los mismos artefactos observados en el mapa de sensibilidad. Sin embargo, cuando la posición de interacción es reconstruida se observan artefactos distintos con forma de anillos concéntricos en ambos escáneres, aunque más visibles para el escáner basado en cristales cuboides. En todos los casos la imagen obtenida para el escáner basado en cristales trapezoidales tiene un mayor grado de uniformidad.

Por otra parte, se observa cómo la imagen obtenida a través del método ML-EM es mucho menos ruidosa que la imagen obtenida con el método FBP.

## Conclusiones

Los cristales continuos han mostrado ser una alternativa interesante para aumentar la sensibilidad sin degradar la resolución espacial. La mayor dificultad del uso de cristales continuos es precisamente la determinación de las tres coordenadas espaciales de la posición de interacción del rayo gamma en el cristal a partir de la distribución de la luz detectada para lo que son necesarios algoritmos precisos para la determinación de la posición.

En esta tesis se ha logrado desarrollar una cabeza detectora basada en cristales continuos pintados de blanco acoplados a fotomultiplicadores de silicio con una alta resolución espacial



intrínseca. Para ello, se ha adaptado y estudiado en profundidad el modelo analítico de la distribución de la luz propuesto en [13] aplicándolo tanto a datos experimentales como simulados. El modelo se ha adaptado a nuestros datos de una manera simple con el objetivo de obtener la mayor precisión en el posicionamiento y la mejor resolución dejando a un lado las implicaciones físicas y las modificaciones necesarias para estudios futuros. El modelo original considera reflexiones especulares en las paredes del cristal con el mismo peso para dichas reflexiones que para la luz directa. En el caso de tener reflexiones puramente especulares, incluir este tipo de reflexiones mejora los resultados. Sin embargo, se ha probado que si el comportamiento de las reflexiones no es perfectamente especular, es mejor limitar la influencia de las reflexiones internas (modelo Independiente VS1\*) o incluso eliminar ese tipo de reflexiones del modelo (VS0). Se ha medido una resolución sobre la superficie del detector (centro y bordes) de 0.9 mm para el cristal de 5 mm de grosor pintado de blanco y 1.2 mm FWHM para el de 10 mm de grosor pintado de blanco. La resolución de DoI obtenida experimentalmente para ambos cristales ha sido de 2 mm FWHM. La influencia del tamaño del haz no ha sido sustraída de los resultados obtenidos. Los resultados obtenidos para el cristal de 10 mm son muy buenos comparados con los obtenidos por otros sistemas similares incluso teniendo en cuenta el AR desfavorable de nuestro detector.

Una vez caracterizada la cabeza detectora y tras obtener buenos resultados en cuanto a la resolución espacial intrínseca. Se ha puesto a prueba su capacidad para producir imágenes con un prototipo PET basado en dos cabezas detectoras que toma medidas tomográficas girando en torno a la fuente.

Haciendo uso del conocimiento adquirido en la caracterización de la cabeza detectora, se han desarrollado simulaciones detalladas de un anillo completo. Puesto que uno de los principales aspectos que se quiere estudiar es la sensibilidad, se han diseñado dos escáneres de dimensiones iguales (igual radio interno, igual separación mínima entre cristales y mismo grosor de cristal centelleador) uno basado en cristales trapezoidales y otro en cristales cuboides. La idea detrás de la construcción de un anillo basado en cristales trapezoidales es la de aumentar la sensibilidad al llenar de material centelleador los huecos en forma de cuña que se generan entre detectores contiguos en las configuraciones convencionales basadas en cristales cuboides. La respuesta de los escáneres se ha caracterizado mediante el protocolo NEMA. Un aumento en la sensibilidad media sobre el campo de visión axial del 13.63% se ha obtenido para la geometría trapezoidal mientras que los resultados en resolución espacial muestran valores equivalentes. Para ambos maniquís la actividad a la cual ocurre el pico tanto del NECR como de la tasa de cuentas verdaderas es menor y el valor de la tasa de cuentas del pico es mayor para el escáner basado en cristales trapezoidales que para el escáner basado en cristales cuboides. Además, se ha mostrado un mayor grado de homogeneidad en el mapa de

sensibilidad y una reconstrucción más uniforme de zonas homogéneas de actividad debido a la reducción de los huecos entre detectores contiguos con el uso de cristales trapezoidales.

En resumen, esta tesis ha mostrado una respuesta de alta resolución de una cabeza detectora basada en cristales continuos acoplados a SiPMs usando un modelo analítico para la distribución de luz en el cristal. La respuesta de la cabeza detectora se ha puesto a prueba con resultados satisfactorios en un prototipo preliminar PET basado en dos cabezas detectoras que rotan en torno al objeto de estudio para tomar medidas tomográficas. Con el objetivo de aumentar la sensibilidad en la configuración de un anillo completo, incrementando la cobertura de ángulo sólido, se ha estudiado la respuesta de un escáner basado en cristales trapezoidales mediante simulaciones y se ha comparado con la respuesta de un escáner basado en cristales cuboides de las mismas dimensiones. Los resultados han mostrado un aumento significativo de la sensibilidad y una recuperación más uniforme de regiones homogéneas debido a una disposición más compacta de las cabezas detectoras para el caso del escáner basado en cristales trapezoidales. Por otro lado, se han obtenido valores de resolución espacial equivalentes para ambas configuraciones siguiendo el protocolo NEMA.

# References

- [1] G Llosá, J Barrio, C Lacasta, MG Bisogni, A Del Guerra, S Marcatili, P Barrillon, S Bondil-Blin, C de La Taille, and C Piemonte. Characterization of a PET detector head based on continuous LYSO crystals and monolithic, 64-pixel silicon photomultiplier matrices. *Phys. Med. Biol.*, 55(23):7299, 2010.
- [2] Andrzej Czarnecki and Savely G Karshenboim. Decays of positronium. *arXiv preprint hep-ph/9911410*, 1999.
- [3] William W Moses. Fundamental limits of spatial resolution in PET. *Nuclear Instruments and Methods in Physics Research Section A: Accelerators, Spectrometers, Detectors and Associated Equipment*, 648:S236–S240, 2011.
- [4] Craig S Levin and Edward J Hoffman. Calculation of positron range and its effect on the fundamental limit of positron emission tomography system spatial resolution. *Physics in medicine and biology*, 44(3):781, 1999.
- [5] Gopal B Saha. Basics of PET imaging: Physics, Chemistry, and Regulations, Springer, 2010.
- [6] Simon R Cherry, James A Sorenson, and Michael E Phelps. *Physics in nuclear medicine*. Elsevier Health Sciences, 2012.
- [7] Sascha Moehrs, Alberto Del Guerra, Deborah J Herbert, and Mark A Mandelkern. A detector head design for small-animal PET with silicon photomultipliers (SiPM). *Phys. Med. Biol.*, 51(5):1113, 2006.
- [8] Yuchuan Wang, Jurgen Seidel, Benjamin MW Tsui, Juan J Vaquero, and Martin G Pomper. Performance evaluation of the GE healthcare eXplore VISTA dual-ring small-animal PET scanner. *Journal of Nuclear Medicine*, 47(11):1891–1900, 2006.
- [9] Emilie Roncali, Jennifer E Phipps, Laura Marcu, and Simon R Cherry. Pulse shape discrimination and classification methods for continuous depth of interaction encoding PET detectors. *Physics in medicine and biology*, 57(20):6571, 2012.
- [10] Christoph Werner Lerche, JM Benlloch, F Sanchez, N Pavon, B Escat, EN Gimenez, M Fernandez, I Torres, M Gimenez, J Martínez, et al. Depth of  $\gamma$ -ray interaction within continuous crystals from the width of its scintillation light-distribution. *IEEE Trans. Nucl. Sci.*, 52(3):560–72, 2005.

- [11] Matteo Morrocchi, Giovanni Ambrosi, Maria Giuseppina Bisogni, Piergiorgio Cerello, Francesco Corsi, Maria Ionica, Naema Marino, Cristoforo Marzocca, Francesco Pennazio, Giovanni Pirrone, et al. Development of a PET detector module with Depth of Interaction capability. *Nucl. Instrum. in Phys. Res. A*, 732:603–6, 2013.
- [12] T Ling, TH Burnett, TK Lewellen, and RS Miyaoka. Parametric positioning of a continuous crystal PET detector with depth of interaction decoding. *Phys. Med. Biol.*, 53(7):1843, 2008.
- [13] Zhi Li, M Wedrowski, P Bruyndonckx, and G Vandersteen. Nonlinear least-squares modeling of 3D interaction position in a monolithic scintillator block. *Phys. Med. Biol.*, 55(21):6515, 2010.
- [14] Simon R Cherry and Magnus Dahlbom. PET: physics, instrumentation, and scanners. In *PET*, page 23. Springer, 2006.
- [15] Karol Brzeziński. *Study of a High-Resolution PET System using a Silicon Detector Probe*. PhD thesis, Ph. D. thesis, Universitat de Valencia, 2015.
- [16] David Brasse, Paul E Kinahan, Carole Lartizien, Claude Comtat, Mike Casey, and Christian Michel. Correction methods for random coincidences in fully 3D whole-body PET: impact on data and image quality. *Journal of nuclear medicine*, 46(5):859–867, 2005.
- [17] Josep F Oliver and Magdalena Rafecas. Improving the singles rate method for modeling accidental coincidences in high-resolution pet. *Physics in medicine and biology*, 55(22):6951, 2010.
- [18] Josep F Oliver and M Rafecas. Modelling random coincidences in positron emission tomography by using singles and prompts: A comparison study. *PloS one*, 11(9), 2016.
- [19] Glenn F Knoll. *Radiation detection and measurement*. John Wiley & Sons, 2010.
- [20] Stefaan Tavernier. *Experimental techniques in nuclear and particle physics*. Springer Science & Business Media, 2010.
- [21] Zhi Li. *Study of 3D position determination of the interaction point in monolithic scintillator blocks for PET*. PhD thesis, Ph. D. thesis, University of Vrije, 1-168, 2011.
- [22] Pat Zanzonico. Positron emission tomography: a review of basic principles, scanner design and performance, and current systems. In *Seminars in nuclear medicine*, volume 34, pages 87–111. WB Saunders, 2004.
- [23] Simon R Cherry. The 2006 Henry N. Wagner Lecture: of mice and men (and positrons)—advances in PET imaging technology. *Journal of Nuclear Medicine*, 47(11):1735–1745, 2006.
- [24] Martin Janecek and William W Moses. Simulating scintillator light collection using measured optical reflectance. *Nuclear Science, IEEE Transactions on*, 57(3):964–970, 2010.

- [25] Emilie Roncali and Simon R Cherry. Simulation of light transport in scintillators based on 3D characterization of crystal surfaces. *Physics in medicine and biology*, 58(7):2185, 2013.
- [26] Stefaan Vandenberghe and Paul K Marsden. PET-MRI: a review of challenges and solutions in the development of integrated multimodality imaging. *Physics in medicine and biology*, 60(4):R115, 2015.
- [27] P Buzhan, B Dolgoshein, A Ilyin, V Kantserov, V Kaplin, A Karakash, A Pleshko, E Popova, S Smirnov, Yu Volkov, et al. An advanced study of silicon photomultiplier. *ICFA Inst. Bull*, 21:28, 2001.
- [28] Nicoletta Dinu. Instrumentation on silicon detectors: from properties characterization to applications, Université Paris Sud-Paris XI. 2013.
- [29] A Tapfer, V Spanoudaki, A Mann, and SI Ziegler. Comparison of three approaches for timing optimization of a dual layer Iso-apd small animal pet scanner. In *World Congress on Medical Physics and Biomedical Engineering, September 7-12, 2009, Munich, Germany*, pages 533–536. Springer, 2009.
- [30] R Greim, H Gast, T Kirn, J Olzem, G Roper Yearwood, S Schael, N Zimmermann, G Ambrosi, P Azzarello, R Battiston, et al. Silicon photomultiplier arrays-a novel photon detector for a high resolution tracker produced at FBK-irst, Italy. *arXiv preprint arXiv:0903.3883*, 2009.
- [31] Hans-Gunther Moser. Silicon photomultipliers, a new device for low light level photon detection. *Calorimetry in High Energy Physics*, 867:98–105, 2006.
- [32] Junwei Du, Jeffrey P Schmall, Yongfeng Yang, Kun Di, Emilie Roncali, Gregory S Mitchell, Steve Buckley, Carl Jackson, and Simon R Cherry. Evaluation of matrix9 silicon photomultiplier array for small-animal pet. *Medical physics*, 42(2):585–599, 2015.
- [33] Harrison H Barrett, William CJ Hunter, Brian William Miller, Stephen K Moore, Yichun Chen, and Lars R Furenlid. Maximum-likelihood methods for processing signals from  $\gamma$ -ray detectors. *IEEE Trans. Nucl. Sci.*, 56(3):725–35, 2009.
- [34] Jinhun Joung, Robert Miyaoka, and Thomas Lewellen. cMiCE: a high resolution animal PET using continuous LSO with a statistics based positioning scheme. *Nucl. Instrum. in Phys. Res. A*, 489(1):584–98, 2002.
- [35] Herman T Van Dam, Stefan Seifert, Ruud Vinke, Peter Dendooven, Herbert Löhner, Freek J Beekman, and Dennis R Schaart. A practical method for depth of interaction determination in monolithic scintillator PET detectors. *Phys. Med. Biol.*, 56(13):4135, 2011.
- [36] Peter Bruyndonckx, Sophie Léonard, Stefaan Tavernier, Cedric Lemaître, Olivier Devroede, Yibao Wu, and Magalie Krieguer. Neural network-based position estimators for PET detectors using monolithic LSO blocks. *IEEE Trans. Nucl. Sci.*, 51(5):2520–5, 2004.

- [37] P Bruyndonckx, S Leonard, C Lemaitre, S Tavernier, and Y Wu. Performance study of a PET detector module based on a continuous scintillator. *Nuclear Science, IEEE Transactions on*, 53(5):2536–2542, 2006.
- [38] George F Luger. *Artificial intelligence: structures and strategies for complex problem solving*. Pearson education, 2005.
- [39] P Garcia de Acilu, I Sarasola, M Canadas, R Cuerdo, P Rato Mendes, L Romero, and C Willmott. Study and optimization of positioning algorithms for monolithic PET detectors blocks. *Journal of Instrumentation*, 7(06):C06010, 2012.
- [40] Thomas F Coleman and Yuying Li. An interior trust region approach for nonlinear minimization subject to bounds. *SIAM Journal on optimization*, 6(2):418–45, 1996.
- [41] Adam Alessio and Paul Kinahan. PET image reconstruction. *Nuclear Medicine*, 2, 2006.
- [42] Frederic H Fahey. Data acquisition in PET imaging. *Journal of nuclear medicine technology*, 30(2):39–49, 2002.
- [43] Miles N Wernick and John N Aarsvold. *Emission tomography: the fundamentals of PET and SPECT*. Academic Press, 2004.
- [44] Dale L Bailey, David W Townsend, Peter E Valk, and Michael N Maisey. *Positron emission tomography*. Springer, 2005.
- [45] David W Townsend and Michel Defrise. *Image reconstruction methods in positron tomography*, volume 92. CERN, 1993.
- [46] John C Russ. *The image processing handbook*. CRC press, 2015.
- [47] Michel Defrise and Paul Kinahan. Data acquisition and image reconstruction for 3D PET. In *The Theory and Practice of 3D PET*, pages 11–53. Springer, 1998.
- [48] Christoph Hoeschen, Magdalena Rafecas, and Timo Aspelmeier. Algorithms for Image Reconstruction. In *Radiation Physics for Nuclear Medicine*, pages 211–232. Springer, 2011.
- [49] Paul E Kinahan and JG Rogers. Analytic 3D image reconstruction using all detected events. *Nuclear Science, IEEE Transactions on*, 36(1):964–968, 1989.
- [50] ME Daube-Witherspoon and G Muehllehner. Treatment of axial data in three-dimensional PET. *Journal of nuclear medicine: official publication, Society of Nuclear Medicine*, 28(11):1717, 1987.
- [51] V Sossi, MW Stazyk, PE Kinahan, and TJ Ruth. The performance of the single-slice rebinning technique for imaging the human striatum as evaluated by phantom studies. *Physics in medicine and biology*, 39(3):369, 1994.
- [52] Robert M Lewitt, Gerd Muehllehner, and Joel S Karp. 3D image reconstruction for PET by multi-slice rebinning and axial filtering. In *Nuclear Science Symposium and Medical Imaging Conference, 1991., Conference Record of the 1991 IEEE*, pages 2054–2061. IEEE, 1991.

- [53] Michel Defrise, Paul E Kinahan, David W Townsend, Christian Michel, Merence Sibomana, and Danny F Newport. Exact and approximate rebinning algorithms for 3-D PET data. *Medical Imaging, IEEE Transactions on*, 16(2):145–158, 1997.
- [54] Samuel Matej, Joel S Karp, Robert M Lewitt, and Amir J Becher. Performance of the Fourier rebinning algorithm for PET with large acceptance angles. *Physics in medicine and biology*, 43(4):787, 1998.
- [55] Samuel Matej and Robert M Lewitt. Practical considerations for 3-D image reconstruction using spherically symmetric volume elements. *Medical Imaging, IEEE Transactions on*, 15(1):68–78, 1996.
- [56] Michael H Buonocore, William R Brody, and Albert Macovski. A natural pixel decomposition for two-dimensional image reconstruction. *Journal of Computer Assisted Tomography*, 5(6):950, 1981.
- [57] JE Ortuño, G Kontaxakis, JL Rubio, P Guerra, and A Santos. Efficient methodologies for system matrix modelling in iterative image reconstruction for rotating high-resolution pet. *Physics in medicine and biology*, 55(7):1833, 2010.
- [58] Ana Iriarte, Roberto Marabini, Samuel Matej, Carlos Oscar Sánchez Sorzano, and Robert M Lewitt. System models for pet statistical iterative reconstruction: A review. *Computerized Medical Imaging and Graphics*, 48:30–48, 2016.
- [59] Lawrence A Shepp and Yehuda Vardi. Maximum likelihood reconstruction for emission tomography. *Medical Imaging, IEEE Transactions on*, 1(2):113–122, 1982.
- [60] Irene Torres Espallardo. Image Reconstruction and Correction Methods for MADPET-II based on Monte Carlo Techniques. 2010.
- [61] H Malcolm Hudson and Richard S Larkin. Accelerated image reconstruction using ordered subsets of projection data. *Medical Imaging, IEEE Transactions on*, 13(4):601–609, 1994.
- [62] S Jan, G Santin, D Strul, Steven Staelens, K Assie, D Autret, S Avner, R Barbier, M Bardies, PM Bloomfield, et al. Gate: a simulation toolkit for pet and spect. *Physics in medicine and biology*, 49(19):4543, 2004.
- [63] Sea Agostinelli, John Allison, K al Amako, J Apostolakis, H Araujo, P Arce, M Asai, D Axen, S Banerjee, G Barrand, et al. Geant4—a simulation toolkit. *Nuclear instruments and methods in physics research section A: Accelerators, Spectrometers, Detectors and Associated Equipment*, 506(3):250–303, 2003.
- [64] G Llosá, P Barrillon, J Barrio, MG Bisogni, J Cabello, A Del Guerra, A Etxebeste, JE Gillam, C Lacasta, JF Oliver, et al. High performance detector head for PET and PET/MR with continuous crystals and SiPMs. *Nuclear Instruments and Methods in Physics Research Section A: Accelerators, Spectrometers, Detectors and Associated Equipment*, 702:3–5, 2013.
- [65] Pierre Barrillon, S Blin, T Caceres, M Heller, C de La Taille, P Puzo, and N Seguin-Moreau. MAROC: multi-anode readout chip. In *Topical Workshop on Electronics for Particle Physics*, pages 3–7, 2007.

- [66] Rihua Mao, Liyuan Zhang, and Ren-Yuan Zhu. Optical and Scintillation Properties of Inorganic Scintillators in High Energy Physics. *IEEE Trans. Nucl. Sci.*, 55(4, Par):2425–531, 2008.
- [67] DJ Jan Van der Laan, Dennis R Schaart, Marnix C Maas, Freek J Beekman, Peter Bruyndonckx, and Carel WE van Eijk. Optical simulation of monolithic scintillator detectors using GATE/GEANT4. *Phys. Med. Biol.*, 55(6):1659, 2010.
- [68] C Wanarak, W Chewpraditkul, and A Phunpueok. Light yield non-proportionality and energy resolution of Lu 1.95 Y 0.05 SiO 5: Ce and Lu 2 SiO 5: Ce scintillation crystals. *Procedia Engineering*, 32:765–71, 2012.
- [69] Cecilia O Steinbach, Ferenc Ujhelyi, and Eموke Lorincz. Measuring the Optical Scattering Length of Scintillator Crystals. *IEEE Trans. Nucl. Sci.*, 61(5):2456–63, 2014.
- [70] K Pauwels, C Dujardin, S Gundacker, K Lebbou, P Lecoq, M Lucchini, F Moretti, AG Petrosyan, X Xu, and E Auffray. Single crystalline LuAG fibers for homogeneous dual-readout calorimeters. *J. Instrum.*, 8(09):P09019, 2013.
- [71] J Va’vra. Measurement of EPOTEK-301-2 optical glue refraction index and a reflectivity from EPOTEK-301-2/fused silica interface. *BABAR DIRC Note*, 140, 2001.
- [72] Jorge Cabello, Ane Etxebeste, Gabriela Llosá, and Sibylle I Ziegler. Simulation study of PET detector limitations using continuous crystals. *Phys. Med. Biol.*, 60(9):3673, 2015.
- [73] M Streun, R Al-Kaddoum, C Parl, U Pietrzyk, Karl Ziemons, and S Van Waasen. Simulation studies of optical photons in monolithic block scintillators. In *IEEE Nucl. Sci. Conf. R.*, pages 1380–2. IEEE, 2011.
- [74] Dennis R Schaart, Herman T van Dam, Stefan Seifert, Ruud Vinke, Peter Dendooven, Herbert Löhner, and Freek J Beekman. A novel, SiPM-array-based, monolithic scintillator detector for PET. *Phys. Med. Biol.*, 54(11):3501, 2009.
- [75] Peter Bruyndonckx, Cedric Lemaître, Dennis Schaart, Marnix Maas, Magalie Krieguer, Olivier Devroede, Stefaan Tavernier, et al. Towards a continuous crystal APD-based PET detector design. *Nucl. Instrum. in Phys. Res. A*, 571(1):182–6, 2007.
- [76] Ch W Lerche, Michael Döring, Ana Ros, V Herrero, R Gadea, RJ Aliaga, Ricardo Colom, F Mateo, JM Monzó, N Ferrando, et al. Depth of interaction detection for  $\gamma$ -ray imaging. *Nucl. Instrum. in Phys. Res. A*, 600(3):624–34, 2009.
- [77] Pedro Rato Mendes, Icíar Sarasola Martín, Mario Cañadas, Paz García de Acilu, Robin Cuypers, José Manuel Pérez, and Carlos Willmott. Characterization and performance of monolithic detector blocks with a dedicated ASIC front-end readout for PET imaging of the human brain. *Nucl. Instrum. in Phys. Res. A*, 633:S33–5, 2011.
- [78] Stefan Seifert, Gerben Van der Lei, Herman T Van Dam, and Dennis R Schaart. First characterization of a digital SiPM based time-of-flight PET detector with 1 mm spatial resolution. *Phys. Med. Biol.*, 58(9):3061, 2013.



- [79] Samuel España, Radoslaw Marcinkowski, Vincent Keereman, Stefaan Vandenberghe, and Roel Van Hoken. DigiPET: sub-millimeter spatial resolution small-animal PET imaging using thin monolithic scintillators. *Phys. Med. Biol.*, 59(13):3405, 2014.
- [80] William CJ Hunter, Harrison H Barrett, Thomas K Lewellen, and Robert S Miyaoka. Multiple-hit parameter estimation in monolithic detectors. *IEEE Trans. Med. Imaging*, 32(2):329–37, 2013.
- [81] Steven Staelens, Yves D’Asseler, Stefaan Vandenberghe, Michel Koole, Ignace Lemahieu, and Rik Van de Walle. A three-dimensional theoretical model incorporating spatial detection uncertainty in continuous detector PET. *Phys. Med. Biol.*, 49(11):2337, 2004.
- [82] P Aguiar, A Iglesias, B Couce, and C Lois. A feasibility study on the use of arrays of discrete SiPMs for MR compatible LYSO readout using Monte Carlo simulation. *J. Instrum.*, 7(06):P06002, 2012.
- [83] Ane Etxebeste, John Barrio, Enrique Muñoz, Josep F Oliver, Carles Solaz, and Gabriela Llosá. 3D position determination in monolithic crystals coupled to SiPMs for PET. *Physics in medicine and biology*, 61(10):3914, 2016.
- [84] <http://lists.opengatecollaboration.org/mailman/private/gate-users/2015-April/008280.html>.
- [85] Daniel AB Bonifacio, Nicola Belcari, Sascha Moehrs, Mauricio Morales, Valeria Rosso, Sara Vecchio, and Alberto Del Guerra. A time efficient optical model for GATE simulation of a LYSO scintillation matrix used in PET applications. *Nuclear Science, IEEE Transactions on*, 57(5):2483–2489, 2010.
- [86] DW Cooke, KJ McClellan, BL Bennett, JM Roper, MT Whittaker, RE Muenchausen, and RC Sze. Crystal growth and optical characterization of cerium-doped Lu<sub>1</sub>. 8Y<sub>0</sub>. 2SiO<sub>5</sub>. *Journal of Applied Physics*, 88(12):7360–7362, 2000.
- [87] Qingyang Wei. Intrinsic Radiation in Lutetium Based PET Detector: Advantages and Disadvantages. *arXiv preprint arXiv:1501.05372*, 2015.
- [88] Brian Gough. *GNU scientific library reference manual*. Network Theory Ltd., 2009.
- [89] Lewitt et al. *IEEE Trans. Nucl. Sci.*, 3:2054 – 61, 1991.
- [90] National Electrical Manufacturers Association et al. NEMA standards publication NU 4-2008: performance measurements of small animal positron emission tomographs. Rosslyn, VA: *National Electrical Manufacturers Association*, 2008.
- [91] Esther Vicente, Joaquin L Herraiz, Samuel España, Elena Herranz, Manuel Desco, Juan José Vaquero, and José Manuel Udías. Improved dead-time correction for pet scanners: application to small-animal pet. *Physics in medicine and biology*, 58(7):2059, 2013.
- [92] Melanie Hohberg. *Monte Carlo Simulation Studies and Image Reconstruction Methods for a Small Animal PET Scanner*. PhD thesis, München, Technische Universität München, Diss., 2012, 2012.

- [93] Alberto Galindo and Pedro Pascual. Angular momentum. In *Quantum Mechanics I*, pages 189–219. Springer, 1990.

# Appendix A

## GATE Generic Repeater to build a scanner based on tapered crystals

The list of transformations applied to each repeated detector head are described in detail below. As it has been explained in section 3.1.2.2, each detector head must be rotated twice. Each rotation ( $R_e(\theta)$ ) will be represented by a unitary vector ( $\hat{e}$ ) and a rotation angle ( $\theta$ ). The first rotation applied to all the repeaters was  $90^\circ$  around Y-axis, which can be expressed by the unitary vector  $\hat{j}=(0,1,0)$  and the angle of rotation  $\theta'=90^\circ$ . Secondly, the detectors were rotated around Z-axis,  $\hat{k}=(0,0,1)$ , and angle of rotation  $\theta=\theta''_{n_i}$  which depends on the detector number, see equation (3.3).

In general, the composition of two rotations  $R_e(\theta) = R_{e''}(\theta'')R_{e'}(\theta')$ , represented by the unitary vector  $\hat{e}$  and the angle of rotation  $\theta$ , was expressed as a function of the known parameters of each individual rotation according to the following expression [93]:

$$\vec{\tau} = \frac{\vec{\tau}' + \vec{\tau}'' + \vec{\tau}' \times \vec{\tau}''}{1 - \vec{\tau}' \cdot \vec{\tau}''}, \quad (\text{A.1})$$

where  $\vec{\tau}$  represents the product of the unitary vector of the rotation axis by the tangent of half the rotation angle,  $\vec{\tau}=\hat{e} \cdot \tan(\frac{\theta}{2})$ ,  $\vec{\tau}'=\hat{e}' \cdot \tan(\frac{\theta'}{2})$ ,  $\vec{\tau}''=\hat{e}'' \cdot \tan(\frac{\theta''}{2})$ .

Applying equation (A.1) to the specific situation mentioned above, where  $\vec{\tau}'$  represents the first rotation around  $\hat{j}$  and  $\vec{\tau}''$  the second rotation around  $\hat{k}$ ,  $\vec{\tau}$  of the resulting rotation was obtained as a function of the rotation angle around the Z-axis ( $\theta''_{n_i}$ ).

$$\vec{\tau} = \hat{e} \cdot \tan(\frac{\theta}{2}) = (-\tan(\frac{\theta''_{n_i}}{2}), 1, \tan(\frac{\theta''_{n_i}}{2})), \quad (\text{A.2})$$

From equation (A.2) the parameters  $\hat{e}$  and  $\theta$  of the composition of rotations can be obtained straightforward for each detector in order to introduce them in the placements file of the

simulation. Table A.1 shows the rotation parameters and the translation vector ( $\vec{T}_{n_i}$ ) for each detector head identified by the detector number head ( $n_i = 1, \dots, N_{sectors}$ ).

Table A.1 Values of the transformations applied to each detector head using the generic repeater that must be specified in GATE placements file.

Transformations	
Rotation angle	$\theta_{n_i} = 2 \cdot \arctan \sqrt{1 + 2 \tan(\theta_{n_i}'')^2}$
Rotation unitary vector	$\hat{e}_{n_i} = \left( \frac{-\tan(\frac{\theta_{n_i}''}{2})}{\sqrt{1+2 \tan(\theta_{n_i}'')^2}}, \frac{1}{\sqrt{1+2 \tan(\theta_{n_i}'')^2}}, \frac{\tan(\frac{\theta_{n_i}''}{2})}{\sqrt{1+2 \tan(\theta_{n_i}'')^2}} \right)$
Translation	$\vec{T}_{n_i} = (R \cos(\theta_{n_i}''), R \cos(\theta_{n_i}''), 0)$

# Appendix B

## Contributions related to the thesis

### Publications directly associated with the thesis

#### Journal publications

- [1] Ane Etxebeste, John Barrio, Enrique Muñoz, Josep F. Oliver, Carles Solaz, and Gabriela Llosá. 3D position determination in monolithic crystals coupled to SiPMs for PET. *Phys. Med. Biol.*, 61(10):3914, 2016.
- [2] Jorge Cabello, Ane Etxebeste, Gabriela Llosá, and Sibylle I. Ziegler. Simulation study of PET detector limitations using continuous crystals. *Phys. Med. Biol.*, 60(9):3673, 2015.
- [3] Gabriela Llosá, Pierre Barrillon, John Barrio, Maria Giuseppina Bisogni, Jorge Cabello, Alberto Del Guerra, Ane Etxebeste, John E. Gillam, Carlos Lacasta, Josep F. Oliver, Magdalena Rafecas, Carles Solaz, and Vera Stankova. High performance detector head for PET and PET/MR with continuous crystals and SiPMs. *Nucl. Inst. Meth. Phys. Res. Sec. A*, 702:3–5, 2013.

#### Conference Proceedings

- [1] Ane Etxebeste, John Barrio, Carlos Lacasta, Gabriela Llosá, Enrique Muñoz, Carles Solaz, Paola Solevi, and Josep F. Oliver. Simulation study of sensitivity and resolution for a small animal PET ring based on continuous crystals. In *Nuclear Science Symposium and Medical Imaging Conference (NSS/MIC)*, pages 1–4. IEEE, 2015.
- [2] Ane Etxebeste, John Barrio, Jorge Cabello, John E. Gillam, Carlos Lacasta, Gabriela Llosá, Josep F. Oliver, and Magdalena Rafecas. Tomógrafo PET de alto rendimiento basado en la tecnología cristal continuo/SiPM. In *XXXIV Reunión Bienal de la Real Sociedad Española de Física*, pages 772–3. RSEF, 2013.

## Congress contributions directly associated with the thesis

- [1] Ane Etxebeste, John Barrio, Carlos Lacasta, Enrique Muñoz, Josep F. Oliver, Pablo G. Ortega, Carles Solaz, and Gabriela Llosá. Determinación de la posición en cristales continuos. 2016. Talk at I Jornadas RSEF/IFIMED de Física Médica. Valencia, España.
- [2] Ane Etxebeste, John Barrio, Carlos Lacasta, Gabriela Llosá, Enrique Muñoz, Carles Solaz, Paola Solevi, and Josep. F. Oliver. Simulation Study of Sensitivity and Resolution for a small animal PET ring based on Continuous Crystals. 2015. Poster presented at IEEE NSS-MIC, November, San Diego, CA, USA.
- [3] Ane Etxebeste, John Barrio, Jorge Cabello, Carlos Lacasta, Josep F. Oliver, Magdalena Rafecas, Carles Solaz, and Gabriela Llosá. (M10-80) Monte Carlo Simulation of a Continuous Crystal Coupled to a SiPM Array. 2014. Poster presented at IEEE NSS-MIC, November 8–15, Seattle, WA, USA.
- [4] Ane Etxebeste, John Barrio, Jorge Cabello, John E. Gillam, Carlos Lacasta, Gabriela Llosá, Josep F. Oliver, and Magdalena Rafecas. Tomógrafo PET de alto rendimiento basado en la tecnología cristal continuo/SiPM. 2013. Talk at XXXIV Reunión Bienal de la Real Sociedad Española de Física.
- [5] Ane Etxebeste, John Barrio, Jorge Cabello, John E. Gillam, Gabriela Llosá, Carlos Lacasta, Josep F. Oliver, and Magdalena Rafecas. High Resolution PET detector based on Continuous Crystals and SiPMs. 2013. Talk at II PCI2011 Workshop at IFIC, Valencia.

## Other work related to the thesis

The position estimation algorithm developed in this thesis has been employed in other work of the IRIS group which is not directly associated with the work presented in this thesis.

### Journal publications

- [1] Gabriela Llosá, Marco Trovato, John Barrio, Ane Etxebeste, Enrique Muñoz, Carlos Lacasta, Josep F. Oliver, Magdalena Rafecas, Carles Solaz, and Paola Solevi. First Images of a Three-layer Compton Telescope prototype for Treatment Monitoring in hadron therapy. *Frontiers in oncology*, 6, 2016.

- [2] John Barrio, Ane Etxebeste, Carlos Lacasta, Enrique Muñoz, Josep F. Oliver, Carles Solaz, and Gabriela Llosá. Performance of VATA64HDR16 ASIC for medical physics applications based on continuous crystals and SiPMs. *Journal of Instrumentation*, 10(12):P12001, 2015.

### Conference Proceedings

- [1] Enrique Muñoz, John Barrio, Ane Etxebeste, Carlos Lacasta, Josep F. Oliver, Carles Solaz, Paola Solevi, Marco Trovato, and Gabriela Llosá. Characterization and simulation results of a two/three-layer compton telescope with LaBr<sub>3</sub> and SiPMs. In *Nuclear Science Symposium and Medical Imaging Conference (NSS/MIC), 2015 IEEE*, pages 1–4. IEEE, 2015.
- [2] John Barrio, Jorge Cabello, Ane Etxebeste, Carlos Lacasta, Josep F Oliver, Magdalena Rafecas, Carles Solaz, Vera Stankova, and Gabriela Llosá. Electronics upgrade and crystal geometry optimization for a sub-millimeter small animal PET based on continuous crystals and SiPMs. In *Nuclear Science Symposium and Medical Imaging Conference (NSS/MIC)*, pages 1–4. IEEE, 2013.
- [3] John Barrio, Pierre Barrillon, Maria Giuseppina Bisogni, Jorge Cabello, Alberto Del Guerra, Ane Etxebeste, Carlos Lacasta, Josep F Oliver, Magdalena Rafecas, Carles Solaz, Vera Stankova, Christophe de-la Taille, and Gabriela Llosá. Studies for performance improvement of a small animal PET prototype based on continuous LYSO crystals and SiPM matrices. In *Nuclear Science Symposium and Medical Imaging Conference (NSS/MIC)*, pages 3205–3208. IEEE, 2012.

